Design and characterization of multiferroic composites spinel perovskite with (0-3) and core shell nanofiber connectivities

Youness Hadouch, Daoud Mezzane, M'Bark Amjoud, Mimoun El Marssi, Yaovi Gagou

Thèse de Doctorat

Mention : Physique
Spécialité : Physique de la Matière Condensée

présentée à ***l'Ecole Doctorale en Sciences Technologie et Santé (ED 585)*** **de**
l'Université de Picardie Jules Verne
et
à l'Ecole doctorale en Science et Techniques et Sciences Médicales
de l'Université Cadi Ayyad

par

Youness HADOUCH

pour obtenir le grade de Docteur de l'Université de Picardie Jules Verne

Design and characterization of multiferroic composites spinel perovskite with (0-3) and core shell nanofiber connectivities

Soutenue le 07 Juillet 2023, après avis des rapporteurs, devant le jury d'examen :

M. Abdelilah BENYOUSSEF, Professeur, Académie Hassan II	**Président**
M. Jean JURASZEK, Maître de Conférences HDR, Université de Rouen	**Rapporteur**
M. Zdravko KUTNJAK, Professeur, Institut Jožef Stefan	**Examinateur**
M. Lahoucine HAJJI, Professeur, Université Cadi Ayyad	**Examinateur**
M. Mimoun EL MARSSI, Professeur, Université de Picardie Jules Verne	**Directeur de thèse**
M. Daoud MEZZANE, Professeur, Université Cadi Ayyad	**Directeur de thèse**
M. M'barek AMJOUD, Professeur, Université Cadi Ayyad	**Co- encadrant**
M. Yaovi GAGOU, Professeur, Université de Picardie Jules Verne	**Co- encadrant**

DEDICATION

In honor of my father, who sadly did not live long enough to see the termination of an adventure that he was quite proud of.

To my mother Fatima, my sister Fatiha, my brothers Mustapha and Abdeljalil for their exceptional love and support. Their constant prayers for me and my progress during this entire journey have allowed me to successfully complete this project.

To my wife, Farah, who has been extraordinarily supportive and understanding throughout the entire journey, providing me with inspiration and motivation.

May this work serve as a testament to my unending love for them.

ACKNOWLEDGEMENT

First and foremost, I would like to thank God, the almighty, who has granted countless blessing, knowledge, and opportunities throughout all the challenging moments of completing this dissertation.

In line with Nelson Mandela's words, ***"None of us, acting alone, can achieve success"*** I recognize that the completion of this thesis owes much of its success not only to my own efforts but also to the invaluable encouragement and guidance provided by many others. Therefore, I would like to sincerely express my gratitude to all those who have contributed to the successful completion of this thesis.

This thesis was carried out in collaboration with:

- *Laboratory of Innovative Materials, Energy and Sustainable Development (IMED), Cadi- Ayyad University, Faculty of Sciences and Technology, Marrakesh, Morocco;*
- *Laboratory of Physics of Condensed Matter (LPMC), University of Picardie Jules Verne, Amiens, France;*
- *Jozef Stefan Institute, Ljubljana, Slovenia;*
- *Aix-Marseille University - CNRS, IM2NP Faculté Des Sciences de Saint-Jérôme Marseille, France ;*
- *Institute of Physics AS CR, Prague, Czech Republic.*

Financial support was provided by the CNRST Priority Program (PPR 15/2015), European Union Horizon 2020 Research and Innovation actions MSCA-RISE-ENGIMA (No. 778072) / MSCA-RISE-MELON (No. 872631) and Slovenian Research Agency grant program (P1-0125).

I am immensely grateful to my supervisors, Prof. Daoud MEZZANE Prof. M'barek AMJOUD, Prof. Mimoun EL MARSSI and Prof. Yaovi GAGOU, for their invaluable guidance, expertise, constructive criticism, numerous helpful suggestions, and valuable advice throughout my work on this particular topic. I would like to extend my sincere thanks to them for not only providing me with the opportunity to work in their groups, but also for facilitating collaborations with other research teams.

I would like to sincerely thank Prof. Daoud MEZZANE for his invaluable guidance as my thesis supervisor. His unwavering academic and personal support, along with his constant encouragement, have been instrumental in my success. His mentorship has been akin to that

of a second father, and without his steadfast commitment, I would not have been able to achieve this accomplishment.
I gratefully acknowledge my appreciation to Prof. M'barek AMJOUD as the thesis co-supervisor for his continual supervision. He has provided me with insightful comments on my research that have been a substantial aid in this accomplishment.

I extend my gratitude to my supervisor, Prof. Mimoun EL MARSSI for his careful instruction and constructive advices, his contribution was extremely beneficial to materialize this work.

I would like to thank Prof. Abdelilah LAHMAR, Prof. Mustapha JOUIAD, Prof. Jamal BELHADI, Prof. Bouchra ASBANI and Mrs Manal BENYOUSSEF from LPMC (Amiens, France) for providing me the opportunity to collaborate with them and for instructing me to Raman spectroscopy and ferroelectric measurements, and their discussions on ferroelectric materials.

A huge gratitude is also addressed to Professors Zdravko KUTNJAK, Khalid HOUMMADA, Valentyn LAGUTA for giving me the chance to work in their laboratories.

I would also like to thank all the scientific and technical staff (Prof. Voicu DOLOCAN, Prof. Matjaž SPREITZER, Prof. Hana URŠIČ, Prof. Nikola NOVAK, Mr. Nouredine OUELDNA and Mr. Damjan VENGUST) from the three laboratories with whom I had a lot of fun working with on the characterization of my samples. Thank you all for your kindness and for sharing your knowledge and experience with me; it has been an honor and a great pleasure to work with you during my secondments.

I express my sincere gratitude to Professors Lahoucine HAJJI, Elhassan CHOUKRI, Abdelhadi ALIMOUSSA and Lahcen ESSALEH from IMED-Lab (UCA-Marrakesh) for their invaluable support, abundant insightful suggestions, and valuable counsel during my research on this specific subject.

My special thanks go to my colleagues and friends Nayad ABDALLAH, Ismail EL IDRISSI, Radia BELKEZIZ, Marwa ZAHID, Salma TOUILI, Salima LAHBABI, Sara GHAZI, Mohamed OUBANI for their kindness and for all the discussions, helps and collaborations.

I would also like to warmly thank all the members of the laboratory (IMED-Lab) having directly or indirectly encouraged or contributed to the realization of this thesis.
I would like to sincerely thank Prof. Ali BACHNOU and Mrs. Fatiha CHAYEB for their unwavering support over the course of my academic career. I am incredibly appreciative of their guidance, oversight, and, most importantly, their parental love and care. My academic progress has been greatly influenced by their steadfast support, and I really appreciate everything they have done.

I express my special thanks to my brother-in-law, Mohamed IDRAMI, for being incredibly kind and supportive during my first days of my internship in Amiens. I am truly grateful for his valuable advice and suggestions, which helped me navigate this new experience.

I would like to extend my gratitude to my cousin, Khalid ID HADOUCH, who has consistently stood by my side, providing unwavering support in both my personal and professional undertakings. I am truly thankful for his constant presence and assistance throughout my journey.

Youness HADOUCH

Table of Content

List of Figures

Résumé long en Français de la Thèse

Contexte Générale

La microélectronique a vu une évolution vers des circuits intégrés de plus en plus petits offrant des fonctionnalités de plus en plus sophistiquées. Cette tendance à la miniaturisation vise à accélérer les performances, réduire la consommation d'énergie et les coûts. Le développement de matériaux multifonctionnels, qui combinent des propriétés bien connues en un seul composé, est encouragé par cette tendance[1], [2]. Les matériaux multiferroïques (MF) avec coexistence d'au moins deux ordres ferroïques (ferroélectrique (FE), ferro(antiferro/ferri) magnétique et ferroélastique) ont attiré plus d'attention en raison de leur potentiel d'applications en tant que dispositifs multifonctionnels. Un couplage entre ces ordres ferroïques peut produire des effets intéressants tels que l'effet magnétoélectrique (ME). L'effet ME est l'apparition d'une polarisation électrique P en présence d'un champ magnétique H (appelé effet ME direct ou effet M_{EH} : $P=\alpha H$) et/ou l'apparition d'une aimantation M en présence d'un champ électrique E (connu sous le nom d'effet ME inverse ou effet M_{EE} : $M=\alpha E$). En bref, les matériaux ME ont la capacité de commuter et/ou d'ajuster la polarisation (P) par un champ magnétique (H) et la magnétisation (M) peut être manipulée via un champ électrique (E)[3], [4]. Cette propriété offre actuellement une toute nouvelle perspective sur la prochaine génération de dispositifs électroniques révolutionnaires tels que les dispositifs de mémoire à états multiples qui peuvent être écrits électriquement et lus magnétiquement, le déphaseur à micro-ondes contrôlé électriquement ou la résonance ferromagnétique contrôlée en tension, les dispositifs électro-optiques ou magnétiques contrôlés magnétiquement, les dispositifs piézoélectriques, cellules de mémoire magnétoélectriques et capteurs magnétiques ultra-sensibles[5], [6].

Les matériaux magnétoélectriques peuvent être classés en deux types : (i) les matériaux multiferroïques monophasés, où les champs magnétiques et électriques sont intrinsèquement couplés, mais le couplage entre eux est généralement faible, et (ii) les composites multiphasés constitués de phases piézoélectriques et magnétostrictives, qui sont spatialement séparés et reliés par une interface[7], [8], [9], [10]. Dans ces composites, le couplage magnétoélectrique est indirectement induit par l'interaction de contrainte entre les effets piézoélectrique et magnétostrictif. En effet, lorsqu'un champ électrique est appliqué à un matériau composite, il crée une contrainte mécanique sur la phase piézoélectrique, qui passe alors à la phase magnétostrictive et modifie son moment magnétique. L'effet inverse est également

possible[11]. Un facteur crucial pour obtenir des effets ME robustes dans les composites multiphases est de maximiser le transfert de contrainte entre les différentes phases. Par conséquent, la zone d'interface entre les phases piézoélectriques et magnétostrictives joue un rôle critique dans ce type de couplage ME médié par la contrainte mécanique[12], [13].

Plusieurs types de matériaux peuvent servir de phase magnétostrictive dans les matériaux composites, notamment les alliages de terres rares, les rubans amorphes, les manganites et la ferrite. Les matériaux magnétostrictifs géants à base de terres rares comme le Terfenol-D (avec la formule chimique $Tb_{0.3}Dy_{0.7}Fe_{1.9}$) présentent des résultats exceptionnels en raison de leurs propriétés magnétostrictives puissantes[7]. Le coût élevé et la disponibilité limitée des terres rares ont conduit à un intérêt croissant pour l'utilisation de ferrites à la place. La ferrite de cobalt $CoFe_2O_4$, par exemple de cette famille, présente des propriétés magnétostrictives et magnétocaloriques remarquables, c'est pourquoi nous l'avons sélectionnée pour nos composites multiferroïques et nos applications de réfrigération magnétique [14].

D'autre part, les matériaux à base de plomb sont couramment utilisés comme phase piézoélectrique dans les composites multiferroïques en raison de leurs propriétés de polarisation et piézoélectriques exceptionnelles. Cependant, ces matériaux ont des effets préjudiciables sur l'environnement, ce qui justifie la recherche de matériaux alternatifs ayant des propriétés similaires mais présentant moins d'inconvénients environnementaux. Par conséquent, le titanate de baryum $BaTiO_3$ (BT) est l'un des principaux candidats pour un composite multiferroïque sans plomb. Cependant, BT a une faible constante diélectrique, une température de Curie élevée et de faibles propriétés de stockage d'énergie. Une façon d'améliorer ces propriétés est le dopage, où les sites A et les sites B sont substitués par d'autres éléments. Plusieurs études ont rapporté les effets du dopage BT avec Sn et Ca, et leur impact sur le comportement diélectrique, la transition de phase T_C et les propriétés électrocaloriques. Le co-dopage dans les deux sites peut entraîner la formation de la phase morphotropique (MPB), qui améliore les propriétés diélectriques, piézoélectriques et électrocaloriques.

L'objectif principal de cette thèse est double. Dans un premier temps, il vise à approfondir notre compréhension des propriétés structurales, ferroélectriques et magnétiques des matériaux piézoélectriques sélectionnés ($Ba_{0.95}Ca_{0.05}Ti_{0.89}Sn_{0.11}O_3$ en abrégé BCTSn) et magnétostrictifs ($CoFe_2O_4$ en abrégé CFO). Deuxièmement, il vise à quantifier le couplage magnétoélectrique entre ces matériaux via deux types de connectivités : les composites particulaires 0-3 et les nanofibres Core-shell.

Les résultats obtenus au cours de cette thèse sont présentés sous forme d'articles publiés dans des revues indexées :

Le premier travail a été publié dans « Journal of Materials Science : Materials in Electronics » le 15 novembre 2021. Le manuscrit intitulé « Electrocaloric effect and high energy storage efficiency in lead-free $Ba_{0.95}Ca_{0.05}Ti_{0.89}Sn_{0.11}O_3$ ceramic elaborated by sol–gel method ».

https://doi.org/10.1007/s10854-021-07411-2

Le deuxième travail a été publié dans « Journal of Magnetism and Magnetic Materials » le 4 septembre 2022. Le manuscrit intitulé « Enhanced Relative cooling Power and large inverse magnetocaloric effect of cobalt ferrite nanoparticles synthesized by auto-combustion method».

https://doi.org/10.1016/j.jmmm.2022.169925

Le troisième travail a été publié dans « Journal of Materials Science : Materials in Electronics » le 20 février 2023. Le manuscrit intitulé « Piezoelectric, magnetic and magnetoelectric properties of a new lead-free multiferroic (1-x) $Ba_{0.95}Ca_{0.05}Ti_{0.89}Sn_{0.11}O_3$ - (x) $CoFe_2O_4$ particulate composites».

https://doi.org/10.1007/s10854-023-10145-y

Le quatrième travail a été soumis au journal « ACS Applied Nano Materials»et il est en révision. Le manuscrit intitulé « Multiferroic $CoFe_2O_4$-$Ba_{0.95}Ca_{0.05}Ti_{0.89}Sn_{0.11}O_3$ Core-Shell Nanofibers for Magnetic Field Sensor Applications».

Elaboration et caractérisation de la céramique BCTSn

Cette partie présente une étude expérimentale du stockage de l'énergie en température et des propriétés électrocaloriques de la céramique $Ba_{0.95}Ca_{0.05}Ti_{0.89}Sn_{0.11}O_3$ (BCTSn). Le BCTSn a été élaboré par le procédé sol-gel et fritté à 1350°C pendant 7h. Pour évaluer l'effet électrocalorique, la relation de Maxwell a été utilisée comme approche expérimentale indirecte (voir chapitre 1).

En utilisant le programme de raffinement Rietveld, les résultats XRD ont été affinés et indiquent que la composition de nos matériaux est une combinaison d'une structure tétragonale avec le groupe spatial (P4mm) et la structure orthorhombique (Amm2) (Figure 1.a). La céramique BCTSn frittée présente de grandes microstructures avec des joints de grains bien définis, et sa distribution granulométrique est estimée à environ 28 ± 0,7 µm (Figure 1.b). La céramique a une densité apparente de 5,73 g cm^{-3} et une densité relative de 92 %. L'analyse qualitative

confirme la présence des éléments Ba, Ca, Ti, Sn et O, et leurs pourcentages atomiques sont en accord avec les rapports attendus (Voir chapitre 3).

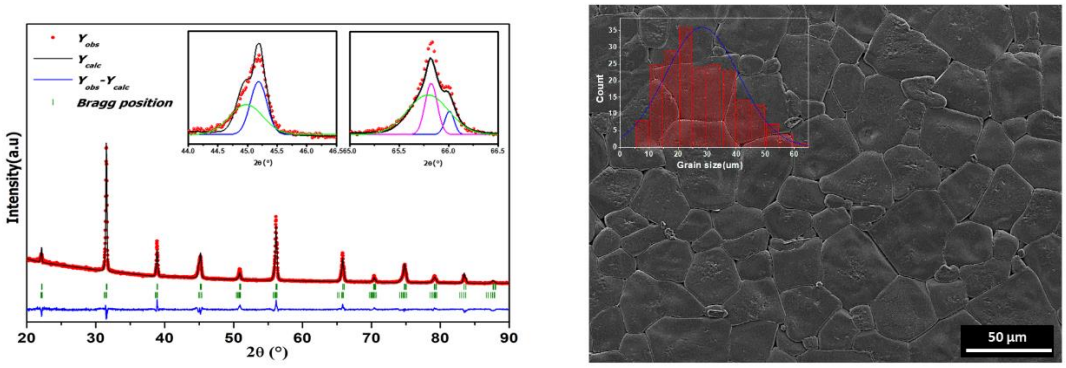

Figure 1 : *(a) Diagrammes de diffraction des rayons X de la céramique BCTSn ; (b) Micrographie MEB de la céramique BCTSn, l'encart de la figure montre la distribution granulométrique.*

Les propriétés diélectriques de la céramique ont été étudiées en fonction de la température et de la fréquence (Figure 2.a). Les résultats ont montré trois pics distincts à 12, 31 et 47 °C qui correspondaient à différentes transitions de phase. En comparant avec BT, le remplacement de Ti^{4+} par des ions Sn^{4+} a déplacé les températures de transition vers des valeurs plus élevées et réduit T_C [15]. Les propriétés ferroélectriques ont été analysées à l'aide de boucles d'hystérésis P-E, qui ont montré le comportement ferroélectrique de la céramique en dessous de T_C (Figure 2.b). Au-dessus de 383 K, la polarisation a montré un comportement linéaire, indiquant la présence de la phase paraélectrique.

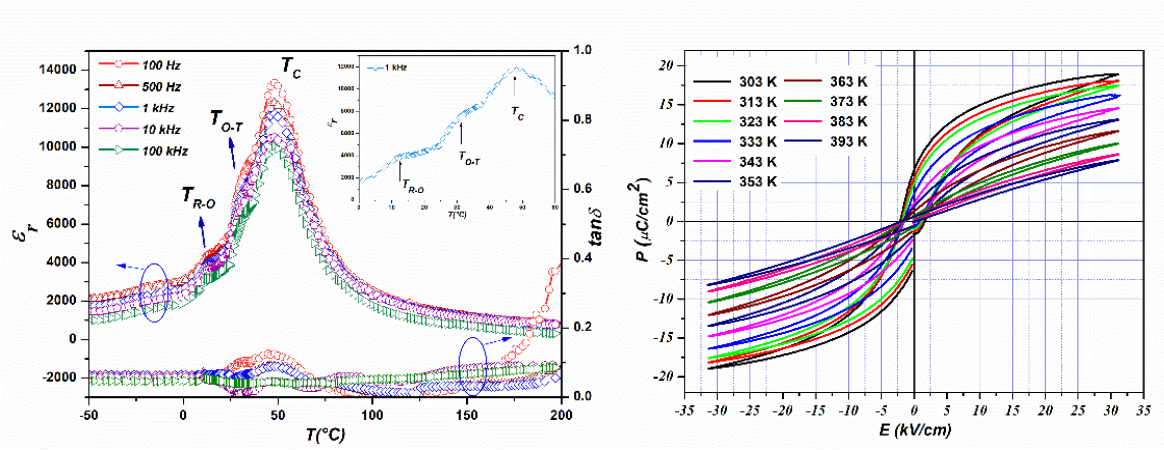

Figure 2: *(a) Dépendance en température de la constante diélectrique et de la perte diélectrique à différentes fréquences pour la céramique BCTSn frittée à 1350/7h (l'encart : Zoom sur la courbe de la constante diélectrique en fonction de T à 1 kHz) ;(b) Boucles d'hystérésis P-E de l'échantillons BCTSn.*

Les propriétés de stockage d'énergie de la céramique BCTSn ont été évaluées en calculant la densité d'énergie récupérable, la densité d'énergie totale et l'efficacité du stockage d'énergie.

Ces valeurs ont été obtenues à l'aide des équations (1.28 - 1.31) rapportées au chapitre 1. Notre matériau a montré des propriétés prometteuses avec une densité d'énergie récupérable de 107,25 mJ cm^{-3} et une efficacité de stockage de 51% à température ambiante (Figure 3). Avec l'augmentation de la température, la densité d'énergie totale diminue, mais la densité d'énergie récupérable restait stable dans une certaine plage de températures. Le matériau a surpassé les autres matériaux céramiques sans plomb rapportés dans la littérature, y compris la céramique $Ba_{0.85}Ca_{0.15}Zr_{0.1}Ti_{0.9}O_3$ (BCZT)[16]–[20].

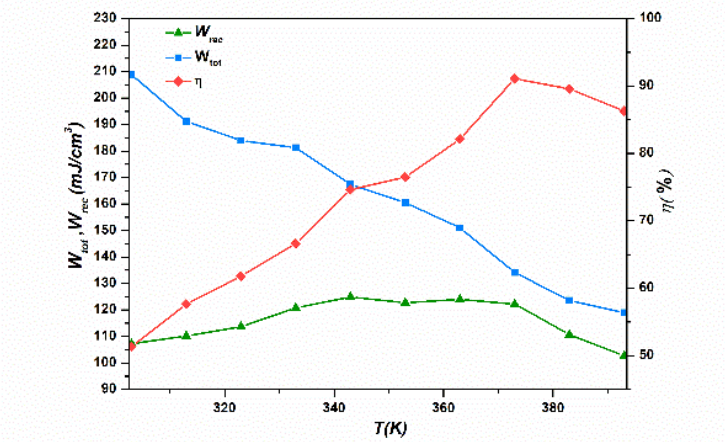

Figure 3 : *Performances de stockage d'énergie dans la céramique BCTSn.*

La méthode expérimentale indirecte a été utilisé pour évaluer l'effet électrocalorique (EC) dans les céramiques BCTSn en analysant leurs résultats P(E,T) (voir la partie III-2-5 du chapitre 1). Le changement de température adiabatique réversible a montré deux grands pics correspondant aux transitions de phase à 315 K et 337 K (Figure 4.a). L'échantillon a montré une réponse EC élevée et a atteint une sensibilité électrocalorique effective de 0,268 K mm kV^{-1} à 30 kV cm^{-1}. L'étude suggère que la réponse EC exceptionnelle dans BCTSn est principalement due à la coexistence de plusieurs phases, ce qui peut améliorer les changements d'entropie via des dipôles polaires désordonnés/ordonnés. Par conséquent, une approche prometteuse pour améliorer les propriétés EC des systèmes de matériaux consiste à envisager une coexistence de phases multiples[21]–[23].

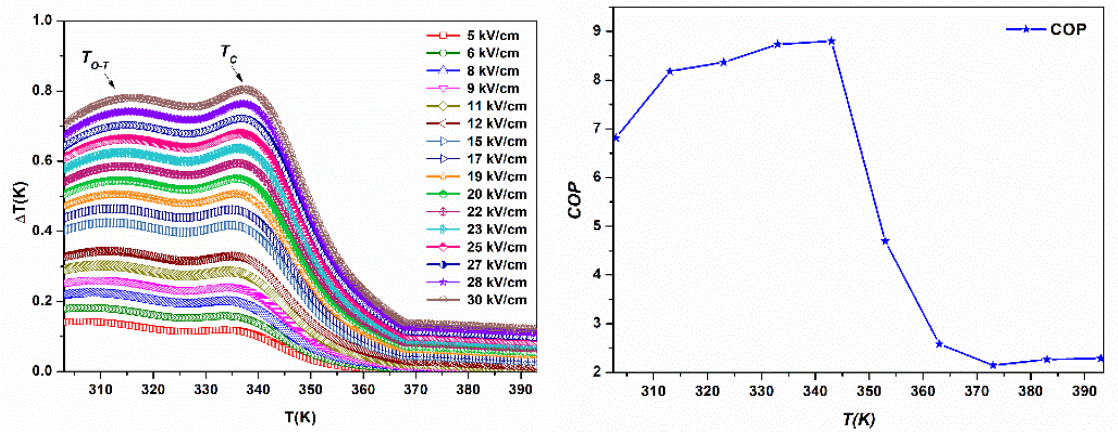

Figure 4 : *Dépendance à la température de (a) ΔT, (b) COP*

L'efficacité EC d'un échantillon BCTSn a été évaluée pour une application industrielle en utilisant le coefficient de performance (COP) tel que défini par l'équation 1.35. La valeur COP augmente légèrement avec la température et atteint un maximum de 8,8 à 342 K, avant de diminuer au-dessus de la température de transition. Cette valeur de COP est supérieure à celles trouvées dans d'autres matériaux rapportés (Figure 4.a).

Pour résumer, la céramique $Ba_{0.95}Ca_{0.05}Ti_{0.89}Sn_{0.11}O_3$ respectueuse de l'environnement a été élaborée par la méthode sol-gel. L'étude a ensuite porté sur la structure, les propriétés diélectriques, les transitions de phase, les performances de stockage d'énergie et les propriétés électrocaloriques. Les résultats ont montré que BCTSn présente d'excellentes performances de stockage d'énergie, avec un W_{rec} de 124 mJ cm^{-3} et η de 91,07 % à 373 K sous un champ électrique de 30 kV cm^{-1}. De plus, le matériau présentait une réponse électrocalorique significative, avec un ΔT de 0,807 K, ΔS de 0,844 J kg^{-1} K^{-1} et ζ de 0,268 K mm kV^{-1} sous 30 kV cm^{-1}, et une valeur COP de 8,8 à 343 K. Ces résultats suggèrent que le BCTSn, étant sans plomb, présente un potentiel considérable pour des applications de réfrigération et de stockage à haute énergie respectueuses de l'environnement.

Elaboration et caractérisation de la céramique CFO

L'effet magnétocalorique (MC) a attiré l'attention des chercheurs en raison de son utilisation potentielle dans diverses applications industrielles. Des efforts sont déployés pour développer des matériaux magnétiques écologiques et respectueux des technologies de chauffage et de refroidissement[24], [25]. L'effet MC est une propriété intrinsèque des matériaux magnétocaloriques qui provoque un changement de température réversible et adiabatique lorsqu'ils sont exposés à un champ magnétique variable[25]. L'effet MC a été observé dans diverses familles de matériaux magnétiques, notamment les manganites pérovskites, les alliages

de manganite et les ferrites spinelles. L'ordre de transition de phase des matériaux magnétocaloriques détermine l'amplitude de l'effet MC, les matériaux présentant une transition de phase du premier ordre ayant généralement un changement d'entropie magnétique et un changement de température adiabatique plus importants.

Parmi les ferrites de spinelle, la ferrite de cobalt ($CoFe_2O_4$, CFO) a montré un grand intérêt scientifique en raison de ses propriétés uniques, notamment une magnétisation à saturation modérée, une coercivité élevée, de bonnes propriétés magnétostrictives, une température de Curie élevée, une isolation électrique et une stabilité chimique[26]–[28]. CFO a une large gamme d'applications dans divers domaines, y compris la réfrigération magnétique, la thérapie du cancer par hyperthermie et les applications biomédicales[29], [30]. La méthode de synthèse des nanoparticules CFO a un impact significatif sur leurs propriétés magnétiques, la taille des grains et la microstructure, qui à leur tour influencent leurs propriétés MC[31], [32]. La combinaison des techniques sol gel et auto-combustion a récemment suscité l'intérêt des chercheurs. Cette méthode produit des échantillons de ferrite avec une excellente homogénéité chimique, une grande pureté et une forte cristallisation. De plus, il ne nécessite qu'un équipement de base, un processus de préparation simple, prend peu de temps et utilise peu d'énergie externe[33], [34].

Dans cette partie, nous étudions les propriétés structurales, magnétiques et magnétocaloriques de $CoFe_2O_4$ sur une plage de températures élevées de 300 K à 900 K. Notre approche impliquait l'utilisation d'une combinaison de techniques sol-gel et auto-combustion, où l'ammoniac servait de neutralisant, l'éthylène glycol comme agent de polymérisation et l'acide acétique comme carburant.

L'image MEB des poudres de CFO (Figure 5.a) a montré des agglomérats de particules régulières quasi sphériques avec une taille de grain moyenne de 160 nm. L'analyse EDX a confirmé la présence d'éléments métalliques (Co et Fe) et révélé la répartition des éléments dans l'échantillon. La teneur en oxygène a été observée à 3,9683 atomes par maille.

L'analyse DRX révèle que les poudres de CFO sont bien cristallisées sans aucune impureté détectée. La structure cristalline a été indexée sur une structure de spinelle cubique (carte JCPDS n ° 22-1086), Le paramètre de réseau "a" de CFO s'avère être de 8,4013 Å en se basant sur le programme de raffinement de Rietveld. La taille moyenne des cristallites est de 57,6 nm et la taille des grains de 160 nm, respectivement (Figure 5.b).

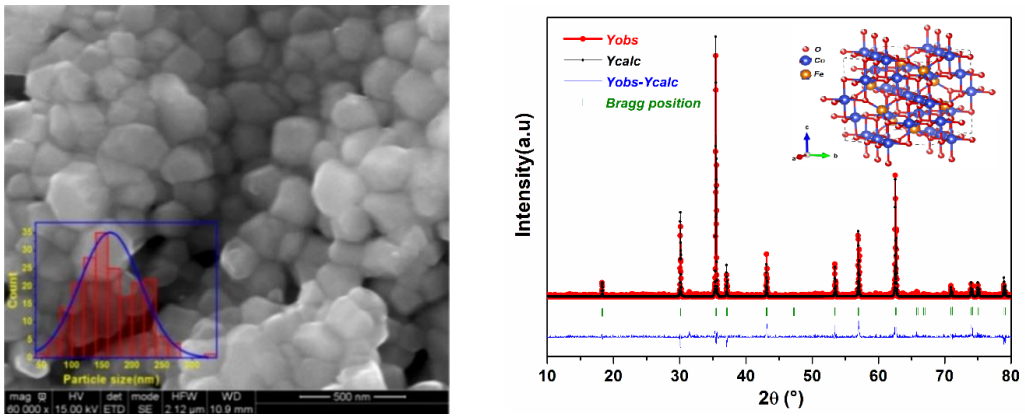

Figure 5: *(a) Micrographie SEM de nanoparticules de CFO, l'encart de l'image montre la distribution granulométrique, (b) Diagramme de diffraction des rayons X affiné des nanoparticules de CFO.*

Le comportement d'aimantation de la poudre de CFO sous un champ magnétique de 0,4 Oe a été étudié et une transition de phase FM-PM de premier ordre a été observée à la température de Curie T_C. La dépendance à la température des courbes d'aimantation et la dérivée dM/dT ont été utilisées pour déterminer la température de Curie, qui s'est avérée être de 785 K (Figure 6.a). Cette valeur est confirmée à l'aide de la loi de Curie.

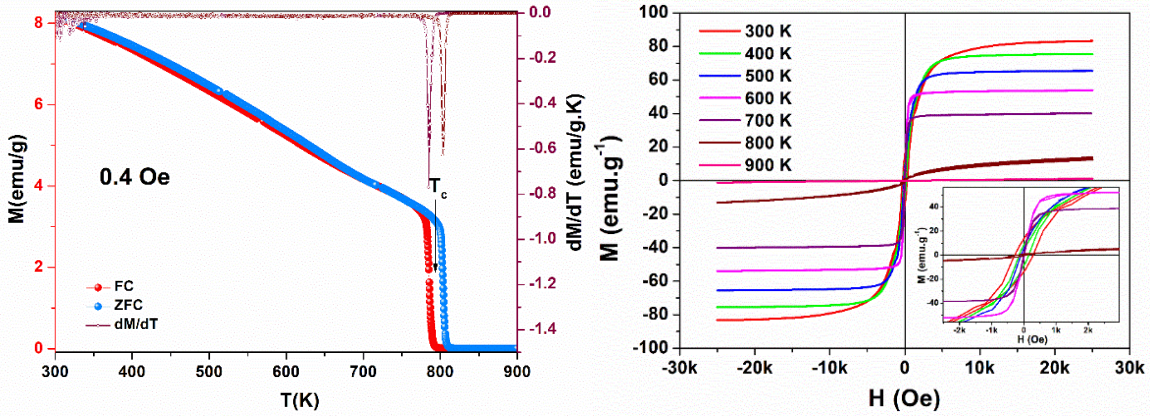

Figure 6: *(a) Les courbes FC-ZFC pour l'échantillon de CFO mesurées à un champ magnétique appliqué de 0,4 Oe, (b) Courbes d'aimantation isotherme de CFO à différentes températures sous un champ magnétique appliqué de 25 kOe*

Les boucles d'hystérésis (M-H) des nanoparticules de CFO sont mesurées à différentes températures allant de 300 K à 900 K (Figure 6.b). Pour T<Tc, on observe une boucle d'hystérésis saturée, indiquant le caractère ferro/ferrimagnétique de CFO. L'aimantation diminue avec l'augmentation de la température et disparaît complètement lorsque T > Tc, indiquant l'apparition d'un caractère paramagnétique. La valeur importante de M_s (83 emu g^{-1}) observée à faible Hc (284 Oe), révèle la nature magnétique douce du CFO[35]. Notre échantillon de CFO montre des résultats améliorés par rapport à ceux rapportés par d'autres travaux utilisant différentes méthodes de synthèse de CFO[27], [36]–[38].

L'effet magnétocalorique du matériau a été étudié en utilisant la méthode indirecte (voir chapitre 1) basée sur la mesure de M(H). Les courbes résultantes (Figure 7.a et b) de ΔS et ΔT ont révélé deux anomalies magnétiques. La première anomalie observée à 600 K peut être attribuée à la distorsion du réseau et à la dynamique des parois de domaine ou à « domain Wall Pinning », tandis que l'anomalie à 700 K correspond à la transition de phase FM-PM [39], [40]. La réorientation maximale à T_C conduit à l'entropie maximale de 6,2 $J.kg^{-1}K^{-1}$ et à un changement de température électrocalorique adiabatique de 11,2 K. La valeur magnétocalorique améliorée peut être attribuée à la transition de phase du premier ordre du CFO, tandis que la valeur améliorée de ΔT peut être lié à la taille des grains[31], [32].

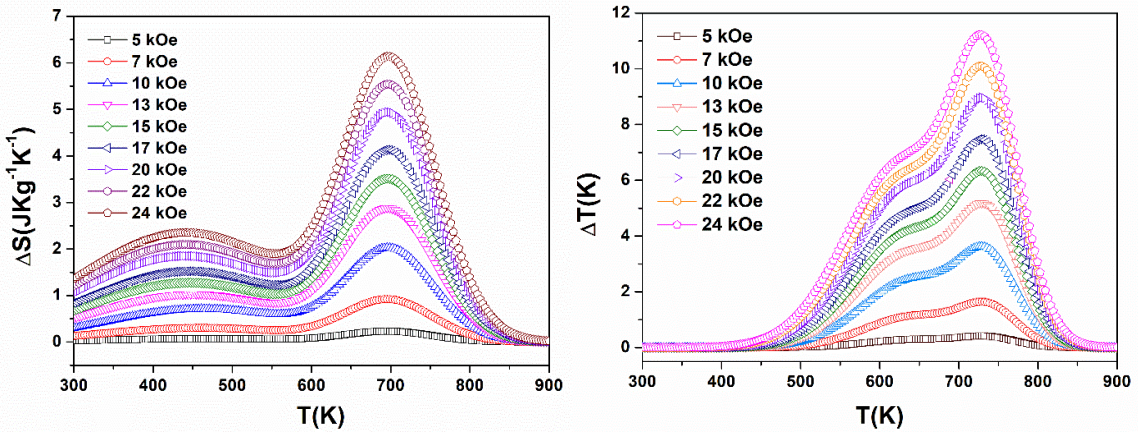

Figure 7 : *La variation de (a) l'entropies magnétiques ΔS et la température adiabatique ΔT (b) en fonction de la température sous divers champs magnétiques pour la poudre de $CoFe_2O_4$*

Pour des applications de réfrigération industrielle, la performance de l'effet MC de l'échantillon CFO a été évaluée à l'aide de la puissance de refroidissement relative (RCP) et du TEC (voir chapitre 1). Notre échantillon CFO présente une valeur RCP élevée et une valeur TEC significative (Figure 8), ce qui en fait un bon candidat pour les applications de chauffage et de refroidissement magnétiques.

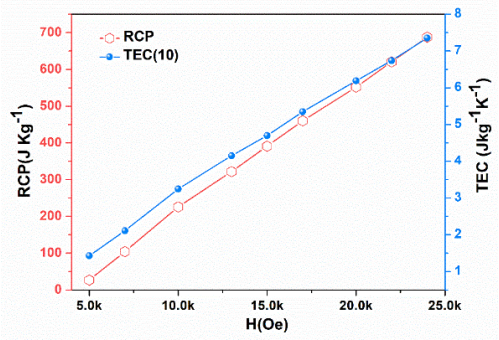

Figure 8 : *Dépendance au champ magnétique du RCP et du TEC*

En résumé, des nanoparticules de cobalt de fer CFO ont été préparées en utilisant la méthode sol-gel couplée à l'auto-combustion, puis ont été soumises à une analyse de leurs propriétés structurelles, magnétiques et magnétocaloriques. Les nanoparticules de CFO présentent une structure de spinelle cubique avec une transition de phase PM-FM de premier ordre et une température de Curie de 785 K. En raison de leur entropie magnétique élevée et de leur RCP élevée, les nanoparticules de CFO sont considérées comme des candidats prometteurs pour la réfrigération magnétique et pour des applications médicales nécessitant des températures supérieures à 300 K.

Elaboration et caractérisation de composites particulaires (1-x) $Ba_{0.95}Ca_{0.05}Ti_{0.89}Sn_{0.11}O_3$-(x) $CoFe_2O_4$

Les matériaux multiferroïques peuvent être classés en monophasés et composites. Cependant, les matériaux monophasés avec couplage ME intrinsèque ne sont pas largement étudiés car ils ont un faible effet ME à ou près de la température ambiante. En revanche, les composites multiferroïques synthétiques ont un excellent couplage ME extrinsèque créé par une interaction interfaciale élastique ferroélectrique-ferromagnétique combinant une magnétostriction élevée et une grande réponse piézoélectrique. Ces composites se présentent sous diverses formes de connectivité : (0-3), (2-2) et core shell sous forme 0 D ou 1 D.

Cette étude porte sur les propriétés d'un nouveau composite magnétoélectrique de type (0-3) élaboré en combinant $Ba_{0.95}Ca_{0.05}Ti_{0.89}Sn_{0.11}O_3$ (BCTSn) comme phase piézoélectrique et $CoFe_2O_4$ (CFO) comme phase magnétostrictive. Les propriétés du composite sont étudiées systématiquement en faisant varier la fraction pondérale (x) de CFO dans le composite.

Les pics de diffraction des phases ferroélectrique et ferrite ont été observés dans les échantillons composites sans aucune impureté, indiquant qu'il n'y avait pas de réaction chimique pendant le processus de frittage (Figure 9.a). Le raffinement structurel des systèmes composites confirme la coexistence des phases BCTSn et CFO. Les paramètres de réseau des phases ont montré une variation en fonction de la composition, peut-être due à une déformation créée à l'interface des phases ferrite et pérovskites (voir table 1 chapitre 4)[41]. Il a été constaté que la distorsion du réseau (c/a) des phases orthorhombique et tétragonale dans BCTSn affectait le couplage magnétoélectrique. Le composite ayant une composition de 0,7 BCTSn - 0,3 CFO présentait le plus haut degré de pseudocubicité (Figure 9.b).

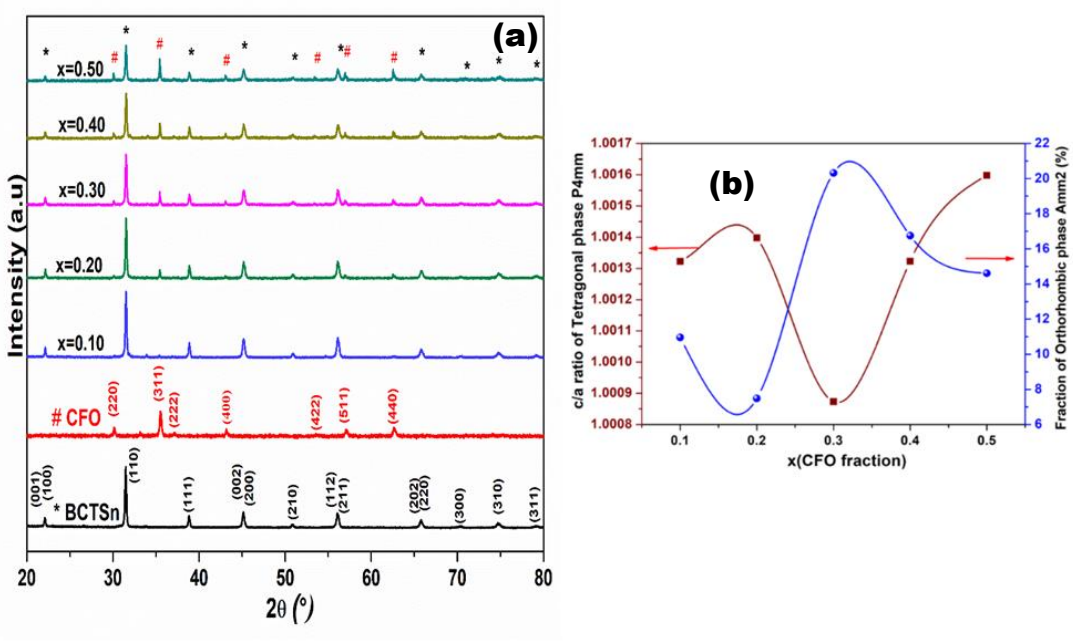

Figure 9 *(a) Diagrammes DRX des composites (1-x) BCTSn - (x) CFO, (b) Variation de la distorsion du réseau et pourcentage de la phase cristalline Amm2 avec teneur en CFO dans les composites*

Les images MEB, présentées dans la figure 10.a, montrent des grains sphériques clairs de BCTSn et des grains à facettes gris plus foncés de CFO dans les composites multiferroïques 0,7 BCTSn - 0,3 CFO. Ceci est confirmé par l'analyse EDX présentée dans la figure 10 (c et d). La densité des composites frittés augmente à mesure que la proportion de CFO augmente, atteignant un maximum de 5,5 pour x=0,3 (figure 10(b)). Cette différence s'explique par la forte densification du CFO à une température de frittage de 1300°C, alors que le BCTSn a une densification très faible à cette température, conduisant à une microstructure poreuse. En raison de la présence d'une phase de ferrite avec une porosité et une conductivité élevée, une polarisation complète n'a pas pu être obtenue, ce qui a entraîné une dégradation des propriétés multiferroïques des composites. La distribution aléatoire des grains de CFO dans la matrice BCTSn a également un effet sur la densité et les propriétés multiferroïques de la céramique.

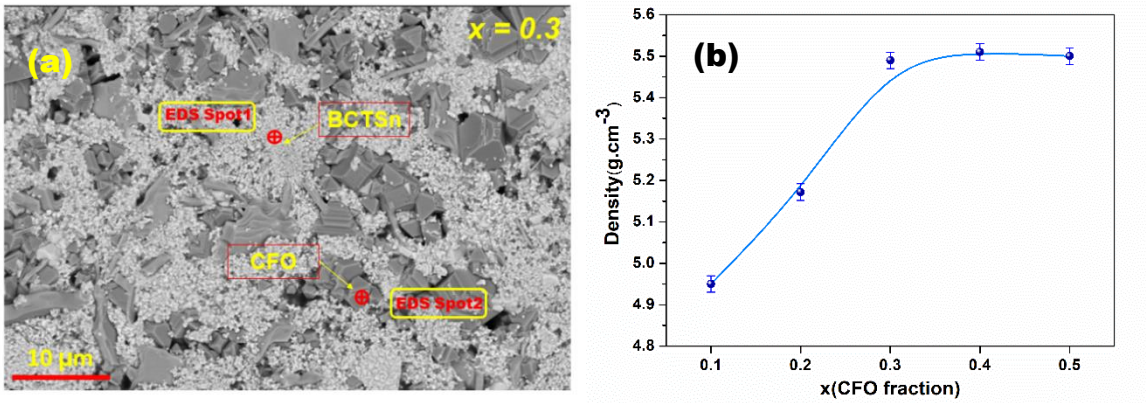

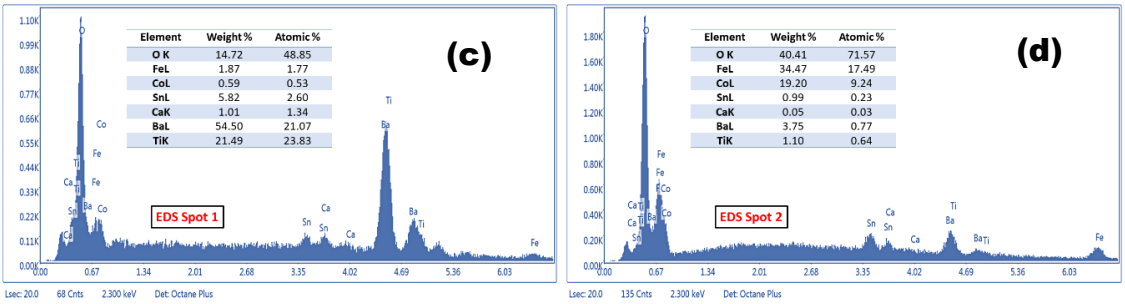

Figure 10 : *(a) micrographie MEB, (b) densité apparente en fonction de la teneur en ferrite de divers composites (1-x) BCTSn - (x) CFO et (c et d) spectre EDX pour le composite avec x=0,3.*

La figure 11 présente les propriétés magnétiques des composites (1-x) BCTSn - (x) CFO ainsi que de CFO pur. Les boucles d'hystérésis des composites présentent un comportement similaire à celui du CFO pur, ce qui suggère le comportement ferromagnétique des composites. Les valeurs des paramètres magnétiques M_s et M_r diminuent de manière systématique à mesure que la proportion de BCTSn augmente, en raison de la diminution du moment magnétique par unité de volume causée par la phase non magnétique de BCTSn. Une augmentation de la proportion de CFO entraîne une augmentation de la coercivité, probablement due à la formation de clusters de CFO et de structures interconnectées. La magnétisation réduite (M_r/M_s) des composites a également été calculée et s'est avérée varier d'environ 1 %, ce qui indique l'absence de diffusion chimique ou d'interaction significative entre les phases BCTSn et CFO.

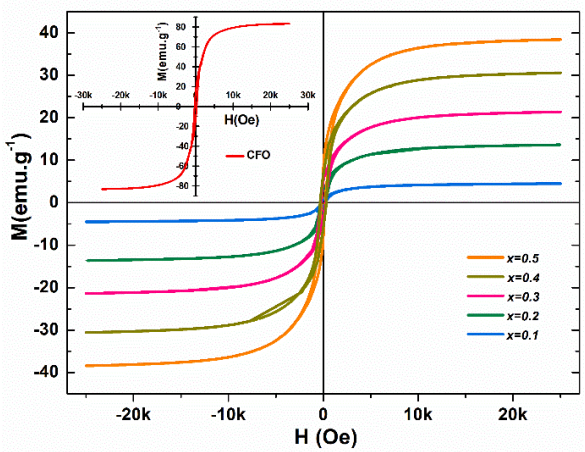

Figure 11 : *Boucles d'hystérésis magnétiques des composites (1-x) BCTSn - (x) CFO avec x= 0,10, 0,20, 0,30, 0,40 et 1,0 mesurés à température ambiante (l'encart montre la courbe M–H du CFO pur)*

Les propriétés ferroélectriques des composites BCTSn-CFO ont été étudiées par la mesure des boucles d'hystérésis P-E sous un champ électrique de 20 kV cm^{-1}, comme indiqué dans la figure 12. Les résultats confirment la nature ferroélectrique des composites, mais avec un P_r inférieur

et un E_c supérieur par rapport au BCTSn pur. Cette différence est attribuée au comportement conducteur du CFO. En outre, l'augmentation de la concentration de CFO autour des particules de BCTSn empêche le mouvement des parois du domaine dans les grains de BCTSn, réduisant ainsi la polarisation ferroélectrique[11], [42]. Le champ électrique appliqué du BCTSn pur atteint 30 kV cm^{-1} (encart figure 12), tandis que celui du composite multiferroïque est limité à 20 kV cm^{-1} en raison de la conductivité de la phase ferromagnétique CFO, qui réduit les propriétés piézoélectriques et magnétoélectriques du composite.

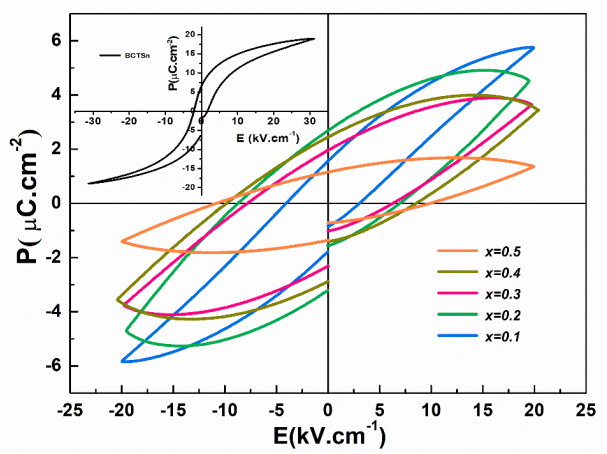

Figure 12: *Boucles d'hystérésis ferroélectriques des composites (1-x) BCTSn - (x) CFO avec x = 0,10, 0,20, 0,30, 0,40 et 0,5 à température ambiante (l'encart montre la courbe P-E du BCTSn pur).*

La figure 13 présente la variation du coefficient piézoélectrique (d_{33}) en fonction de la teneur en CFO. Les valeurs de d_{33} pour les composites (1-x) BCTSn-(x) CFO diminuent progressivement de 203 pm.V^{-1} pour le BCTSn pur à 27 pm.V^{-1} pour x=0,5. Le maximum de d_{33} obtenu pour le BCTSn pur n'est pas la valeur piézoélectrique maximale, ceci est probablement due à la faible densité de la céramique et du faible champ électrique utilisé pour polariser les échantillons. De plus, en raison de la nature conductrice de la ferrite, la polarisation de la céramique est difficile, ce qui conduit à une diminution de la piézoélectricité avec l'ajout de CFO. En résumé, les propriétés piézoélectriques dépendent de la densité, de la taille des grains, de la température de frittage et des conditions de polarisation.

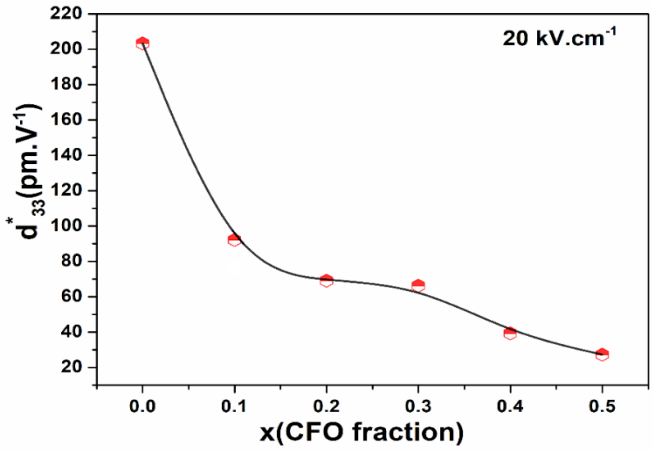

Figure 13 : *Variation du coefficient piézoélectrique d*$^*_{33}$ *des composites (1-x) BCTSn - (x) CFO avec x = 0,10, 0,20, 0,30, 0,40 et 0,50 à une fréquence de 10 Hz à température ambiante.*

L'effet ME est mesuré par le coefficient ME (α_{ME}), qui peut être calculé à l'aide de l'équation (2.7). Le couplage magnétoélectrique des échantillons (1-x) BCTSn - (x) CFO a été étudié à température ambiante à l'aide de la méthode dynamique. Les détails de la préparation des échantillons sont décrits au chapitre 1.

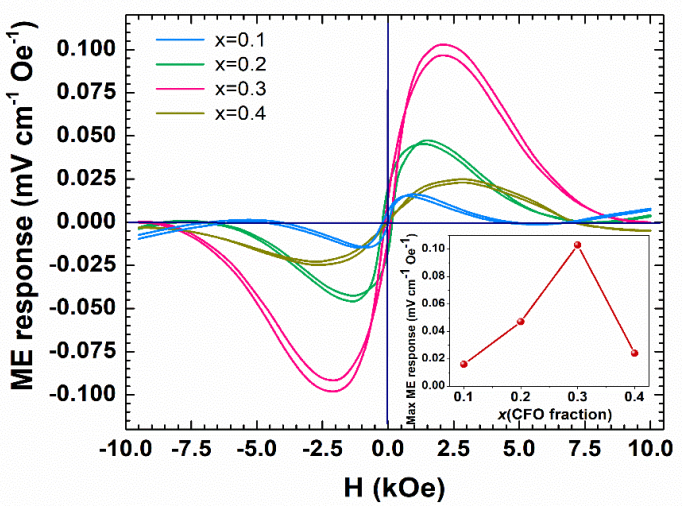

Figure 14 : *Amplitude du coefficient de couplage ME pour les échantillons avec x=0,1, 0,2, 0,3 et 0,4 en fonction du champ magnétique continu.*

La réponse ME augmente avec l'augmentation du contenu magnétique CFO jusqu'à x = 0,3, puis il diminue fortement au fur et à mesure que la proportion de la phase CFO augmente (encart Fig.14). Ceci est lié au fait qu'à x=0,4, l'échantillon ne peut pas être bien polariser. En effet, augmenter le contenu CFO (supérieur à 30 %) réduit la résistivité globale du composite et crée des fuites de charge en raison d'une augmentation des électrons migrateurs le long de l'interface entre les deux phases. Par conséquent, la polarisation électrique devient plus difficile pour créer un dipôle en appliquant un champ magnétique, entraînant une réduction dans le couplage ME

dans les composites [11]. Le coefficient ME a un maximum au champ d'environ 2,5 kOe. Le couplage ME s'explique par le fait que le champ magnétique crée une contrainte dans la phase de ferrite, et la déformation provoque une contrainte dans la phase ferroélectrique en raison des interactions mécaniques de la ferrite et de la phase pérovskites. Vue que les contraintes mécaniques favorisent la polarisation, une tension est produite dans les grains [43]. Comme un résultat, l'interface entre les grains ferroélectrique et les grains ferromagnétiques est critique dans ce type de couplage ME médié par la contrainte mécanique.

En conclusion, un nouveau type de matériau composite sans plomb (1-x) BCTSn – (x) CFO a été synthétisé par mélange mécanique. Les composites ont été analysés par diffraction des rayons X (DRX) et microscopie électronique à balayage (MEB), confirmant leur pureté et la coexistence de phases pérovskite BCTSn et spinelle CFO. Les composites présentent des propriétés multiferroïques à température ambiante, comme en montrant les mesures de boucles d'hystérésis ferroélectriques et magnétiques. Le plus grand coefficient ME de 0,1 mv cm^{-1} Oe^{-1} a été observé dans la composition 0,7BCTSn-0,3CFO. Cependant, les résultats pourraient être améliorés en modifiant les tailles et les morphologies des grains des phases ferroélectrique et magnétique et en concevant d'autres connectivités de structures nanométriques.

Elaboration et caractérisation de nanofibres core-shell CFO/BCTSn

Le développement de composites ME, à l'intermédiaire des contraintes mécaniques, représente une voie prometteuse pour la conception de nouveaux matériaux multifonctionnels avec des applications potentielles dans une variété de domaines, y compris les capteurs, les actionneurs et les dispositifs de récupération d'énergie. Cependant, des recherches supplémentaires sont nécessaires pour optimiser l'effet ME dans ces composites et pour explorer leur plein potentiel dans des applications pratiques.

Les connectivités des composites multiferroïques ont été explorés à travers différentes conceptions telles que les types 0-3, 1-3 et 2-2. Le type 0-3, qui consiste à disperser des particules nanométrique (0D) dans une matrice (3D), est le plus étudié. Cependant, l'agglomération de ces particules réduit l'effet ME, d'où la nécessité de créer des interfaces unidimensionnelles à l'échelle nanométrique. Les nanofibres cœur-coquille offrent une solution recommandée grâce à leur grande surface interfaciale et leur rapport surface/volume élevé.

Pour produire ces nanocomposites multiferroïques 1D, plusieurs techniques ont été utilisées telque les méthodes hydrothermales et l'électrofilage. L'électrofilage est particulièrement avantageux car il permet de fabriquer des nanofibres composites multiferroïques avec des

structures continues, de contrôler la taille des nanostructures, avec un rapport de forme élevé et un faible rapport coût-efficacité.

Dans cette partie, nous allons essayer d'améliorer l'efficacité du couplage ME dans les composites céramiques BCTSn-CFO via l'élaboration des fibres de nanostructures cœur-coquille en utilisant la méthode d'électrospinning, avec un cœur $CoFe_2O_4$ et une coque $Ba_{0.95}Ca_{0.05}Ti_{0.89}Sn_{0.11}O_3$. Les propriétés des NF CFO@BCTSn résultants, y compris leurs structures, morphologies, propriétés magnétiques et ferroélectriques, ainsi que leurs propriétés magnétoélectriques, sont étudiées dans le but d'améliorer l'efficacité du couplage ME pour des applications multiferroïques à l'échelle nanométriques.

Les morphologies des nanofibres CFO@BCTSn calcinés ont été observées par MEB et MET. La figure 15.a représente une image MEB des NF CFO@BCTSn, démontrant que les NF individuels ont une structure continue avec une faible densité relative de 71 % et des diamètres allant de 150 à 250 nm. La surface d'un seul CFO@BCTSn NF est illustrée sur la figure 15b, indiquant que la fibre est composée de petits grains de l'ordre de dizaines de nanomètres, qui peuvent être de la phase BCTSn car ils forment la coquille de la fibre. Des observations détaillées d'une fibre individuelle sont représentées sur les figures 15c et d. Le cœur et la coque sont bien identifiés, avec un cœur CFO de 110 nm de diamètre et une coque BCTSn de 370 nm d'épaisseur.

Le diffractogramme SAED dans l'encart de la figure 15.c, obtenu à partir de la zone du cercle en rouge, montre plusieurs anneaux de diffraction, suggérant une structure polycristalline de CFO @ BCTSn NF. Les plans cristallographiques (400), (440), (422) et (620) sont attribués au CFO, tandis que les plans (220) et (223) sont attribués au BCTSn, confirmant la coexistence des phases magnétique et ferroélectrique.

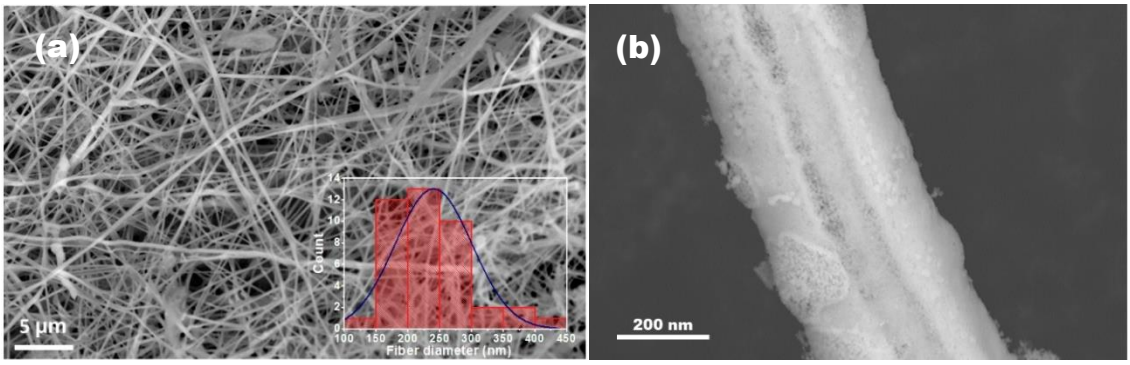

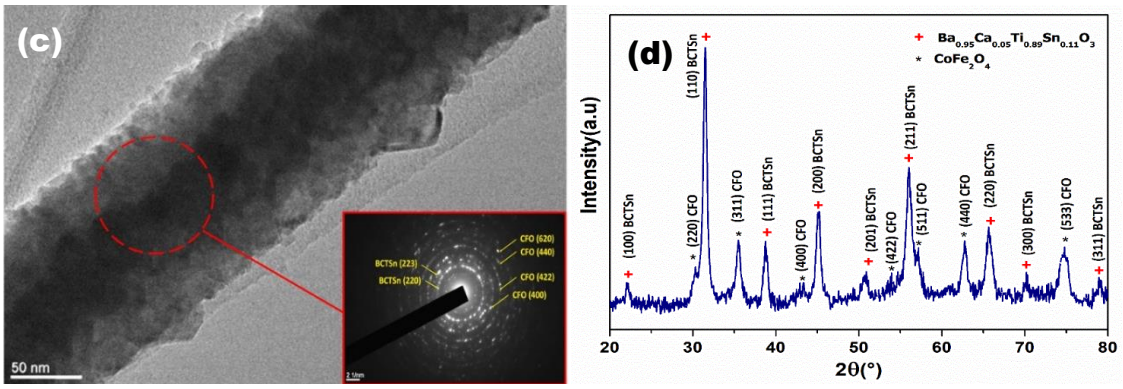

Figure 15 : *Images MEB de (a) CFO@BCTSn NF, l'encart de l'image montre une distribution de diamètre de fibre, (b) un seul CFO@BCTSn NF, (c) image MET d'un CFO@BCTSn NF individuel, en encart dans (c): diagramme de diffraction acquis à partir du cercle de couleur rouge, (d) diagramme DRX à température ambiante des NF CFO @ BCTSn.*

L'aimantation en fonction du champ magnétique pour les nanofibres de CFO@BCTSn à 300 K est illustrée à la Figure 16. La boucle M-H montre un comportement ferromagnétique classique avec une très petite composante paramagnétique due à l'interdiffusion possible d'un petit nombre d'atomes magnétiques dans la coquille. Nous déterminons un champ coercitif de 221 Oe, une aimantation rémanente M_r de 1,43 emu g^{-1} (seulement 12% de la valeur maximale), et une aimantation maximale M_s de 11,63 emu g^{-1} à température ambiante. Il faut souligner que l'aimantation n'est pas complètement saturée sous 25 kOe. L'aimantation a été déterminée à partir de la masse totale des fibres cœur-coquille, et cette valeur doit donc être considérée comme une valeur minimale car la présence de la phase BCTSn non magnétique a contribué à la masse totale de l'échantillon. La M_s du CFO pur a une valeur comprise entre 80 et 94 emu g^{-1} (pour une spinelle inverse idéal, le M_s du CFO est de 71,4 emu g^{-1})[41], [44], [45]. Dans les pastilles frittées des composites de CFO-BCTSn de type (0-3), une Ms de 38,4 emu g^{-1} a été mesurée[41]. Dans des fibres CFO pures élaborés par la même méthode (image non montrée), une magnétisation de 78,75 emu g^{-1} à température ambiante a été trouvée, également proche de la valeur apparente. On note que le NF CFO@BCTSn a un rapport (M_r/M_s) plus petit que le CFO pur. Une faible valeur de Mr a également été observée dans les films très minces et dans les nanoparticules[46], [47]. Un rapport de (M_r/M_s) plus élevé de 0,19 a été mesuré dans les pastilles des composites CFO-BCTSn. La taille des cristallites et la méthode de préparation ont une influence considérable sur les propriétés magnétiques des matériaux. Par exemple, Lu et al. ont présenté une étude comparative sur les propriétés magnétiques des nanofibres et des nanoparticules, ils ont constaté que le M_s, le M_r et le H_c des nanofibres CFO sont différents de ceux des nanoparticules[48]. Le faible rapport de (M_r/M_s) à température ambiante (qui

augmente à 0,63 à basse température) pourrait suggérer une température de blocage autour ou en dessous de la température ambiante, qui sera étudiée dans de futures expériences.

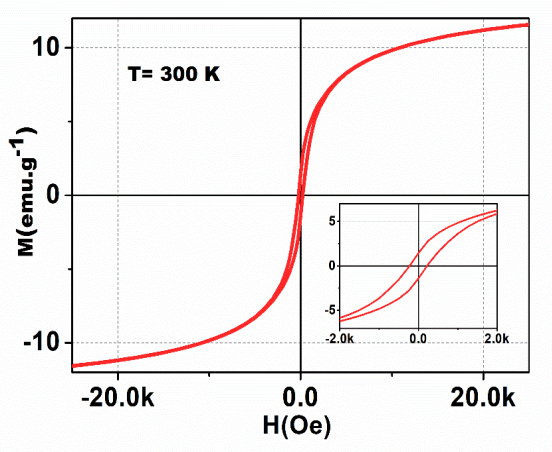

Figure 16 : *Boucle d'hystérésis magnétiques pour les nanofibres CFO@BCTSn à température ambiante.*

Les images PFM verticales et latérales des nanofibres sur le substrat Si sont illustrées dans la figure 17. Les nanofibres montrent une réponse piézoélectrique améliorée, qui peut être vue comme des zones claires dans les figures 17 (c) et (e), sauf au centre des nanofibres dans l'image d'amplitude PFM latérale, où il n'y a pas de signal piézoélectrique (les taches sombres marquées par flèches bleues). Ces zones pourraient éventuellement correspondre à la phase magnétique à l'intérieur des nanofibres. De plus, les boucles PFM locales mesurées indiquent le comportement de commutation des domaines ferroélectriques à l'intérieur des nanofibres (Figures. 17 (g) et (h)).

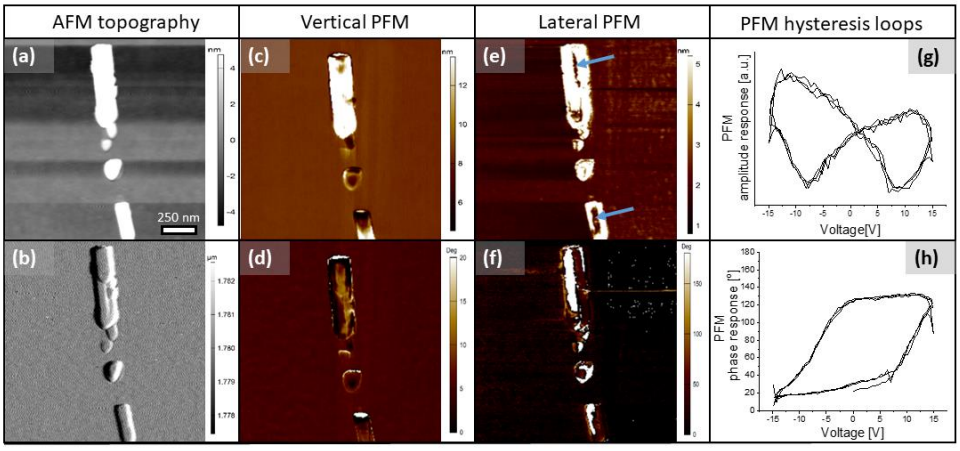

Figure 17 : *Images AFM/PFM des nanofibres CFO@BCTSn ; Topographie AFM (a) hauteur, (b) déviation, PFM vertical (c) amplitude, (d) phase et PFM latéral (e) amplitude et (f) images de phase. Boucles d'hystérésis locales PFM obtenues en commutant le mode de spectroscopie ; (g) boucles d'amplitude et (h) de phase (trois cycles).*

Pour déterminer le coefficient piézoélectrique local d_{33}^{eff} des nanofibres, l'analyse PFM a été effectuée en mode PFN à fréquence unique (Figure 18) à une fréquence de 240 kHz. La réponse piézoélectrique maximale d_{33}^{eff} était de 40 pm/7V~ 6 pm/V. Nous sommes conscients qu'il ne s'agit que d'une valeur approximative de d_{33}^{eff} car le substrat Si est semi-conducteur. Cependant, nous avons essayé de fixer les nanofibres également sur des substrats revêtus de Pt, mais dans ce cas, les plaques n'adhèrent pas complètement au substrat, de sorte que les nanofibres se sont déplacées pendant le balayage PFM et l'analyse n'a pas été possible.

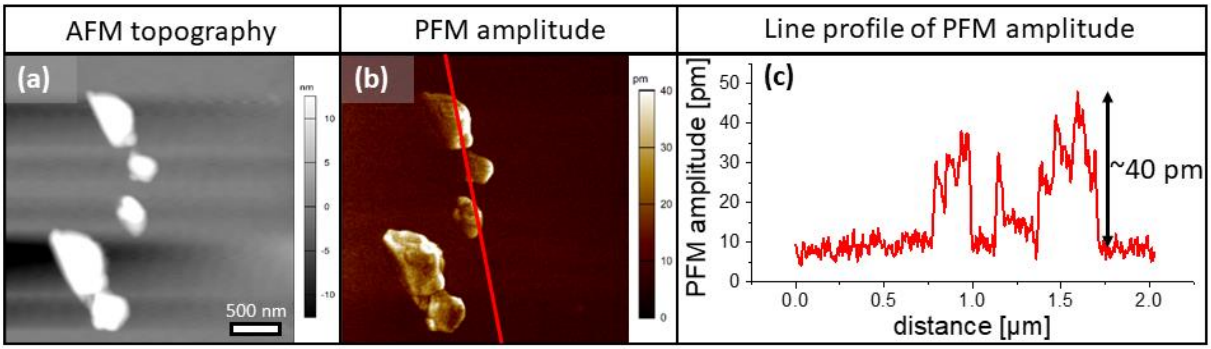

Figure 18 : *(a) Topographie AFM - image de hauteur, (b) image d'amplitude PFM verticale mesurée en mode monofréquence PFN hors résonance et (c) profil de ligne d'amplitude PFM (voir la ligne rouge dans la figure b) de CFO@BCTSn NF sur substrat Si.*

L'effet ME est mesuré par le coefficient ME (α_{ME}) avec la même méthode utilisé dans la partie **IV**. Le coefficient ME montre une augmentation non linéaire avec l'augmentation du champ magnétique DC, atteignant une valeur de 346 mV cm^{-1} Oe^{-1} au champ magnétique 10 kOe (la figure 19).

En raison des interactions mécaniques entre les phases de ferrite et de pérovskite ferroélectrique/piézoélectrique dans toute la fibre, le champ magnétique induit une contrainte dans la phase de ferrite, ce qui entraîne une contrainte dans la phase ferroélectrique. Cette contrainte produit une tension dans la coque via l'effet piézoélectrique.

Comme indiqué dans la partie précédente, l'interface entre les phases ferroélectriques et ferromagnétiques et la connectivité de phase par l'intermédiaire des contraintes mécaniques sont cruciales dans les composites ME. Le coefficient magnétoélectrique amélioré obtenu dans les NF CFO@BCTSn est directement lié au processus d'électrofilage. En effet, les NF CFO@BCTSn produits par électrofilage comprennent des grains de BCTSn et de CFO à l'échelle nanométrique, comme le montrent les images MEB. De tels sorte que les grains nanométriques peuvent constituer une grande surface interfaciale, favorisant les interactions

mécaniques entre les phases piézoélectrique et magnétostrictive. De plus, nos fibres composites ont également une bonne connectivité de phase, comme observé dans les images MET. Cela peut assurer un transfert de contrainte complet entre les phases CFO et BCTSn, améliorant les propriétés magnétoélectriques de ces composites. En conséquence, le αME observé est supérieur au α_{ME}=13,3 mV cm^{-1} Oe^{-1} rapporté pour les fibres composites $BaTiO_3/CoFe_2O_4$, α_{ME}=150,58 mV cm^{-1} Oe^{-1} rapporté pour CFO@BT@PDA/(P(VDF-TrFE) et α_{ME} = 51 mV cm^{-1} Oe^{-1} rapportés pour les nanotiges de $CoFe_2O_4$ intégrées dans la matrice $BaTiO_3$. Cependant, la valeur α_{ME} obtenue dans les nanofibres CFO@BCTSn est inférieure à 2,95 10^4 mV cm^{-1} Oe^{-1} rapporté pour $CoFe_2O_4$–$Pb(Zr_{0.52}Ti_{0.48})O_3$ nanofibres core-shell, ce qui peut être attribué au coefficient piézoélectrique d_{33} de $Pb(Zr_{0.52}Ti_{0.48})O_3$ qui est trois ou quatre fois plus élevé que celui du $BaTiO_3$ dopé[49]–[52]. Selon cette comparaison, les NF CFO@BCTSn ont le potentiel d'être utilisés dans des applications électroniques comme capteurs de champ magnétique à température ambiante.

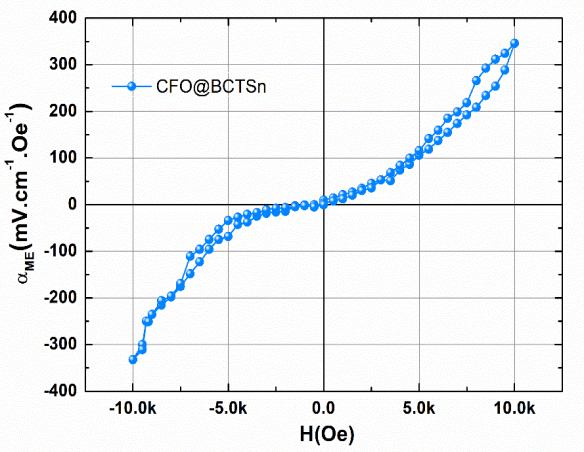

Figure 19 : Amplitude du coefficient de couplage ME des nanofibres CFO@BCTSn en fonction du champ magnétique continu à température ambiante.

Cette étude a examiné les propriétés des nanofibres core-shell $CoFe_2O_4$-$Ba_{0.95}Ca_{0.05}Ti_{0.89}Sn_{0.11}O_3$ élaborés par la méthode d'électrofilage. L'analyses DRX et SAED ont confirmé la présence de structures de pérovskite et de spinelle dans les nanofibres. Les images MEB et MET ont montré que les nanofibres avaient une connectivité cœur-coque. Les nanofibres présentaient également des propriétés piézoélectriques et ferromagnétiques, comme le démontrent les cartographies PFM/AFM et les boucles d'hystérésis M-H. Le coefficient de couplage magnétoélectrique déterminé expérimentalement de 346 mV cm^{-1} Oe^{-1} a été attribué aux grandes surfaces interfaciales des nanofibres et à l'excellente interconnectivité entre les deux phases ferroïques, ce qui en fait un candidat prometteur pour les applications nanométriques de capteurs magnétiques ultra-sensibles à température ambiante.

Conclusions et perspectives

Ce manuscrit décrit une étude sur des nouveaux matériaux composites multiferroïques à l'échelle nanométrique, en mettant l'accent sur l'amélioration de l'effet magnétoélectrique. Les composites magnétoélectriques de type (0-3) avec la formule (1–x) $Ba_{0.95}Ca_{0.05}Ti_{0.89}Sn_{0.11}O_3$ - (x) $CoFe_2O_4$ avec ($0 \leq x \leq 0.5$) et les nanofibres core-shell CFO@BCTSn sont les matériaux de choix pour cette étude. Les phases individuelles, ferroélectrique BCTSn et ferromagnétique CFO, ont été étudiées séparément et caractérisées à l'aide de l'analyses DRX, Raman et EDX, qui confirment la coexistence et la pureté des deux phases dans les composites. L'étude ferroélectrique de BCTSn a révélé des performances de stockage d'énergie améliorées, alors que les mesures magnétiques ont montré une transition de phase PM-FM de premier ordre dans CFO avec un RCP amélioré de 687,56 J Kg^{-1} et une grande valeur de changement de température magnétocalorique de ΔT = 11,2 K. Les propriétés multiferroïques à température ambiante des composites (0-3) ont été confirmées à l'aide des mesures de boucles d'hystérésis ferroélectriques et magnétiques. Le coefficient piézoélectrique inverse (d^*_{33}) a été mesuré et rapporté pour tous les composites. Pour les NF CFO@BCTSn, les propriétés ferroélectriques et piézoélectriques ont été confirmées par des cartographies PFM, et les boucles d'hystérésis M-H ont été utilisées pour prouver les propriétés ferromagnétiques. Pour le composite particulaire CFO-BCTSn, le plus grand coefficient ME est de 0,1 mV cm^{-1} Oe^{-1} observé dans la composition 0,7BCTSn-0,3CFO, qui est proche de la symétrie pseudocubique et relativement dense, ce qui a conduit à la réduction de la déformation du réseau et à la favorisation de la commutation de domaine. Cependant, les NF CFO@BCTSn montrent un coefficient ME élevé de 346 mV cm^{-1} Oe^{-1}. Ces résultats suggèrent que la conception de couplages nanostructurés peut augmenter la surface interfaciale, favorisant les interactions mécaniques entre les phases piézoélectrique et magnétostrictive, améliorant ainsi l'effet magnétoélectrique.

En bref, ce travail fournit des informations importantes sur le développement de matériaux composites magnétoélectriques avec des propriétés améliorées, qui ont des applications potentielles dans divers domaines, notamment la récupération d'énergie, la détection magnétique et le stockage d'informations.

Dans l'ensemble, ce travail fournit une base solide pour le développement continu de matériaux composites magnétoélectriques avec des propriétés améliorées pour diverses applications.

Il existe de nombreux sujets de futurs travaux qui pourraient s'étendre pour améliorer les performances des composites élaborés. Les points suivants, qui peuvent être repris comme futures études :

• Étudier l'effet des épaisseurs des core/shell sur les propriétés magnétoélectriques ;

• Étudier l'effet de la température sur l'effet magnétoélectrique des composites élaborés ;

• Étudier l'effet d'autres types d'interfaces entre les phases piézoélectrique et magnétostrictive sur l'effet magnétoélectrique ;

• Conception d'autres composites magnétoélectriques en faisant varier les phases piézoélectriques ;

• Elaboration de BCTSn-CFO/Polymère pour dispositif de récupération d'énergie multiferroïque ;

• Développer des modèles théoriques pour comprendre les mécanismes sous-jacents aux propriétés observées du composite ;

• Étudier le potentiel d'intégration du composite dans les technologies existantes, telles que les dispositifs MEMS ou les capteurs magnétiques.

Références

[1] J. Ma, J. Hu, Z. Li, and C.-W. Nan, 'Recent Progress in Multiferroic Magnetoelectric Composites: from Bulk to Thin Films', *Adv. Mater.*, p. 26, 2011.

[2] N. Ortega, A. Kumar, J. F. Scott, and R. S. Katiyar, 'Multifunctional magnetoelectric materials for device applications', *J. Phys.: Condens. Matter*, vol. 27, no. 50, p. 504002, Dec. 2015, doi: 10.1088/0953-8984/27/50/504002.

[3] M. Etier, V. V. Shvartsman, S. Salamon, Y. Gao, H. Wende, and D. C. Lupascu, 'The Direct and the Converse Magnetoelectric Effect in Multiferroic Cobalt Ferrite-Barium Titanate Ceramic Composites', *J. Am. Ceram. Soc.*, vol. 99, no. 11, pp. 3623–3631, Nov. 2016, doi: 10.1111/jace.14362.

[4] V. V. Shvartsman, F. Alawneh, P. Borisov, D. Kozodaev, and D. C. Lupascu, 'Converse magnetoelectric effect in $CoFe_2O_4$–$BaTiO_3$ composites with a core–shell structure', *Smart Mater. Struct.*, vol. 20, no. 7, p. 075006, Jul. 2011, doi: 10.1088/0964-1726/20/7/075006.

[5] M. Fiebig, 'Revival of the magnetoelectric effect', *J. Phys. D: Appl. Phys.*, vol. 38, no. 8, pp. R123–R152, Apr. 2005, doi: 10.1088/0022-3727/38/8/R01.

[6] C.-W. Nan, M. I. Bichurin, S. Dong, D. Viehland, and G. Srinivasan, 'Multiferroic magnetoelectric composites: Historical perspective, status, and future directions', *Journal of Applied Physics*, vol. 103, no. 3, p. 031101, Feb. 2008, doi: 10.1063/1.2836410.

[7] H. J. Xiang, S.-H. Wei, M.-H. Whangbo, and J. L. F. Da Silva, 'Spin-Orbit Coupling and Ion Displacements in Multiferroic TbMnO 3', *Phys. Rev. Lett.*, vol. 101, no. 3, p. 037209, Jul. 2008, doi: 10.1103/PhysRevLett.101.037209.

[8] C.-Y. Kuo *et al.*, 'Single-domain multiferroic BiFeO3 films', *Nat Commun*, vol. 7, no. 1, p. 12712, Nov. 2016, doi: 10.1038/ncomms12712.

[9] M. Hadouchi, F. L. Marrec, Z. Mahhouti, J. Belhadi, M. E. Marssi, and A. Lahmar, 'Enhanced magnetization in multiferroic nanocomposite Bi0.9Gd0.1Fe0.9Mn0.05X0.05O3 (X= Cr, Co) thin films', *Thin Solid Films*, vol. 709, p. 138025, Sep. 2020, doi: 10.1016/j.tsf.2020.138025.

[10] J. P. Praveen, K. Kumar, A. R. James, T. Karthik, S. Asthana, and D. Das, 'Large piezoelectric strain observed in sol–gel derived BZT–BCT ceramics', *Current Applied Physics*, vol. 14, no. 3, pp. 396–402, Mar. 2014, doi: 10.1016/j.cap.2013.12.026.

[11] L. K. Pradhan, R. Pandey, R. Kumar, and M. Kar, 'Lattice strain induced multiferroicity in PZT-CFO particulate composite', *Journal of Applied Physics*, vol. 123, no. 7, p. 074101, Feb. 2018, doi: 10.1063/1.5008607.

[12] Z. Zhang *et al.*, 'Mesoporous Silica-Coated Gold Nanorods as a Light-Mediated Multifunctional Theranostic Platform for Cancer Treatment', *Adv. Mater.*, vol. 24, no. 11, pp. 1418–1423, Mar. 2012, doi: 10.1002/adma.201104714.

[13] J. F. Scott, 'Applications of magnetoelectrics', *J. Mater. Chem.*, vol. 22, no. 11, p. 4567, 2012, doi: 10.1039/c2jm16137k.

[14] Y. Hadouch, 'Enhanced Relative cooling Power and large inverse magnetocaloric effect of cobalt ferrite nanoparticles synthesized by auto-combustion method', *Journal of Magnetism and Magnetic Materials*, p. 8, 2022.

[15] M. Chen *et al.*, 'Enhanced piezoelectricity in broad composition range and the temperature dependence research of (Ba1−xCax)(Ti0.95Sn0.05)O3 piezoceramics', *Physica B: Condensed Matter*, vol. 433, pp. 43–47, Jan. 2014, doi: 10.1016/j.physb.2013.10.014.

[16] W. Cai *et al.*, 'Synergistic effect of grain size and phase boundary on energy storage performance and electric properties of BCZT ceramics', *J Mater Sci: Mater Electron*, vol. 31, no. 12, pp. 9167–9175, Jun. 2020, doi: 10.1007/s10854-020-03446-z.

[17] S. Merselmiz *et al.*, 'High energy storage efficiency and large electrocaloric effect in lead-free BaTi0.89Sn0.11O3 ceramic', *Ceramics International*, vol. 46, no. 15, pp. 23867–23876, Oct. 2020, doi: 10.1016/j.ceramint.2020.06.163.

[18] D. Zhan, Q. Xu, D.-P. Huang, H.-X. Liu, W. Chen, and F. Zhang, 'Contributions of intrinsic and extrinsic polarization species to energy storage properties of Ba 0.95 Ca 0.05 Zr 0.2 Ti 0.8 O 3 ceramics', *Journal of Physics and Chemistry of Solids*, vol. 114, pp. 220–227, Mar. 2018, doi: 10.1016/j.jpcs.2017.10.038.

[19] H. Mezzourh *et al.*, 'Enhancing the dielectric, electrocaloric and energy storage properties of lead-free Ba0.85Ca0.15Zr0.1Ti0.9O3 ceramics prepared via sol-gel process', *Physica B: Condensed Matter*, vol. 603, p. 412760, Feb. 2021, doi: 10.1016/j.physb.2020.412760.

[20] Z. Hanani *et al.*, 'Thermally-stable high energy storage performances and large electrocaloric effect over a broad temperature span in lead-free BCZT ceramic', *RSC Adv.*, vol. 10, no. 51, pp. 30746–30755, 2020, doi: 10.1039/D0RA06116F.

[21] Z. Luo *et al.*, 'Enhanced electrocaloric effect in lead-free $BaTi_{1-x}Sn_xO_3$ ceramics near room temperature', *Appl. Phys. Lett.*, vol. 105, no. 10, p. 102904, Sep. 2014, doi: 10.1063/1.4895615.

[22] M. Sanlialp *et al.*, 'Direct measurement of electrocaloric effect in lead-free $Ba(Sn_xTi_{1-x})O_3$ ceramics', *Appl. Phys. Lett.*, vol. 111, no. 17, p. 173903, Oct. 2017, doi: 10.1063/1.5001196.

[23] Y. Liu, J. F. Scott, and B. Dkhil, 'Some strategies for improving caloric responses with ferroelectrics', *APL Materials*, vol. 4, no. 6, p. 064109, Jun. 2016, doi: 10.1063/1.4954056.

[24] V. K. Pecharsky and K. A. Gschneidner, 'Tunable magnetic regenerator alloys with a giant magnetocaloric effect for magnetic refrigeration from ~20 to ~290 K', *Appl. Phys. Lett.*, vol. 70, no. 24, pp. 3299–3301, Jun. 1997, doi: 10.1063/1.119206.

[25] E. V. Gopalan, I. A. Al-Omari, D. S. Kumar, Y. Yoshida, P. A. Joy, and M. R. Anantharaman, 'Inverse magnetocaloric effect in sol–gel derived nanosized cobalt ferrite', *Appl. Phys. A*, vol. 99, no. 2, pp. 497–503, May 2010, doi: 10.1007/s00339-010-5573-8.

[26] S. Amiri and H. Shokrollahi, 'The role of cobalt ferrite magnetic nanoparticles in medical science', *Materials Science and Engineering: C*, vol. 33, no. 1, pp. 1–8, Jan. 2013, doi: 10.1016/j.msec.2012.09.003.

[27] R. Safi, A. Ghasemi, R. Shoja-Razavi, E. Ghasemi, and T. Sodaee, 'Rietveld structure refinement, cations distribution and magnetic features of CoFe2O4 nanoparticles synthesized by co-precipitation, hydrothermal, and combustion methods', *Ceramics International*, vol. 42, no. 5, pp. 6375–6382, Apr. 2016, doi: 10.1016/j.ceramint.2016.01.032.

[28] Q. Lin, J. Lin, Y. He, R. Wang, and J. Dong, 'The Structural and Magnetic Properties of Gadolinium Doped $CoFe_2O_4$ Nanoferrites', *Journal of Nanomaterials*, vol. 2015, pp. 1–6, 2015, doi: 10.1155/2015/294239.

[29] M. Eshraghi and P. Kameli, 'Magnetic properties of CoFe2O4 nanoparticles prepared by thermal treatment of ball-milled precursors', *Current Applied Physics*, vol. 11, no. 3, pp. 476–481, May 2011, doi: 10.1016/j.cap.2010.08.032.

[30] P. Poddar *et al.*, 'Magnetocaloric effect in ferrite nanoparticles', *Journal of Magnetism and Magnetic Materials*, vol. 307, no. 2, pp. 227–231, Dec. 2006, doi: 10.1016/j.jmmm.2006.04.007.

[31] A. Verma, T. C. Goel, R. G. Mendiratta, and M. I. Alam, 'Dielectric properties of NiZn ferrites prepared by the citrate precursor method', *Materials Science and Engineering: B*, vol. 60, no. 2, pp. 156–162, Jun. 1999, doi: 10.1016/S0921-5107(99)00019-7.

[32] L. Lv *et al.*, 'Grain size effect on the dielectric and magnetic properties of NiFe2O4 ceramics', *Physica E: Low-dimensional Systems and Nanostructures*, vol. 43, no. 10, pp. 1798–1803, Aug. 2011, doi: 10.1016/j.physe.2011.06.014.

[33] B. G. Toksha, S. E. Shirsath, S. M. Patange, and K. M. Jadhav, ‘Structural investigations and magnetic properties of cobalt ferrite nanoparticles prepared by sol–gel auto combustion method’, *Solid State Communications*, vol. 147, no. 11–12, pp. 479–483, Sep. 2008, doi: 10.1016/j.ssc.2008.06.040.

[34] A. Franco and F. C. e Silva, ‘High temperature magnetic properties of cobalt ferrite nanoparticles’, *Appl. Phys. Lett.*, vol. 96, no. 17, p. 172505, Apr. 2010, doi: 10.1063/1.3422478.

[35] D. K. Pradhan *et al.*, ‘Correlation of dielectric, electrical and magnetic properties near the magnetic phase transition temperature of cobalt zinc ferrite’, *Phys. Chem. Chem. Phys.*, vol. 19, no. 1, pp. 210–218, 2017, doi: 10.1039/C6CP06133H.

[36] K. Maaz, A. Mumtaz, S. K. Hasanain, and A. Ceylan, ‘Synthesis and magnetic properties of cobalt ferrite (CoFe2O4) nanoparticles prepared by wet chemical route’, *Journal of Magnetism and Magnetic Materials*, vol. 308, no. 2, pp. 289–295, Jan. 2007, doi: 10.1016/j.jmmm.2006.06.003.

[37] R. H. Kadam, S. T. Alone, M. L. Mane, A. R. Biradar, and S. E. Shirsath, ‘Phase evaluation of Li+ substituted CoFe2O4 nanoparticles, their characterizations and magnetic properties’, *Journal of Magnetism and Magnetic Materials*, vol. 355, pp. 70–75, Apr. 2014, doi: 10.1016/j.jmmm.2013.11.054.

[38] P. C. R. Varma, R. S. Manna, D. Banerjee, M. R. Varma, K. G. Suresh, and A. K. Nigam, ‘Magnetic properties of CoFe2O4 synthesized by solid state, citrate precursor and polymerized complex methods: A comparative study’, *Journal of Alloys and Compounds*, vol. 453, no. 1–2, pp. 298–303, Apr. 2008, doi: 10.1016/j.jallcom.2006.11.058.

[39] J. Y. Law *et al.*, ‘A quantitative criterion for determining the order of magnetic phase transitions using the magnetocaloric effect’, *Nat Commun*, vol. 9, no. 1, p. 2680, Dec. 2018, doi: 10.1038/s41467-018-05111-w.

[40] N. T. Trung, V. Biharie, L. Zhang, L. Caron, K. H. J. Buschow, and E. Brück, ‘From single- to double-first-order magnetic phase transition in magnetocaloric Mn1−xCrxCoGe compounds’, *Appl. Phys. Lett.*, vol. 96, no. 16, p. 162507, Apr. 2010, doi: 10.1063/1.3399774.

[41] Y. Hadouch *et al.*, ‘Piezoelectric, magnetic and magnetoelectric properties of a new lead-free multiferroic (1-x) Ba0.95Ca0.05Ti0.89Sn0.11O3—(x) CoFe2O4 particulate composites’, *J Mater Sci: Mater Electron*, vol. 34, no. 8, p. 725, Mar. 2023, doi: 10.1007/s10854-023-10145-y.

[42] A. S. Kumar, C. S. C. Lekha, S. Vivek, K. Nandakumar, M. R. Anantharaman, and S. S. Nair, ‘Effect of CoFe2O4 weight fraction on multiferroic and magnetoelectric properties of (1 − x)Ba0.85Ca0.15Zr0.1Ti0.9O3 − xCoFe2O4 particulate composites’, *J Mater Sci: Mater Electron*, vol. 30, no. 9, pp. 8239–8248, May 2019, doi: 10.1007/s10854-019-01140-3.

[43] A. A. Momin, M. A. Zubair, Md. F. Islam, and A. K. M. A. Hossain, ‘Enhance magnetoelectric coupling in xLi0.1Ni0.2Mn0.6Fe2.1O4–(1 − x)BiFeO3 multiferroic composites’, *J Mater Sci: Mater Electron*, vol. 30, no. 14, pp. 13033–13046, Jul. 2019, doi: 10.1007/s10854-019-01665-7.

[44] W. Liu *et al.*, 'Understanding the formation of ultrafine spinel CoFe2O4 nanoplatelets and their magnetic properties', *Journal of Applied Physics*, vol. 112, no. 10, p. 104306, Nov. 2012, doi: 10.1063/1.4765033.

[45] A. S. Ponce, E. F. Chagas, R. J. Prado, C. H. M. Fernandes, A. J. Terezo, and E. Baggio-Saitovitch, 'High coercivity induced by mechanical milling in cobalt ferrite powders', *Journal of Magnetism and Magnetic Materials*, vol. 344, pp. 182–187, Oct. 2013, doi: 10.1016/j.jmmm.2013.05.056.

[46] N. Sangeneni, K. Taddei, N. Bhat, and S. Shivashankar, 'Magnetic properties of superparamagnetic, nanocrystalline cobalt ferrite thin films deposited at low temperature', *Journal of Magnetism and Magnetic Materials*, vol. 465, pp. 590–597, Nov. 2018, doi: 10.1016/j.jmmm.2018.06.038.

[47] S. Xu, Y. Ma, B. Geng, X. Sun, and M. Wang, 'The remanence ratio in CoFe2O4 nanoparticles with approximate single-domain sizes', *Nanoscale Res Lett*, vol. 11, no. 1, p. 471, Dec. 2016, doi: 10.1186/s11671-016-1691-3.

[48] R. E. Lu *et al.*, 'Magnetic properties of different $CoFe_2O_4$ nanostructures: nanofibers versus nanoparticles', *J. Mater. Chem. C*, vol. 2, no. 40, pp. 8578–8584, Aug. 2014, doi: 10.1039/C4TC01415D.

[49] Y. Deng *et al.*, 'Three-dimensional phases-connectivity and strong magnetoelectric response of self-assembled feather-like CoFe2O4–BaTiO3 nanostructures', *Chemical Physics Letters*, vol. 496, no. 4–6, pp. 301–305, Aug. 2010, doi: 10.1016/j.cplett.2010.07.048.

[50] J. Hao, W. Li, J. Zhai, and H. Chen, 'Progress in high-strain perovskite piezoelectric ceramics', *Materials Science and Engineering: R: Reports*, vol. 135, pp. 1–57, Jan. 2019, doi: 10.1016/j.mser.2018.08.001.

[51] A. Baji, Y.-W. Mai, R. Yimnirun, and S. Unruan, 'Electrospun barium titanate/cobalt ferrite composite fibers with improved magnetoelectric performance', *RSC Adv.*, vol. 4, no. 98, pp. 55217–55223, 2014, doi: 10.1039/C4RA09449B.

[52] S. H. Xie *et al.*, 'Multiferroic CoFe2O4–Pb(Zr0.52Ti0.48)O3 nanofibers by electrospinning', *Appl. Phys. Lett.*, vol. 92, no. 6, p. 062901, Feb. 2008, doi: 10.1063/1.2837185.

General introduction

Recently, the microelectronics industry has developed increasingly small integrated circuits with even more sophisticated functions with the tendency toward miniaturizing devices to increase speed, reduce power consumption, and lower cost. This trend promotes the development of multifunctional materials, which combine well-known characteristics into a single component. Among them, multiferroic (MF) materials with coexistence of at least two ferroic orders (Ferroelectric (FE), ferro(antiferro/ferri) magnetic and ferroelastic) have attracted more attention as a result of their potential for applications as multifunctional devices. Interesting outcomes, like the magnetoelectric (ME) effect, can result from coupling between these ferroic orders. Therefore, ME materials have the ability to switch and/or tune the polarization (P) by a magnetic field (H) and to control the magnetization (M)by an electric field (E). Now this property provides a whole new perspective on the upcoming generation of innovative electronic devices such as multiple-state memory devices that can be written electrically and read magnetically, electrically controlled microwave phase shifter or voltage-controlled ferromagnetic resonance, magnetically controlled electro-optic or piezoelectric devices, magnetoelectric memory cells and ultra-sensitive magnetic sensors.

There are two types of magnetoelectric materials: (i) single-phase multiferroic materials, where magnetic and electric fields are intrinsically coupled, but the coupling between them is usually weak, and (ii) multi-phase composites with spatially distinct piezoelectric and magnetostrictive phases connected via an interface. In these composites, the magnetoelectric coupling is indirectly induced by the strain interaction between the piezoelectric and magnetostrictive effects. In fact, the application of an electric field to a composite material induces the piezoelectric phase to undergo mechanical stress, which subsequently transfers to the magnetostrictive phase and changes its magnetic moment. The reverse effect is also possible. A crucial factor in achieving robust ME effects in multi-phase composites is to maximize the transfer of strain between different phases. Therefore, the interface area between piezoelectric and magnetostrictive phases plays a critical role in this type of strain-mediated ME coupling.

Several types of materials can serve as the magnetostrictive phase in composite materials, including rare earth alloys, amorphous ribbons, manganites and ferrite. Rare earth-based giant magnetostrictive materials like Terfenol-D (with the chemical formula $Tb_{0.3}Dy_{0.7}Fe_{1.9}$) exhibit exceptional results due to their powerful magnetostrictive properties. However, the high cost and limited availability of rare earths have led to a growing interest in using ferrites instead.

The remarquable magnetostrictive and magnetocaloric characteristics of cobalt ferrite $CoFe_2O_4$ as an example of this family are the reasons, we have chosen it for our multiferroic composites and magnetic refrigeration applications.

On the other hand, lead-based materials are commonly utilized as the piezoelectric phase in multiferroic composites owing to their outstanding polarization and piezoelectric properties. However, these materials have a detrimental impact on the environment, which calls for the exploration of alternative materials with comparable properties but less environmental drawbacks. Therefore, barium titanate $BaTiO_3$(BT) and its derivatives are the main primary candidates for a Pb-free multiferroic composites.

The aim of this study is to develop new magnetic materials(magnetostrictive) and ferroelectric (piezoelectric) and multiferroic composites with different connectivities for applications in magnetic refrigeration and storage of data bits written by electric field and read using the magnetic field.

This thesis has a dual-fold major goal. First, it aims to improve our understanding of the structural, ferroelectric and magneticproperties of the selected piezoelectric ($Ba_{0.95}Ca_{0.05}Ti_{0.89}Sn_{0.11}O_3$ abbreviated as BCTSn) and magnetostrictive ($CoFe_2O_4$ abbreviated as CFO) materials. Second, it intends to quantify the magnetoelectric coupling between these materials via two types of connectivities: 0-3 and Core-shell nanofibers.

The first chapter will provide an overview of the literature on multiferroic composites, covering their fundamental principles, properties, and potential applications. It will also present a comprehensive overview of magnetism and ferroelectricity and their origin. Furthermore, this chapter will discuss the different types of multiferroic materials, their properties, and the nature of their coupling.

The second chapter will present the experimental protocol for the synthesis of CFO and BCTSn phases, as well as the different experimental techniques used to characterize the obtained powders/fibers.

The third chapter will focus on two key materials used in the multiferroic composites - BCTSn and CFO. This chapter will be devoted to the discussion of (i) structural and morphological results, ferroelectric, electrocaloric and energy storage properties of the BCTSn ceramics prepared by sol-gel method and (ii) structural results, magnetic and magnetocaloric properties of the CFO elaborated by sol-gel self-combustion method. The two sections will be

presented by Hadouch et al. The two parts will be presented as two different articles published by *Hadouch et al.*

Investigations of the morphological, structural, ferroelectric, piezoelectric, magnetic and magnetoelectric properties of multiferroic composite materials (CFO-BCTSn) types 0-3 and core-shell nanofibers (1-3) will be the main topic of the fourth chapter. The results will be presented in the form of two publications by *Hadouch et al.*, each one focusing on a different type of coupling.

Finally, the thesis will be concluded with a summary of the main findings and an outlook on future possibilities for investigation.

Chapter 1

MULTIFERROICS: FUNDAMENTALS AND APPLICATIONS

I. Introduction to multiferroics

Magnetism, ferroelectricity and ferroelasticity are among the basic physical properties that that are in great demand in advanced technological applications. A material that possesses more than one of these primary properties, with the interaction between them, is known as multiferroic. The term “multiferroic” is commonly used to describe magnetoelectric materials that exhibits both ferromagnetic and ferroelectric properties. However, the big challenge is to find the coupling between these two properties. Achieving this coupling, i.e. switching polarization by magnetic field application and vice versa, can extend the functionality of the materials. One of the most potential applications of multiferroics in electronics is the writing of magnetic information into an MRAM memory (Magnetic Random Access Memory) using an electric field. This allows for a significant energy gain over producing a magnetic field taking the advantage of magnetoelectric coupling, we can write four polarization states instead of two. This technique has the potential to increase the amount of storable data without reducing storage surfaces. Further, multiferroics have the potential to offer numerous advanced applications, such as enhancing computing power in electronic devices, reducing energy consumption, and minimizing waste by combining electrical and magnetic in a single material. On the other hand, multiferroic field of study is an interesting scientific topic due to the large number of materials that can be used, as well as the nanoscale sizes that allow new and unique physical behaviors.

An overview of the literature on multiferroic composites is given in this opening chapter. The general basics about magnetism and ferroelectricity will be discussed. The different type of multiferroics will be introduced, along with their coupling nature.

II. Multiferroics background

II.1. Historical overview of multiferroics research

A **ferroic** is a material that exhibits a spontaneous orientation of its order parameter, is stable, and shows a hysteresis cycle of this order parameter when subjected to cyclic solicitation of the associated field [1]. The main ferroic orders include, among many others, **ferroelasticity** (hysteresis of the deformation under cyclic stress), **ferromagnetism** (hysteresis of magnetization under a cyclic magnetic field), and **ferroelectricity** (hysteresis of electric polarization under a cyclic electric field) [2].

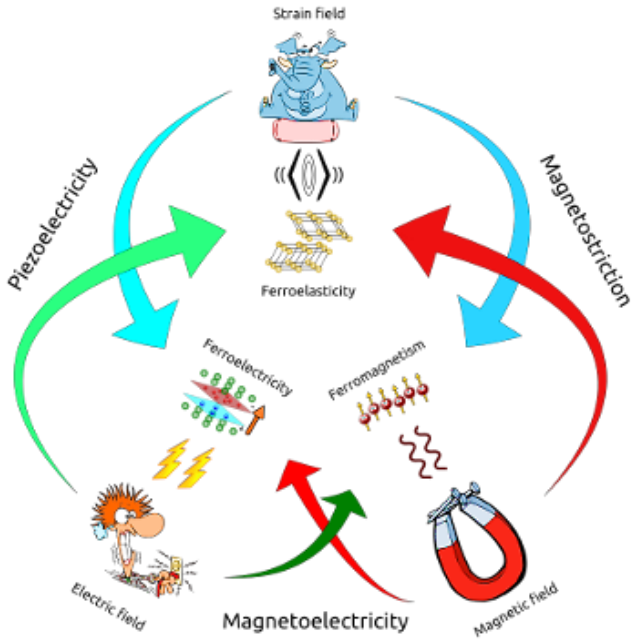

Figure 1. 1: *The multiferroics totem illustrating the three main ferroic orders with their respective fields and crossed interactions.*

"Symmetry breaking is what ***"creates the phenomenon"****" said Curie Pierre.*

Historically, in 1894, P. Curie started the first discussion about existence of a linear relationship between the electrical and magnetic properties, i.e., that some materials in nature can be polarized by a magnetic field and can be magnetized by an electric field [3]. The study of multiferroic materials became increasingly popular in the 1960s thanks to the discovery and exploitation of the properties of ferroelectric materials like Cr_2O_3 and $BaTiO_3$ (BT) in the 1940s[4], following Dzyaloshinskii's generic prediction one year earlier[5]. In 1972, particulate composites containing either ferroelectric and magnetic particles were extensively studied for their potential applications[6]. Nevertheless, the low magnetoelectric coupling observed in these composites, as well as the high dielectric losses, have affected their practical applications.

A new wave of interest in magnetoelectricity emerged in the 2000s, along with new advanced experimental methods for the synthesis and characterization of nanomaterials. [for example, piezoresponse force microscopy (PFM), scanning transmission electron microscopy (TEM), and advanced pulsed laser deposition (PLD) techniques]. Starting at this time, new multiferroic composites are appearing with various connectivities [e.g., laminated composites, vertically aligned nanocomposites and nanoporous materials.], and the use of organic compounds with piezoelectric properties [7] (Figure 1.2). According to *Google scholar*, the increase in the number of scientific publications from 601 to 12100 per year between 2000 and 2023, is evidence of this.

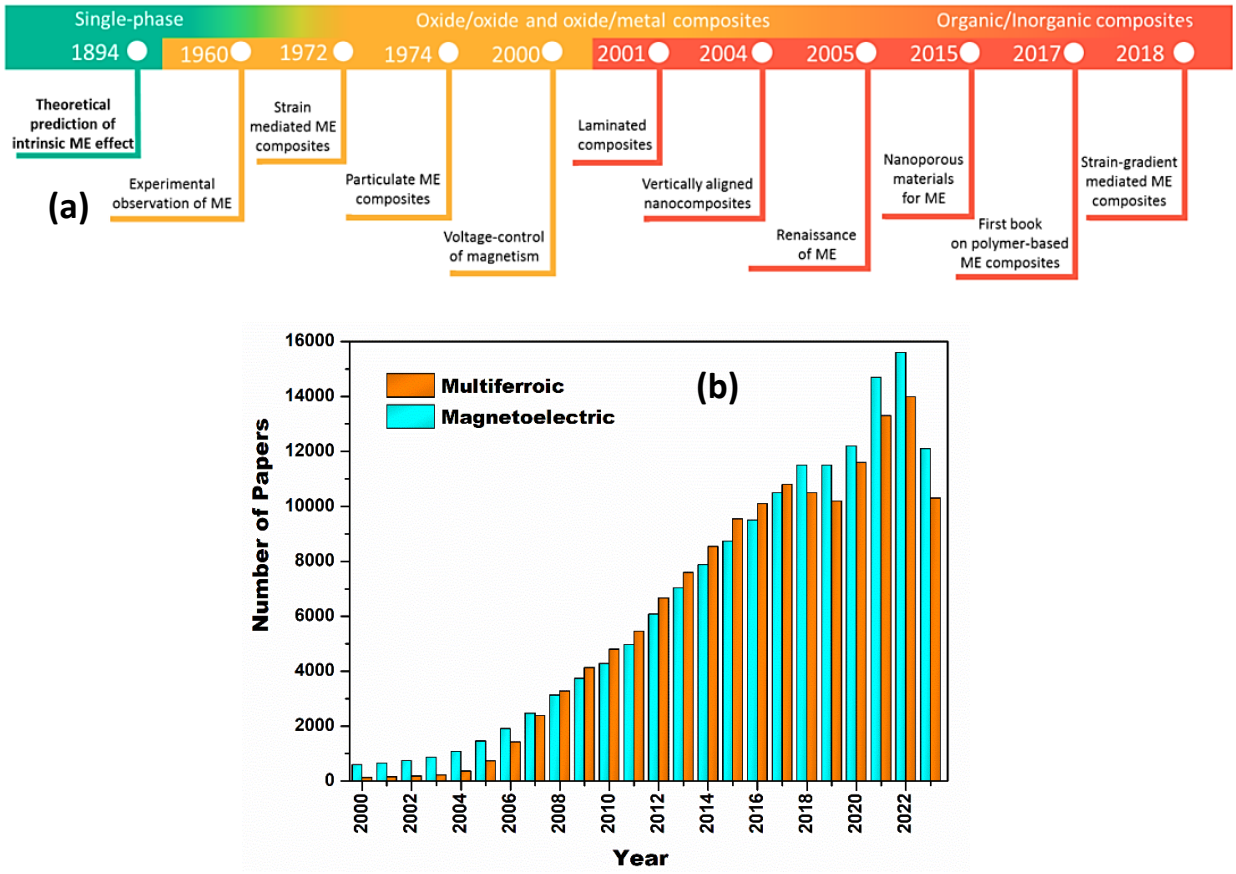

Figure 1. 2: *(a) Timeline showing the emergence of various types of ME materials [7]; (b) Number of scientific papers (according to the 'Google scholar') using the keyword 'magnetoelectric', and 'multiferroic', during the period 2000–2023.*

II.2. Multiferroic materials: potential applications in emerging technologies

Due to their unique properties and potential applications, multiferroic materials have received increased attention in recent years. The following are a few of the key areas where multiferroics are projected to have a significant impact:

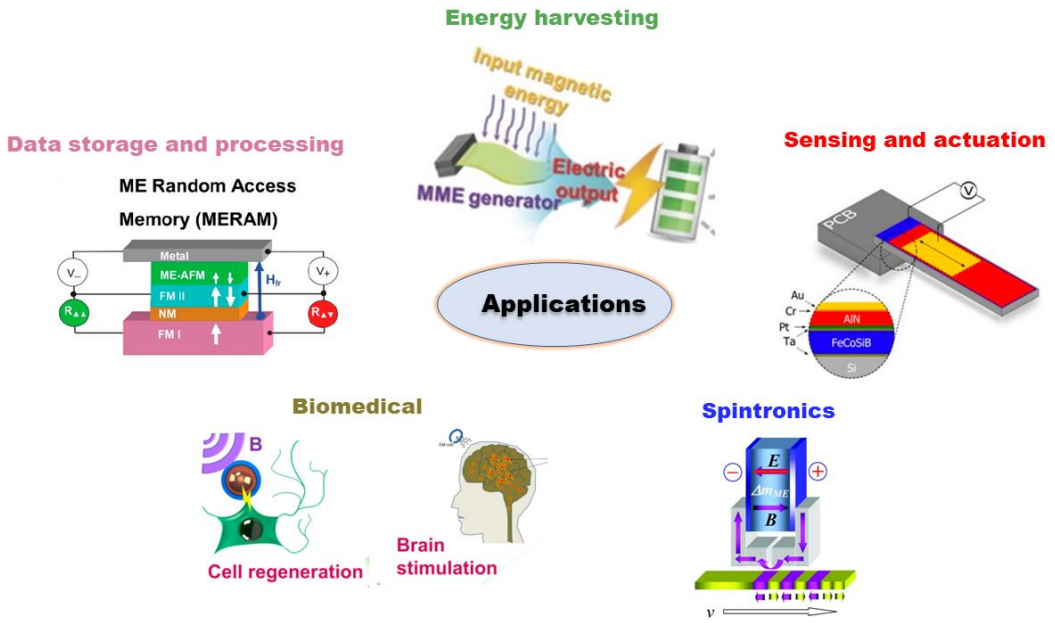

Figure 1. 3: *Various applications of magnetoelectric (ME) composites.*

- ***Data storage and processing*****:** By enabling faster, more energy-efficient, and higher-density devices, multiferroic materials have the potential to revolutionize data storage and processing. The coexistence of electric polarization and magnetization in a single-phase makes them suitable for multistate memory devices, as P and M are used to encode binary information in FRAM (FE random-access memories) and MRAM (magnetic random-access memories), respectively [8].
- ***Sensing and actuation*****:** Because they can respond to both electric and magnetic fields, multiferroic materials can be used in sensors and actuators. Multiferroic materials, for example, can be used to make magnetic field sensors that are more sensitive and accurate than traditional sensors. Typical engineering applications of ME sensors covered in this review include object detection and localization, speed and displacement sensing, stress and strain sensing, and biological magnetic measuring [9].
- ***Energy harvesting*****:** Energy can be harvested from a variety of sources, including mechanical vibrations and magnetic fields, by multiferroic materials. This could open the door for more efficient and versatile energy harvesting technologies to emerge. This is an intriguing study on the use of ME materials in the field of energy harvesting. In practice, a multiferroic ME module was developed for scavenging biomechanical energy for the long-term operation of personal mobile electronics by converting mechano-magneto-electric energy [10].

- ***Spintronics:*** Multiferroic materials have potential applications in spintronics, as they can be used to control the spin of electrons with an electric field. Some investigations have demonstrated a method to switch spin currents on and off electrically, offering a potential solution to the heating problem associated with energy dissipation in computers. Using an insulator, they transported spins without moving electrons themselves, reducing energy dissipation and providing a pathway to increase computing power. Spin-based devices could replace charge currents and greatly reduce energy consumption in electronic devices[11].
- ***Biomedical applications:*** Multiferroic materials have the potential to be applied in various biomedical devices and therapies, including magnetic drug delivery and magnetic hyperthermia, which is a non-invasive method for treating cancer by utilizing magnetic nanoparticles to generate heat and eliminate cancer cells. Additionally, multiferroic nanoparticles can serve as both magnetic and electric field sensors for biomedical imaging and drug delivery. The magnetic properties of these nanoparticles can be used to target specific regions of the body, whereas their electric field properties can be used to regulate drug release [12].

II.3. Challenges and drawbacks of existing multiferroic materials

In recent years, there has been a lot of interest in the field of multiferroics and magnetoelectrics [13], [14]. Nevertheless, there remain a lot of challenges and limitations that require further research. Several studies have highlighted the need to better understand the fundamental mechanisms underlying multiferroic behavior [15]. The coupling between a material's electrical and magnetic properties is complicated and still poorly understood, making it difficult to predict and design specific materials. More research is required to develop new techniques for controlling and modifying the properties of these materials [16]. Furthermore, the nonlinear behavior of multiferroic materials makes controlling their properties more complicated [17]. Another obstacle is the need to develop new multiferroic materials with improved coupling between ferroelectric and magnetic properties. Indeed, current multiferroic materials' applications are limited due to their weak magnetoelectric coupling and the requirement for large external magnetic fields to control their properties, necessitating the effort to find novel materials with improved magnetoelectric coupling that could enable new technological applications[18].

Another significant challenge is the difficulty faced during the synthesis and characterization of multiferroic materials. Indeed, multiferroic materials frequently have

complex crystalline structures that necessitate the use of highly developed techniques to synthesize. This can result in high production costs and limited scalability. As a result, new synthesis techniques and less complicated treatment methods with low costs are required[19].

To conclude, while existing multiferroic materials have several challenges and drawbacks, research is taking place to develop new materials with improved properties. Multiferroic materials will hold great promise for a wide range of applications in the future, with continued advances in synthesis, processing, and characterization techniques.

III. Basic knowledge of multiferroics

III.1. Magnetism

III.1.1. Origins of magnetization

The electron is a fundamental particle with mass $\boldsymbol{m_e}$ and charge $\boldsymbol{e}$ and two angular moment origins. The first angular moment is the *orbital moment*, which is related to the rotation of the electron around the nucleus. The second is the *spin moment*, an angular moment unique to the electron. The magnetic moment of a magnetic atom originates from these two moments. The orbital magnetic moment and the spin magnetic moment are then differentiated based on their origin, and are coupled by the spin-orbit interaction.

Magnetization *M*, also known as magnet polarization, is induced by the alignment of orbital magnetic moments and spin, and it can be influenced by applying a magnetic field *H*. The following expression describes how the magnetic field and magnetization are linearly related for relatively low magnetic field values:

$$M = \chi H \qquad (1.1)$$

Where χ is the magnetic susceptibility. It can be included in the magnetic induction expression:

$$B = \mu_0(1 + \chi)H = \mu_0\mu_r H = \mu H \qquad (1.2)$$

Here, μ_0 is the constant of permeability of a vacuum, the term μ_r is termed as the relative magnetic permeability of a material.

III.1.2. Classes of magnetic materials

Depending on the existence and alignment of magnetic moments with or without application of magnetic field, three types of magnetism can be defined:

III.1.2.1. Diamagnetic

In this type of material, all electrons are coupled, so there is no permanent net magnetic moment per atom. By applying a magnetic field, diamagnetic material is slightly repelled and do not retain the magnetic properties when the external field is removed. It has a weak and negative susceptibility (e.g., Au: -2.74 10^{-6} and Cu: -0.77 10^{-6}). Most elements in the periodic table, including copper, silver, and gold, are diamagnetic. Water, graphite, copper, silver, and the majority of organic compounds are examples of diamagnetic materials.

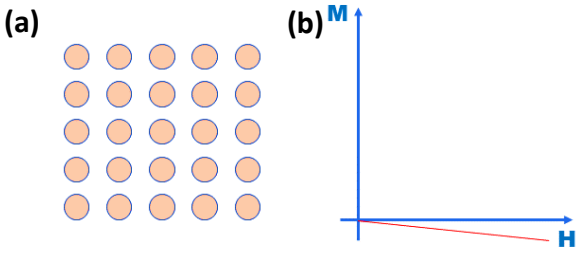

Figure 1. 4: *Atomic (a), magnetic (b) behavior of diamagnetic materials.*

III.1.2.2. Paramagnetic

The magnetic moments of paramagnetic material are randomly oriented and hence do not produce any net magnetic field. However, when subjected to a magnetic field, it acquires magnetization oriented in the same direction as the external magnetic field. The susceptibility in this type of materials is positive but very small (e.g., β-Sn: 0.19 10^{-6}; Pt: 21.04 10^{-6}; Mn: 66.10 10^{-6}). The magnetism of paramagnetic materials frequently results from the permanent magnetic moments that all or some of the atoms hold. These magnetic moments practically do not interact with each other and can orient themselves freely in any direction. The magnetization in paramagnetic material decreases with increasing temperature, so thermal agitation is crucial. As temperature rises, the M-H curve becomes more and more linear. Examples of paramagnetic materials include most transition metals, oxygen and some molecules.

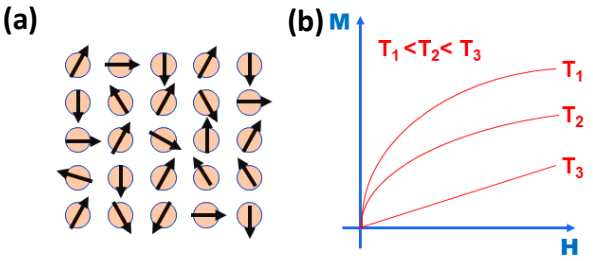

Figure 1. 5: *(a) Atomic, (b) magnetic behavior of paramagnetic materials.*

III.1.2.3. Antiferromagnetic

The magnetism of antiferromagnetic materials is similar to that of paramagnetic materials with a weak and positive susceptibility (Cr: 3.6 10^{-6}). However, the magnetic moments are organized in antiparallel arrangement below a critical temperature called Neel temperature (T_N). This antiparallel arrangement is the result of negative exchange interactions, or interactions between nearby atoms. In the absence of a magnetic field, the total magnetization is zero because of the splitting of material into two sub-lattices of magnetic moments with equal and opposite magnetization. This phenomenon is observed in oxides and salts of transition metals such as MnO, NiO, MnF_2.

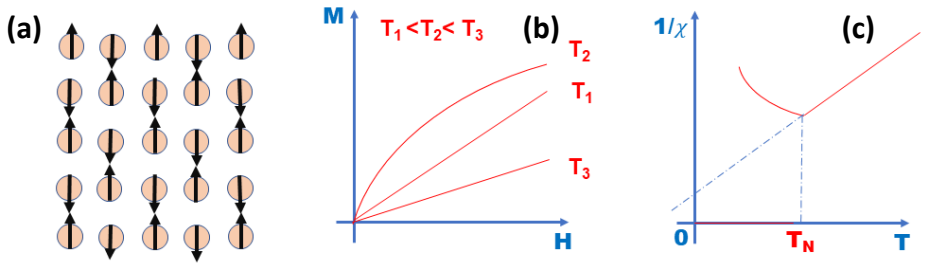

Figure 1. 6: *Atomic (a), magnetic (b) behavior and temperature dependance of the inverse susceptibility (c) of antiferromagnetic materials.*

III.1.2.4. Ferrimagnetic

A ferrimagnetic material also has two types of arrangement with an antiparallel orientation that do not fully compensate for each other (from this point of view, antiferromagnetism is a particular case of ferrimagnetism). Ferrimagnetic materials, like ferromagnetics, exhibit significant spontaneous magnetization at room temperature. They also have magnetically saturated domains, magnetic saturation, and hysteretic properties. Their spontaneous magnetization disappears above the Curie temperature, and they become paramagnetic.

To achieve ferrimagnetism, the sublattices must be made up of two different materials or two different oxidation states of the same element, such as Fe^{2+} and Fe^{3+} ions with different magnetic moments. A ferromagnetic material is made up of multiple states of various transition elements (e.g., Nickel, Ferrite and Ferrous ferrite). The susceptibility is extremely high and positive.

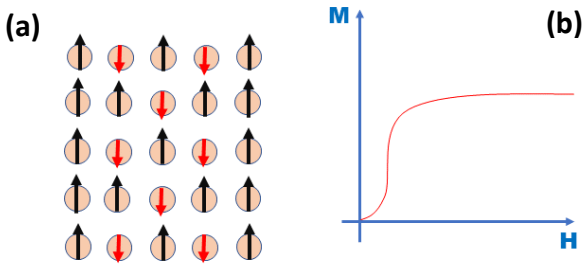

Figure 1. 7: *Atomic (a), magnetic (b) behavior of ferrimagnetic materials.*

III.1.2.5. Ferromagnetic

In ferromagnetic materials, the exchange interactions are positive, favoring the parallelism of the magnetic moments of the closeness neighboring atoms. Similar to antiferromagnetic materials, thermal agitation at high temperatures ($T>T_c$ with T_c: Curie temperature) results in a susceptibility similar to that of a paramagnetic material, this is the Curie Weiss law ($\chi = C/T-T_c$). The thermal agitation is primarily dominated by interactions below T_C. In spite of this preferred parallelism between magnetic moments, the presence of uniform spontaneous magnetization M_s in below the T_c is not always achieved. In fact, the material has been divided into several regions, with a uniform magnetization but differs in orientation. These regions are so-called "*Weiss domains*" (Figure 1.8.d). When an external magnetic field is applied, the distribution of the domain's shifts, and under significantly stronger fields, the magnetization has a tendency to saturate.

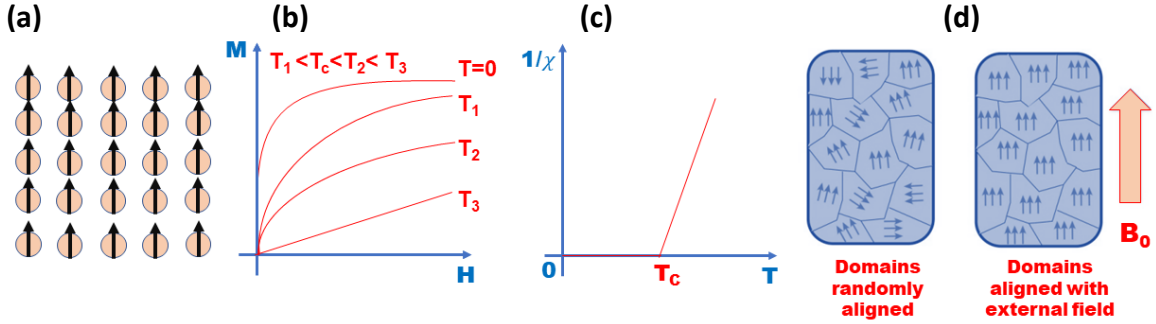

Figure 1. 8: *Atomic (a), magnetic (b) behavior, temperature dependance of the inverse susceptibility (c) and magnetic field effect on magnetic domains(d) of ferromagnetic materials.*

As a result of the magnetic field, ferromagnetic materials have the ability to display a magnetization hysteresis cycle. The parameters of this magnetization curve are as follows:

- A saturation magnetization $\boldsymbol{M_S}$ is the maximum magnetization value of a material for which all of its magnetic moments are aligned;
- A remanent magnetization $\boldsymbol{M_r}$, which is the magnetization at zero field after being exposed to a saturating external field. Depending on the material's magnetic history, this can be directed along **+** $\boldsymbol{M_r}$ or **-** $\boldsymbol{M_r}$;
- A magnetic field at saturation HS, with all moments aligned with the magnetic field for $\boldsymbol{H}$>$\boldsymbol{H_S}$;
- A coercive field $\boldsymbol{H_c}$, i.e., the field for which the magnetization becomes zero upon return from a completely saturated state.

Because of this property, ferromagnetic materials are useful in a wide range of applications, including electric motors, generators, and transformers. Materials containing iron, cobalt, nickel, and some rare-earth metals (with incompletely filled d orbitals) are examples of ferromagnetic materials.

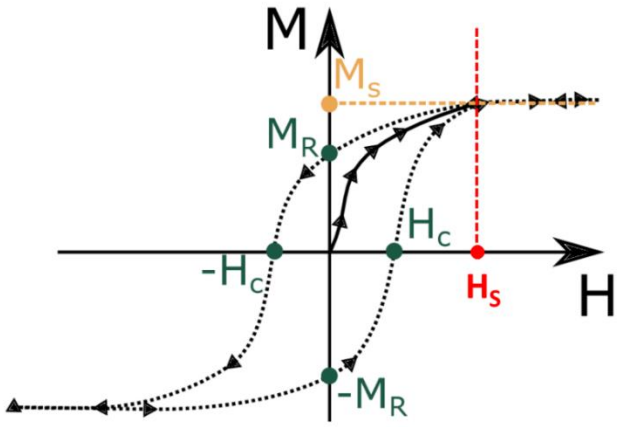

Figure 1. 9: *Magnetic hysteresis loop.*

III.1.3. Hard and Soft magnets

Ferro and ferrimagnetic materials are classified as hard or soft magnets based on their hysteresis properties. **Soft magnetic materials** have high saturation magnetization values, low coercivity, high permeability, and are easily magnetized and demagnetized. These materials are used to create temporary magnets. Even after the magnetic field is removed, **hard magnetic materials** retain their magnetism. They exhibit high saturation magnetization but are distinguished by high coercivity and are difficult to magnetize and demagnetize. These materials are used to create permanent magnets. Permanent magnets prevent the domain wall

from moving. They are made by heating and then cooling magnetic materials to the required temperature. Impurities improve the toughness of hard magnetic materials.

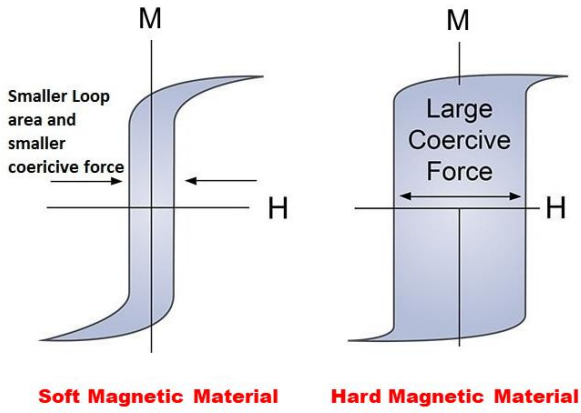

Figure 1. 10: *Hysteresis curve of soft / hard magnetic materials[20]***.**

III.1.4. The Exchange Interaction

The spontaneous magnetization of Weiss domains is mainly due to the spin magnetic moment of the electrons. However, there are restrictions on the relative orientation of these spins. According to the Pauli principle, two electrons cannot have the same quantum state. If two electrons in a system have the same spin, this principle implies that the electrons are spatially separated in the system. Despite Coulomb repulsion, if the spins are antiparallel, the two electrons can be together in a much smaller region of space. The exchange interaction, introduced by Heisenberg in 1929 [21], explains this behavior.

The energy associated with this interaction between two neighboring atoms ***i*** and ***j*** is expressed as follows:

$$E_{ex} = -2J_{ex}S_i.S_j = -2JS_i.S_j \cos \boldsymbol{\phi} \qquad (1.3)$$

where $\boldsymbol{S_i}$ and $\boldsymbol{S_j}$ are the spin angular moments of atoms ***i*** and ***j***, $\boldsymbol{\phi}$ is the angle between the spins, and $\boldsymbol{J_{ex}}$ is called the exchange integral. $\boldsymbol{J_{ex}}$ is the difference in energy between two electrons with parallel and antiparallel spins.

When the value is positive, the spin configuration parallel is preferred; when the value is negative, the antiparallel configuration has the lowest energy. The term $\boldsymbol{J_{ex}}$ depends on the ratio between the radius of an atom and the radius of its *3d* layer: **a/r**. The evolution of the interaction energy of exchange according to this ratio is depicted in ***Figure 1.11***. Only when we are interested in electrons whose orbits coincide may $\boldsymbol{J_{ex}}$ differ from zero. In other words, we only consider this interaction for atoms that are nearby.

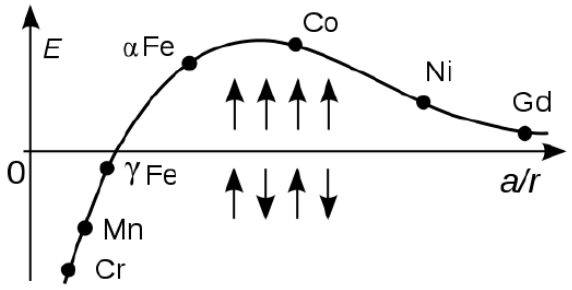

Figure 1. 11: *The evolution of exchange interaction energy as a function of an atom's radius and the radius of its 3d or 4f shell.*

III.1.5. The double-exchange and super-exchange interaction

The super exchange theory modeled by Anderson [22] can be described qualitatively using ***Figure 1.12***. Taking iron oxide Fe_3O_4 as an example, the coexistence of Fe^{2+} and Fe^{3+} cations in ferrites causes this phenomenon of super-exchange.

Hund's rule dictates that the spins of the five electrons in the d-subshell of the Fe^{3+} ion be parallel to one another. In contrast, the Fe^{2+} cation has an additional spin-down electron in the d-subshell. Electron transport between Fe^{2+} and Fe^{3+} ions occurs at B sites via the oxygen ion, which is known as ***double-exchange interaction*** (***Figure 1.12 a***). In this interaction, the additional electron at the Fe^{2+} site can only jump into the Fe^{3+} site if the ion spins are parallel. This process causes the extra electron to delocalize, increasing its band width and, as a result, minimizing its kinetic energy. As a result, this interaction tends to ferromagnetically couple the ions.

In contrast, Fe^{3+} ions at B sites can interact with another Fe^{3+} ion at A sites via oxygen ion via a mechanism known as ***super-exchange interaction*** (***Figure 1.12 b***). This interaction causes the spins of Fe^{3+} ions at the A and B sites to be antiparallel, resulting in the antiferromagnetic alignment of their spins and cancellation of their magnetic moments of $5\mu_B$ out. This results in a net magnetic moment of $4\mu_B$, which is entirely due to the Fe^{2+} ion. The high Curie temperature of 860 K is thought to be caused by this superexchange interaction.

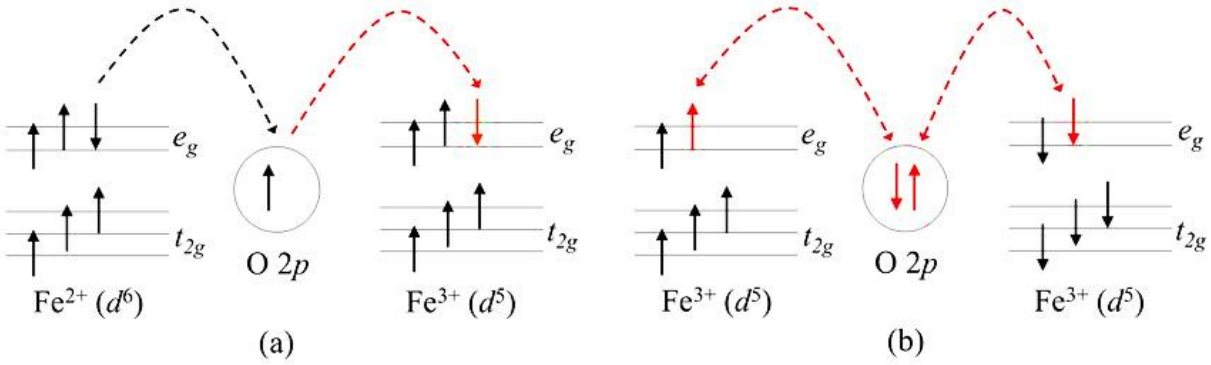

Figure 1. 12: *Diagrams of (a) double-exchange and (b) superexchange interactions in Fe_3O_4.*

III.1.6. Magnetic nanoparticles

In 1968, Brown [23] provided a clarification that the magnetic state of a small particle can exist in one of two states: monodomain if the particle is sufficiently small, and multidomain if the particle is large enough. Reducing the size of grains in a magnetic material significantly requires a considerable amount of energy to create Bloch walls. Thus, the monodomain state, which contains only one Weiss domain, becomes the most stable. To determine the critical radius of a small spherical particle with uniaxial anisotropy, the following equation [24] can be used:

$$R_C = \frac{9\sqrt{AK}}{\mu_0 M_S^2} \qquad (1.4)$$

where $\boldsymbol{A}$ is a constant representing the exchange interaction between two individual spins, $\boldsymbol{K}$ is the magnetic anisotropy constant, $\boldsymbol{\mu_0}$ is the vacuum permeability, and $\boldsymbol{M_s}$ is the saturation magnetization.

III.1.7. Superparamagnetism

Superparamagnetism is a phenomenon observed in ferromagnetic or ferrimagnetic materials characterized by nanoscale grains, where their magnetization can spontaneously reverse due to temperature fluctuations, with the average time between two reversals being referred to as the Néel relaxation time [25]. In the absence of an applied magnetic field, if the measurement time of the magnetization of the grains is much longer than the Néel relaxation time, the measured magnetization will be zero, corresponding to the superparamagnetic state. Although the grains in this state can be magnetized by an external magnetic field, similar to a paramagnetic material, the magnetic susceptibility of superparamagnetic grains is much higher.

Consider measuring the magnetization of a single superparamagnetic grain, where $\boldsymbol{\tau_m}$ represents the measurement duration. If $\boldsymbol{\tau_m}$ is much higher than the relaxation time, the grain's magnetization will spin multiple times, resulting in a measured magnetization of zero. If $\boldsymbol{\tau_m}$ is much smaller than the relaxation time, the grain's magnetization will not spin, and the measured magnetization will be the grain's magnetic moment. In the first case, the grain is referred to as superparamagnetic, while in the second, it is said to be ferromagnetic, or blocked. The particle's state (superparamagnetic or ferromagnetic) is thus dependent on the measurement time. A transition between the two states occurs when $\boldsymbol{\tau_m}$ equals the relaxation time. In various experiments, the magnetization measurement time remains constant while the temperature changes, allowing the observation of the ferromagnetic-superparamagnetic transition at a certain temperature. The temperature at which $\boldsymbol{\tau_m}$ equals the relaxation time is known as the blocking temperature, below which the magnetization of the grain appears blocked on the measurement time scale.

$$T_B = \frac{KV}{K_B \ln(\frac{\tau_m}{\tau_0})} \qquad (1.5)$$

where **K**, **V**, and $\mathbf{k_B}$ are anisotropy constants, particle volume, and Boltzmann constants, respectively[26].

III.1.8. Ferrites and their magnetic properties

III.1.8.1. Crystal structure of ferrites

The spinel network gets its name from the mineral $MgAl_2O_4$ cubic structure. It was discovered for the first time by Bragg and Nishikawa [27]. Ferrites are spinel materials with the space group Fd3m (number 227 in international tables) and the chemical formula MFe_2O_4 where M is a divalent metal ion (Co^{2+}, F^{2+}, Zn^{2+}). The oxygen ions, whose dimensions are relatively large, form a face-centered cubic (FCC) lattice, defining tetrahedral and octahedral cationic sites. The tetrahedral sites are located between four oxygen ions and are denoted by the letter A, while the octahedral sites are located between six oxygen ions and are denoted by the letter B.

The spinel structure's elemental unit cell contains 32 O^{2-} ions and 24 metal cations distributed among 64 tetrahedral sites and 32 octahedral sites. In the tetrahedral sites, there are 8 metal cations, each of which is coordinated by four oxygen ions. In the octahedral sites, there are 16 metal cations, each of which is coordinated by six oxygen ions. The distribution of

divalent and trivalent metal cations between the tetrahedral (A) and octahedral (B) sites in the spinel structure determines the type of spinel. There are two main types of spinels: normal or direct spinel, and inverse spinel.

III.1.8.2. Spinel and inverse spinel crystal structures

Spinel containing divalent and trivalent ions is classified with respect to the $MgAl_2O_4$ spinel based on whether the divalent cation occupies the A or B sites. When the divalent cation occupies the A sites, the spinel is called "normal" or "direct", for example $ZnFe_2O_4$ ($(Zn^{2+})_A[Fe^{3+}{}_2]_BO_4$). When the divalent cation occupies the B sites, the spinel is called "inverse". Barth and Posnjak [28] showed that the distribution of ions can be done in another way, meaning that the M^{2+} cations occupy half of the octahedral sites while the Fe^{3+} ions are distributed equally between the A and B sites. Spinel compounds such as cobalt ferrites $CoFe_2O_4$ possessing this type of ionic distribution are called inverse spinels and the representation of the cobalt ferrite with the distribution of cations can be written as $(Fe^{3+})_A(Fe^{3+}Co^{2+})_BO_4{}^{2-}$. The distances between the nearest neighbors A and B are r_{AB}=0.3473 nm, r_{BB}=0.2962 nm, r_{AA}=0.3625 nm, and its lattice parameter is 0.8392 nm.

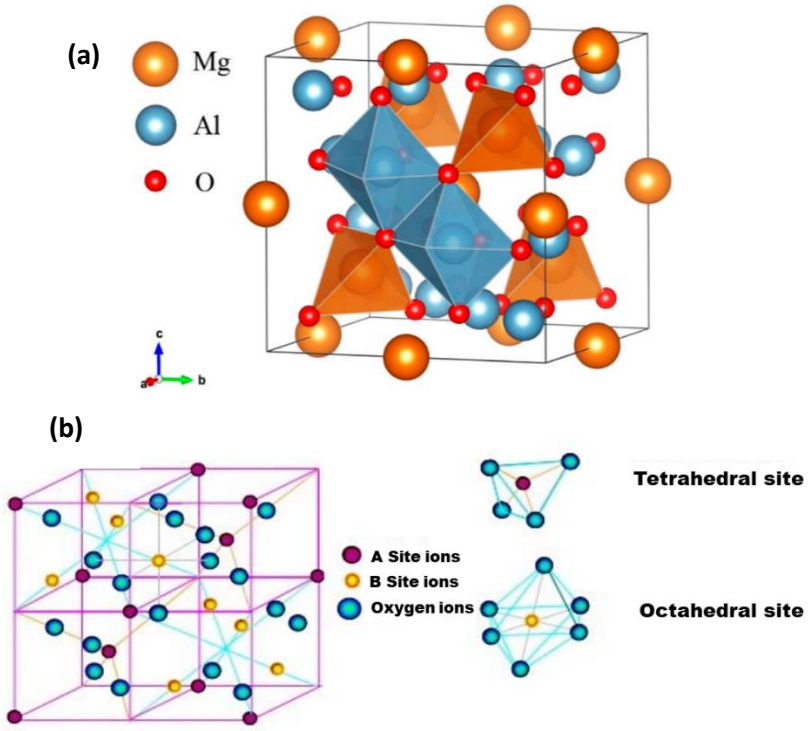

Figure 1. 13: *(a) Crystal structure of $MgAl_2O_4$ spinel, (b) tetrahedral and octahedral sites in the crystal structure of spinel ferrite.*

The presence of tetrahedral and octahedral sites within the cubic network allows for variable ion distributions between these crystallographic sites, which can be described using a term called ***the degree of inversion λ***. The formula for such an oxide is as follows:

$$A_{1-2\lambda}^{2+}B_{2\lambda}^{3+}\left[A_{2\lambda}^{2+}B_{2-2\lambda}^{3+}\right]O_4^{2-}$$

Where λ is the ***degree of inversion*** ($0 \leq \lambda \leq 0.5$)

$\lambda = 0$: The spinel is described as "normal."

$0 < \lambda < 0.5$: The spinel is said to be statistically disorganized.

$\lambda = 0.5$: The spinel is referred to as "inverse."

III.1.8.3. Magnetism in ferrites

In most oxide materials, the exchange energy between neighboring metal atoms' spins is negative, which means that the spins are antiparallel to achieve their lowest energy state. This applies to the interactions between A-A, A-B, and B-B sites. However, these interactions are not always of the same strength and, therefore, do not occur simultaneously.

The interaction between ions occupying octahedral and tetrahedral sites results in spin asymmetry, which arises due to the geometry of the involved orbitals. The ***superexchange*** interaction between sites A and B is the strongest due to its geometry, resulting in parallel alignment of all A moments and antiparallel alignment with B moments. Therefore, the A-B interaction is the most important factor determining the magnetic properties of the oxide materials. It results in an antiparallel alignment of B spins, with each A spin pointing in the same direction. This parallel alignment of A spins and antiparallel alignment of B spins lead to a net magnetization that is directed along a specific direction, depending on the arrangement of the atoms in the material.

III.1.8.4. Magnetostriction effect

The phenomenon known as magnetostriction is primarily a result of the interaction between spin and orbit, also known as spin-orbit coupling, which is responsible for the crystalline anisotropy. Although the coupling is typically weak, the orientation of spin can deviate from the easy magnetization axis. However, in the case of magnetostrictive materials, the coupling is exceptionally strong. When an external magnetic field is applied, the magnetic moment of the spin will rotate, and the coupled orbital magnetic moment will follow suit. This

motion causes the electronic cloud to shift, resulting in local atomic movement, which ultimately leads to a global deformation of the material.

III.1.8.5. Magnetocaloric refrigeration:

a. Introduction and short history on magnetocaloric effect:

MCE refers to the change in temperature or entropy experienced by a magnetic material when it is exposed to a varying magnetic field. In 1918, Pierre Weiss and Auguste Piccard presented a theoretical explanation of MCE from a thermodynamic perspective to the Paris Academy of Sciences [29]. It wasn't until 1926-1927 that Peter Debye [30] and William Giauque [31] were able to offer a thermodynamic explanation of this phenomenon and propose the use of adiabatic magnetization/demagnetization processes to achieve low temperatures. William Francis Giauque and P.D. McDougall later confirmed this mechanism experimentally using a prototype that employed the paramagnetic salt of gadolinium $Gd_2(SO_4)_3$, $8H_2O$ under a magnetic field of 0.8 T [31]. This apparatus allowed for a temperature of 0.25 K to be reached from an initial temperature of 1.5 K. William Giauque's extensive contributions to the field of thermodynamic chemistry, particularly in relation to the behavior of substances at extremely low temperatures, earned him the Nobel Prize in Chemistry in 1949[32].

b. Definition and principle

The magnetocaloric effect is an inherent characteristic of specific magnetic materials, which causes their temperature to alter when subjected to an external magnetic field, a phenomenon known as adiabatic demagnetization or magnetization. This effect results from the relationship between the magnetic arrangement of the material and the external magnetic field, leading to a change in material entropy. The total material entropy comprises three components: magnetic entropy (S_m), lattice entropy (S_r), and electronic entropy (S_e). While the electronic and lattice entropies are usually independent of the magnetic field (H), the magnetic entropy depends heavily on it. When a magnetic field is applied, the magnetic moments align, causing a reduction in magnetic entropy. At a constant temperature (T) and for a change in the applied field (ΔH), the magnetic entropy varies $\Delta S_M(T, \Delta H)$, while the values of Sr and Se remain constant. This quantity is known as the change in isothermal entropy and can be seen in Fig X.

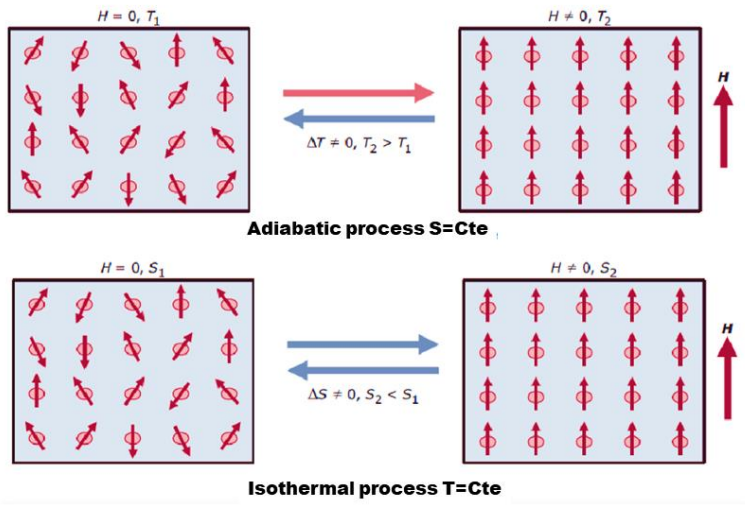

Figure 1. 14: *Principle of the magnetocaloric effect*

Due to the absence of heat exchange between the system and the external environment, known as adiabatic conditions, the total entropy of the material remains constant. Consequently, as the magnetic entropy decreases, the lattice entropy and electronic entropy increase, and their combined change can be expressed as $\Delta(S_R+S_E) = -\Delta S_M$. This alteration in S_R and S_E affects the temperature of the magnetic material by either increasing or decreasing the amplitude of the lattice vibrations, depending on the sign of ΔH. The resulting temperature variation is referred to as the adiabatic temperature change $\Delta T_{ad}\,(T)_{\Delta H}$, as depicted in *Figure 1.15*.

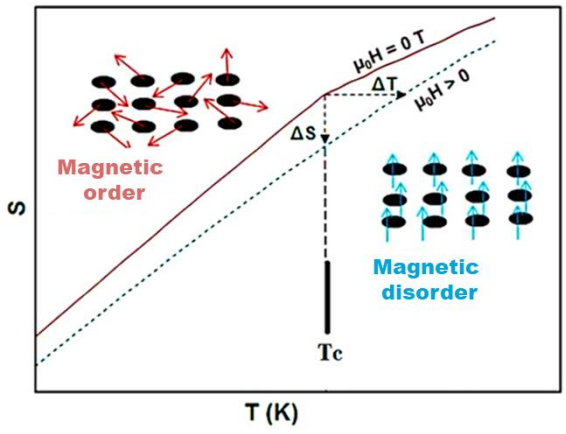

Figure 1. 15: *S-T diagram of a ferromagnetic material*

c. Thermodynamic approaches

To fully investigate the magnetocaloric effect, it is necessary to look at the thermodynamic properties of a system when subjected to a magnetic field. The free enthalpy function, G, characterizes the system and is dependent on the intensive variables of temperature (T), pressure (P), and magnetic field strength (H).

$$G = G(T, P, H) = U + PV - ST - \vec{M}\vec{H} \qquad (1.6)$$

Knowing that the materials studied are mostly solids, the effects of volume and pressure can be ignored. The precise total differential of free enthalpy is as follows:

$$dG = \left(\frac{\partial G}{\partial T}\right) dT + \left(\frac{\partial G}{\partial H}\right) dH = -SdT - MdH \qquad (1.7)$$

Given that for an exact total differential the second cross partial derivatives are identical, then:

$$\frac{\partial}{\partial \vec{H}}\left(\frac{\partial G}{\partial T}\right) = \frac{\partial}{\partial T}\left(\frac{\partial G}{\partial \vec{H}}\right) \qquad (1.8)$$

Hence the relations of Maxwell Wiess:

$$\left(\frac{\partial S}{\partial H}\right)_T = \left(\frac{\partial M}{\partial T}\right)_H \qquad (1.9)$$

and

$$\left(\frac{\partial S}{\partial T}\right)_H = \frac{1}{T} C_H \qquad (1.10)$$

For a reversible transformation the differential of the entropy S is:

$$dS = \left(\frac{\partial S}{\partial T}\right) dT + \left(\frac{\partial S}{\partial H}\right)_H dH = \frac{C_H}{T} dT + \left(\frac{\partial M}{\partial T}\right)_H dH \qquad (1.11)$$

In the case of an adiabatic transformation, the previous equations can be developed to lead to other more practical equations, such as the adiabatic variation of temperature ΔT_{ad} and the variation of magnetic entropy ΔS_m, which are useful for characterizing the magnetocaloric effect.

$$\Delta S_m(T, \Delta H) = \int_0^{Hmax} \left(\frac{\partial M}{\partial T}\right)_H dH \qquad (1.12)$$

$$S_m(T, H) = \int_0^T \frac{C_H(T, H)}{T} dT + S(0, H) \qquad (1.13)$$

$$\Delta S_m(T, \Delta H) = S_m(T, 0) - S_m(T, H) \qquad (1.14)$$

$$\Delta T_{ad}(T, H) = -\frac{T \Delta S_m(T, \Delta H)}{C_H(T, 0)} \qquad (1.15)$$

Finally, we can conclude that the magnetocaloric effect is dependent on magnetization and applied field variations, and that the two adiabatic variations of temperature and magnetic entropy are thermodynamic parameters that allow us to characterize the magnetocaloric effect.

d. Application of MCE in magnetic refrigeration

Magnetic refrigeration is a novel method of producing cold temperatures that makes use of solid magnetic substances as the primary components. These materials magnetize and demagnetize, and their heat transfer medium can be water, alcohols, or inert gases. This technology is based on the magnetocaloric effect, which causes a change in material temperature when exposed to changes in external magnetic fields. Magnetic refrigeration is a promising and alternative technology to traditional refrigeration systems that rely on the compressors to perform thermodynamic cycles involving the compression and expansion of refrigerant fluids.

Magnetic refrigeration has two major economic and environmental advantages:

- ✓ Higher energy efficiency, which can reach 60%, whereas current systems are around 40%);
- ✓ A lack of dangerous gases such as chlorofluorocarbons (CFCs), hydrofluorocarbons (HFCs), and hydro chlorofluorocarbons (HCFCs). Unfortunately, they are greenhouse gases that contribute to global warming.

A four-step cycle (Figure 1.16) defines magnetic refrigeration operation:

- **Adiabatic magnetization:** The intensity of the magnetic field H is increased to bring the material's temperature up to that of the hot reservoir.
- **Isothermal entropy transfer:** The material is brought into direct thermal contact with the hot reservoir. The intensity of H is gradually increased in order to transfer entropy from the material to the hot reservoir at a constant temperature.
- **Adiabatic demagnetization:** The material is thermally insulated, and the intensity of H is quickly reduced to match the temperature of the system to be refrigerated.
- **Isothermal transfer of entropy**: The material is brought into thermal contact with the cooling system. The intensity of H is gradually reduced in order to achieve entropy transfer from the system to the material at constant temperature.

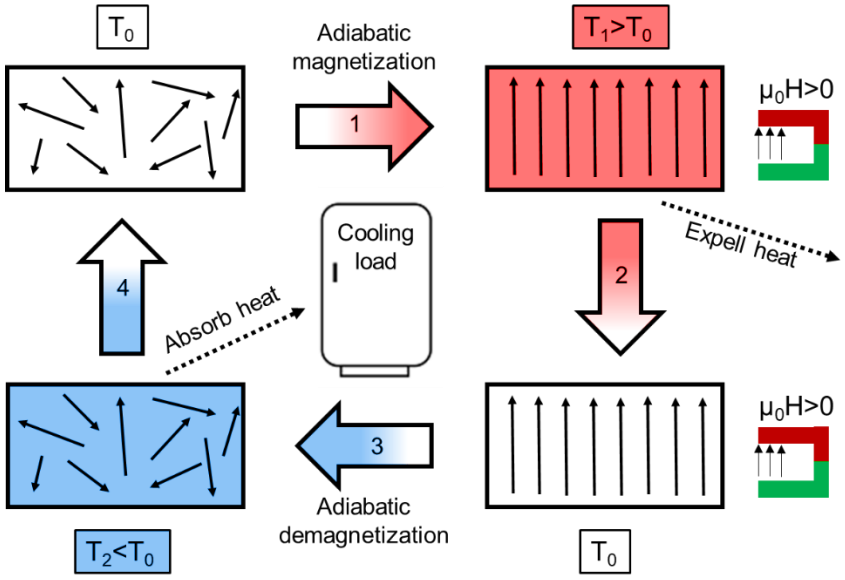

Figure 1. 16: *Adiabatic magnetization-demagnetization process cycle*

e. Important parameters for the magnetic refrigeration efficiency

It should be noted that the magnetocaloric effect is directly related to the variation of magnetization and applied field. Thus, the analysis of two thermodynamic quantities, S_m and T_{ad}, of magnetic material gives direct indications of its magnetocaloric properties. Furthermore, from the value of S_m, one can calculate the capacity of the refrigeration (Relative Cooling Power, denoted RCP), which corresponds to the amount of heat that can be transferred between the hot and cold sources. It is defined by the relation:

$$RCP = -\Delta S_M^{max} \times \delta_{FWHM} \qquad (1.16)$$

Here ΔS_M^{max} refers to the maximum value of the magnetic entropy, and $\delta_{FWHM} = (T_{hot} - T_{cold})$ is the full width at half maximum of the curve ΔS_M^{max}.

To investigate the magnetic refrigeration efficiency, the ΔS, ΔT and RCP alone are insufficient to identify the potential of the refrigerant material for applications in solid-state refrigeration technologies. In this respect, the temperature-averaged entropy change (TEC) should be calculated:

$$TEC(\Delta T_{H-C}) = \frac{1}{\Delta T_{H-C}} max \left\{ \int_{T_{mid}+\Delta T_{H-C}}^{T_{mid}-\Delta T_{H-C}} |\Delta S_M(T)| dT \right\} \qquad (1.17)$$

Herein $\Delta T_{H\text{-}C}$ denotes the temperature difference between the device's cold and hot heat exchangers. T_{mid} is the temperature at which the $TEC(\Delta T_{H\text{-}C})$ is maximized for a given $\Delta T_{H\text{-}C}$.

III.2. Ferroelectricity

III.2.1. Basic knowledge

III.2.1.1. Dielectric materials

Dielectric materials are frequently used as electrical insulators because they do not contain electrical charges that can move macroscopically. One of their properties is the ability to polarize. The electric moment within the dielectric is zero in the absence of an electric field because the centers of gravity of the positive (+q) and negative (-q) charges coincide. When an electric field is applied, these gravity centers no longer coincide, and polarization occurs.

The polarization current is +q and -q shifting each other with limited distance (~d), this coupling is named dipole and moment (electric dipole moment) is given by:

$$\vec{p} = d\vec{q} \qquad (1.18)$$

III.2.1.2. Polarization and dielectric permittivity

Due to the properties of the chosen atoms and their arrangement in a crystal lattice, such as strong chemical bonds and atomic coordination, the electrons in a dielectric material are limited in their ability to move in long distances. However, when subjected to an electric field, electrons and atomic nuclei can undergo short-range displacements, leading to various forms of polarization.

Electronic polarization is due to an oscillation of the center of gravity of electronic charges with respect to the nucleus under the influence of an electric field. Due to the low mass of electrons, these oscillations occur at very high frequencies, greater than 10^{14}-10^{16} Hz (corresponding to wavelengths between 3 and 0.03 μm). Electronic polarization is present in all dielectrics, without exception. This contribution is predominant in the optical domain since it is the only domain where the Maxwell's equation relation n=$\sqrt{\boldsymbol{\varepsilon_r}}$ is verified.

Ionic (or atomic) polarization is created when nuclei move relative to each other. The corresponding inertia will appear for the frequencies much lower than the optical frequencies. Typically, this polarizability will be effective for frequencies of the order of 10^{13} Hz (λ=30μm) i.e. in the infrared domain. This type of polarization is well characterized by vibrational spectroscopy.

Dipole polarization (also known as orientation or Debye polarization) is concerned with systems (crystals, molecules) that contain entities with a permanent dipole moment. The structure of these entities is asymmetrical: the negative charges' center of gravity does not coincide with that of the positive charges. Response times will vary greatly depending on the strength of interactions between entities that must reorient themselves. This type of polarization is observed in the field of radio waves.

Interfacial polarization is caused by the accumulation of free charges at the interfaces between different media. This phenomenon will be significant in systems with a high interface density.

III.2.1.3. Polarization and hysteresis loop:

There are several types of dielectrics that can be polarized by applying an external force, such as heat for pyroelectrics or mechanical force for piezoelectric. The ferroelectric materials have constant dipole moments that are oriented in the same direction and can be returned by the action of the electric field. To observe this property, the material's crystalline network must be non-centrosymmetric.

If the applied electric field is alternating, the polarization describes a hysteresis cycle. The cycle provides access to the values of saturation polarization (ideally, equal to spontaneous polarization), remanent polarization P_r and the value of the coercive field E_C. Above a critical temperature T_C, called the Curie temperature, the spontaneous polarization disappears: the material becomes paraelectric.

Consider the BT example (Barium Titanate). Above T_C=120°C, its lattice structure is cubic and does not exhibit spontaneous polarization. It is said to be in a paraelectric state. Below this transition temperature, its lattice deforms, reducing its degree of symmetry (more information will be provided below). Because of the position of each of the atoms that constitute the lattice, the centers of gravity of the charges do not coincide, resulting in the emergence of a spontaneous polarization (see Figure 1.17).

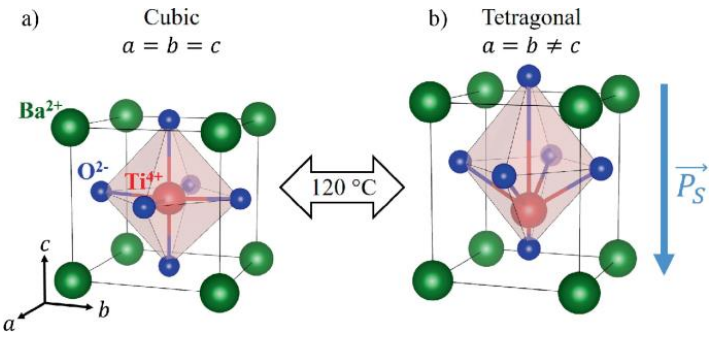

Figure 1. 17: *a) Perovskite-type BT unit cell in the symmetric cubic state above Tc b) Tetragonally distorted unit cell below Tc.*

In the absence of an external electrical field, the polarization of the material is null. Indeed, the monocrystal is made up of different domains where polarization varies from one domain to the next. This configuration allows for the reduction of electrostatic energy.

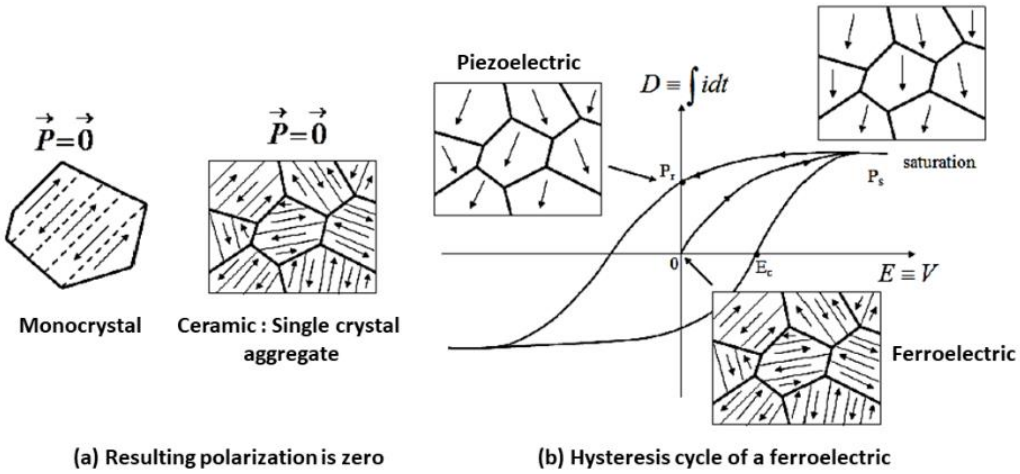

Figure 1. 18: *Diagram of the polarization inside the grains of a ferroelectric and cycle hysteresis*.

The polarization of a ceramic material, which is an aggregate of single crystals, is also null at the origin. To make a ferroelectric material piezoelectric, it must be polarized so that it retains remanent polarization. Ferroelectrics have a hysterical behavior, as illustrated in Figure 1.18, which depicts the evolution of the induced electric as a function of the electric field. The sum of the polarization and electric field is the electrical induction.

$$\vec{D} = \varepsilon_0 \vec{E} + \vec{P} = \varepsilon_0 (1 + \chi_e) \vec{E} = \varepsilon_r \varepsilon_0 \vec{E} \qquad (1.19)$$

ε_r is relative permittivity, more normally is named dielectric permittivity or dielectric constant. At zero frequency, it is named static dielectric permittivity. Generally, it is a complex but the real part is still named dielectric permittivity. χ_e is electric susceptibility.

The capacitance is defined as:

$$C = \boldsymbol{\varepsilon_r \varepsilon_0 \frac{S}{d}} \qquad (1.20)$$

The surface area of the electrodes is represented by **S**, and d is the thickness of the dielectric materials separating the electrodes.

When compared to a capacitor with a vacuum, this capacity is expressed as:

$$C_0 = \boldsymbol{\varepsilon_0 \frac{S}{d}} \qquad (1.21)$$

The ratio of these two expressions gives:

$$\boldsymbol{\varepsilon_r = \frac{\varepsilon}{\varepsilon_0} = \frac{C}{C_0}} \qquad (1.22)$$

The quantity of charge Q is then:

$$Q = CV = \boldsymbol{\varepsilon_r C_0 V} \qquad (1.23)$$

However, no dielectric is perfect; there is always a low conductivity at low frequencies due to various microscopic mechanisms (particularly defects). Then we talk about dielectric losses. To account for these losses, the relative dielectric constant must be expressed in the following complex form:

$$\varepsilon_r^* = \varepsilon_r' + i\varepsilon_r'' \qquad (1.24)$$

ε_r' represents the real part of the relative permittivity while ε_r'' is related to the losses of the system.

The part of the electrical energy that is transformed into heat in the dielectric media is called dielectric loss. A part of these losses, due to the momentary current, is called ohmic. However, the other part associated with the displacement of the charges is called dielectric losses. The loss angle is defined by the following formula:

$$\tan\delta = \frac{\varepsilon_r''}{\varepsilon_r'} \qquad (1.25)$$

III.2.1.4. Ferroelectricity, piezoelectricity and pyroelectricity

Ferroelectricity is a property of certain materials in which the electric polarization of the material can be reversed by applying an electric field. These materials are known as

ferroelectrics, and they are widely used in electronics, such as capacitors, memory devices, actuators, sensors, and transducers.

Ferroelectricity can exist only in certain crystal structures. Indeed, crystals are classified according to their symmetry in 230 groups of spaces distributed along all 32 crystal classes (***Figure 1.19***). Twenty-one of these 32 classes are non-centrosymmetric. Among these 21, 20 are piezoelectric.

Piezoelectricity is the ability of certain materials to generate an electrical energy in response to an applied mechanical stress or pressure (direct piezoelectric effect), or to generate a mechanical deformation in response to an applied electric field (indirect piezoelectric effect). This phenomenon is due to the internal polarization of the material, which results in a separation of positive and negative charges. When the material is mechanically deformed, this polarization changes, resulting in the generation of an electric field and a corresponding electric charge.

Only ten of the piezoelectric crystal classes have spontaneous electrical polarization (polar), which is temperature dependent; these are known as pyroelectrics.

Pyroelectricity is the ability of certain materials to generate electrical energy in response to a change in temperature. Like piezoelectricity, this phenomenon is due to the internal polarization of the material. When the temperature of a pyroelectric material changes, its internal polarization changes, resulting in the generation of an electric field. This effect can be used in temperature sensors, infrared detectors, and other applications that require a response to changes in temperature. Finally, not all pyroelectric crystals are ferroelectric.

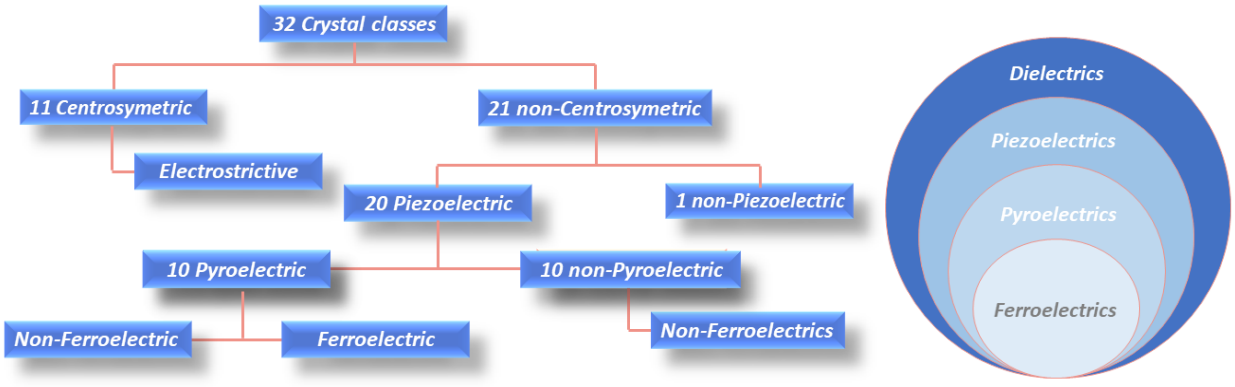

Figure 1. 19: *(a)Schematic representation of piezoelectricity, pyroelectricity, and ferroelectricity based on crystal symmetry, (b) A Venn diagram depicting how ferroelectrics range into the various dielectric material classes.*

III.2.2. Origins of ferroelectricity

The first ferroelectric compound $NaKC_4H_4O_6$-$4H_2O$, known as Rochelle salt or Seignette salt, was produced in a pharmacy in 1655 by Dr. Seignette for its purgative powers which were less unpleasant than senna leaves. In 1920, Valasek demonstrated the ferroelectric properties of this compound. In 1935, ferroelectricity received renewed attention with the discovery of the entire family of compounds based on dihydrogen phosphates and arsenates with different types of cations, particularly potassium dihydrogen phosphate, KH_2PO_4 (KDP). Moreover, since the structure of these compounds is simpler than that of Rochelle salt, the very first microscopic models can be developed. Thus, Slater's model, based on the presence of hydrogen bonds (the origin of ferroelectricity), was proposed as early as 1941. This model was quickly abandoned after the discovery of BT by Wul and Goldman, who showed that hydrogen bonding is not a necessary condition for the appearance of ferroelectricity. This discovery is particularly important because it is the first compound in the large family of ferroelectric perovskites, whose simplicity of perovskite structure also allowed for a new theoretical effort for a better understanding of ferroelectric phase transition mechanisms that can be displacive or order-disorder type. Among these perovskite-structured compounds, a new class of materials called complex perovskite-structured materials was added in the late 1950s, with the model compound being Pb $(Mg_{1/3}Nb_{2/3})$ O_3 (PMN) [33].

Until now, Perovskite materials have been the most studied materials for ferroelectric applications. Many ferroelectric materials have been discovered since then, with the most studied being barium titanate BT and lead titano-zirconate PZT ($PbZr_xTi_{1-x}O_3$).

To understand the origin of ferroelectricity in this type of material, it is necessary to recall the perovskite structure. Take BT as an example.

BT was the first ferroelectric oxide with a perovskite structure, discovered by Gray at Erie Resister (patent submitted in 1946) and Shepard Roberts (published in 1947). It has been studied by many researchers for use in multilayer capacitors, thermistors, and electro-optical devices, with a large permittivity and a low Curie temperature (Tc = 120-135°C).

BT has a Perovskite ABO_3 structure with a cubical phase. The larger cations Ba^{2+} occupy cube corner positions (0, 0, 0), small cations Ti^{4+} occupy the center positions (½, ½, ½), and the anions O^{2-} are located at face-centered positions, as depicted in Figure 1.17. Ba ions are coordinated by twelve oxygens, while Ti ions are coordinated by six oxygens in octahedral coordination.

This structure corresponds to the so-called high temperature phase, whose unit cell has a symmetry center that prevents spontaneous polarization. At high temperatures, BT is thus a para-electric material with a lattice parameter of about 4Å.

When cooled below a critical temperature (T_C = 400 K), the crystal structure undergoes a phase transition to a tetragonal phase, resulting in a non-centrosymmetric crystal structure due to a distortion in the Ti-O-Ti bond angle. This non-centrosymmetric atom arrangement causes spontaneous polarization in the material.

Further cooling causes two more phase transitions (Quadratic-Orthorhombic around 285 K and Orthorhombic-Rhombohedral around 196 K), with the material retaining its ferroelectric properties. The lattice lengthens along a specific direction during a transition, with several directions being crystallographically equivalent. As a result, several polar axes are possible, producing a domain structure. The polarization vector's direction varies from one domain to another, and it can be changed by applying an electric field. Each phase transition involves a change in the polarization value, resulting in a permittivity maximum [34].

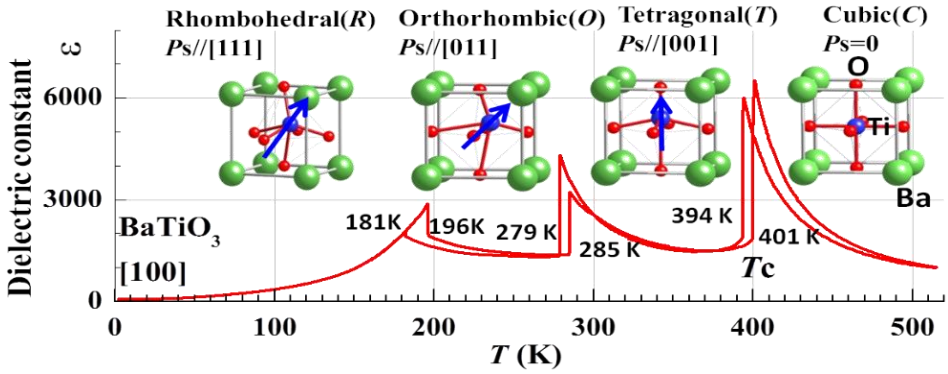

Figure 1. 20: *Temperature-dependent changes in the dielectric constant and crystal structure of $BaTiO_3$ [35].*

III.2.3. Structural and crystallographic aspects of phase transitions

In terms of crystallography, the phase transition causes atoms in the lattice to shift. Two types of mechanisms are highlighted to explain these transitions:

III.2.3.1. Displacive transition

In this type of transition, the atoms move relative to their initial positions, which generates a deformation and a change in the crystal lattice parameters in well-defined directions (figure 1.17). Therefore, the symmetry varies as well as the polar or non-polar character [36].

III.2.3.2. The order-disorder transition

Even at high temperature, permanent dipoles exist, but their relative orientation is perfectly random and therefore the macroscopic polarization is zero. It is the orientation of these dipoles (under the effect of the fields or cooling) according to preferential axes of the structure which causes the appearance of a spontaneous polarization.

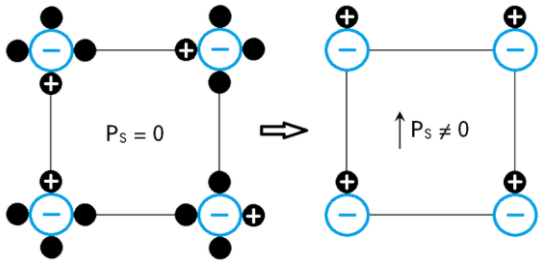

Figure 1. 21: *A diagram of an order-disorder para/ferroelectric transition.*

III.2.3.3. Thermodynamic aspects of phase transitions

The free enthalpy function (G) represents the thermodynamic side of phase transitions. There are two kinds of transitions after that:

First-order or discontinuous transition: the thermal variations of permittivity and polarization are discontinuous. The Curie-Weiss temperature T_0 is lower than the Curie temperature T_C.

Second order or continuous transition: they are characterized by continuous thermal variations of permittivity and polarization. The Curie-Weiss temperature T_0 is equal to the Curie temperature T_C.

In ferroelectric compounds, the order of the phase transition is defined by the discontinuity of the partial derivatives of the material's Gibbs free energy (G) at the transition temperature. The n^{th} order derivative of G is a discontinuous function of transition temperature for an n^{th} order transition. Thus, at the phase transition for a second order transition, the polarization changes continuously. In contrast, for a first order transition, this change is abrupt. Other materials, known as relaxors, have a diffuse phase transition behavior.

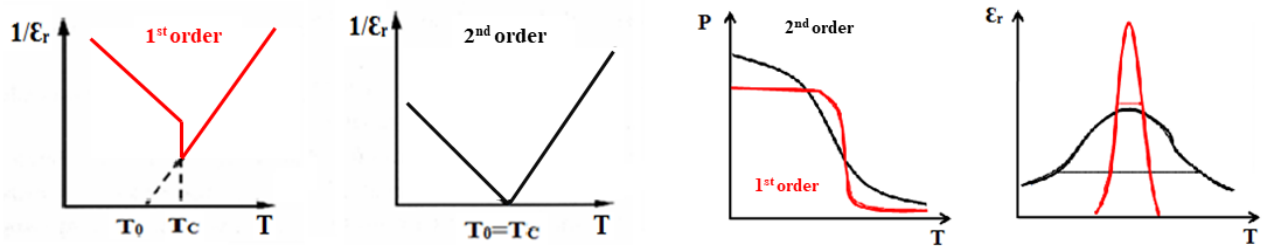

Figure 1. 22: *Variation of the inverse of permittivity and polarization in a first and second order phase transition.*

III.2.3.4. Normal versus relaxor ferroelectrics: dielectric and P-E loop behaviors

According to the characteristics of phase transitions and their frequency behavior, two types of ferroelectric materials are distinguished. Normal ferroelectrics and relaxor ferroelectrics:

Normal ferroelectrics are distinguished by a sharp phase transition from the polar to the non-polar phase at Tc (Figure 1.24.a), which is frequency independent. The relative dielectric constant follows the Curie-Weiss law beyond T_C:

$$\boldsymbol{\varepsilon' = \frac{C}{(T - T_0)}} \qquad (1.26)$$

Where C is the Curie constant, T represent the temperature of the material and T_0 is the Curie-Weiss temperature.

A diffuse phase transition is observed in **ferroelectric relaxors**. Furthermore, as the frequency increases, the temperature of maximum of the real part of the permittivity (ε') moves towards high temperatures (Figure 1.24.a). As a result, this temperature no longer corresponds to the Curie temperature, and its designation as T_m (temperature of maximum permittivity) is more appropriate. In the ferroelectric phase, the frequency behavior can be described as a relaxation: a sudden drop in the real part (ε') associated with a maximum in the imaginary part (ε''). Furthermore, the dielectric constant's behavior as a function of temperature does not follow the Curie-Weiss law.

$$\boldsymbol{\frac{1}{\varepsilon_r} - \frac{1}{\varepsilon_m} = \frac{(T - T_m)^{\gamma}}{C'}} \qquad (1.27)$$

Where ε_r is the dielectric constant at T, ε_m and T_m are the permittivity and the temperature at the maximum of the curve, C' is a constant and γ is the characteristic diffusivity coefficient of the relaxing behavior in the material.

In general, the value of γ is between 1 and 2. In the case where γ = 1 the material follows the normal Curie-Weiss law, whereas for a relaxor: γ = 2.

In the low temperature ferroelectric phase (polar state), the P-E hysteresis loop serves as the characteristic of a ferroelectric. The cooperative nature of this phenomenon is reflected through the large remanent polarization (P_r) and coercive field (E_c) displayed in the loop. On the other hand, a slim loop is observed in relaxor ferroelectrics which indicates the presence of cooperative freezing of dipolar (or nanodomain) orientations. The nanodomains in relaxors can be oriented with high electric fields, leading to a significant polarization, however, on removing the field, most of these domains return to their random orientations resulting in a small P_r. In normal ferroelectrics, P_r and P_s decline as the temperature increases and vanish at T_c. The polarization disappearance is discontinuous for a first-order transition and continuous for a second-order phase transition below T_c, where no polar domain regions occur above T_c [37].

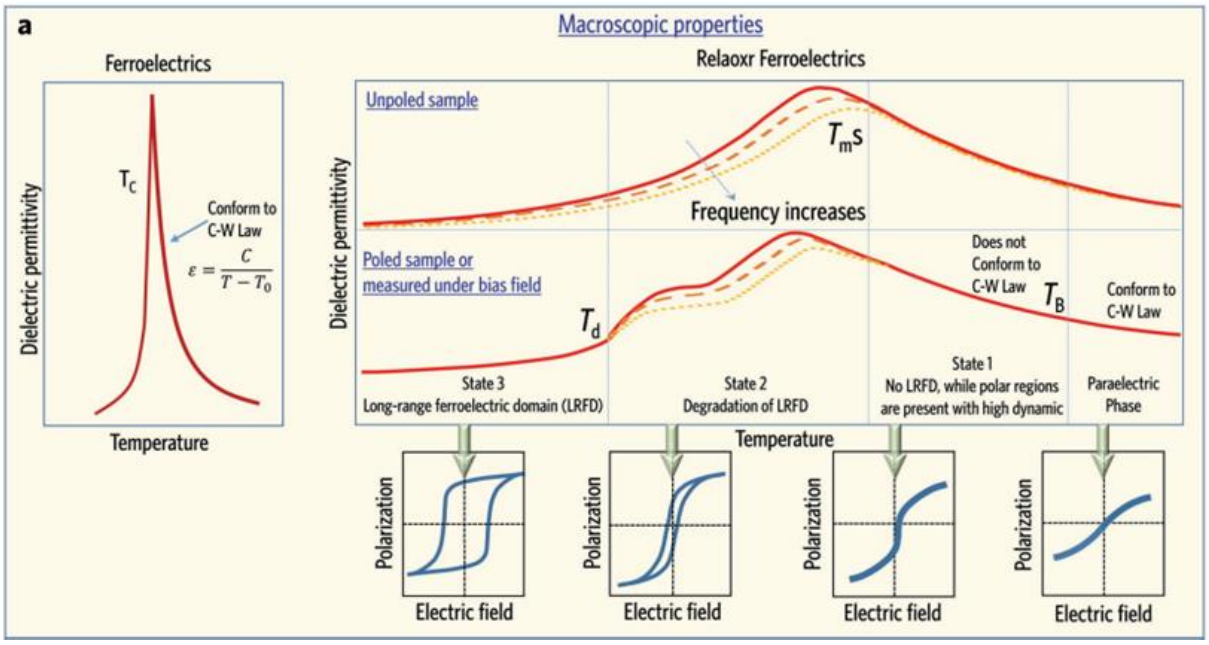

Figure 1. 23: *(a) A diagram of the macroscopic properties of relaxor ferroelectrics, showing the temperature dependence of dielectric permittivities (poled and unpoled samples) and polarization-electric field (PE) loops for relaxor ferroelectrics.*

III.3. Energy storage in ferroelectric materials

Dielectric capacitors are passive devices that play a significant role in various electronic and electrical power systems. They serve multiple purposes, such as coupling, decoupling, filtering, and suppressing high-frequency vibrations. However, their fundamental operating principle revolves around the charging and discharging of electrical energy. They are known for their fast discharge rate, making them a preferred choice for pulsed systems. However, their energy

storage density is typically low. Therefore, the need for dielectric capacitors with high energy-storage performance arises, which mainly includes high energy-storage density, low loss, and excellent temperature stability.

Bulk ceramics, specifically relaxor ferroelectrics, are considered to be highly promising materials for next-generation high energy storage capacitors at elevated temperatures [1]. When subjected to an external voltage during the charging process, charges of equal magnitude but opposite sign accumulate at the electrodes. These accumulated charges create an internal electric field that opposes the external field and intensifies as more charges are gathered. The charging process concludes once the internal electric field induced by the collected charges (Q) equals the external field (V/d). The capacitor's capacitance (C) can be expressed as Q/V. During charging, work is required to move charges between the conductor electrodes via the external electric field, and the electrostatic energy is concurrently stored in the dielectric layer. The amount of energy (W) stored can be computed using the following formula:

$$W = \int_0^{Qmax} V dq = \int_0^{Qmax} \frac{q}{C} dq = \frac{1}{2}\frac{Q^2}{C} = \frac{1}{2}CV^2 = \frac{1}{2}\frac{\varepsilon A}{d}(Ed)^2 \qquad (1.28)$$

where Q_{max} is the maximum charge when the charging process is finished, dq is the increment of charge, ε is the dielectric constant, A is the area of overlap of the two plates of the capacitor, and d is the distance between the plates of the capacitor.

III.3.1. Energy storage performances

Linear dielectrics typically exhibit low ε_r, low dielectric loss (tan δ), and high breakdown strength BDS. An ideal linear dielectric's permittivity remains constant regardless of the electric field. This means that its polarization increases linearly with the electric field, without any hysteresis, as illustrated in Figure 1.25. All of the energy stored during the charging process can be released from the dielectric during the discharging process. However, in reality, no such ideal dielectric material exists.

In ferroelectrics, the electric-field-derived movement of domains consumes energy as well. In other words, only a portion of the stored energy may be released during the discharge process because some of it is lost during the charge and discharge processes. W_{rec} denotes the recoverable energy density, while W_{loss} denotes the lost energy density. As a result, the total energy density, W_{tot}, is given by:

$$W_{tot} = \int_0^{P_{max}} EdP = W_{rec} + W_{loss} \qquad (1.29)$$

It should be noted that the relative dielectric constant of a material varies with temperature and frequency. As a result, the total energy density, W_{tot}, also depends on temperature and frequency. The energy density can be calculated by determining the integral area of the hysteresis loop (P-E) and the longitudinal axis, as described by Equation 1.29. To calculate W_{tot}, the areas representing W_{rec} and W_{loss} must be added together, as illustrated in Figure 1.25. The light pink-colored area corresponds to W_{rec}, which represents the energy density recoverable during the discharging process and can be determined by integrating the area between the polarization axis and the upper branch curve of the unipolar P-E hysteresis loop. On the other hand, the dark pink-colored area represents W_{loss}, which is caused by domain orientation and can be determined by integrating the P-E loop area.

$$W_{loss} = \int_{P_r}^{P_{max}} EdP \qquad (1.30)$$

where P_{max} and P_r denote the maximal and remnant polarization. According to these equations, superior energy storage performances in ferroelectric materials require a high dielectric constant, a large P_S, a low P_r, and a high BDS.

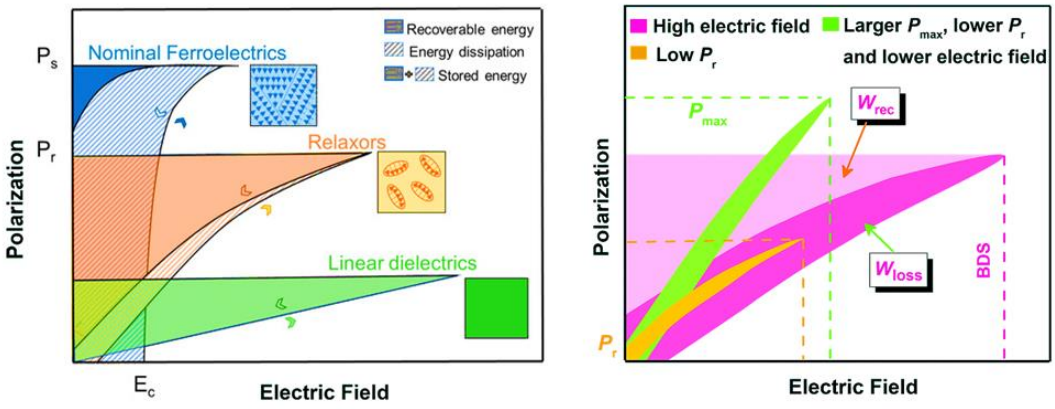

Figure 1. 24: *In left, Polarization versus electric field (P−E) for typical ferroelectrics, relaxors, and linear dielectrics; in right, Schematic of approaches used to improve the energy storage properties of relaxor ferroelectrics.*

An important parameter for assessing the performance of energy storage is the energy storage efficiency (η), as defined in the following equation 1.31.

$$\eta(\%) = \frac{W_{Rec}}{W_{tot}} \times 100 = \frac{W_{rec}}{W_{rec}+W_{loss}} \times 100 \qquad (1.31)$$

During the depolarization process, some of the stored energy (W_{tot}) is lost as energy loss density. When a high electric field is applied to increase energy density, the electronic/ionic

conductivity of the sample increases, resulting in an increase in tan δ, which reduces the amount of recoverable energy during discharge.

III.3.2. Electrocaloric refrigeration

III.3.2.1. Definition and principle

The electrocaloric effect refers to the phenomenon where the temperature of a material changes in response to an applied electric field. Indeed, when an electric field is applied to a ferroelectric material, the polarization of the material changes, which can cause a change in temperature. This is due to the fact that the polarization of the material is related to its entropy, or disorder, and changing the polarization can lead to a change in entropy and thus a change in temperature. With the cancellation of the electric field, variations in the electric field cause a change in the dipole state in a dielectric material from the less ordered to the more ordered.

In general, the total entropy of a dipolar material can be described as the contribution of two entropies: an entropy of vibration ΔS_L (phonons entropy) associated with the vibrations of the constituent atoms of the crystal lattice, and an entropy of orientation ΔS_D which depends on the electrical order. The total variation of entropy must be equal to zero in the adiabatic process of the electro caloric effect.

The schematic diagram of the ECE cooling cycle is depicted in Figure 1.26, which consists of four steps (a-d) comprising of two isothermal and two adiabatic processes. The initial state of the cycle is presented in panel (a) where the EC material is at a temperature (T), which could be ambient, and no electric field is applied (E=0). In step (b), an electric field (E) is applied to the EC material, resulting in a rapid decrease in entropy of the material (dipoles align along the direction of the electric field) and a rise in its temperature, which is an adiabatic process (no heat exchange with the surroundings). The transition from state (b) to state (c) is an isothermal process where the material slowly cools down at a constant field, releasing heat to a sink and decreasing its entropy to state (c). Upon reducing the field to zero, the material further cools down through adiabatic depolarization, which results in an increase in entropy (dipoles return to randomly oriented). This leads the material to state (d), and from there, an isothermal process takes place, where the material warms up to its original state (a) by absorbing heat from a load, for instance, a refrigerator. Depending on the entropy change, the applied electric field can be either direct ECE (heating) or inverse ECE (cooling), which may provide an opportunity to enhance refrigeration cycles [38].

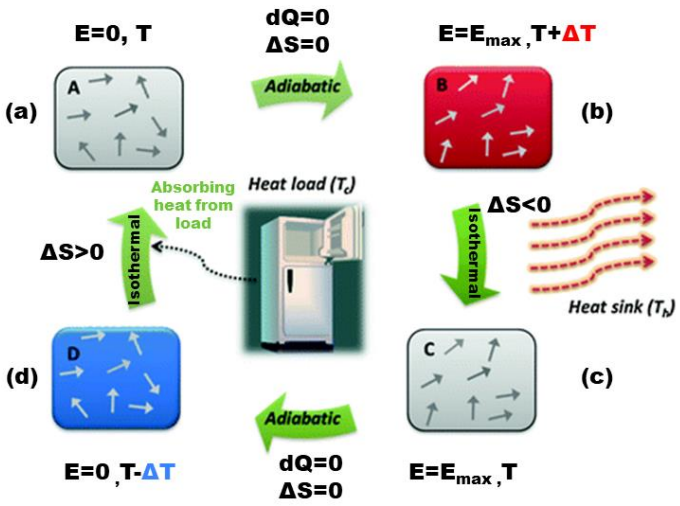

Figure 1. 25: *Sketch of the typical four-step refrigerant cycle based on electrocaloric materials*

III.3.2.2. Measurement of ECE in ferroelectric materials: Indirect method

The indirect method for determining the temperature change in a ferroelectric material is based on Maxwell relations. This involves analyzing the temperature-dependent behavior of the P-E hysteresis loop to extract the ECE temperature change. To estimate the temperature change (ΔT), measurements of the pyroelectric current (dP/dT) are taken. The variation of the adiabatic temperature can be calculated using the following equation:

$$\Delta T_{EC} = -\int_{E_1}^{E_2} \frac{T}{\rho C_E}\left(\frac{\partial P}{\partial T}\right) dE \qquad (1.32)$$

The variation of isothermal entropy can be calculated using the following equation:

$$\Delta S_{EC} = \int_{E_1}^{E_2} \left(\frac{\partial P}{\partial T}\right) dE \qquad (1.33)$$

here, S is the entropy, E is the electric field, T is the temperature of the electrocaloric material, P is the polarization, ΔT is the adiabatic temperature change, ρ is the material's density, and C_E is the specific heat capacity.

III.3.2.3. Electrocaloric effect performances

Different parameters can be used to evaluate the suitability of an electrocaloric material for practical cooling devices:

-The effective electrocaloric responsivity is defined as the ratio of the electrocaloric temperature change (ΔT) to the amplitude of the electric field (ΔE) [39]. Regardless of the magnitude of the applied electric field, the EC responsivity always exhibits a peak temperature at Tc for E=0.

$$\xi = \frac{\Delta T}{\Delta E} \qquad (1.34)$$

-For industrial application, the efficiency of a cooling cycle and the performance of a material are commonly evaluated using the coefficient of performance (COP), which is defined as the ratio of input power to output cooling power [39]. Equation 1.35 can be used to estimate COP, where Q represents the isothermal heat and W_{tot} is the total energy density.

$$COP = \frac{|Q|}{|W_{tot}|} = \frac{|T\Delta S|}{|W_{tot}|} \qquad (1.35)$$

IV. State of the art on multiferroics

IV.1. Magnetoelectric effect

Multiferroic materials with at least two ferroic behaviors (ferroelectric, ferromagnetic, or ferroelastic) are becoming increasingly appealing due to their potential application in multifunction devices. The coupling of these different ferroic behaviors in this type of material can result in the appearance of new effects, such as magnetoelectric effect (ME for the magnetoelectric effect).

The magnetoelectric effect is the appearance (or variation) of an electric polarization **P** when a field **H** is applied (this is the direct magnetoelectric effect), or the appearance of a magnetization **M** when a field **E** is applied (this is the inverse magnetoelectric effect). We take note of **α**, the **ME** coefficient.

Many ME materials have since been discovered or synthesized [40]. Unfortunately, the materials discovered had only limited potential for use in applications because the effects obtained were only significant at low temperatures. Recently (2013), a ME effect significant enough to be used in applications was discovered in a zirconium barium titanate with a small Fe substitution due to the coexistence of a paramagnetic and ferroelectric phase [41].

IV.2. Limited availability of intrinsic ME materials

A magnetoelectric (ME) material is defined as being both ferro/ferrimagnetic and ferroelectric, requiring a variety of physical, structural, and electronic properties. The causes of the limited availability of intrinsic ME materials are unknown, but this section will provide examples of factors that limit their availability.

Ferroelectricity requires a non-centrosymmetric phase to allow for the formation of electrical polarization. There are 31 crystallographic classes that allow spontaneous electrical polarization (see chapter 1) and 31 that allow spontaneous magnetic polarization; only 13 of them coincide. Although this greatly reduces the number of possible crystal structures (there are 122 in total), many materials in these classes are neither ferromagnetic nor ferroelectric, so symmetry is not the most important criterion more restrictive.

A ferroelectric is, by definition, an insulating material; otherwise, an electric field would cause the circulation of free charges, preventing polarization variation. Conversely, ferromagnets, which do not require specific electrical properties, are frequently metals and thus conductors. The high density of states at the Fermi level of elements such as Fe, Ni, and Co, for example, is the fundamental element of their ferromagnetism as well as their metallic character. When considering ferrimagnetics, which are mostly insulators, the argument about limited availability of magnetic insulators falls apart.

We can now look at the distribution of electrons in the upper layer d with greater precision. The classic ABO_3 ferroelectric perovskite structure shows an empty d layer for the cation B. It is self-evident that if there is no electron producing a localized magnetic moment, there can be no magnetic order. However, it appears that in most cases, once the cation's d shell is partially occupied, the tendency to form a non-centrosymmetric phase disappears [42].

IV.3. Towards artificial ME composites

IV.3.1. The extrinsic ME effect of composites

Composite materials are an alternative to materials that naturally exhibit the magnetoelectric effect. We can recreate a coupling through mechanical stresses by placing magnetostrictive and piezoelectric materials in contact. Although neither of the two phases has a magnetoelectric property, their combination produces the effect. In the case of the direct effect, the following two figures (Figure 1.27 a and b) explain the principle of this extrinsic magnetoelectric effect.

The application of a magnetic field causes mechanical stresses to appear within the magnetostrictive material. These will spread to the piezoelectric material and change the electrical polarization. As a result, the magnetoelectric effect observed here is extrinsic. The coupling is strongly influenced by the intrinsic properties of the materials used, as well as the contact surfaces between each phase. The decomposition of the effect can be seen using the following formula:

$$ME_{effect} = \frac{\text{magnetic}}{\text{mechanical}} \times \frac{\text{mechanical}}{\text{electrical}} \; or \; \frac{\text{electrical}}{\text{mechanical}} \times \frac{\text{mechanical}}{\text{magnetic}} \qquad (1.36)$$

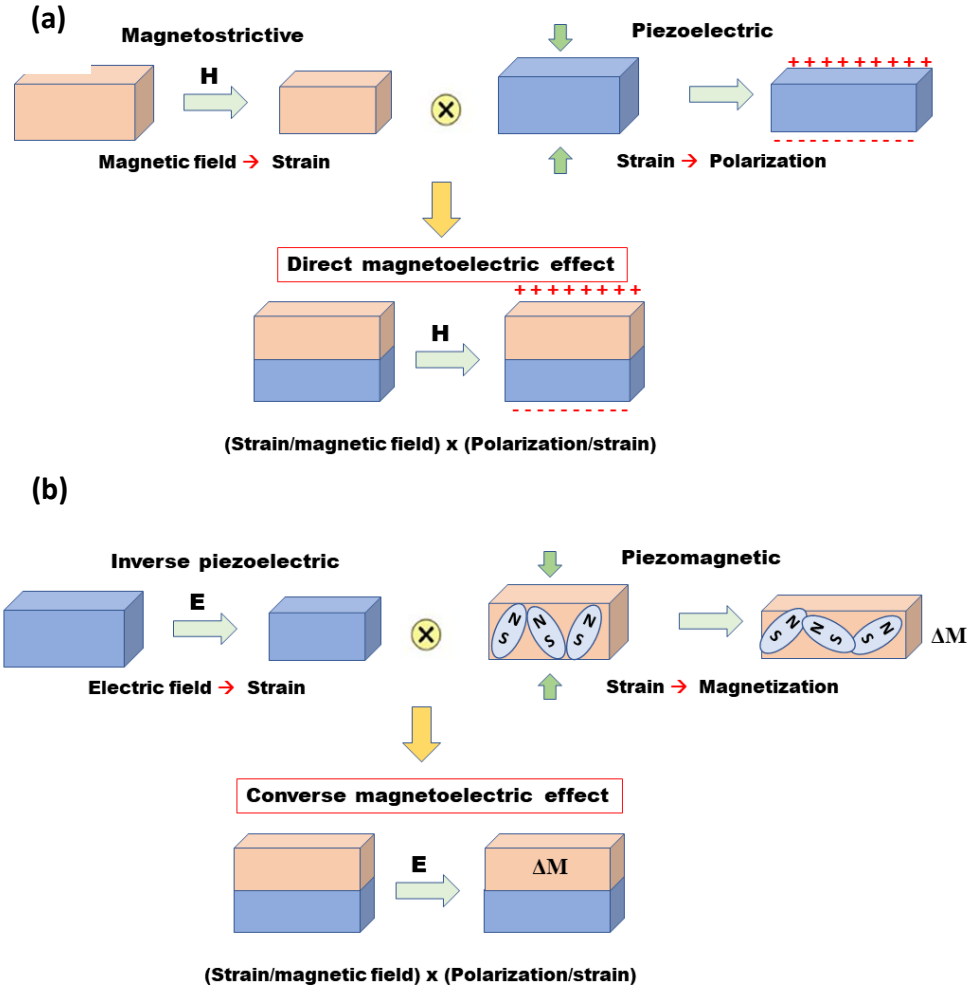

Figure 1. 26: *Schematic illustration of strain-mediated ME effect in a composite system consisting of a magnetic layer (beige) and ferroelectric layer (blue). (a) Direct ME effect and (b) converse ME effect.*

IV.3.2. Types of multiferroics and natures of couplings

Using the concept of phase connectivity introduced by Newnham [43]. When describing the structure of a two-phase composite, the notation 0-3, 2-2, 1-3, etc. is used, where each number represents the connectivity of each phase. A 0-3 particulate composite, for example, is made up of single-phase particles (denoted by 0) embedded in a matrix of a different phase (denoted by 3). For films, 2-2 horizontal heterostructures, and 1-3 vertical heterostructures of multiferroic ME composites made up of ferroelectric and magnetic phases are some of the common connectivity schemes that have been examined so far.

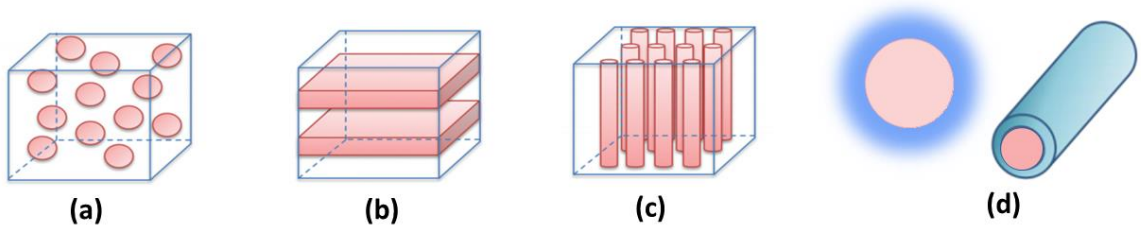

Figure 1. 27: *Diagrams of the four major types of composite connectivity arrangement: (a) 0-3 particulate composite, (b) 2-2 laminated composite, (c) 1-3 sticks embedded in a matrix, and (d) core-shell structure (nanoparticles or fibers).*

Composite magnetoelectric multiferroic systems have attracted interest considerable in recent years due to their multifunctionality and their high ME coupling coefficients around and at room temperature. Scientists at Philips laboratories made a significant discovery shortly after realizing that a magnetoelectric effect could be achieved by combining magnetostrictive phase and piezoelectric via mechanical coupling. They conducted experiments and found that the effect could be significant in composites. Using the Fe-Co-Ti-Ba-O system, they created ceramic composites of $BaTiO_3$-$CoFe_2O_4$ through unidirectional solidification and measured the ME coefficients up to 0.13 mV cm^{-1} Oe^{-1} at room temperature. The obtained ME effect is up to 100 times greater than that found for the multiferroics at a single phase [44].

The subject gradually lost its prominence and did not receive much attention, until 1990 when Newnham [45]and a Russian team [46] utilized a conventional sintering process to produce a particulate composite using $BaTiO_3$ and PZT. This novel synthetic technique was relatively uncomplicated compared to previous methods and enabled the combination of phases with distinct structures. However, the resulting ME coefficients were significantly lower.

The application of rare earth alloys (Terfenol-D, $Tb_{1-x}Dy_xFe_2$) to giant magnetostriction in 2001 marked an important moment in the development of massive composites, allowing for very significant ME effects (ME coefficient >1V $cm^{-1}Oe^{-1}$) [47]. There was a lot of interest back then in nano-structured composites in thin layers based on oxides. Zheng et al were the first to experiment with cobalt oxide films on $BaTiO_3$ [48]. Then, as growth methods improved, it became possible to accelerate research on these structures [49]. The comparative advantage of these thin layers is in atomic-level phase control or obtaining an accurate design by matching the different networks, thereby facilitating ME coupling at the atomic scale [50].

This thesis will focus entirely on massive ceramic composites and core-shell fibers.

IV.3.2.1. 0-3 particulate composite

This type of composite material has the advantage of being simple to process, making it a low-cost option. The composite is characterized by a large interfacial surface area between the two materials - ferroelectric and ferromagnetic - which is essential for achieving a high ME response. However, the ferromagnetic materials used are often semiconductors or poor electrical insulators. As a result, the insulation of the composite is compromised, resulting in leakage issues that prevent the required magnetic fields for switching magnetization. To ensure good dispersion of the ferromagnetic phase in the ferroelectric matrix, percolation and agglomeration of the ferromagnetic content must be avoided, as they can create an electrical conductor that interferes with the charges developed in the ferroelectric matrix. Unfortunately, achieving a high concentration of ferromagnetic phase in the matrix is limited by percolation. Porosity, cracks, and interfaces between the ferroelectric and ferromagnetic materials can also lead to space charge polarization, which makes it difficult to accurately measure the true strength of the ME coupling. Additionally, the densification of the composites using high-temperature treatments can lead to undesirable reactions due to interfacial interdiffusion. However, new processes are being developed to address these issues and improve the ME response factors[51], [52].

IV.3.2.2. 2-2 laminated composite

The issue of leaks commonly faced in 0-3 composites can be prevented in laminates of configuration (2-2). These laminates consist of alternating horizontal layers of ferroelectric and magnetoelectric phases which are bound together using a binder/glue/epoxy. The ferromagnetic ferroelectric interface in (2-2) laminates is smaller compared to 0-3 composites, which helps to reduce losses resulting from poor interface quality. However, similar to 0-3 composites, interdiffusion and secondary reactions at the interfaces stay to be a significant challenge. To address this issue, it is advised to use treatments at moderate temperatures.

IV.3.2.3. 1-3 composite

To create type 1-3 composites, ferromagnetic rods or fibers are bonded to a ferroelectric matrix. It is thus possible to avoid the effects of particle percolation and agglomeration and introduce a large volume fraction of the magnetic phase into the ferroelectric matrix. It should also be noted that the poor quality of the ferroelectric-ferromagnetic interfaces prevents composites 1-3 from exhibiting significant ME response. Add to that the low interfacial surface, which is still one of the main issues with this type of composite.

IV.3.2.4. Core-shell composite

To achieve a stronger magnetoelectric effect in type 0-3 composites, it is important to ensure an even distribution of the ferromagnetic phase within the ferroelectric matrix. This can be achieved by using nano-sized composite powders (spherical or fibers) with a core-shell structure, where ferromagnetic cores are surrounded by ferroelectric shells. This configuration, known as ferromagnetic@ piezoelectric, has gained the interest of many research groups. The core-shell structure provides better insulation for the magnetic particles, resulting in higher resistivity of the samples and improved polarization process.

IV.4. The magnetoelectric system choice

The quality of a ME composite is determined not only by its geometry and coupling interface, but also by other factors. The ability of the materials used in the composite to convert electrical energy to magnetic energy (and vice versa) is critical for determining the overall quality of the composite.

IV.4.1. Choice of ferroelectric phase (piezoelectric)

To date, a variety of piezoelectric ceramics have been used, including PZT (Lead Zirconate Titanium), and PMN-PT (Lead Magnesium Niobate - Lead Titanate). However, it is clear from the literature that PZT is the most commonly used piezoelectric material. It sinters easily, has a high electromechanical coupling, and exhibits no signs of chemical reaction with other components. Motivated by environmental concerns, because of the toxicity of lead oxide, more recent research has focused on the search for "lead-free", particularly those based on $BaTiO_3$ [48], [50], [53]. The piezoelectric coefficient d_{33} of pure BT fabricated using conventional solid-state method is approximately 190 pC N^{-1} [54]. It is well known that the morphotropic phase boundary (MPB) separating rhombohedral (R) and tetragonal (T) phases plays an important role in enhancing piezoelectric properties for BT piezoelectric family [55].

In order to enhance the piezoelectric properties of BT, chemical modification was used to form MPB compositions via tuning their T_{R-O} and/or T_{O-T} to RT. Indeed, the addition of Ca^{2+} is often used to shift the T_{R-O} and or T_{O-T} values to a low temperature by modifying the A-sites (Ba^{2+}), and substituting Zr^{4+}, Sn^{4+}, Hf^{4+}, Nb^{5+} and Co^{3+} in the B-sites (Ti^{4+}), which can increase both the T_{R-O} and/or the T_{O-T} values [56]. As a result, doping with two or more elements can form phase boundaries at/near RT for BT ceramics by shifting their T_{R-O} and T_{O-T}, leading to enhanced strain and piezoelectric properties [57], [58]. Zhu Li-Feng et al. demonstrated experimentally that Ca doping in the A-site and Sn doping in the B-site of BT can improve the

piezoelectric coefficient. In fact, they reported that $(Ba_{1-x}Ca_x)(Ti_{0.89}Sn_{0.11})O_3$ (x = 0.01–0.06) ceramics possess a high piezoelectric coefficient of d_{33} up to 500 pC N^{-1} at room temperature. A high piezoelectric coefficient of 670pC N^{-1} was obtained for (x = 0.05) and explained by constructing an MPB composition at this composition [59].

$Ba_{0.95}Ca_{0.05}Ti_{0.89}Sn_{0.11}O_3$ is ferroelectric at room temperature and has good piezoelectric properties, making it interesting in combination with a magnetostrictive material to achieve magnetoelectric coupling.

IV.4.2. Choice of ferromagnetic phase (magnetostrictive)

Cobalt ferrite is a popular choice for the magnetostrictive phase in composite magnetoelectric materials due to its unique combination of properties. $CoFe_2O_4$ is ferrimagnetic at room temperature. Its Curie temperature is 793 K (520 °C), making its magnetic properties temperature stable for most common applications. It has a magneto-crystalline anisotropy constant K_1 of 2.106 erg.cm^{-3} at a temperature which is 30 times that of $NiFe_2O_4$ and $MnFe_2O_4$, resulting in field values with a high coercive field of up to 3000 Oe at room temperature[60], [61].

The density of CFO is ρ= 5.304 g.cm^{-3}, its Young's modulus is 188.4 GPa, and its elastic constants are C_{11}=257 GPa, C_{12}=150 GPa, C_{44}=85.3 GPa, with the elastic modulus C'=53.5 GPa [62]. C' is a measure of the cubic lattice's resistance to tetragonal elastic distortion. Its value is particularly low when compared to other ferrites, which helps to explain why it is more magnetostrictive. It has relatively high magnetostriction values, with a magnetostriction coefficient λ_{100} of the order of -200 ppm. In other words, the negative sign indicates that a magnetic field compresses the material, and the relative elongation of CFO at saturation between the unmagnetized and magnetic states is 200.10^{-6}. This parameter is higher than for most ferrites, making cobalt ferrite particularly interesting for stress transfers at the interface with another material.

$CoFe_2O_4$ is a ferrimagnetic inverse spinel at room temperature, with a high Curie temperature, high coercive field values, and strong magnetostriction. It is an ideal magnetic material to use in an artificial magnetoelectric multiferroic, especially if a magnetoelectric coupling passing through the stress at the interfaces between phases is desired.

IV.4.3. Coupling motivation of $CoFe_2O_4$ / $Ba_{0.95}Ca_{0.05}Ti_{0.89}Sn_{0.11}O_3$

As stated in the introduction part, the demand for multifunctional materials, high density information storage, energy efficiency, and environmental friendliness is increasing in the electronic industry. Magnetoelectric multiferroics have received special attention in this context because they meet the majority of these criteria.

While the interest of multiferroics composites is obvious, understanding the global system becomes more difficult. One of the future challenges will be to fully understand the mechanisms involved, whether from the perspective of the individual phases or their interactions. Comprehensive studies of such systems are rare at the moment. To date, most studies of artificial multiferroics have focused on the measurement of a coupling magnetoelectric rather than its origin.

The combination of ferrimagnetic ferrite $CoFe_2O_4$ and ferroelectric perovskite $Ba_{0.95}Ca_{0.05}Ti_{0.89}Sn_{0.11}O_3$ appeared natural. Individually, all of the phases have the desired properties. At room temperature, one is ferrimagnetic, has a high Curie temperature, and is very magnetostrictive. The other is ferroelectric at room temperature and highly piezoelectric. Additionally, both materials have been extensively studied individually (chapter 2). The combination of these two piezoelectric and magnetostrictive materials raises the prospect of achieving a coupling via stress effects.

Following this idea, our thesis topic is focused on the effect of connectivity on magnetoelectric coupling, which we investigated by creating structural architectures that combine CFO and BCTSn via 0-3 connectivity and core-shell nanofibers.

References

[1] J. Kreisel and M. Kenzelmann, ‘Multiferroics - the challenge of coupling magnetism and ferroelectricity’, *Europhysics News*, vol. 40, no. 5, pp. 17–20, Sep. 2009, doi: 10.1051/epn/2009702.

[2] M. Fiebig, ‘Revival of the magnetoelectric effect’, *J. Phys. D: Appl. Phys.*, vol. 38, no. 8, pp. R123–R152, Apr. 2005, doi: 10.1088/0022-3727/38/8/R01.

[3] P. Curie, ‘Sur la symétrie dans les phénomènes physiques, symétrie d’un champ électrique et d’un champ magnétique’, *J. Phys. Theor. Appl.*, vol. 3, no. 1, pp. 393–415, 1894, doi: 10.1051/jphystap:018940030039300.

[4] V. A. Astaf’Ev, ‘ON THE MOMENTUM SPECTRUM OF 7T+ MESONS FROM THE REACTION 7T+ + P’.

[5] G. T. Rado and V. J. Folen, ‘Magnetoelectric Effects in Antiferromagnetics’, 2014.

[6] C.-W. Nan, M. I. Bichurin, S. Dong, D. Viehland, and G. Srinivasan, ‘APPLIED PHYSICS REVIEWS—FOCUSED REVIEW’, *J. Appl. Phys.*.

[7] ‘Liang et al. - 2021 - Roadmap on Magnetoelectric Materials and Devices.pdf’.

[8] D. Apalkov, B. Dieny, and J. M. Slaughter, ‘Magnetoresistive Random Access Memory’, *Proc. IEEE*, vol. 104, no. 10, pp. 1796–1830, Oct. 2016, doi: 10.1109/JPROC.2016.2590142.

[9] J. Gao, Z. Jiang, S. Zhang, Z. Mao, Y. Shen, and Z. Chu, ‘Review of Magnetoelectric Sensors’, *Actuators*, vol. 10, no. 6, p. 109, May 2021, doi: 10.3390/act10060109.

[10] H. Wu, A. Tatarenko, M. I. Bichurin, and Y. Wang, ‘A multiferroic module for biomechanical energy harvesting’, *Nano Energy*, vol. 83, p. 105777, May 2021, doi: 10.1016/j.nanoen.2021.105777.

[11] R. de Sousa, ‘Multiferroics Are a Spintronics Game Changer’, *Physics*, vol. 15, p. 124, Aug. 2022, doi: 10.1103/Physics.15.124.

[12] C. M. Bedoya-Hincapié, E. Restrepo-Parra, and L. D. López-Carreño, ‘Applications of magnetic and multiferroic core/shell nanostructures and their physical properties’, *DYNA*, vol. 85, no. 207, pp. 29–35, Oct. 2018, doi: 10.15446/dyna.v85n207.69203.

[13] Y.-H. Chu, L. W. Martin, M. B. Holcomb, and R. Ramesh, ‘Controlling magnetism with multiferroics’, *Materials Today*, vol. 10, no. 10, pp. 16–23, Oct. 2007, doi: 10.1016/S1369-7021(07)70241-9.

[14] ‘ramesh2007.pdf’.

[15] P. Barone and S. Picozzi, ‘Mechanisms and origin of multiferroicity’, *Comptes Rendus Physique*, vol. 16, no. 2, pp. 143–152, Mar. 2015, doi: 10.1016/j.crhy.2015.01.009.

[16] S. Dong, J.-M. Liu, S.-W. Cheong, and Z. Ren, ‘Multiferroic materials and magnetoelectric physics: symmetry, entanglement, excitation, and topology’, *Advances in Physics*, vol. 64, no. 5–6, pp. 519–626, Nov. 2015, doi: 10.1080/00018732.2015.1114338.

[17] Z.-M. Hu, Y. Su, and J. Li, ‘Nonlinear magnetoelectric effects of multiferroic composites’, *International Journal of Solids and Structures*, vol. 212, pp. 96–106, Mar. 2021, doi: 10.1016/j.ijsolstr.2020.12.008.

[18] K. F. Wang, J.-M. Liu, and Z. F. Ren, ‘Multiferroicity: the coupling between magnetic and polarization orders’, *Advances in Physics*, vol. 58, no. 4, pp. 321–448, Jul. 2009, doi: 10.1080/00018730902920554.

[19] R. Ramesh, ‘Materials for a Sustainable Microelectronics Future: Electric Field Control of Magnetism with Multiferroics’, *J Indian Inst Sci*, vol. 102, no. 1, pp. 489–511, Jan. 2022, doi: 10.1007/s41745-021-00277-7.

[20] G. E. Bacha, S. Milano, and J. Viola, ‘Hysteresis Mitigation in Current Sensor ICs Using Ferromagnetic Cores’.

[21] ‘Zur Theorie des Ferromagnetismus’.

[22] I. Mayer and S. A. Angelov, ‘EHF Description of superexchange: Relations to Anderson’s model’, *Int. J. Quantum Chem.*, vol. 18, no. 3, pp. 783–796, Sep. 1980, doi: 10.1002/qua.560180312.

[23] W. F. Brown, ‘The Fundamental Theorem of Fine-Ferromagnetic-Particle Theory’, *Journal of Applied Physics*, vol. 39, no. 2, pp. 993–994, Feb. 1968, doi: 10.1063/1.1656363.

[24] N. A. Frey, S. Peng, K. Cheng, and S. Sun, ‘Magnetic nanoparticles: synthesis, functionalization, and applications in bioimaging and magnetic energy storage’, *Chem. Soc. Rev.*, vol. 38, no. 9, p. 2532, 2009, doi: 10.1039/b815548h.

[25] L. Néel, ‘Théorie du traînage magnétique des ferromagnétiques en grains fins avec application aux terres cuites’.

[26] J. L. Dormann, ‘Le phénomène de superparamagnétisme’, *Rev. Phys. Appl. (Paris)*, vol. 16, no. 6, pp. 275–301, 1981, doi: 10.1051/rphysap:01981001606027500.

[27] V. A. M. Brabers, ‘Chapter 3 Progress in spinel ferrite research’, in *Handbook of Magnetic Materials*, Elsevier, 1995, pp. 189–324. doi: 10.1016/S1567-2719(05)80032-0.

[28] Tom. F. W. Barth and E. Posnjak, ‘Spinel structures: with and without variate atom equipoints’, *Zeitschrift für Kristallographie - Crystalline Materials*, vol. 82, no. 1–6, pp. 325–341, Nov. 1932, doi: 10.1524/zkri.1932.82.1.325.

[29] P. Weiss and A. Piccard, ‘Le phénomène magnétocalorique’, *J. Phys. Theor. Appl.*, vol. 7, no. 1, pp. 103–109, 1917, doi: 10.1051/jphystap:019170070010300.

[30] P. Debye, ‘Einige Bemerkungen zur Magnetisierung bei tiefer Temperatur’, *Ann. Phys.*, vol. 386, no. 25, pp. 1154–1160, 1926, doi: 10.1002/andp.19263862517.

[31] W. F. Giauque, ‘A THERMODYNAMIC TREATMENT OF CERTAIN MAGNETIC EFFECTS. A PROPOSED METHOD OF PRODUCING TEMPERATURES CONSIDERABLY BELOW 1° ABSOLUTE’, *J. Am. Chem. Soc.*, vol. 49, no. 8, pp. 1864–1870, Aug. 1927, doi: 10.1021/ja01407a003.

[32] A. N. Stranges, ‘William Francis Giauque: An adventure in low-temperature research’, *J. Chem. Educ.*, vol. 67, no. 3, p. 187, Mar. 1990, doi: 10.1021/ed067p187.

[33] L. E. Cross and R. E. Newnham, ‘History of Ferroelectrics’.

[34] W. J. Merz, ‘The Electric and Optical Behavior of BaTi O 3 Single-Domain Crystals’, *Phys. Rev.*, vol. 76, no. 8, pp. 1221–1225, Oct. 1949, doi: 10.1103/PhysRev.76.1221.

[35] D. Fu and M. Itoh, ‘Role of Ca off-Centering in Tuning Ferroelectric Phase Transitions in Ba(Zr,Ti)O3System’, in *Ferroelectric Materials - Synthesis and Characterization*, A. Peláiz-Barranco, Ed., InTech, 2015. doi: 10.5772/61017.

[36] W. Zhong, D. Vanderbilt, and K. M. Rabe, ‘Phase Transitions in BaTi O 3 from First Principles’, *Phys. Rev. Lett.*, vol. 73, no. 13, pp. 1861–1864, Sep. 1994, doi: 10.1103/PhysRevLett.73.1861.

[37] F. Li, S. Zhang, D. Damjanovic, L. Chen, and T. R. Shrout, ‘Local Structural Heterogeneity and Electromechanical Responses of Ferroelectrics: Learning from Relaxor

Ferroelectrics', *Adv. Funct. Mater.*, vol. 28, no. 37, p. 1801504, Sep. 2018, doi: 10.1002/adfm.201801504.

[38] C. Cazorla, 'Novel mechanocaloric materials for solid-state cooling applications', *Applied Physics Reviews*, vol. 6, no. 4, p. 041316, Dec. 2019, doi: 10.1063/1.5113620.

[39] Z. Kutnjak, B. Rožič, and R. Pirc, 'Electrocaloric Effect: Theory, Measurements, and Applications', in *Wiley Encyclopedia of Electrical and Electronics Engineering*, Hoboken, NJ, USA: John Wiley & Sons, Inc., 2015, pp. 1–19. doi: 10.1002/047134608X.W8244.

[40] N. A. Spaldin and M. Fiebig, 'The Renaissance of Magnetoelectric Multiferroics', *Science*, vol. 309, no. 5733, pp. 391–392, Jul. 2005, doi: 10.1126/science.1113357.

[41] M. Kumari, C. Prakash, and R. Chatterjee, 'Room-temperature magnetoelectric properties of Fe doped $BaZr_{0.05}Ti_{0.95}O_3$', *Journal of Applied Physics*, vol. 113, no. 17, p. 17D918, May 2013, doi: 10.1063/1.4795425.

[42] N. A. Hill, 'Why Are There so Few Magnetic Ferroelectrics?', *J. Phys. Chem. B*, vol. 104, no. 29, pp. 6694–6709, Jul. 2000, doi: 10.1021/jp000114x.

[43] R. E. Newnham, D. P. Skinner, and L. E. Cross, 'Connectivity and piezoelectric-pyroelectric composites', *Materials Research Bulletin*, vol. 13, no. 5, pp. 525–536, May 1978, doi: 10.1016/0025-5408(78)90161-7.

[44] J. VAN DEN BOOMGAARD, D. R. TERRELL, R. A. J. BORN, and H. F. J. I. GILLER, 'An in situ grown eutectic magnetoelectric composite material', *JOURNAL OF MATERIALS SCIENCE*, p. 5, 1974, doi: 10.1007/BF00553210.

[45] Harshe, G., Dougherty, J. P., & Newnham, R. E. (, 'Theoretical modelling of multilayer magnetoelectric composites. International journal of applied electromagnetics in materials', *International journal of applied electromagnetics in materials*, vol. 6, no. 4, p. 145, 1993.

[46] M. I. Bichurin, I. A. Kornev, V. M. Petrov, et I. V. Lisnevskaya, 'Investigation of magnetoelectric interaction in composite', *Ferroelectrics*, vol. 204, no. 1, pp. 289–297.

[47] J. Ryu, A. V. Carazo, K. Uchino, and H.-E. Kim, 'Magnetoelectric Properties in Piezoelectric and Magnetostrictive Laminate Composites', *Jpn. J. Appl. Phys.*, vol. 40, no. 8R, p. 4948, Aug. 2001, doi: 10.1143/JJAP.40.4948.

[48] H. Zheng *et al.*, 'Multiferroic $BaTiO_3$-$CoFe_2O_4$ Nanostructures', *Science*, vol. 303, no. 5658, pp. 661–663, Jan. 2004, doi: 10.1126/science.1094207.

[49] L. W. Martin, Y.-H. Chu, and R. Ramesh, 'Advances in the growth and characterization of magnetic, ferroelectric, and multiferroic oxide thin films', *Materials Science and Engineering: R: Reports*, vol. 68, no. 4–6, pp. 89–133, May 2010, doi: 10.1016/j.mser.2010.03.001.

[50] J. Ma, J. Hu, Z. Li, and C.-W. Nan, 'Recent Progress in Multiferroic Magnetoelectric Composites: from Bulk to Thin Films', *Adv. Mater.*, vol. 23, no. 9, pp. 1062–1087, Mar. 2011, doi: 10.1002/adma.201003636.

[51] M. A. Qaiser *et al.*, '0–3 type Bi3TaTiO9:40wt%BiFeO3 composite with improved high-temperature piezoelectric properties', *Journal of Alloys and Compounds*, vol. 740, pp. 1–6, Apr. 2018, doi: 10.1016/j.jallcom.2017.12.365.

[52] V. Corral-Flores, D. Bueno-Baqués, and R. F. Ziolo, ‘Synthesis and characterization of novel CoFe2O4–BaTiO3 multiferroic core–shell-type nanostructures’, *Acta Materialia*, vol. 58, no. 3, pp. 764–769, Feb. 2010, doi: 10.1016/j.actamat.2009.09.054.

[53] M. Naveed-Ul-Haq *et al.*, ‘Strong converse magnetoelectric effect in (Ba,Ca)(Zr,Ti)O3 - NiFe2O4 multiferroics: A relationship between phase-connectivity and interface coupling’, *Acta Materialia*, vol. 144, pp. 305–313, Feb. 2018, doi: 10.1016/j.actamat.2017.10.048.

[54] S. Agarwal, O. F. Caltun, and K. Sreenivas, ‘Magneto electric effects in BaTiO3–CoFe2O4 bulk composites’, *Solid State Communications*, vol. 152, no. 21, pp. 1951–1955, Nov. 2012, doi: 10.1016/j.ssc.2012.08.002.

[55] D. Damjanovic, ‘A morphotropic phase boundary system based on polarization rotation and polarization extension’, *Appl. Phys. Lett.*, vol. 97, no. 6, p. 062906, Aug. 2010, doi: 10.1063/1.3479479.

[56] M. Rafique, A. Herklotz, K. Dörr, and S. Manzoor, ‘Giant room temperature magnetoelectric response in strain controlled nanocomposites’, *Appl. Phys. Lett.*, vol. 110, no. 20, p. 202902, May 2017, doi: 10.1063/1.4983357.

[57] W. Liu and X. Ren, ‘Large Piezoelectric Effect in Pb-Free Ceramics’, *Phys. Rev. Lett.*, vol. 103, no. 25, p. 257602, Dec. 2009, doi: 10.1103/PhysRevLett.103.257602.

[58] W. Liu, L. Cheng, and S. Li, ‘Prospective of (BaCa)(ZrTi)O3 Lead-free Piezoelectric Ceramics’, *Crystals*, vol. 9, no. 3, p. 179, Mar. 2019, doi: 10.3390/cryst9030179.

[59] L.-F. Zhu, B.-P. Zhang, L. Zhao, and J.-F. Li, ‘High piezoelectricity of $BaTiO_3$–$CaTiO_3$–$BaSnO_3$ lead-free ceramics’, *J. Mater. Chem. C*, vol. 2, no. 24, pp. 4764–4771, 2014, doi: 10.1039/C4TC00155A.

[60] S. Amiri and H. Shokrollahi, ‘The role of cobalt ferrite magnetic nanoparticles in medical science’, *Materials Science and Engineering: C*, vol. 33, no. 1, pp. 1–8, Jan. 2013, doi: 10.1016/j.msec.2012.09.003.

[61] R. Safi, A. Ghasemi, R. Shoja-Razavi, E. Ghasemi, and T. Sodaee, ‘Rietveld structure refinement, cations distribution and magnetic features of CoFe2O4 nanoparticles synthesized by co-precipitation, hydrothermal, and combustion methods’, *Ceramics International*, vol. 42, no. 5, pp. 6375–6382, Apr. 2016, doi: 10.1016/j.ceramint.2016.01.032.

[62] Z. LI, E. S. FISHER*, J. Z. LIU t, M. V. NEVITT, ‘Single-crystal elastic constants of Co-AI and Co-Fe spinels’, *JOURNAL OF MATERIALS SCIENCE*, vol. 26, pp. 2621–2624, 1991.

Chapter 2

METHODS AND EXPERIMENTAL TECHNIQUES

Introduction

The purpose of this chapter is to describe the main experimental techniques used in this thesis. Particular emphasis will be placed on techniques that, due to the limited availability of devices, may be more unusual.

Processing of samples

Several methods for elaborating oxides have been discussed in the literature, including solid-state reactions, synthesis by self-combustion, sol-gel methods, hydrothermal methods, and synthesis by coprecipitation, among others. In this chapter, we aim to explore cost-effective and simple ways of synthesizing materials, including self-combustion and sol-gel techniques to produce high-quality oxides. We also present some experimental techniques for characterizing the elaborated samples and studying their properties. We provide a description of the instruments used, as well as an overview of their operating principles.

III.1. Elaboration technics of nanopowders

Soft chemistry developed in response to the 1974 energy crisis, when scientists decided to seek to reduce the energy costs associated with material production. The development of highly powerful instruments for analysis, such as scanning electron microscopy and high-resolution transmission electron microscopy, enabled the use of advanced techniques beyond traditional ceramic methods.

Solid-state chemistry provides a range of physicochemical and electrocatalytic techniques for synthesizing mixed oxides. The physicochemical properties of these oxides can be affected by the method and conditions employed during synthesis, as well as the temperature of thermal treatments such as annealing and sintering.

III.1.1. Self-combustion method (Auto-combustion method):

The self-combustion synthesis route using fuel is one of the most widely used and useful processes for the preparation of simple and pure phases, as well as complex oxide materials. The oxidant and the fuel present in the precursor solution, which can be glycine, citric acid, urea, or sucrose, undergo an oxidation-reduction reaction. Among the various wet chemical processes, the self-combustion route is simple and profitable for the synthesis of very fine

homogeneous crystalline nanopowders that do not require the decomposition steps and/or intermediate calcinations required by other conventional synthetic routes. An aqueous solution of a redox system composed of metal precursor nitrate ions acting as the oxidizer, and a fuel, are heated at moderate temperatures leading to the formation of a viscous gel, which swells during the decomposition and in the final stage of nitrate dehydration, ultimately leading to burning.

The self-combustion method is a very rapid, highly energy-efficient process and produce materials with high purity levels, this is because the reaction is exothermic. It is a low-cost process, as it does not require expensive equipment or solvents.

III.1.2. Sol-gel method:

The sol-gel method involves the transformation of a sol, which is a stable colloidal suspension of solid particles in a liquid, into a gel, a solid or semi-solid framework that retains the liquid within its structure. This process involves several stages, including hydrolysis, condensation, and gelation.

In the first stage of the sol-gel process, a metal alkoxide or other precursor is hydrolyzed in a solvent, typically water or an alcohol, to form a sol. The hydrolysis reaction produces metal hydroxide and alcohol, which then react further to form metal oxide or other ceramic materials. The sol is typically stabilized by the addition of a surface-active agent, such as a surfactant or a stabilizing agent.

In the second stage of the sol-gel process, the sol is subjected to a condensation reaction, which results in the formation of a three-dimensional framework of particles. The particles are typically cross-linked by chemical bonds, such as covalent bonds, or physical interactions, such as van der Waals forces.

In the final stage of the sol-gel process, the gel is formed by the continued cross-linking of particles until that a solid or semi-solid network is formed. The gel can then be dried, calcined, or sintered to produce a final product with desirable properties, such as high surface area, uniform porosity, and excellent mechanical strength.

The sol-gel process has a number of advantages over traditional processing methods, including the ability to produce materials with unique properties, such as high purity, uniformity, and

controlled pore size distribution. The method is also relatively simple, versatile, and scalable, which making it suitable for a wide range of applications, including optics, electronics, catalysis, and biomedicine.

III.2. Elaboration technic of Core–Shell nanofibers.

III.2.1. Electrospinning method

Nanofibers, which are fibers with a thickness of less than 100 nanometers, possess unique properties due to their high surface-to-weight ratio. This makes them particularly useful in applications that require large surface areas for chemical reactions to occur, as increasing the surface area accelerates the reaction. Several techniques can be used to create nanofibers, including drawing, template synthesis, phase separation, self-assembly, and electrospinning. In this study, electrospinning was chosen as the method for elaborating nanofibers.

Electrospinning is a novel technique that has been identified as one of the most efficient method for producing polymer nanofibers. It has been already used in nanotechnology and materials science since 1980s and has recently gained popularity. Furthermore, it appears that this is the only process that can be developed for mass production of one-by-one continuous nanofibers from a variety of polymers. When combined with sol-gel chemistry, various composite materials can be directly electrospun into nanofibers. Additionally, by introducing nanoparticles, nanorods, nanowires, nanotubes, and nanosheets with different dimensions and morphologies into polymer solutions, mixtures could be obtained and utilized for electrospinning.

III.2.2. Principle of Electrospinning

The process of electrospinning involves electrifying a liquid droplet to generate a jet that is then stretched and elongated to form fibers. The basic setup for electrospinning involves a high-voltage power supply, a syringe pump with a metallic needle, a spinneret, and a conductive collector. Upon electrification, the liquid droplet forms a Taylor cone (see next section), from which a charged jet is ejected and undergoes bending instabilities, resulting in the deposition of solid fibers on the collector. The electrospinning process can be divided into four steps, including the charging of the droplet, extension of the jet, thinning of the jet due to electrical bending instability, and solidification and collection of the fibers.

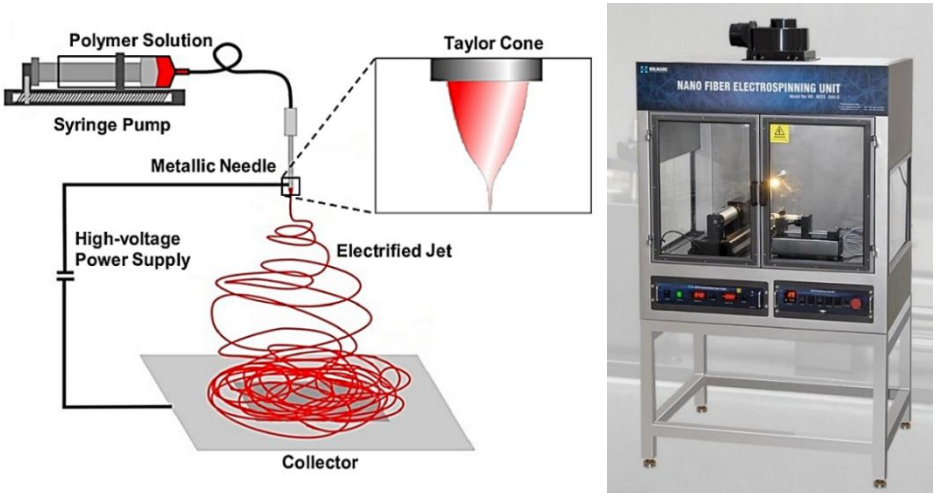

Figure 2. 1: *Principle of electrospinning system.*

III.2.3. Taylor cone

The conical shape formed when the electrostatic forces exceed the surface tension of a solution is known as the Taylor cone. This cone ejects a liquid jet when the electric field is strong enough. The elongation of this electrified jet produces an extremely thin and lengthy jet, which moves towards a collector having lower potential. During its trajectory, the solvent evaporates, and eventually, the jet solidifies to form fibers, ranging from tens of nanometers to hundreds of micrometers in size.

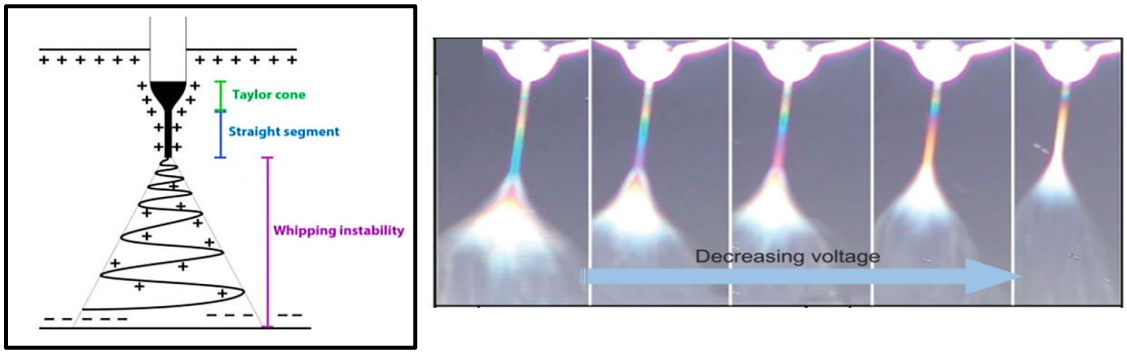

Figure 2. 2: The formation of a Taylor cone during the charging of a drop of liquid.

III.2.4. Electrospinning Process Parameters

To tailor electrospun fibers for various applications, it is necessary to understand the effects of different parameters. Although, many different parameters can be controlled in electrospinning:

- ***Properties of solution:*** Polymer molecular weight, viscosity, elasticity, conductivity, surface tension, solvent dielectric effect, and polymer concentration;

- ***Processing conditions:*** Voltage, solution flow rate, collector type, needle diameter and distance from needle to collector, collection time**;**
- ***Ambient conditions:*** Temperature, relative humidity, atmosphere type…

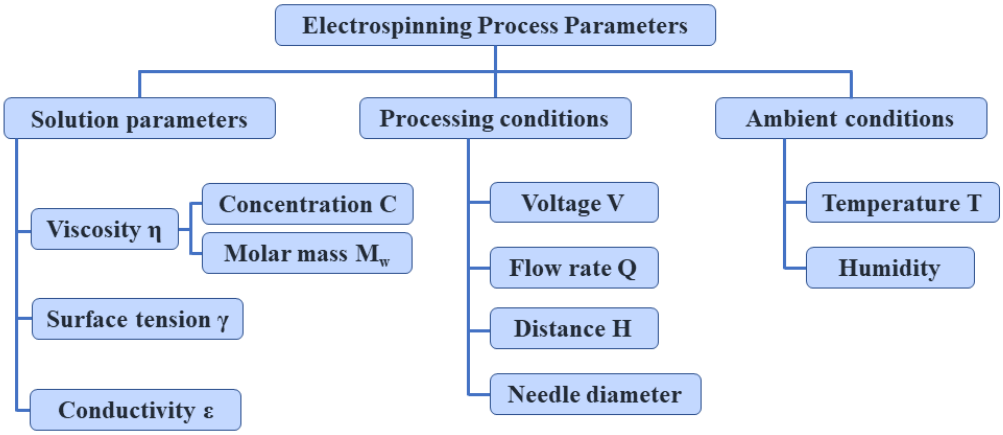

Figure 2. 3: *Flowchart of electrospinning parameters.*

III.2.5. Coaxial electrospinning

Coaxial electrospinning is a technique used to produce core-sheath nanofibers with a high level of control over the composition of the fibers. This technique involves using a coaxial needle consisting of two concentric hollow needles, an inner needle and an outer needle. Two separate fluids are fed through the inner and outer needles using syringe pumps, and when they meet at the exit end of the needle, the outer fluid wraps around the inner fluid to form a compound Taylor cone in the presence of an external electric field. This results in the ejection of a coaxial jet, which ultimately forms core-shell nanofibers.

To ensure successful coaxial electrospinning, it is essential to maintain high coaxiality of the needle, where the inner and outer fluids form a compound jet and stay together in a concentric manner. This requires that the inner and outer fluids have sufficient viscosities to keep the jets continuous, and that they are immiscible to prevent mixing or inversion of the two fluids. Further, these fluids should also have similar dielectric properties to ensure a similar electrical force.

By adjusting the flow rates of the two fluids, the diameter of the nanofibers and the thickness of the sheath can be tailored. Coaxial electrospinning has enabled the incorporation of various materials, such as polymers, oligomers, metal salts, proteins, oils, liquid crystals, and even cells/bacteria/viruses, into the core of a core-shell nanofiber. It also allows for the facile fabrication of nanofibers from unspinnable liquids as they can be supplied as the inner fluid to

produce nanofibers under the guidance of the outer fluid. Overall, coaxial electrospinning offers a promising technique for the controlled synthesis of core-shell nanofibers with various applications in tissue engineering, drug delivery, and energy storage, among others.

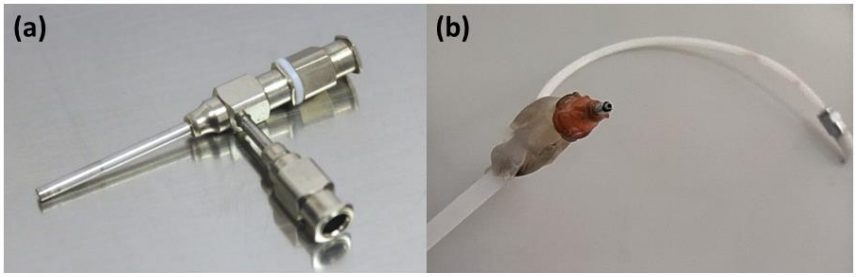

Figure 2. 4: *Commercial coaxial syringes and laboratory-made coaxial syringes*

III.3. Elaboration processes of BCTSn nanopowders

The sol-gel method is a widely used technique for the synthesis of oxide ceramic materials due to its simplicity and the ability to control the chemical composition and microstructure of the final product by adjusting parameters such as precursor concentration, pH, temperature, and duration of heat treatment. These advantages made it a suitable choice for elaborating the $Ba_{0.95}Ca_{0.05}Ti_{0.89}Sn_{0.11}O_3$ powders. The synthesis steps have been summarized in Figure 2.6, while the detailed process has been published in our previous work [1].

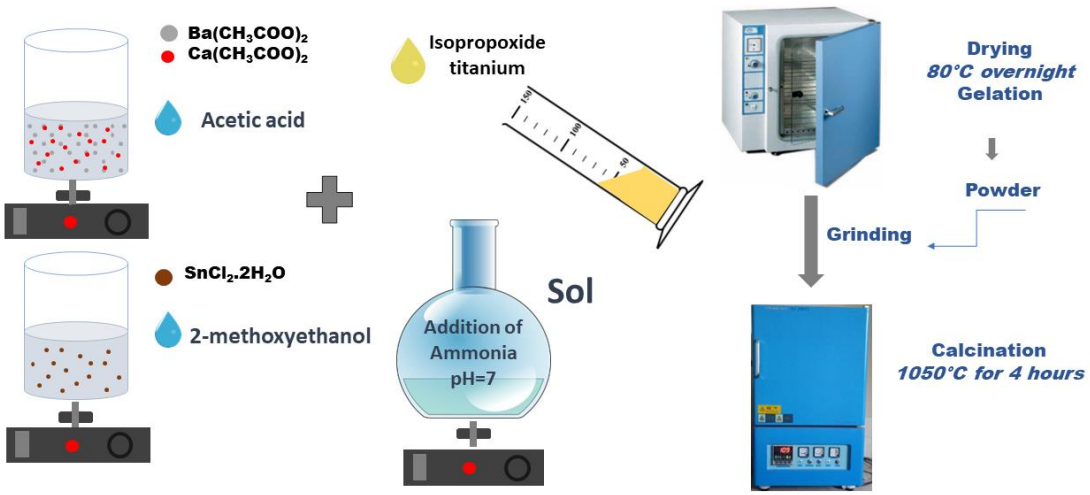

Figure 2. 5: *Experimental procedure used to elaborate BCTSn powders (sol-gel method).*

III.4. Elaboration processes of CFO nanopowders

$CoFe_2O_4$ nanoparticles were prepared by combining sol–gel auto combustion. This method produced ferrite samples with excellent chemical homogeneity, high purity, and superior crystallization. Moreover, this method requires basic equipment, a straightforward preparation process, a short processing time, and low external energy consumption. In our case, ammonia was used as neutralizer agent, ethylene glycol as polymerizing agent and acetic acid as fuel. The synthesis procedure is illustrated in Figure 2.7. while additional details can be found in reference [2] .

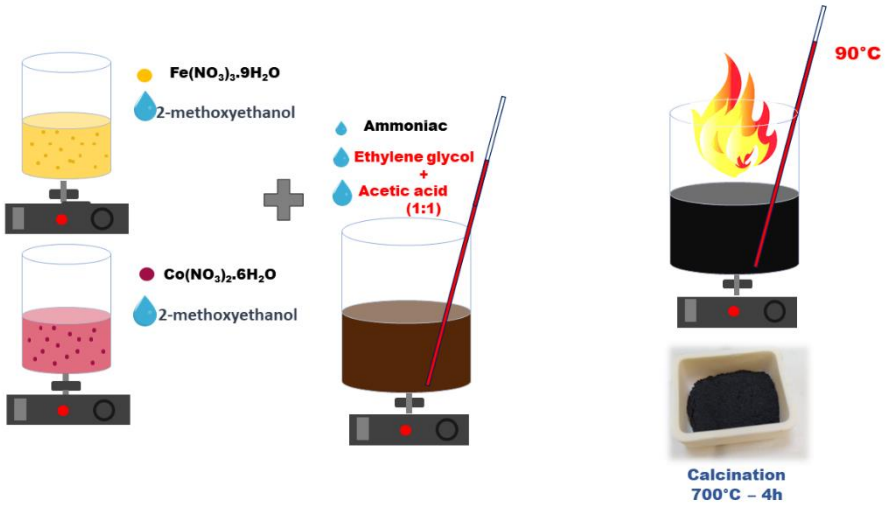

Figure 2. 6: *Experimental procedure used to elaborate CFO powders (solgel-auto combustion method).*

III.5. Elaboration processes of (1-x) BCTSn – (x) CFO particulate composites:

Polycrystalline (1-x) BCTSn – (x) CFO particulate composites with different weight fractions x (x = 0.1, 0.2, 0.3, 0.4 and 0.5) were fabricated by mechanical mixing of the calcined and milled individual ferroic phases of BCTSn and CFO and then pressed into cylindrical pellets under 50 bars using the uniaxial hydraulic press and sintered at 1300 °C for 4 h (Figure 2.8). Finally, the pellets were coated with silver paste on both surfaces for electrical and magnetoelectrical measurements [3].

Figure 2. 7: *Schematic diagram of the fabrication process of (1-x) BCTSn—(x) CFO sintered ceramics composite.*

III.6. Elaboration processes of CFO/BCTSn Core–Shell nanofibers

CFO@BCTSn nanofibers were prepared by sol-gel method based electrospinning method. The CFO and BCTSn precursors were dissolved separately in the appropriate solvents to prepare the sols for each phase. Poly(vinyl pyrrolidone) (PVP) was dissolved in ethanol to produce the polymer solution. The CFO and BCTSn solutions were added to the PVP solution and stirred continuously to form homogeneous CFO and BCTSn polymer solutions. Individual polymer solutions were transferred to glass syringes for electrospinning. The as-spun NFs were dried at 80 °C under vacuum for 12 hours before being annealed at 700 °C in an air atmosphere for 4 hours (Figure 2.8).

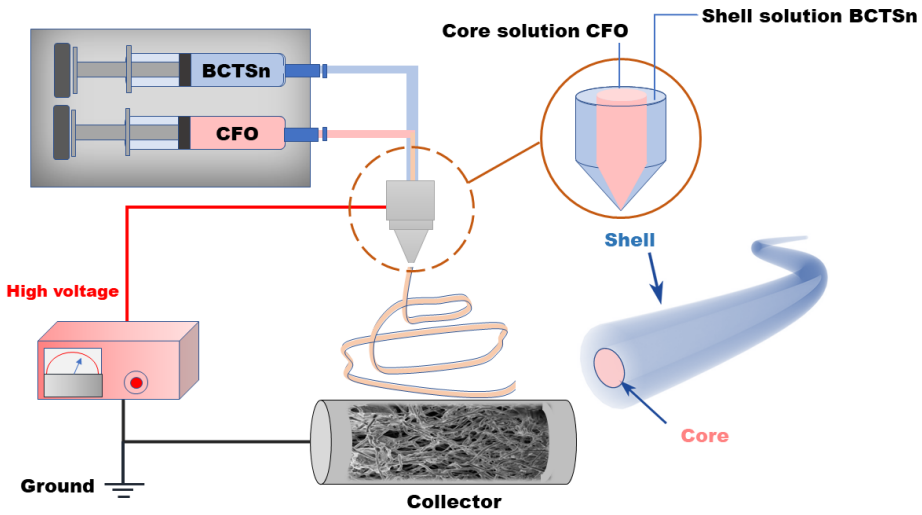

Figure 2. 8: *Coaxial electrospinning of core-shell nanofibers: setup schematics.*

Experimental techniques

IV.1. Structure and phase analysis

IV.1.1. X-ray Diffraction

X-ray diffraction (XRD) is a nondestructive and versatile technique that is primarily used for characterizing the crystallographic properties of solid materials. It allows obtaining structural information (crystalline symmetry, lattice parameters, distribution of atoms in the crystalline lattice), textural information (crystallite dimensions, internal stresses in the lattice) and compositional information (qualitative and quantitative, comparing the position and intensity of the obtained diffraction lines).

Materials and software: Panalytical X-Pert Pro was used to examine the crystalline structure of powders, ceramics and fibers. The step angle used was 0.02° within the 2θ range of 10° to 80°, and Cu-Kα radiation (λ~1.5406 Å) was utilized. The HighScore Plus software from Panalytical and reference structure data from the Crystallography Open Database (COD) 2020 were used to identify the phases. The Rietveld refinement method, coupled with EdPCR and WinPLOTR tools in the FullProf Suite software, was used to perform quantitative phase composition analysis of all our samples.

IV.1.2. Raman spectroscopy

Raman spectroscopy is a non-destructive analytical technique that is used to study the vibrational, rotational, and other low-frequency modes of a system. It involves the interaction of monochromatic light, such as laser light, with a sample, leading to a shift in the frequency of the scattered light, which is proportional to the vibrational energy of the sample. This shift is known as the Raman shift, and it provides information about the chemical composition, structure, phase transition and bonding of the sample.

Materials and software: The Raman spectra of pure CFO and (1-x) BCTSn – (x) CFO samples were recorded using a micro-Raman Renishaw spectrometer equipped with a filter for the analysis of the low-frequency spectral range down to 50 cm^{-1}. An optical microscope with a ×50 objective was employed to focus the incident light as a 2 μm diameter spot on the sample. The studied samples were excited using the polarized radiation of an argon laser (λ = 514.5 nm) and registered and analyzed with a Near-Excitation Tunable (NExT) filter. For temperature-dependent micro-Raman measurements, a well calibrated Linkam freezing stage with temperature stability of 0.1 K was used.

IV.2. Morphology and composition

IV.2.1. Scanning Electron Microscopy (SEM)

SEM is one of the most versatile tools for examining and analyzing the morphology of a solid at the nanoscale level by scanning it with a focused beam of electrons over the area of interest. A cold-cathode field emission gun produces electrons with kinetic energies ranging from 0.5 to 30 keV. Electrons have strong interactions with sample material and can reveal information other than topography. Back-scattered electrons can be elastically scattered while retaining beam energy. Inelastic scattering is responsible for the emission of low-energy secondary electrons (SE), also can produce bremsstrahlung and conventional X-ray radiation. Energy or wavelength dispersive spectroscopy, or EDS and WDS, can be used to analyze and quantify specific electronic transitions.

IV.2.2. Energy Dispersive X-Ray Spectroscopy (EDXS)

EDXS is an analytical technique related to SEM. By selecting scan types such as line scan, point scan, and elemental mapping of the entire image, this method allows for elemental analysis of the specimen while imaging in SEM. EDS is a type of X-ray fluorescence spectroscopy that analyzes X-rays emitted by matter when it is hit by electrons. Its basic premise is that each element has a distinct atomic structure, allowing X-rays that are characteristic of an element's atomic structure to be distinguished from the atoms present in the scanned area.

Materials and software: The SEM imaging for the sintered BCTSn ceramics were performed by using Tescan VEGA3 scanning electron microscope at a voltage of 10 kV. CFO powders morphology was observed using SEM, Philips XL30, having an attachment for energy-dispersive X-ray spectroscopy (EDS). For the CFO-BCTSn particulate composites and core-shell fibers, the scanning was performed by using HELIOUS 600 Nanolab setup from FEI. The grain size and fiber diameter distributions of the samples were determined using Image J. For pure CFO, pure BCTSn and CFO-BCTSn particulate composites an energy dispersive X-ray spectrometer (EDXS, Inca Oxford 350 EDS SSD, Oxford Instruments) was used to determine the atomic percentages.

IV.2.3. Transmission Electron Microscopy (TEM)

Transmission electron microscopy is a technique based on the principle of interaction of electrons with matter. It involves projecting a high-energy electron beam onto a thin sample. All the elastically transmitted and diffused electron beams passing through the sample are used

to form the image or diffraction diagram projected onto a fluorescent screen. The transmission electron microscope can observe objects in two modes:

Imaging mode: When electrons interact with the material, they produce a non-uniform distribution of the beam at the sample's exit. A portion of the beam is selected using a contrast diaphragm placed in the focal plane of the objective to produce a high-quality image.

Diffraction mode: When the intermediate lenses are adjusted to observe the focal plane image of the objective, a diffraction pattern is obtained for certain sample orientations. This pattern corresponds to all of the diffraction directions of the sample's (hkl) lattice planes in the Bragg position. The diffraction pattern reveals information about the sample's crystal structure and orientation, such as lattice parameters, crystal symmetry, and phase identification. The selected area electron diffraction (SAED) method is used to describe this mode.

Materials and software: In the last part of the thesis, JEOL-ARM 200F Cold FEG TEM/STEM operating at 200 kV and equipped with a spherical aberration (Cs) probe and image correctors (point resolution 0.12 nm in TEM mode and 0.078 nm in STEM mode), was used to observe the morphogenesis in CFO@BCTSn nanofibers powders with complex morphologies. Selected Area Electron Diffraction (SAED) allowed the phase identification of the core and shell area. While, the coupling of High-Angle Annular Dark-Field (HAADF) detector and Scanning Transmission Electron Microscope (STEM), was used to observe the core-shell structuration of CFO@BCTSn nanofibers.

Figure 2. 9: *Photograph of TEM equipment used at IJS in Ljubljana, Slovenia.*

IV.3. Magnetic and electrical measurements

IV.3.1. Magnetic measurements: Vibrating Sample Magnetometer (VSM)

The system is equipped with an internally pulsed cryogenic cooling tube, as shown in Figure ***2.10***. The cooling is achieved by condensing a small amount of helium gas to produce liquid helium at 1.7 K. This cryostat enables us to maintain a temperature of superconducting magnets at 4 K and also control the temperature in the measurement area. The temperature of the sample under study can be lowered from 400 K to 1.9 K in just 40 minutes. The superconducting magnets, cooled at 4 K, induce a magnetic field of up to 9 Tesla (90kOe). During measurements, the samples are in a controlled vacuum environment with an integrated cryogenic pump.

A magnetic field ***H*** produced by a magnetometer (using an electromagnet or a superconducting coil). The studied sample is placed in the measuring coil's center and vibrates at a constant frequency ***f*** and constant amplitude. The magnetic moment of the sample generates an induced voltage **V** by vibrating periodically in the air gap, which is related to the magnetic flux $\boldsymbol{\varphi}$ by Lenz's law:

$$V = \frac{\partial \varphi}{\partial t} \qquad (2.1)$$

Detection coils measure the induced voltage. By the reciprocity theorem, the flux $\boldsymbol{\varphi}$ is related to the magnetic field ***B*** created by an active current ***I*** circulating in the detection coils:

$$\varphi = BI\mu \qquad (2.2)$$

We can therefore calculate the magnetic moment $\boldsymbol{\mu}$ of the sample as a function of the magnetic field ***B*** using the measured voltage ***V***. The precision of these measurements is on the order of 10^{-7} emu.

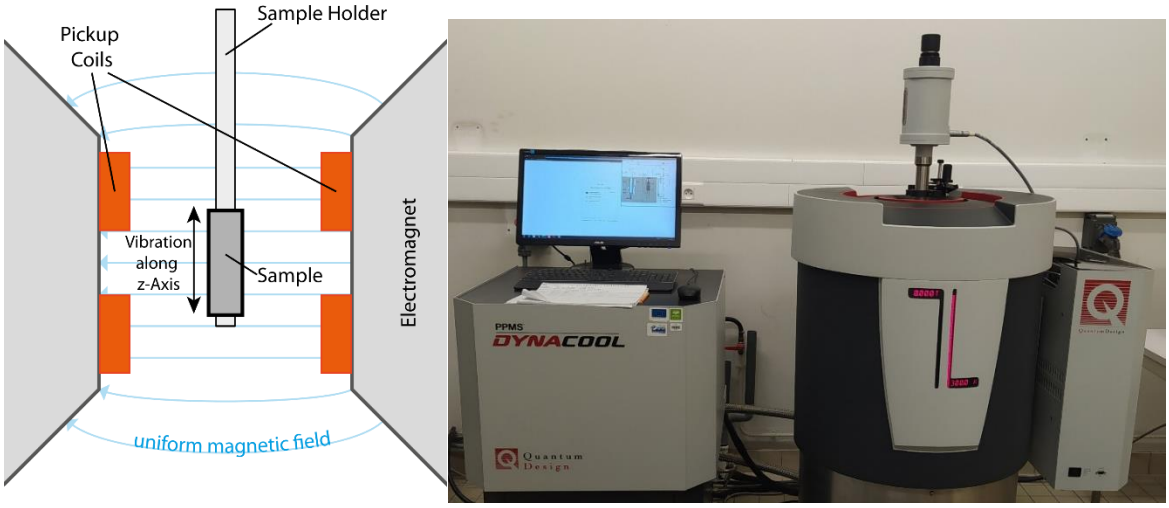

Figure 2. 10: *(a) Schematic of working principle of VSM, (b) Photograph of VSM apparatus used in LPMC Amiens, France.*

Materials and software: Magnetic properties of pure CFO, particulate composites and core-shell fibers composite were measured using a physical property measurement system (PPMS-DynaCool) Quantum design apparatus that operated at room temperature under a magnetic field range of 0-2.5 kOe.

During this thesis work, we performed measurements of magnetization M as a function of temperature T from 900 K to 300 K. The M(T) curves were obtained by cooling without and under magnetic field in ZFC (Zero Field Cooled) and FC (Field Cooled) modes, respectively. Magnetic hysteresis cycles M(H) were also obtained for all of our composites at room temperature. The cycles were obtained using a maximum field intensity of ±25 kOe at 300 K. CFO M(H) cycles were obtained for high temperatures ranging from 300 K to 900 K using the VSM-Oven mode (Figure 2.12).

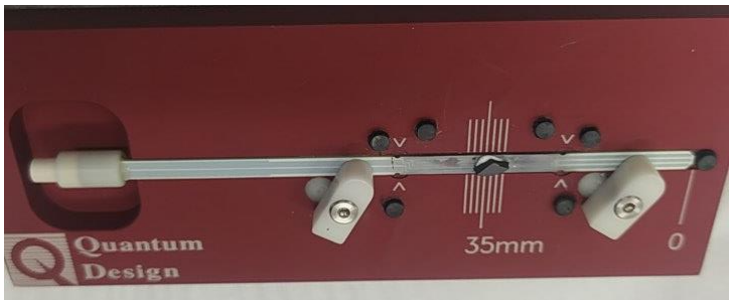

Figure 2. 11: *Photograph of VSM-Oven mode used for high temperature measurement, LPMC Amiens, France.*

IV.4. Electrical measurements

IV.4.1. Dielectric measurements

The LCR impedance analyzer is a precise tool used to evaluate the dielectric properties of materials. It measures capacitance, loss factor, inductance, and AC conductance at various frequencies by subjecting the sample to an alternating voltage and calculating the ratio of terminal voltage to current. It can determine the amplitude impedance and the phase angle between voltage and current. The analyzer assumes a parallel model for RC measurements and a series model for LR measurements. The electrical equivalent of a composite ceramic can be represented by a parallel combination of capacitance ***Cp*** and frequency-dependent resistance ***Rac(ω)***. The capacitance and resistance are measured to determine the dielectric constant and dielectrics losses (***tan δ***). The loss factor of a dielectric material at a specific frequency can be derived from the equivalent resistance and capacitance of the sample.

$$\tan\delta = \frac{1}{\omega R_p C_p} \qquad (2.3)$$

The dielectric constant (***ε***) can be calculated from the capacity value using the equation:

$$\varepsilon = \frac{C_d}{A\varepsilon_0} \qquad (2.4)$$

***Materials and software*:** The permittivity variation (ε) and dielectric losses (tanδ) with temperature in the frequency range of 20 Hz to 1 MHz were performed using an HP 4284A RLC-meter using a voltage of 0.25 V for BCTSn sintered ceramics electroded by silver paste. The dielectric measurement was carried out in a tubular furnace at a heating rate of 2 °C/min with a temperature range between 300-700 K.

IV.4.2. Ferroelectric measurements: P-E hysteresis loops

Polarization may be defined as:

$$P = \frac{Q}{A} \qquad (2.5)$$

where *Q* is the charge developed on the plates (Coulombs) and *A* is the area of the plates (m^2).

The voltage is cycled by the signal generator. Its direction is reversed at high frequency, and the voltage across the reference capacitor is measured. Because they are in series, the charge on the capacitor must be the same as the charge on the ferroelectric capacitor. This means that the charge on the ferroelectric can be determined by:

$$Q = C.V \qquad (2.6)$$

Where C denotes the capacitance of the reference capacitor and V the voltage measured across it. The polarization of a material in an oscillating electric field can thus be calculated. Because the capacitance of the reference capacitor is much greater than the capacitance of the ferroelectric, the majority of the voltage is passed over the ferroelectric. P can only be measured by cycling the polarization through cycling the voltage across the ferroelectric. We cannot measure absolute values in real time, but we can deduce absolute values from changes in polarization.

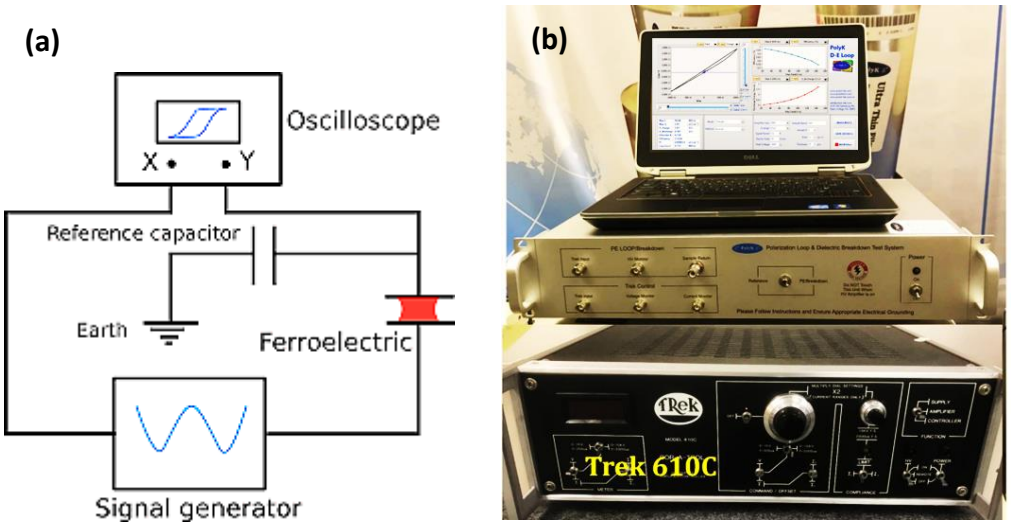

Figure 2. 12: *(a) Schematic of working principle of P−E loop measurements, (b) Photograph of device for measuring the P-E hysteresis loops IMED lab-UCA, Marrakesh, Morocco.*

***Materials and software*:** The polarization–electric field (P-E) hysteresis loops of pure BCTS and CFO-BCTSn ceramics composites were performed by CPE1701, PloyK, USA, with a high-voltage power supply (Trek 609-6, USA) in a silicone oil bath at 20 Hz in the temperature range of 30–120 °C.

IV.4.3. Direct piezoelectric measurements

Direct piezoelectric measurements are experimental techniques used to determine the piezoelectric response of a material. The most common method is the d_{33} method, which measures the charge generated by the piezoelectric material when a mechanical stress is applied perpendicular to the surface of the material. Another method is the d_{31} method, which measures the charge generated when the mechanical stress is applied parallel to the surface of the material. Direct piezoelectric measurements involve the application of a low-frequency oscillating force on the sample. The charge produced is collected via the two probes and

compared to a reference sample, producing a d_{33} reading. The amplitude of the applied stress is measured according to a similar principle, using a known piezoelectric element (PZT) placed in series with the sample.

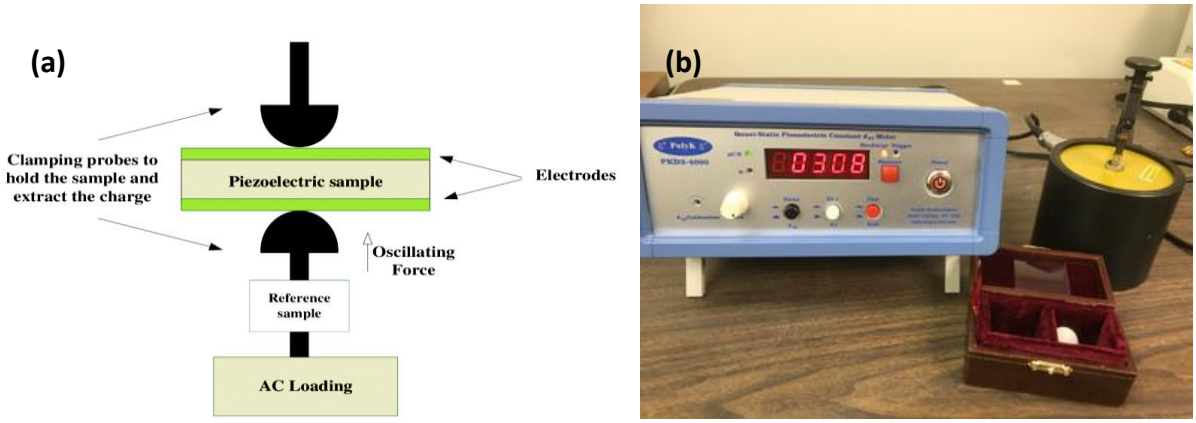

Figure 2. 13: *(a) Schematic of the basic Berlincourt d_{33} measurement setup, (b) Photograph of device for measuring the d_{33} used at IJS in Ljubljana, Slovenia.*

Materials and software: The piezoelectric measurements of CFO-BCTSn ceramics composites were measured by using an AixACCT 6 TF 2000 Analyzer with a SIOS Mebtechnik GmbH laser interferometer and a TREK model 609E-6 high-voltage amplifier. Before measurement, the samples were poled at room temperature in silicon oil under an electric field of 25 kV/cm for 15 min.

IV.4.4. Piezoelectric Force Microscopy (PFM)

Piezo Force Microscopy (PFM) is based on the inverse piezoelectric effect, in which an electrically polarized tip is used to probe the induced piezoelectric deformation. PFM has become the primary tool for studying the static and dynamic properties of ferroelectric materials. It is primarily used to image, manipulate, and study the mechanisms of ferroelectric switching.

PFM uses an Atomic Force Microscope (AFM) to image and manipulate a material's ferroelectric domains. To accomplish this, a conductive tip is brought into contact with the sample, and an alternating potential is applied to the tip to locally excite the sample's deformation via the inverse piezoelectric effect. The AFM microlever oscillates as a result of this deformation, and its movements are detected using a photodiode divided into four parts using the standard method. A synchronous detection amplifier isolates the signal at the working frequency. By scanning the sample surface in this manner, high-resolution images of the topography and structure of the ferroelectric domains can be obtained.

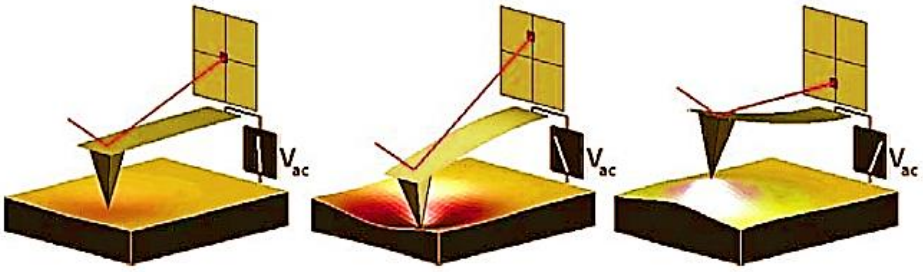

Figure 2. 14: *Depiction of PFM operation. The sample deforms in response to the applied voltage. This, in turn, causes the cantilever to deflect, which can then be measured and interpreted in terms of the piezoelectric properties of the sample*

Materials and software: In this work, the local piezoelectric responses of CFO@BCTSn NFs were investigated by an atomic force microscope (AFM, Jupiter XR Asylum Research, Oxford Instruments, CA, USA) equipped with a piezo-response force module (PFM). Pt-coated silicon tips with a radius of curvature ~10 nm (OMCL-AC240TM-R3, Olympus, Japan) were used for the PFM analysis. To prevent the CFO@BCTSn NFs from sticking to the PFM tip, the fibers were fixed to the Si substrate by heating at 600 °C for 30 min. We chose the nonconductive Si substrate to avoid electrical breakdown through the air and short-circuiting between the tip and the conductive substrate when scanning over the fiber edge and touching the substrate with the PFM tip. The PFM/AFM measurements were done in Jozef Stefan Institute, Ljubljana, Slovenia

IV.5. Magnetoelectric coupling measurement

The direct ME effect is characterized by a change in electric polarization as a result of the applied magnetic field. The goal is to measure this variation of polarization for a given magnetic field variation at a given operating point.

The principle of measuring the direct ME effect is as follows. A direct DC field is applied, allowing the magnetic material's point of polarization to be defined. We then apply a known alternating field AC ($\boldsymbol{H_{ac}}$) to it, which excites the magnetostrictive material and causes it to deform. Knowing the thickness of the piezoelectric material ***ep***, as well as the voltage ***V***, is sufficient to determine the variations of its polarization. The coefficient ME is given by the following equation:

$$\alpha_{ME} = \left(\frac{\partial E}{\partial H}\right) = \frac{V}{d\ H_{ac}} \qquad (2.7)$$

where V is the induced ME voltage across the sample, d represents the thickness of the sample, and H_{ac} is the applied AC magnetic field.

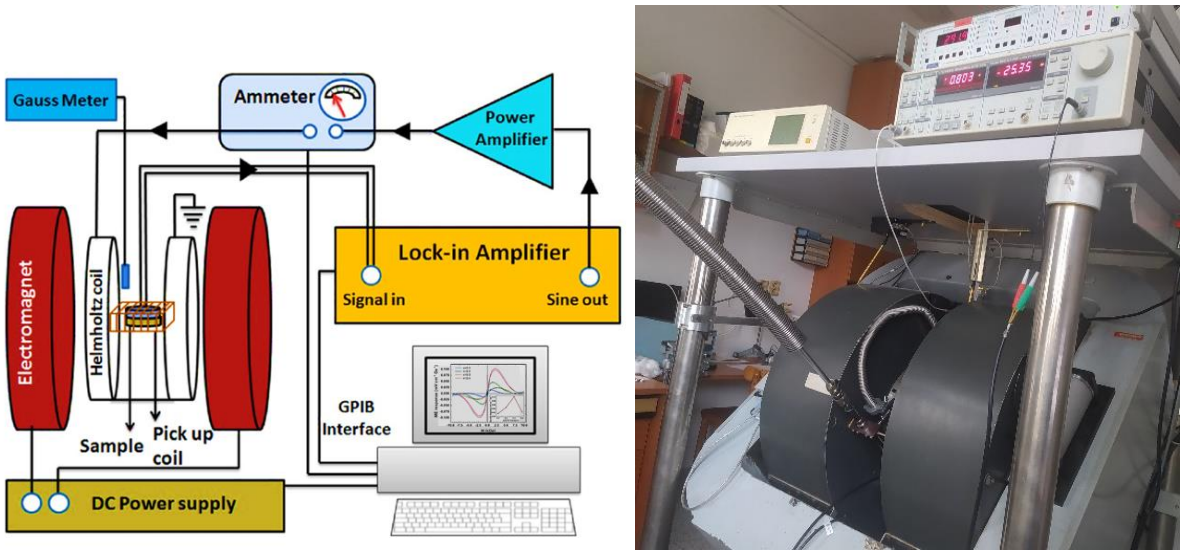

Figure 2. 15: *(a) Schematic of device for measuring the magnetoelectric effect, (b) Photograph of device for measuring the magnetoelectric effect used in FZU, Prague, Czech.*

Materials and software: The ME coefficients were determined by a dynamic method [4]as a function of bias magnetic field H_{dc} at small ac field H_{ac} = 1-5 Oe and frequencies 0.2-1 kHz by measuring the voltage or current across the sample utilizing a lock-in-amplifier with high impedance preamplifier. For measurements, a conventional Bruker EPR spectrometer EMX plus was used. A rectangular sample with a dimension of 3×5×0.3 mm^3 was prepared by bonding the nanofibers with epoxy resin. Before the measurement, the sample was coated with silver electrodes and poled at room temperature by applying a dc electric field of 10 kV/cm for 10 min (More details are described in Ref. [5]).

References

[1] Y. Hadouch *et al.*, 'Electrocaloric effect and high energy storage efficiency in lead-free Ba0.95Ca0.05Ti0.89Sn0.11O3 ceramic elaborated by sol–gel method', *J Mater Sci: Mater Electron*, Jan. 2022, doi: 10.1007/s10854-021-07411-2.

[2] Y. Hadouch, 'Enhanced Relative cooling Power and large inverse magnetocaloric effect of cobalt ferrite nanoparticles synthesized by auto-combustion method', *Journal of Magnetism and Magnetic Materials*, p. 8, 2022.

[3] Y. Hadouch, 'Piezoelectric, magnetic and magnetoelectric properties of a new lead-free multiferroic (1-x) Ba0.95Ca0.05Ti0.89Sn0.11O3—(x) CoFe2O4 particulate composites', *J Mater Sci*, 2023.

[4] M. M. Vopson, Y. K. Fetisov, G. Caruntu, and G. Srinivasan, ‘Measurement Techniques of the Magneto-Electric Coupling in Multiferroics’, *Materials*, vol. 10, no. 8, p. 963, Aug. 2017, doi: 10.3390/ma10080963.

[5] V. V. Laguta *et al.*, ‘Room-temperature paramagnetoelectric effect in magnetoelectric multiferroics Pb(Fe1/2Nb1/2)O3 and its solid solution with PbTiO3’, *J Mater Sci*, vol. 51, no. 11, pp. 5330–5342, Jun. 2016, doi: 10.1007/s10853-016-9836-4.

Chapter 3

ELABORATION AND CHARACTERIZATION OF BCTSn AND CFO CERAMICS

I. Introduction

The properties of the individual phases, ferroelectric BCTSn and ferromagnetic CFO, are investigated in this chapter. The investigation includes a detailed examination of their structural and morphological properties, as well as an examination of electrocaloric (of BCTSn) and magnetocaloric (of CFO) effects. The energy storage properties of the BCTSn phase were also investigated. These investigations provided significant results, which were published as two separate articles in indexed journals.

The first work was published in "Journal of Materials Science: Materials in Electronics" on November 15, 2021. The manuscript is titled "Electrocaloric effect and high energy storage efficiency in lead-free $Ba_{0.95}Ca_{0.05}Ti_{0.89}Sn_{0.11}O_3$ ceramic elaborated by sol–gel method".

https://doi.org/10.1007/s10854-021-07411-2

The second work was published in "Journal of Magnetism and Magnetic Materials" on September 4, 2022. The manuscript is titled "Enhanced Relative cooling Power and large inverse magnetocaloric effect of cobalt ferrite nanoparticles synthesized by auto-combustion method".

https://doi.org/10.1016/j.jmmm.2022.169925

J Mater Sci: Mater Electron

Electrocaloric effect and high energy storage efficiency in lead-free $Ba_{0.95}Ca_{0.05}Ti_{0.89}Sn_{0.11}O_3$ ceramic elaborated by sol–gel method

Youness Hadouch[1,2,*], Said Ben Moumen[1], Hanane Mezzourh[1,2], Daoud Mezzane[1,2], M'barek Amjoud[1], Bouchra Asbani[2], Anna G. Razumnaya[2,4], Yaovi Gagou[2], Brigita Rožič[3], Zdravko Kutnjak[3], and Mimoun El Marssi[2]

[1] Laboratory of Innovative Materials, Energy and Sustainable Development (IMED), Faculty of Sciences and Technology, Cadi-Ayyad University, BP 549, Marrakech, Morocco

[2] Laboratory of Physics of Condensed Matter (LPMC), University of Picardie Jules Verne, Scientific Pole, 33 rue Saint-Leu, 80039 Amiens Cedex 1, France

[3] Jozef Stefan Institute, Jamova Cesta 39, 1000 Ljubljana, Slovenia

[4] Faculty of Physics, Southern Federal University, Rostov-on-Don 344090, Russia

Received: 23 September 2021
Accepted: 15 November 2021

ABSTRACT

Structural, dielectric, ferroelectric, energy storage properties, and electrocaloric effect were studied in lead-free ceramic $Ba_{0.95}Ca_{0.05}Ti_{0.89}Sn_{0.11}O_3$ (BCTSn) elaborated by the sol–gel method. Phase purity structure was confirmed from X-ray data using the Rietveld refinement analysis which revealed the coexistence of tetragonal (*P4mm*) and orthorhombic (*Amm2*) symmetries at room temperature. Phase transitions were detected by dielectric and differential scanning calorimetry measurements. The energy storage properties were determined from *P-E* hysteresis, and the electrocaloric properties were calculated indirectly via the Maxwell approach. The large value of electrocaloric temperature change of $\Delta T = 0.807$ K obtained at a relatively small electric field of 30 kV cm^{-1}, and the high energy storage efficiency can make BCTSn ceramic a promising candidate for environmentally friendly refrigeration and energy storage applications.

1 Introduction

One of the most critical issues in energy consumption is the rising power consumption for air conditioning. The growing demand for cooling and air-conditioning machines increases the world's power consumption. Moreover, most of these devices rely on vapor-compression technology, which emits harmful gases as fluorine. For that reason, environmentalists and scientists are moving to develop new technologies for environmentally friendly refrigeration systems. The electrocaloric effect is an innovative

Address correspondence to E-mail: hadouch.younes@gmail.com; youness.hadouch@edu.uca.ma

https://doi.org/10.1007/s10854-021-07411-2
Published online: 18 January 2022

alternative technology based on the change of temperature (ΔT) and entropy (ΔS) in polar materials under an external electric field [1].

Ferroelectric ceramics have gained increasing attention because of their uses in various applications such as data storage, piezoelectric energy harvesting, and cooling devices [2–4]. Despite their robust properties, Pb-based materials face notable global restrictions, hence why it is necessary to develop new environment-friendly materials. Barium titanate $BaTiO_3$ (BT) is a typical alternative system that can become an important candidate for these applications [5–7]. Nevertheless, it shows a low dielectric constant, high Curie temperature (T_c = 120 °C), and low energy storage properties [8] that calls for strategies to improve these characteristics [9]. Site engineering as solution consists to substitute A-sites (Ba^{2+}) with Ca^{2+}, Sr^{2+}, La^{3+}… and/or B-sites (Ti^{4+})with Sn^{4+}, Zr^{4+}, Hf^{4+} [10]. More than 10 years ago, Desheng Fu et al. [11] studied the effect of substituting Ba^{2+} with Ca^{2+} in $Ba_{1-x}Ca_xTiO_3$ ceramics and reported an improvement of d_{33} from 180 up to 310 pC N^{-1} for $0.02 < x < 0.34$. In this context, several studies highlighted the partial substitution of Sn^{4+} for Ti in $BaTiO_3$, and its effect on the phase transition dielectric behavior, energy storage, and electrocaloric properties [7, 12, 13]. It is well known that pure BT shows three distinct phase transitions with increasing temperature, i.e., the rhombohedral (*R3m*)—orthorhombic (*Amm2*) phase transition at T_{R-O} = − 90 °C, the orthorhombic—tetragonal (*P4mm*) phase transition (T_{O-T} = 0 °C), and the tetragonal-cubic phase transition (T_C = 120 °C) [14]. Incorporating Sn^{4+} in BT can shift T_{O-T} and T_{R-O} to room temperature [12]. Meanwhile, doping of B-sites with Ca^{2+} (up to 21%) can reduce these transitions temperatures with a slight change of the Curie point [15]. Accordingly, co-doping in both sites can lead to the formation of the morphotropic phase boundary (MPB) at ambient temperature resulting in the enhancement of dielectric, piezoelectric, and electrocaloric properties [7, 16, 17]. Theoretically, in the MPB region, energy barriers become lower, making the polarization rotation and extension process easier [18]. Consequently, it is the right choice for promoting electrical properties to create two-phase or multiphase coexistence near room temperature. Wang et al. studied the electrocaloric effect (ECE) in the $Ba_{0.94}Ca_{0.06}Ti_{1-x}Sn_xO_3$ system with multiphase coexistence and achieved a large ECE of ΔT = 0.63 K under 20 kV cm^{-1} [19]. Benefiting from the MBP in BCTSn, Zhu et al. reported that $(Ba_{0.95}Ca_{0.05})(Ti_{1-x}Sn_x)O_3$ compositions displayed a high piezoelectric responses with d_{33} = 670 pC N^{-1} at x = 0.11 [20]. Nevertheless, there have been no investigations on the energy storage performance of the BCTSn materials. However, some recent studies reported a high energy storage density at the polymorphic phase boundaries. For example, Merselmiz et al. [21] achieved improved recovered energy storage (W_{rec}) of 72.4 mJ cm^{-3} with a high energy storage efficiency η = 85.07% in the BTSn ceramic under 25 kV cm^{-1}. In addition, energy performances in $Ba_{0.85}Ca_{0.15}Zr_{0.10}Ti_{0.90}O_3$ with MPB were frequently studied and reached a large W_{rec} of 414.1 mJ cm^{-3}, with electrocaloric responsivity (η = 78.6%) and a significant coefficient of performance (COP = input power/output cooling power) of 6.29 under 55 kV cm^{-1} [22]. On the other hand, the synthesis method is an important factor for designing ceramics with high compositional homogeneity, error-free stoichiometric ratio, and lower calcination and/or sintering temperature due to the mixture of liquid precursors at the molecular level. In this regard, the solid-state reaction route used to prepare BT-based ferroelectric materials necessitates a high calcination temperature (1350 °C) and sintering temperature range of 1400–1550 °C [23, 24]. Wang et al. [25] carried out a comparative study in BCZT elaborated by sol–gel (BCZT-SG) and solid-state (BCZT-SS) methods and reported a very high energy density of 0.52 J cm^{-3} in BCZT-SG compared with BCZT-SS (0.32 J cm^{-3}). Furthermore, many researchers have argued that grain size affects the physicochemical properties of ferroelectric materials [26–28].

In this paper, we have experimentally explored the temperature dependence of the energy storage and electrocaloric properties in the $Ba_{0.95}Ca_{0.05}Ti_{0.89}Sn_{0.11}O_3$ ceramic (BCTSn) elaborated by sol–gel process and sintered at 1350 °C for 7 h. The electrocaloric effect was evaluated using the indirect experimental approach following the Maxwell relation. The enhanced values of ECE, electrocaloric responsivity (η), *COP*, and energy storage were compared with the literature data, suggesting that our BCTSn ceramic could be a promising candidate for environmentally friendly refrigeration and high energy storage applications.

2 Materials and methods

The XRD patterns of BCTSn ceramic were obtained by X-ray diffraction using the Panalytical X-Pert Pro with Cu-Kα radiation (λ = 1.54059 Å) at room temperature. The apparent density of ceramic samples was determined by the Archimedes method, while the relative density was estimated from crystal structure parameters. The surface morphology of ceramic was examined using a scanning electron microscope (SEM, VEGA 3-Tescan) having energy-dispersive X-ray spectroscopy attachment (EDS). The temperature dependence of dielectric properties was measured using an impedance analyzer (HP 4284A) at the temperature, and the frequency ranges – 50–200 °C and 20 Hz–100 kHz, respectively. Differential scanning calorimetry (Perkin Elmer Jade DSC) was used to point out the different phase transitions. The polarization–electric field (*P-E*) hysteresis loops were performed by CPE1701, PloyK, USA, with a high-voltage power supply (Trek 609-6, USA) in a silicone oil bath at 20 Hz in the temperature range of 30–120 °C. The electrocaloric study was carried out by the indirect method using the recorded *P–E* hysteresis loops.

3 Experimental details

Lead-free $(Ba_{0.95}Ca_{0.05})$ $(Ti_{0.89}Sn_{0.11})$ O_3 ceramic (BCTSn) was obtained via a sol–gel reaction technique (Fig. 1). Minutely, a stoichiometric amount of barium acetate $Ba(CH_3COO)_2$ and calcium acetate $Ca(CH3COO)_2$ were dissolved in acetic acid (solution 1) while tin chloride ($SnCl_2{\cdot}2H_2O$) in 2-methoxyethanol (solution 2) separately. The obtained solutions (1 and 2) were mixed at room temperature. Then, a stoichiometric volume of titanium isopropoxide was added to the mixture solutions. The obtained mixture was stirred for 1 h, and then ammonia was dropped wisely to the solution to increase until the solution became transparent (pH = 7). After the aging step for 15 h, the gel was dried at ~ 80 °C, and the resulting powder was calcined at 1050 °C for 4 h based on the TGA results. The process flow chart is shown in Fig. 1. The resulting calcined powder was uni-axially pressed, without any binder, to give a pellet sintered at 1350 °C for 7 h. The pellet was coated with silver-paste electrodes on both surfaces for electrical measurements.

4 Results and discussion

4.1 Structural and microstructural analysis

Figure 2a shows the TGA curve of the uncalcined BCTSn powder. The thermogram represents three main weight losses. From ambient temperature up to around 500 °C, the two losses (23% and 16%) correspond to non-structural water and decomposition of thermally unstable organic compounds. The third loss (6%) is from 500 °C to 1000 °C that can be attributed to the undecomposed organic substances and the formation of the BCTSn perovskite structure [29]. The loss curve remains stable, which denotes that the crystallization temperature of the desired phase starts from 1000 °C. This calcination temperature is less than those reported using the solid-state method [30]. Figure 2b shows the XRD pattern at room temperature of BCTSn powder calcined at 1050 °C for 4 h. All characteristic peaks of the perovskite structure are well observed without any impurity or secondary crystalline phase, suggesting that Ca^{2+} and Sn^{4+} are well incorporated in the $BaTiO_3$ lattice forming a solid solution.

The XRD pattern was refined using the Rietveld refinement program via FullProf software based on the combination of tetragonal structure with the space group (*P4mm*) and orthorhombic structure (*Amm2*). The result proves an excellent agreement between the calculated and the observed diffractograms (Fig. 3a). The deconvoluted peaks between $2\theta \approx 44$–$46°$ and $2\theta \approx 65$–$66°$ indicate the coexistence of tetragonal and orthorhombic phases (inset Fig. 3a) as reported by Mezzourh et al. [31]. The crystallite size was determined using Scherrer's formula [31] and found to be 33 nm. The crystal structure parameters and the quality-of-fit measure (χ^2) extracted from the Rietveld refinements are shown in Table 1.

Figure 3b shows the SEM micrograph and grain-size distribution of BCTSn ceramic sintered at 1350 °C/7 h. As it can be seen, large grains are observed with well-defined grain boundaries. The grain-size distribution estimated by ImageJ® software is found to be around 28 µm. The apparent density of ceramic is 5.73 g cm^{-3}, along with a

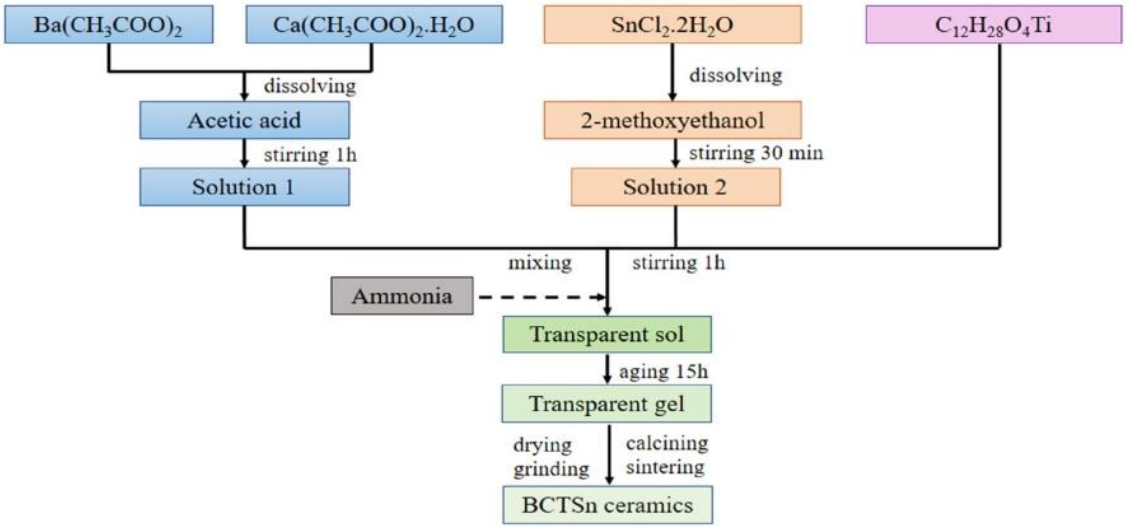

Fig. 1 The synthesis process of BCTSn ceramic by the sol–gel method

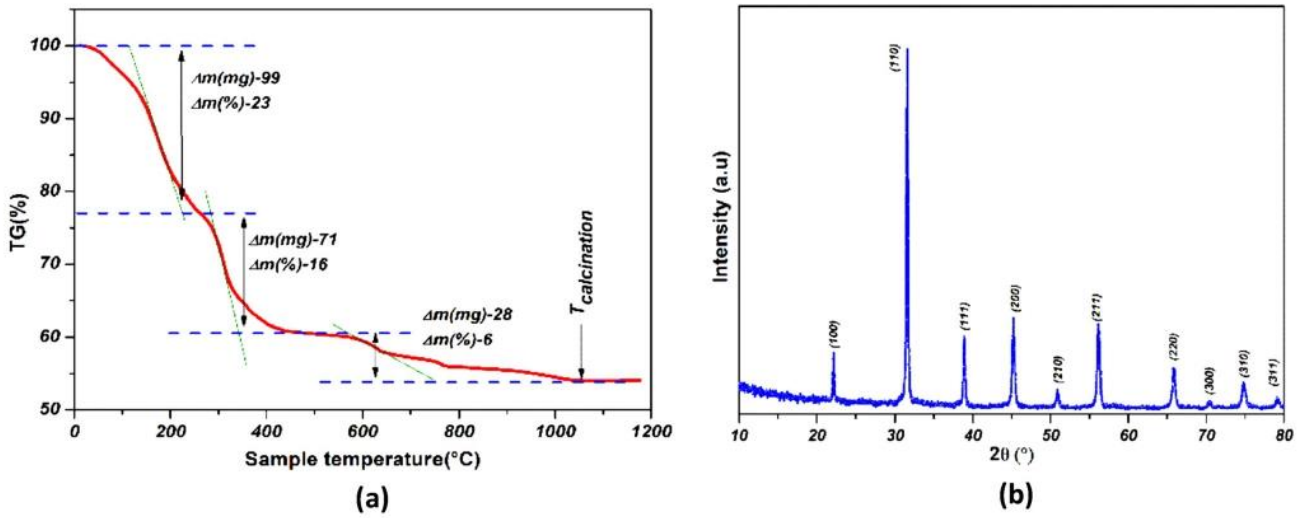

Fig. 2 **a** TGA curve of the BCTSn powder; **b** room-temperature XRD pattern of powder

relative density of 92%. The elemental composition was verified by the EDS analysis. Qualitative analysis reveals the presence of Ba, Ca, Ti, Sn, O, and C elements, and the presence of the carbon is due to the metallization process using the graphitic carbon. The obtained atomic percentage of elements is in agreement to the expected ratios (C: 13.73%; O: 49.68%; Sn: 2.12%; Ca: 1.03%; Ba: 15.25%; and Ti: 18.19%).

4.2 Dielectric properties

The temperature dependence of the dielectric constant ε_r and dielectric loss factor tanδ for BCTSn at the selected frequencies from 100 Hz to 100 kHz is shown in Fig. 4a. The curves at different frequencies display three distinct peaks at 12, 31, and 47 °C that correspond to the phase transitions of R–O (T_{R-O}), O–T (T_{O-T}), and T–C phases (T_C), respectively (see the inset to Fig. 4a). This result is in good agreement with DSC measurements that show three exothermic peaks at the same transition temperature values (T_{R-O}; T_{O-T}, and T_C) (Fig. 4b). Compared to BT, the substitution of Ti^{4+} by Sn^{4+} ions shifts T_{R-O} and T_{O-T} to higher temperatures and reduces T_C, while the substitution of Ba^{2+} by a small amount of Ca^{2+} does not affect the T_C [32]. It is observed that the values of ε_r are higher at low frequencies and decrease with the frequency increase. Some of the polarization

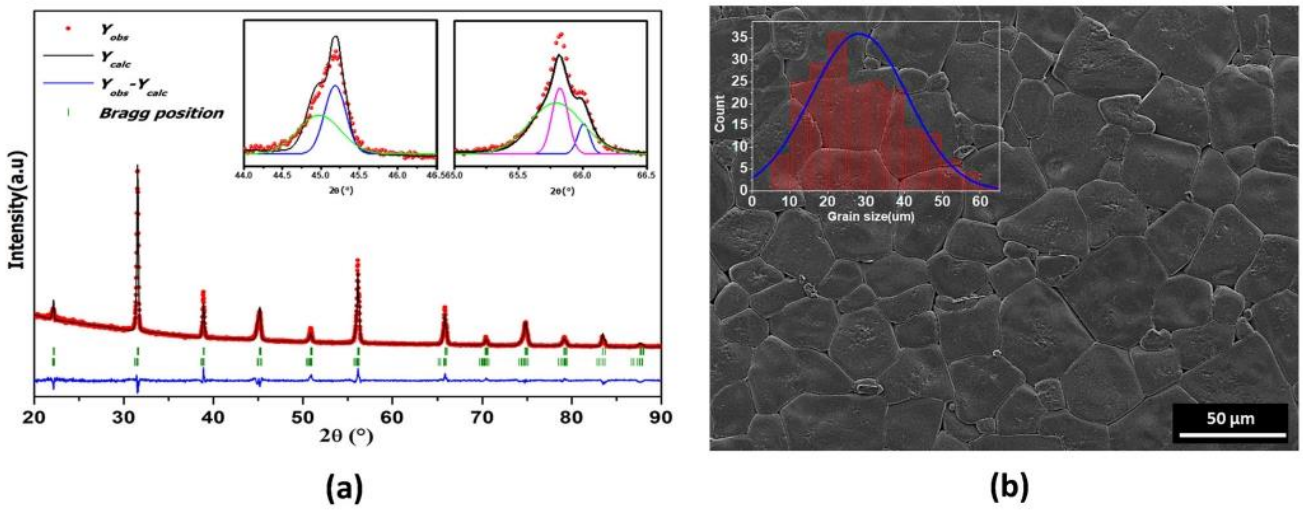

Fig. 3 **a** Rietveld fitted X-ray diffraction patterns of BCTSn ceramic; **b** SEM micrograph of ceramic, the inset to the image shows a grain size distribution

Table 1 Refined structural parameters for BCTSn ceramic at room temperature

Structure	Unit cell parameters					Phase compositions (%)	χ^2	Average crystalline size (nm) by XRD	Average grain size (µm) by SEM
	a(Å)	b(Å)	c(Å)	Angle (°)	V(Å^3)				
Tetragonal *P4mm*	4.0074	4.0074	4.0133	$\alpha = \beta = \gamma = 90$	64.449	72.92	2.703	33	28
Orthorhombic *Amm2*	4.0040	5.7261	5.7261		130.149	27.08			

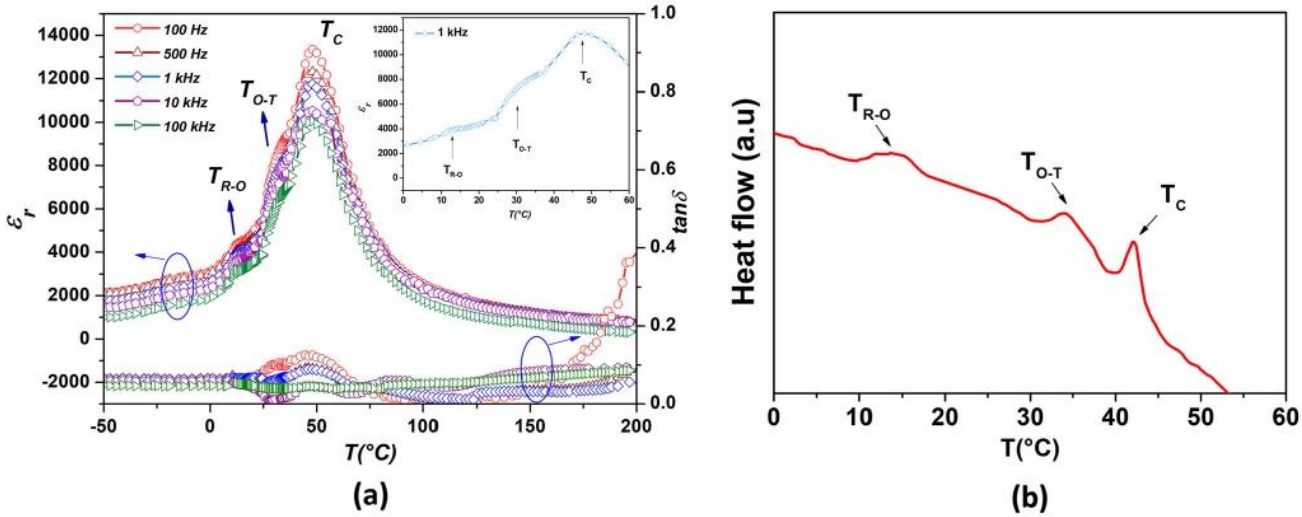

Fig. 4 **a** Temperature dependence of the dielectric constant and dielectric loss at different frequencies for BCTSn ceramic sintered at 1350/7 h (inset: close up of the dielectric constant curve for 1 kHz); **b** DSC heat flow of BCTSn

mechanisms do not contribute when the frequency of the electric field increases, which leads to a decrease in the total polarization, and therefore, the decrease in ε_r [33]. It is worth noting that the frequency

increment does not affect the T_c value, confirming that the BCTSn is a classical ferroelectric material without any relaxation behavior [34]. In addition, the maximum dielectric constant at 1 kHz is about 11,979, which is much higher than that of $Ba_{0.95}Ca_{0.05}Ti_{0.89}Sn_{0.10}O_3$ ceramic elaborated by a solid-state method [35].

To quantify the critical behavior of BCTSn, the Curie–Weiss law was initially used (Eq. 1) [33]:

$$\frac{1}{\varepsilon_r} = \frac{T - T_0}{C} (T > T_0), \quad (1)$$

where T_0 is the Curie–Weiss temperature and C is the Curie–Weiss constant.

The value of C is about 1.13×10^5 K (at 1 kHz) which means that BCTSn is displacive-type ferroelectric. The fitting results obtained by Eq. 1 are shown in Table 2. The dielectric constant curve deviates from the Curie–Weiss law at $T_{dev} > T_C$. The degree of this deviation is estimated by Eq. 2:

$$\Delta T_m = T_{dev} - T_m. \quad (2)$$

This deviation is often observed in ferroelectric ceramics and explained by the movement of domain walls [33]. In the BCTSn ceramic, the substitution of Ti^{4+} by Sn^{4+} leads to the distortion of the Ti–O bonds since the ionic radius of Sn^{4+} is bigger than that of Ti^{4+}, and therefore, Sn^{4+} ions have less free space to move in the oxygen octahedron. The spatial fluctuations of the bonds cause fluctuations in polar density; hence, the Curie peak is enlarged [36]. The diffuseness of the critical behavior of BCTSn can be described empirically by Eq. 3 [37]:

$$\frac{1}{\varepsilon_r} - \frac{1}{\varepsilon_m} = \frac{(T - T_m)^\gamma}{C} (1 < \gamma < 2), \quad (3)$$

where ε_m is the maximum of the dielectric constant, T_m is the temperature that corresponds to ε_m, and γ indicates the character of the phase transition. Thus, $\gamma = 1$ refers to normal ferroelectrics, and $\gamma = 2$ corresponds to relaxor ferroelectrics, as described by Hunpratub et al. [38].

For $1 < \gamma < 2$, the diffuse phase transition is incomplete [38]. The value of γ at 1 kHz is extracted from the fitting curve of $ln(\frac{1}{\varepsilon_r} - \frac{1}{\varepsilon_m})$ versus $\ln(T - T_m)$ and found to be 1.428 that identifies incomplete diffuse phase transition behavior. The results of the dielectric studies are summarized in Table 2 (Fig. 5).

4.3 Ferroelectric properties and energy storage performances

The electric field-dependent polarization characteristics (P-E loops) are shown in Fig. 6a. The polarization loop was measured for various temperatures under the applied electric field of 31 $kVcm^{-1}$ at 20 Hz. Below T_C, moderately saturated hysteresis loops describe the ferroelectric character of BCTSn ceramic. On heating, the hysteresis loops become more slanted and slim that is more desirable for energy storage applications [39]. However, the hysteresis does not disappear above T_C due to the diffuse phase transition behavior in good agreement with dielectric results. Above 383 K, the polarization shows a linear behavior, indicating the appearance of the paraelectric phase. At room temperature, the maximal polarization (P_{max}), the remnant polarization (P_r), and the coercive field (E_c) are found to be 18.93 μC cm^{-2}, 6.77 μC cm^{-2}, and 1.68 kV cm^{-1}, respectively, and decrease with increasing the temperature. However, the charge storage density ($Q_C = P_{max}–P_r$) increases slightly, reaching a maximum of 12.53 μC cm^{-2} before decreasing at 333 K, confirming the ferroelectric-paraelectric phase transition (Fig. 6b) [25]. It should be noted that BCTSn ceramic exhibits a low E_c that makes energy barriers lower and facilitates the domain switching during the poling process due to multiphase coexistence [40].

In order to evaluate the energy storage properties, the recoverable energy density W_{rec}, total energy density W_{tot}, and the energy storage efficiency η are calculated by Eqs. 4, 5, and 6, respectively:

$$W_{tot} = \int_0^{P_{max}} EdP, \quad (4)$$

$$W_{rec} = \int_{P_r}^{P_{max}} EdP, \quad (5)$$

$$\eta(\%) = \frac{W_{rec}}{W_{tot}} \times 100 = \frac{W_{rec}}{W_{rec} + W_{loss}} \times 100, \quad (6)$$

Table 2 Dielectric properties at 1 kHz of the BCTSn ceramic sintered at 1350 °C/7 h

	ε_m	tanδ	T_0 (°C)	C × 10^5 (K)	T_m (°C)	T_{dev} (°C)	ΔT_m (°C)	γ
BCTSn	11,979	0.105	53	1.13	47	79	32	1.428

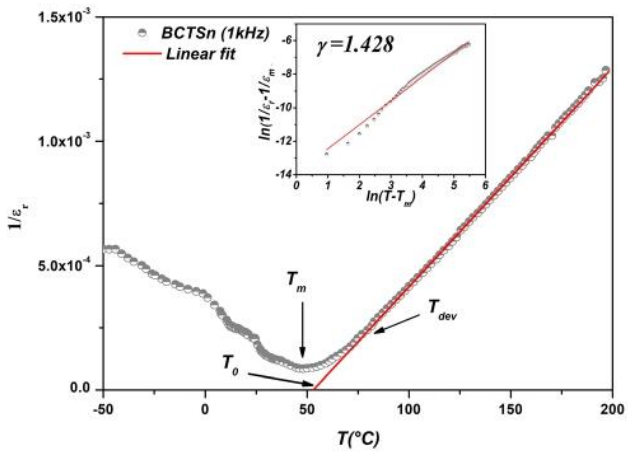

Fig. 5 Curie–Weiss fitting curves of BCTSn sample, the inset is fitted to modified, Curie–Weiss law with slope $\gamma = 1.428$

where P_{max}, E, P_r, and W_{loss} are maximum polarization, applied electric field, remnant polarization, and energy loss density. The W_{tot}, W_{rec}, and W_{loss} are calculated by measuring the internal and external areas of the polarization versus electric field (P–E) curves as mentioned in Fig. 7a.

Figure 7b shows the thermal evolution of W_{rec}, W_{tot}, and η that found to be 107.25, 208.83 mJ cm^{-3}, and 51% at room temperature, respectively. However, with temperature increasing, W_{tot} decreases and attains 118.89 mJ cm^{-3} at 393 K. W_{rec} slowly raises and remains stable at 124 mJ cm^{-3} in the temperature range of 343–373 K and then decreases. Accordingly, η upsurges to reach 91.07% at 373 K. Therefore, it is a promising material for energy storage applications. It is worth noting that, to our knowledge, no research on the energy storage properties of BCTSn has been investigated.

Table 3 presents the energy storage properties of some lead-free ceramics materials reported in the literature. Using an electric field of 20 kV cm^{-1}, Wei Ca reported a recovered energy density of 38.6 mJ cm^{-3} and storage efficiency of 33.9% in the $Ba_{0.85}Ca_{0.15}Zr_{0.1}Ti_{0.9}O_3$ ceramic (BCZT) with almost the same grain size (32 μm) as our BTSn ceramic [41]. Meanwhile, by the same synthesis method we used, Mezzourh et al. found a recovered energy density of 10.4 mJ cm^{-3} and storage efficiency of 59.9% under 8.75 kV cm^{-1} in $Ba_{0.85}Ca_{0.15}Zr_{0.1}Ti_{0.9}O_3$ ceramic [31]. Furthermore, our previous work showed that BCZT ceramic achieved at 300 K an energy storage density of 367.2 mJ cm^{-3} at 60 kV cm^{-1} [22]. It should be noted that our BCTSn ceramic exhibited higher energy storage performances than those found in the BCZT ceramics synthesized via various methods (Table 3).

4.4 Indirect electrocaloric measurements

The indirect experimental method evaluated the EC effect by exploiting $P(E,T)$ results. The reversible adiabatic temperature change ΔT was estimated from the Maxwell Eq. 7. A fifth-order polynomial fitting of the upper polarization branches was carried out at each fixed applied electric field.

$$\Delta T = -\int_{E_2}^{E_1} \frac{T}{\rho C_p}\left(\frac{\partial P}{\partial T}\right)_E \mathrm{d}T, \tag{7}$$

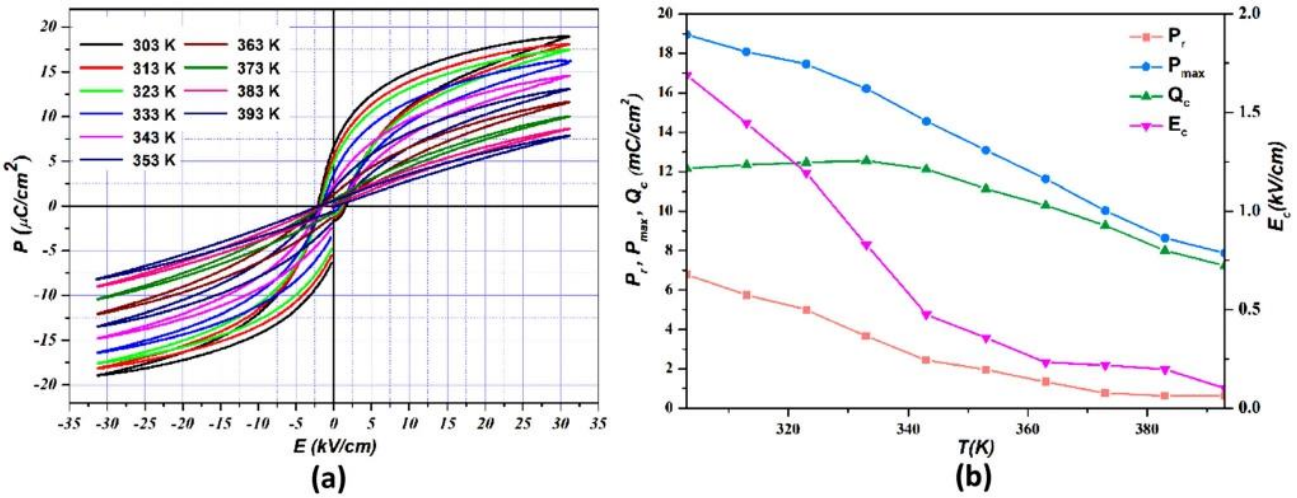

Fig. 6 (**a**) P-E hysteresis loops of the BCTSn samples. (**b**) Thermal evolution of P_r, P_{max}, Q_c, and E_c

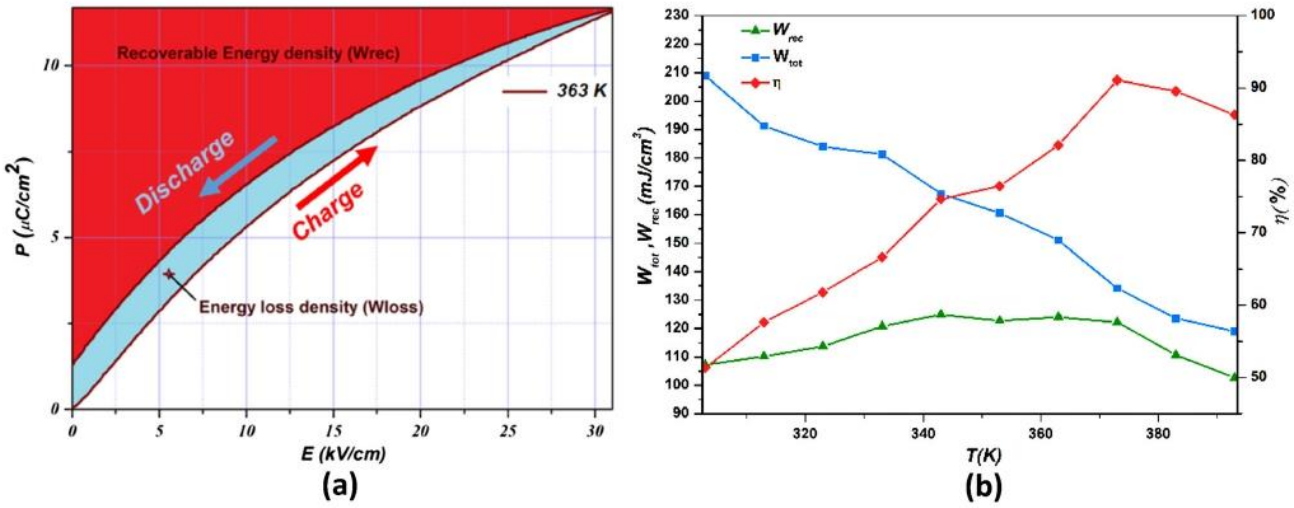

Fig. 7 **a** Schematic illustration of the calculation of W_{rec} and W_{loss} parameters. **b** Energy storage performances in the BCTSn ceramic

Table 3 Various BT-based ceramics along with their respective energy storage properties

Ceramic	Method	W_{tot} (mJ/cm^3)	W_{rec} (mJ/cm^3)	η (%)	E (kV/cm)	T (K)	References
$Ba_{0.95}Ca_{0.05}Ti_{0.89}Sn_{0.11}O_3$	Sol gel	208.83	107.25	51.36	31	303	This work
$Ba_{0.95}Ca_{0.05}Ti_{0.89}Sn_{0.11}O_3$	Sol gel	134.18	122.20	91.07	31	373	This work
$Ba_{0.95}Ca_{0.05}Ti_{0.89}Sn_{0.11}O_3$	Sol gel	167.37	124.91	74.63	31	343	This work
$BaTi_{0.89}Sn_{0.11}O_3$	Solid state	67.9	65.1	95.87	25	373	[42]
$Ba_{0.95}Ca_{0.05}Zr_{0.20}Ti_{0.80}O_3$	Solid state	569.4	410	72	120	303	[43]
$Ba_{0.85}Ca_{0.15}Zr_{0.10}Ti_{0.90}O_3$	Solid state	113.8	38.6	33.9	20	298	[41]
$Ba_{0.85}Ca_{0.15}Zr_{0.10}Ti_{0.90}O_3$	Sol gel	17.36	10.40	59.9	8.75	303	[31]
$Ba_{0.85}Ca_{0.15}Zr_{0.10}Ti_{0.90}O_3$	Hydrothermal	546.1	367.2	67.2	60	300	[22]
$Ba_{0.7}Ca_{0.3}TiO_3$	Solid state	–		58	50	303	[44]

where ρ is the density of ceramic and Cp is the specific heat of the materials estimated at 0.39 J g^{-1} K^{-1} [45].

Figure 8a, b depicts the thermal evolution of the temperature change (ΔT) and the corresponding entropy change (ΔS) at various electric fields for BCTSn ceramic. Two large peaks corresponding to the O–T and T–C phase transitions are observed at 315 K and 337 K for both ΔT and ΔS, respectively, and found to be shifted to high temperature compared with dielectric results. Such differences could result from different thermometries used in each technique. Same behavior was observed in $x(Ba_{0.7}Ca_{0.3})TiO_3$ (1–x) $Ba(Sn_{0.11}Ti_{0.89})O_3$ with (x = 0, 0.1, 0.2, and 0.3) reported by Chunlin Zhao et al. [46]. Our BCTSn sample presents a high EC response and ΔS of 0.804 K and 0.87 J kg^{-1} K^{-1}at 30 kV cm^{-1}, respectively, around the ferroelectric-paraelectric transition. The thermal evolution of electrocaloric responsivity $\zeta = \Delta T/\Delta E$ under different applied electric fields is shown in Fig. 8c, d. ζ followed the same evolution as that of ΔT and ΔS and achieved a high value of 0.268 K mm kV^{-1} at 30 kV cm^{-1}. The obtained results (ΔT = 0.54 K and ζ = 0.275 K mm kV^{-1} at 335 K under 20 kV cm^{-1}) are similar to those found in the $Ba_{0.94}Ca_{0.06}Ti_{0.89}Sn_{0.11}O_3$ composition elaborated via the solid-state method (ΔT = 0.55 K and ζ = 0.28 K mm kV^{-1} at 320 K under 20 kV cm^{-1}) by Wang et al. [19], and more comparisons with other BT-based ceramics are presented in Table 4. The outstanding EC response occurs in the BCTSn sample mainly due to the coexistence of multiple phases at this composition ($Ba_{0.95}Ca_{0.05}Ti_{0.89}Sn_{0.11}O_3$). In reality, the contribution of Ferro-Ferro transitions results in significant

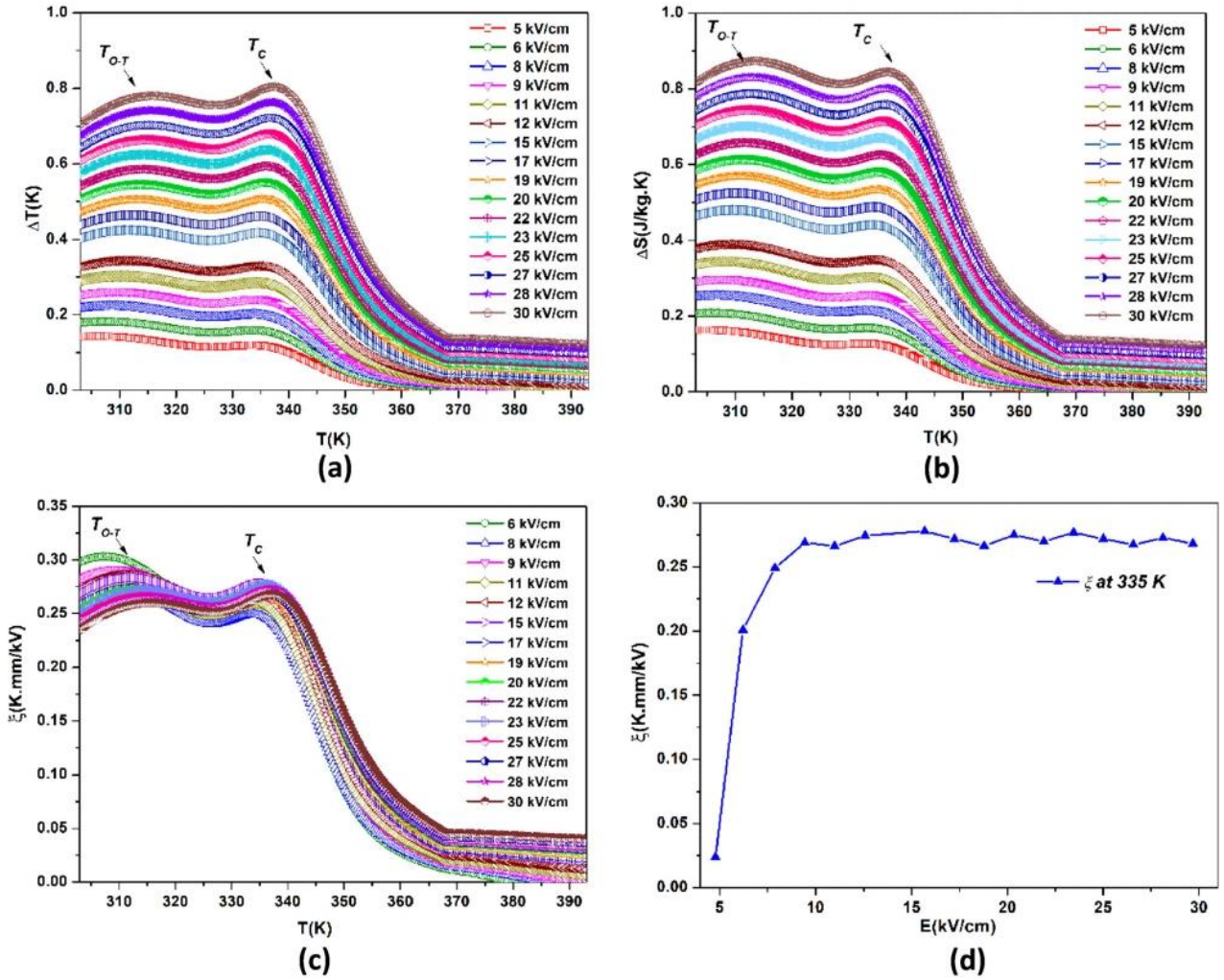

Fig. 8 Temperature dependence of **a** ΔT, **b** ΔS, and **c** ξ at different applied electric fields in the BCTSn ceramic. **d** Electric field dependence of ξ at 335 K

intrinsic ferroelectric polarization, which can improve entropy changes via the disordered/ordered polar dipoles. Thus, a high ΔT compared with other doped BT using a single Ferro-Para transition could be achieved [46–48]. Therefore, designing multiphase coexistence in EC material systems is a good way to improve their EC properties [45, 49, 50]. In addition, various factors contribute to the EC responses, such as grain size, synthesis conditions, and the applied electric field.

For industrial applications, the efficiency of ECE of BCTSn sample was examined via the coefficient of performance *COP* as defined by Eq. 8 [56]:

$$\mathrm{COP} = \frac{|Q|}{|W_{\mathrm{tot}}|} = \frac{|T\Delta S|}{|W_{\mathrm{tot}}|}, \tag{8}$$

where Q represents the isothermal heat.

The COP calculated from 303 to 393 K under 30 kV cm^{-1}is shown in Fig. 9. It increases slightly with temperature and reaches a maximum value of 8.8 at 342 K and then decreases above the transition temperature. Our COP value is larger than those found in $(1–x)K_{0.5}Na_{0.5}NbO_3$-$xLaNbO_3$ ceramic (COP = 4.16) under 50 kV cm^{-1} [56], and in $Ba_{0.85}Ca_{0.15}Zr_{0.10}Ti_{0.90}O_3$ ceramic upon 55 kV cm^{-1} (COP = 6.29 at 365 K) [22].

Table 4 Comparison of the electrocaloric properties of the BCTSn ceramics with other BT-based ceramics reported in the literature using the indirect method

Ceramic	T (K)	ΔT (K)	ΔE (kV cm^{-1})	ξ (K mm kV^{-1})	References
$Ba_{0.95}Ca_{0.05}Ti_{0.89}Sn_{0.11}O_3$	335	0.807	30	0.268	This work
$Ba_{0.95}Ca_{0.05}Ti_{0.89}Sn_{0.11}O_3$	335	0.54	20	0.275	This work
$Ba_{0.95}Ca_{0.05}Ti_{0.89}Sn_{0.11}O_3$	335	0.41	15	0.278	This work
$Ba_{0.94}Ca_{0.06}Ti_{0.90}Sn_{0.10}O_3$	320	0.55	20	0.28	[19]
$Ba_{0.94}Ca_{0.06}Ti_{0.95}Sn_{0.05}O_3$	358	0.59	20	0.30	[19]
$BaTi_{0.89}Sn_{0.11}O_3$	373	0.57	25	0.23	[42]
$0.7BaZr_{0.2}Ti_{0.8}O_3$-$0.3Ba_{0.7}Ca_{0.3}TiO_3$	328	0.3	20	0.15	[51]
$Ba_{0.95}Ca_{0.10}Ti_{0.95}Sn_{0.05}O_3$	398	0.34	12.69	0.27	[52]
$Ba_{0.80}Ca_{0.20}Zr_{0.15}Ti_{0.85}O_3$	307	0.235	22.3	0.105	[53]
$Ba_{0.30}Ca_{0.10}Zr_{0.05}Ti_{0.95}O_3$	392	0.565	30	0.188	[53]
$Ba_{0.92}Ca_{0.08}Zr_{0.05}Ti_{0.92}O_3$	320	0.38	15	0.25	[53]
$Ba_{0.65}Sr_{0.35}TiO_3$	289	0.23	10	0.23	[54]
$Ba_{0.65}Sr_{0.35}TiO_3$	296	0.42	20	0.21	[54]
$Ba_{0.65}Sr_{0.35}TiO_3$	303	2.1	90	0.23	[55]

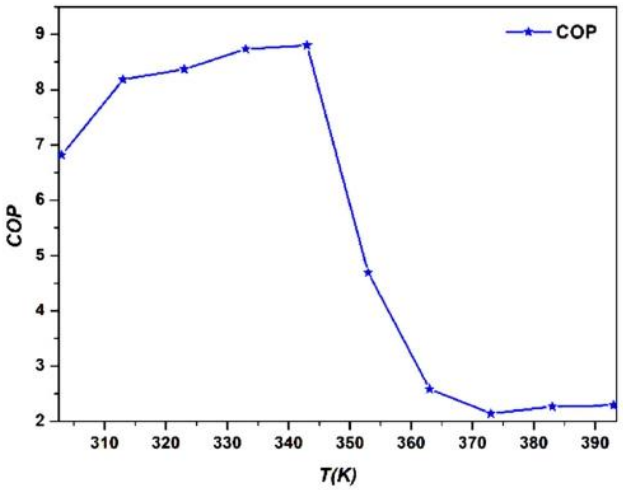

Fig. 9 Temperature dependence of the COP

5 Conclusion

In summary, the environment-friendly $Ba_{0.95}Ca_{0.05}Ti_{0.89}Sn_{0.11}O_3$ ceramic was obtained by the sol–gel method. Structure, dielectric, phase transitions, energy storage, and electrocaloric properties were investigated. As a result, BCTSn showed enhanced energy storage performances of W_{rec} = 124 mJ cm^{-3} and η = 91.07% at 373 K under an electric field of 30 kV cm^{-1}. Moreover, a significant electrocaloric response was achieved (ΔT = 0.807 K, ΔS = 0.844 J kg^{-1} K^{-1}, and ζ = 0.268 K mm kV^{-1} under 30 kV cm^{-1}), with an encouraging COP value of 8.8 at 343 K. Thus, lead-free BCTSn has a significant potential to be considered as a good candidate for environmentally friendly refrigeration and high energy storage applications.

Acknowledgements

The authors gratefully acknowledge the generous financial support of CNRST Priority Program PPR 15/2015, the European Union's Horizon 2020 research, and the Ministry of education and science of the Russian Federation Project #13.2251.21.0042.

Funding

CNRST Priority Program PPR 15/2015; The European Union's Horizon 2020 research; Ministry of Science and Higher Education of the Russian Federation, Grant Agreement No. 075-15-2021-953.

Data availability

Not applicable.

Code availability

Not applicable.

Declarations

Conflict of interest Not applicable.

Ethical approval Not applicable.

Consent to participate We confirm that all authors mentioned in the manuscript have participated in, read and approved the manuscript and have given their consent for the submission and subsequent publication of the manuscript.

Consent for publication We confirm that all the authors mentioned in the manuscript have agreed to publish this paper.

References

1. A.S. Mischenko, Giant electrocaloric effect in thin-film PbZr09.5Ti0.a05O3. Science **311**(5765), 1270–1271 (2006). https://doi.org/10.1126/science.1123811
2. B. Lu et al., Large electrocaloric effect in relaxor ferroelectric and antiferroelectric lanthanum doped lead zirconate titanate ceramics. Sci. Rep. **7**(1), 45335 (2017). https://doi.org/10.1038/srep45335
3. M. Maraj, W. Wei, B. Peng, W. Sun, Dielectric and energy storage properties of Ba(1–x)CaxZryTi(1−y)O3 (BCZT): a review. Materials **12**(21), 3641 (2019). https://doi.org/10.3390/ma12213641
4. J. Tušek, K. Engelbrecht, D. Eriksen, S. Dall'Olio, J. Tušek, N. Pryds, A regenerative elastocaloric heat pump. Nat. Energy **1**(10), 16134 (2016). https://doi.org/10.1038/nenergy.2016.134
5. R.A. Bucur, I. Badea, A.I. Bucur, S. Novaconi, Dielectric, ferroelectric and piezoelectric proprieties of GdCoO3 doped (K0.5Na0.5)NbO3. J. Alloys Compd. **630**, 43–47 (2015). https://doi.org/10.1016/j.jallcom.2015.01.030
6. L.-Q. Cheng, J.-F. Li, A review on one dimensional perovskite nanocrystals for piezoelectric applications. J. Materiomics **2**(1), 25–36 (2016). https://doi.org/10.1016/j.jmat.2016.02.003
7. H. Zaitouni et al., Direct electrocaloric, structural, dielectric, and electric properties of lead-free ferroelectric material Ba0.9Sr0.1Ti1-xSnxO3 synthesized by semi-wet method. Phys. B Condens. Matter **566**, 55–62 (2019). https://doi.org/10.1016/j.physb.2019.04.026
8. Y. Zhang et al., Effects of silica coating on the microstructures and energy storage properties of BaTiO 3 ceramics. Mater. Res. Bull. **67**, 70–76 (2015). https://doi.org/10.1016/j.materresbull.2015.01.056
9. M. Acosta et al., BaTiO3 -based piezoelectrics: Fundamentals, current status, and perspectives. Appl. Phys. Rev. **4**(4), 041305 (2017). https://doi.org/10.1063/1.4990046
10. Q. Lou et al., Ferroelectric properties of Li-doped $BaTiO_3$ ceramics. J. Am. Ceram. Soc. **101**(8), 3597–3604 (2018). https://doi.org/10.1111/jace.15480
11. D. Fu, M. Itoh, S. Koshihara, T. Kosugi, S. Tsuneyuki, Anomalous phase diagram of ferroelectric (Ba, Ca) TiO3 single crystals with giant electromechanical response. Phys. Rev. Lett. **100**(22), 227601 (2008). https://doi.org/10.1103/PhysRevLett.100.227601
12. Y. Yao et al., Large piezoelectricity and dielectric permittivity in $BaTiO_3$–$xBaSnO_3$ system: the role of phase coexisting. EPL **98**(2), 27008 (2012). https://doi.org/10.1209/0295-5075/98/27008
13. N. Horchidan et al., Multiscale study of ferroelectric–relaxor crossover in BaSnxTi1−xO3 ceramics. J. Eur. Ceram. Soc. **34**(15), 3661–3674 (2014). https://doi.org/10.1016/j.jeurceramsoc.2014.06.005
14. D. Fu, M. Itoh, Role of Ca off-centering in tuning ferroelectric phase transitions in Ba(Zr, Ti)O3 system, in *Ferroelectric materials—synthesis and characterization*. ed. by A. Peláiz-Barranco (InTech, London, 2015)
15. X. Wang, H. Yamada, C.-N. Xu, Large electrostriction near the solubility limit in BaTiO3–CaTiO3 ceramics. Appl. Phys. Lett. **86**(2), 022905 (2005). https://doi.org/10.1063/1.1850598
16. W. Liu, L. Cheng, S. Li, Prospective of (BaCa)(ZrTi)O3 lead-free piezoelectric ceramics. Curr. Comput.-Aided Drug Des. **9**(3), 179 (2019). https://doi.org/10.3390/cryst9030179
17. W. Liu, X. Ren, Large piezoelectric effect in Pb-free ceramics. Phys. Rev. Lett. **103**(25), 257602 (2009). https://doi.org/10.1103/PhysRevLett.103.257602
18. D. Damjanovic, A morphotropic phase boundary system based on polarization rotation and polarization extension. Appl. Phys. Lett. **97**(6), 062906 (2010). https://doi.org/10.1063/1.3479479
19. X. Wang et al., Giant electrocaloric effect in lead-free Ba0.94 Ca0.06 Ti1−x Snx O3 ceramics with tunable curie temperature. Appl. Phys. Lett. **107**, 252905 (2015). https://doi.org/10.1063/1.4938134
20. L.-F. Zhu et al., Phase transition and high piezoelectricity in (Ba, Ca)(Ti1−x Snx)O3 lead-free ceramics. Appl. Phys. Lett. **103**(7), 072905 (2013). https://doi.org/10.1063/1.4818732
21. S. Merselmiz et al., Thermal-stability of the enhanced piezoelectric, energy storage and electrocaloric properties of a lead-free BCZT ceramic. RSC Adv. **11**(16), 9459–9468 (2021). https://doi.org/10.1039/D0RA09707A
22. Z. Hanani et al., Thermally-stable high energy storage performances and large electrocaloric effect over a broad

temperature span in lead-free BCZT ceramic. RSC Adv. **10**(51), 30746–30755 (2020). https://doi.org/10.1039/D0RA06116F

23. P. Kantha et al., Effect of sintering method on the microstructure and dielectric properties of lead-free BCZT ceramics. Appl. Mech. Mater. **866**, 263–266 (2017)
24. V.S. Puli et al., Structure, dielectric, ferroelectric, and energy density properties of (1–x)BZT–xBCT ceramic capacitors for energy storage applications. J. Mater. Sci. **48**(5), 2151–2157 (2013). https://doi.org/10.1007/s10853-012-6990-1
25. Z. Wang et al., Synthesis, structure, dielectric, piezoelectric, and energy storage performance of (Ba0.85Ca0.15)(-Ti0.9Zr0.1)O3 ceramics prepared by different methods. J. Mater. Sci. Mater. Electron. **27**(5), 5047–5058 (2016). https://doi.org/10.1007/s10854-016-4392-x
26. R. Pramanik, M.K. Sahukar, Y. Mohan, B. Praveenkumar, S.R. Sangawar, A. Arockiarajan, Effect of grain size on piezoelectric, ferroelectric and dielectric properties of PMN-PT ceramics. Ceram. Int. **45**(5), 5731–5742 (2019). https://doi.org/10.1016/j.ceramint.2018.12.039
27. S. Ben Moumen et al., Structural, dielectric and magnetic studies of (0–3) type multiferroic (1–x) BaTi0.8Sn0.2O3–(x) La0.5Ca0.5MnO3 ($0 \leq x \leq 1$) composite ceramics. J. Mater. Sci. Mater. Electron. **31**(21), 19343–19354 (2020). https://doi.org/10.1007/s10854-020-04468-3
28. Z. Cai, X. Wang, W. Hong, B. Luo, Q. Zhao, L. Li, Grain-size–dependent dielectric properties in nanograin ferroelectrics. J. Am. Ceram. Soc. **101**(12), 5487–5496 (2018). https://doi.org/10.1111/jace.15803
29. S. Kumari, A. Kumar, V. Kumar, *Thermal and structural characterization of Bi and Cu Co-doped BCZT* (AIP Publishing LLC, NY, 2020), p. 030012
30. P. Mishra, P. Kumar, Effect of sintering temperature on dielectric, piezoelectric and ferroelectric properties of BZT–BCT 50/50 ceramics. J. Alloys Compd. **545**, 210–215 (2012). https://doi.org/10.1016/j.jallcom.2012.08.017
31. H. Mezzourh et al., Enhancing the dielectric, electrocaloric and energy storage properties of lead-free Ba0.85Ca0.15Zr0.1Ti0.9O3 ceramics prepared via sol-gel process. Phys. B Condens. Matter **603**, 412760 (2021). https://doi.org/10.1016/j.physb.2020.412760
32. M. Chen et al., Enhanced piezoelectricity in broad composition range and the temperature dependence research of (Ba1−xCax)(Ti0.95Sn0.05)O3 piezoceramics. Phys. B Condens. Matter **433**, 43–47 (2014). https://doi.org/10.1016/j.physb.2013.10.014
33. S. Belkhadir et al., Impedance spectroscopy analysis of the diffuse phase transition in lead-free (Ba0,85Ca0,15)(Zr0.1-Ti0.9)O3 ceramic elaborated by sol-gel method. Superlattices Microstruct. **127**, 71–79 (2019). https://doi.org/10.1016/j.spmi.2018.03.009
34. B. Asbani et al., Structural, dielectric and electrocaloric properties in lead-free Zr-doped Ba0.8Ca0.2TiO3 solid solution. Solid State Commun. **237–238**, 49–54 (2016). https://doi.org/10.1016/j.ssc.2016.04.001
35. L. Zhao, B.-P. Zhang, P.-F. Zhou, L.-F. Zhu, J.-F. Li, Effect of Li2O addition on sintering and piezoelectric properties of (Ba, Ca)(Ti, Sn)O3 lead-free piezoceramics. J. Eur. Ceram. Soc. **35**(2), 533–540 (2015). https://doi.org/10.1016/j.jeurceramsoc.2014.08.042
36. Z. Zhao et al., Grain-size effects on the ferroelectric behavior of dense nanocrystalline BaTiO 3 ceramics. Phys. Rev. B **70**(2), 024107 (2004). https://doi.org/10.1103/PhysRevB.70.024107
37. I.A. Santos, J.A. Eiras, Phenomenological description of the diffuse phase transition in ferroelectrics. J. Phys. Condens. Matter **13**(50), 11733–11740 (2001). https://doi.org/10.1088/0953-8984/13/50/333
38. S. Hunpratub, S. Maensiri, P. Chindaprasirt, Synthesis and characterization of Ba0.85Ca0.15Ti0.9Zr0.1O3 ceramics by hydrothermal method. Ceram. Int. **40**(8), 13025–13031 (2014). https://doi.org/10.1016/j.ceramint.2014.04.166
39. V.S. Puli et al., Observation of large enhancement in energy-storage properties of lead-free polycrystalline 0.5BaZr0.2 Ti0.8 O3–0.5Ba0.7 Ca0.3 TiO3 ferroelectric thin films. J. Phys. Appl. Phys. **52**(25), 255304 (2019). https://doi.org/10.1088/1361-6463/ab161a
40. L.-F. Zhu, B.-P. Zhang, L. Zhao, J.-F. Li, High piezoelectricity of $BaTiO_3$–$CaTiO_3$–$BaSnO_3$ lead-free ceramics. J. Mater. Chem. C **2**(24), 4764–4771 (2014). https://doi.org/10.1039/C4TC00155A
41. W. Cai et al., Synergistic effect of grain size and phase boundary on energy storage performance and electric properties of BCZT ceramics. J. Mater. Sci. Mater. Electron. **31**(12), 9167–9175 (2020). https://doi.org/10.1007/s10854-020-03446-z
42. S. Merselmiz et al., High energy storage efficiency and large electrocaloric effect in lead-free BaTi0.89Sn0.11O3 ceramic. Ceram. Int. **46**(15), 23867–23876 (2020). https://doi.org/10.1016/j.ceramint.2020.06.163
43. D. Zhan, Q. Xu, D.-P. Huang, H.-X. Liu, W. Chen, F. Zhang, Contributions of intrinsic and extrinsic polarization species to energy storage properties of Ba 0.95 Ca 0.05 Zr 0.2 Ti 0.8 O 3 ceramics. J. Phys. Chem. Solids **114**, 220–227 (2018). https://doi.org/10.1016/j.jpcs.2017.10.038
44. D. Fu, M. Itoh, S. Koshihara, Crystal growth and piezoelectricity of BaTiO3–CaTiO3 solid solution. Appl. Phys. Lett. **93**(1), 012904 (2008). https://doi.org/10.1063/1.2956400

45. Z. Luo et al., Enhanced electrocaloric effect in lead-free $BaTi_{1-x}Sn_xO_3$ ceramics near room temperature. Appl. Phys. Lett. **105**(10), 102904 (2014). https://doi.org/10.1063/1.4895615
46. C. Zhao, J. Yang, Y. Huang, X. Hao, J. Wu, Broad-temperature-span and large electrocaloric effect in lead-free ceramics utilizing successive and metastable phase transitions. J. Mater. Chem. A **7**(44), 25526–25536 (2019). https://doi.org/10.1039/C9TA10164K
47. M. Sanlialp, C. Molin, V.V. Shvartsman, S. Gebhardt, D.C. Lupascu, Modified differential scanning calorimeter for direct electrocaloric measurements. IEEE Trans. Ultrason. Ferroelectr. Freq. Control **63**(10), 1690–1696 (2016). https://doi.org/10.1109/TUFFC.2016.2592542
48. A. Pramanick et al., Stabilization of polar nanoregions in Pb-free ferroelectrics. Phys. Rev. Lett. **120**(20), 207603 (2018). https://doi.org/10.1103/PhysRevLett.120.207603
49. M. Sanlialp et al., Direct measurement of electrocaloric effect in lead-free $Ba(Sn_xTi_{1-x})O_3$ ceramics. Appl. Phys. Lett. **111**(17), 173903 (2017). https://doi.org/10.1063/1.5001196
50. Y. Liu, J.F. Scott, B. Dkhil, Some strategies for improving caloric responses with ferroelectrics. APL Mater. **4**(6), 064109 (2016). https://doi.org/10.1063/1.4954056
51. Y. Bai, X. Han, L. Qiao, Optimized electrocaloric refrigeration capacity in lead-free (1–x)BaZr0.2Ti0.8 O3–xBa0.7-Ca0.3TiO3 ceramics. Appl. Phys. Lett. **102**(25), 254 (2013). https://doi.org/10.1063/1.4810916
52. S.K. Upadhyay, I. Fatima, V.R. Reddy, Study of electrocaloric effect in Ca and Sn co-doped $BaTiO_3$ ceramics. Mater. Res. Express **4**(4), 046303 (2017). https://doi.org/10.1088/2053-1591/aa6694
53. M. Abdessalem, I. Kriaa, A. Aydi, N. Abdelmoula, Large electrocaloric effect in lead-free Ba1-xCaxTi1-yZryO3 ceramics under strong electric field at room-temperature. Ceram. Int. **44**(12), 13595–13601 (2018). https://doi.org/10.1016/j.ceramint.2018.04.194
54. B. Li, W.J. Ren, X.W. Wang et al., Combined effects of diffuse phase transition and microstructure on the electrocaloric effect in Ba1−x SrxTiO3 ceramics. Appl. Phys. Lett. **103**(16), 162902 (2013). https://doi.org/10.1063/1.4825266
55. X.Q. Liu, T.T. Chen, Y.J. Wu, X.M. Chen, Enhanced electrocaloric effects in spark plasma-sintered $Ba_{0.65}Sr_{0.35}TiO_3$–based ceramics at room temperature. J. Am. Ceram. Soc. **96**(4), 1021–1023 (2013). https://doi.org/10.1111/jace.12219
56. R. Kumar, A. Kumar, S. Singh, Large electrocaloric response and energy storage study in environmentally friendly (1–x)K0.5Na0.5NbO3–xLaNbO3 nanocrystalline ceramics. Sustain. Energy Fuels **2**(12), 2698–2704 (2018). https://doi.org/10.1039/C8SE00276B

Journal of Magnetism and Magnetic Materials 563 (2022) 169925

Contents lists available at ScienceDirect

Journal of Magnetism and Magnetic Materials

journal homepage: www.elsevier.com/locate/jmmm

Enhanced Relative cooling Power and large inverse magnetocaloric effect of cobalt ferrite nanoparticles synthesized by auto-combustion method

Youness Hadouch [a,b,*], Daoud Mezzane [a,b], M'barek Amjoud [a], Lahoucine Hajji [a], Yaovi Gagou [b], Zdravko Kutnjak [c], Valentin Laguta [d,e], Yakov Kopelevich [f], Mimoun El Marssi [b]

[a] Laboratory of Innovative Materials, Energy and Sustainable Development (IMED), Cadi- Ayyad University, Faculty of Sciences and Technology, BP 549 Marrakech, Morocco
[b] Laboratory of Physics of Condensed Matter (LPMC), University of Picardie Jules Verne, Scientific Pole, 33 rue Saint-Leu, 80039 Amiens Cedex 1, France
[c] Jozef Stefan Institute, Jamova Cesta 39, 1000 Ljubljana, Slovenia
[d] Institute of Physics AS CR, Cukrovarnicka 10, 162 53 Prague, Czech Republic
[e] Institute for Problems of Materials Science, National Ac. of Science, Krjijanovskogo 3, Kyiv 03142, Ukraine
[f] Universidade Estadual de Campinas-UNICAMP, Instituto de Física "GlebWataghin", R. Sergio Buarque de Holanda 777, 13083-859 Campinas, Brazil

ARTICLE INFO

Keywords:
Cobalt ferrite
Sol–gel self-combustion
Nanoparticles
First order
Magnetocaloric effect
Relative Cooling Power

ABSTRACT

This work focuses on the microstructure, magnetic properties and magnetocaloric effect of $CoFe_2O_4$ (CFO) nanoparticles elaborated by the sol–gel auto combustion method. The XRD investigation indicates that CFO is crystallized in a cubic spinel structure with the *Fd* $\bar{3}$ *m* space group and the SEM micrograph shows fine quasi-spherical nanoparticles with an average grain size of 160 nm. The temperature dependence of the Raman spectra reveals the ferromagnetic to paramagnetic conversion started from 723 K. The magnetization temperature dependence reveals the Curie temperature at $T_C = 785$ K. Large value of magnetocaloric temperature change of $\Delta T = 11.2$ K with a high RCP of 687.56 J Kg^{-1} were measured indirectly via the Maxwell approach making our CFO nanopowder suitable candidate for both environmentally friendly magnetic refrigeration and medical applications at ambient temperature.

1. Introduction

The magnetocaloric effect (MCE) has recently attracted much interest from researchers for its use in various industrial applications. It was discovered by German physicist Emil Warburg in 1881 [1]. Scientists are now devoting many efforts to ecological and friendly magnetic materials used in heating and cooling technologies [2,3]. The MCE is an intrinsic property of magnetocaloric materials in which a reversible and adiabatic temperature change is caused when they are exposed to a varying magnetic field [4]. It can be evaluated as an isothermal entropy change ΔS and/or as an adiabatic temperature change ΔT [4].

Several classes of magnetic materials displayed a magnetocaloric effect in the literature, including perovskite manganites, manganite alloys, and spinel ferrites. The magnetocaloric materials can be classified according to the order of the phase transition; first- (FOPT) or second-order (SOPT) type phase transitions. Usually, the FOPT materials exhibit large magnetic entropy and adiabatic temperature changes [5]. Trung et al. investigated the effect of phase transition order on ΔS and ΔT for $Mn_{1-x}Cr_xCoGe$ alloys and demonstrated that the first order enhances the magnetocaloric effect [6].

Recently, the perovskite manganite $La_{0.5}Ca_{0.5-x}\square_xMnO_3$(LCMO) exhibiting an interesting MCE, with a ΔT of 5.6 K, is reported [7]. Meanwhile, several works have shown that spinel ferrites with a second-order magnetic transition are effective instruments for magnetic refrigeration (MR) applications. For example, Oumezzine et al. observed a significant magnetic entropy change ΔS_M of 1.61 J kg^{-1} K^{-1} at 50 kOe in $Zn_{0.6}Cu_{0.4}Fe_2O_4$ with an RCP of 289 J kg^{-1} [8]. Moreover, $Ni_{0.7}Zn_{0.3}Fe_2O_4$ showed a moderate ($-\Delta S_M$) of 1.39 J kg^{-1} K^{-1} at 25 kOe with a high RCP value of 68 J kg^{-1} as reported by Anwar et al. [9].

Among spinel ferrites, cobalt ferrite ($CoFe_2O_4$) has gained great scientific interest owing to its moderate saturation magnetization, high coercivity, good magnetostrictive properties, high Curie temperature (T_C = 520 °C), electrical insulation with low eddy current loss, and chemical stability [10–12]. Benefiting from these properties, $CoFe_2O_4$

* Corresponding author at: Laboratory of Innovative Materials, Energy and Sustainable Development (IMED), Cadi- Ayyad University, Faculty of Sciences and Technology, BP 549 Marrakech, Morocco.
E-mail address: youness.hadouch@etud.u-picardie.fr (Y. Hadouch).

https://doi.org/10.1016/j.jmmm.2022.169925
Received 29 March 2022; Received in revised form 5 July 2022; Accepted 4 September 2022
Available online 9 September 2022
0304-8853/

(CFO) find a variety of applications in several domains such as data storage, sensors, microwave devices, high-frequency applications, catalysis, magnetic refrigeration and the biomedical field [10,13–16]. In refrigeration applications, CFO intended to replace carbon technology to limit global warming and reduce greenhouse gas emissions [17,18]. For biomedical applications, CFO nanoparticles are used in cancer therapy by hyperthermia (cancer treatment). CFO nanoparticles were inserted into tumor tissue and heated after exposure to an external alternating magnetic field [19,20].

Crystallographically, CFO has an inverse spinel structure where octahedral sites are occupied by Co^{2+} cations, while Fe^{3+} cations are equally shared between tetrahedral and octahedral sites [21]. It is known that the magnetic properties are sensitive to the distribution of these cations, which is influenced by the preparation method of CFO nanoparticles [22,23]. Furthermore, ferrite properties depend significantly on grain size and microstructure, which can also be monitored by the synthesis route [24,25]. For example, the saturation of magnetization (M_s) of $NiFe_2O_4$ was increased with increasing ferrite grain size, as reported by Li et al. [25]. Furthermore, several studies reported that the particle size tuned the MCE of magnetic nanoparticles [26,27]. For example, Yin et al. reported that the ΔS_M in $HoCrO_3$ decreases (ΔS_M = 8.73, 7.22, 7.77, and 6.70 J kg^{-1} K^{-1}) and the refrigerant capacity (RC = 388, 354, 330, and 310 J kg^{-1}) for the 60 nm, 190 nm, 320 nm, and 425 nm size particles, respectively. Accordingly, the synthesis methods are crucial in controlling the magnetic properties of ferrites powders and their applications. CFO is typically elaborated using various methods, including co-precipitation sol–gel, ceramic techniques and auto combustion utilizing different fuels [28–30]. Researchers have recently focused on coupling sol–gel and auto combustion method, as it produced ferrite samples with high chemical homogeneity, good purity, and high crystallization. In addition, it demands basic equipment, a simple preparation process, a short processing time and low external energy consumption [31,32].

It is worth noting that the magnetic characteristics of most CFO have been examined over a wide range of temperatures, from room temperature to as low as 4 K. However, the majority of ferrite's applications are suitable at room temperature or above, for example, medical application in which magnetocaloric properties can induce local hyperthermia at cancer sites [33]. Very few reports describe the MCE properties of cobalt ferrite at high temperatures. Herein, we present an investigation at the high-temperature range from 300 K to 900 K on structural, magnetic and magnetocaloric properties of $CoFe_2O_4$ elaborated by combining sol–gel auto combustion using ammonia as a neutralizer agent, ethylene glycol as polymerizing agent and acetic acid as fuel.

2. Chemical synthesis

$CoFe_2O_4$ nanoparticles were prepared using the sol–gel self-combustion method: stoichiometric amounts of Cobalt Nitrate Co $(NO_3)_3{\cdot}6H_2O$ and Ferric Nitrate $Fe(NO_3)_3{\cdot}9H_2O$ were dissolved in 2-Methoxyethonal under constant magnetic stirring for 30 mn. Then ammonia was slowly dropped into the solution to adjust the *pH* to 10. Next, a 1:1 M ratio of acetic acid (fuel agent) and ethylene glycol (polymerizing agent) mixture was separately prepared and added to the solution. After four hours of continuous stirring at 90 °C, the brown solution was completely turned into a dark, puffy, porous gel. Then, the gel was transferred to a furnace, and by heating at 120 °C, it simultaneously burnt in self-propagating combustion until it was completely transformed into fine powder. Finally, the powder was annealed at 700 °C for two hours using a controlled heating rate of 2 °C/min under an air atmosphere.

3. Materials and methods

The XRD patterns of CFO ceramic were obtained by X-ray diffraction using the Panalytical X-Pert Pro with Cu-Kα radiation (λ = 1.54059 Å) at room temperature. The grain morphology of the ceramic was examined using a scanning electron microscope (SEM, Philips XL30), having an attachment for energy-dispersive X-ray spectroscopy (EDS). The Raman spectra were recorded using a micro-Raman Renishaw spectrometer equipped with a CCD detector. Magnetic properties were performed using a Physical Property Measurement System (PPMS-DynaCool) Quantum Design apparatus in the 300–900 K temperature range under a magnetic field range of 0–25 kOe. The magnetization was measured using the vibrating sample magnetometer (VSM) method integrated into the system. The magnetocaloric study was carried out by the indirect method using the recorded $M-H$ hysteresis loops.

4. Results and discussion

4.1. Morphological and structural analysis

The SEM image of the as-prepared $CoFe_2O_4$ nanoparticles shows agglomerates of regular near-spherical particles with average grain sizes of 160 nm, estimated by ImageJ® software as shown in Fig. 1. The large particle sizes are due to the high heating temperatures released during combustion [11]. It should be noted that the magnetic properties of cobalt ferrites are very sensitive to grain sizes.

EDX analysis was performed to verify the elemental composition, and the distribution of elements is shown in Fig. 2. The presence of metal elements Co, Fe and O is revealed by qualitative analysis (the presence of carbon is due to the metallization process). The atomic and weight percentages of the elements present in the sample are shown in the inset, and the obtained atomic percentages agree well with the expected ratios. The oxygen content is found to be 3.9683 atoms per cell.

Fig. 3 shows the room temperature XRD spectra of the CFO powder calcined at 700 °C for 2 h. The obtained diffraction peaks are well-defined, proving that our sample is well crystallized. All the diffraction peaks can be indexed to the cubic crystal structure of cobalt ferrite (JCPDS card no. 22–1086) [34], and no peak related to impurities was detected. The experimental XRD pattern of CFO was refined using the Rietveld refinement program via FullProf software and indexed by a cubic spinel structure with the space group ($Fd\bar{3}m$), and the output data proved an excellent fit between the calculated and observed diffractograms. The "a'' lattice parameter of CFO is found to be 8.4013 Å. According to Scherrer's equation [14,35,36], the average crystallite size (D) was estimated from the full width at half-maximum of the

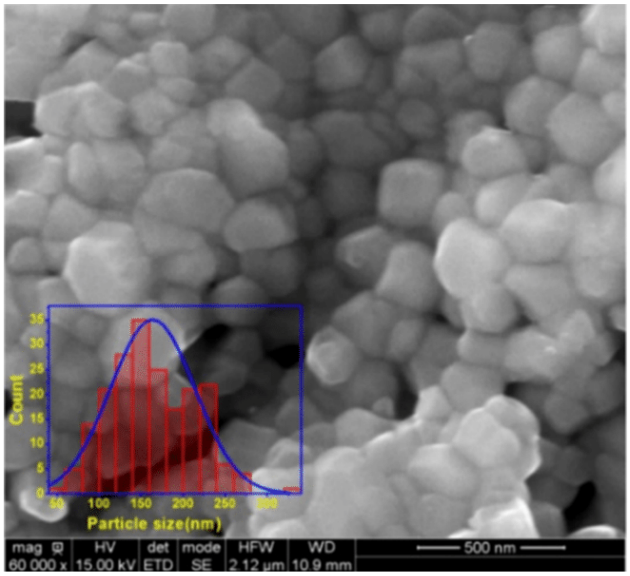

Fig. 1. SEM micrograph of CFO nanoparticles, the inset to the image shows the particle size distribution.

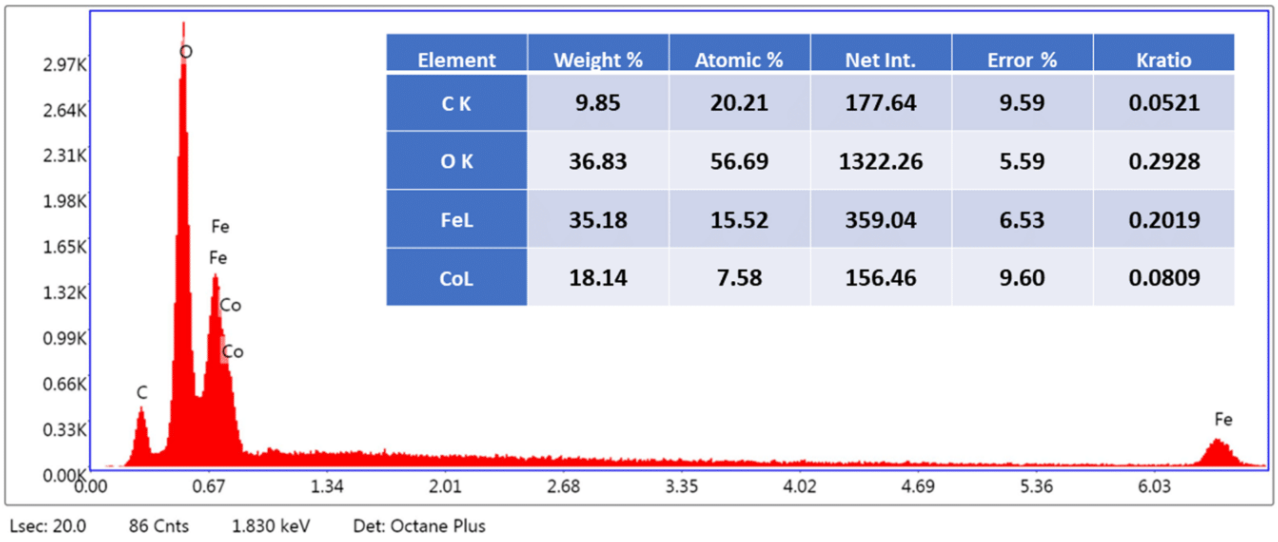

Element	Weight %	Atomic %	Net Int.	Error %	Kratio
C K	9.85	20.21	177.64	9.59	0.0521
O K	36.83	56.69	1322.26	5.59	0.2928
FeL	35.18	15.52	359.04	6.53	0.2019
CoL	18.14	7.58	156.46	9.60	0.0809

Fig. 2. EDS spectrum of CFO nanoparticles.

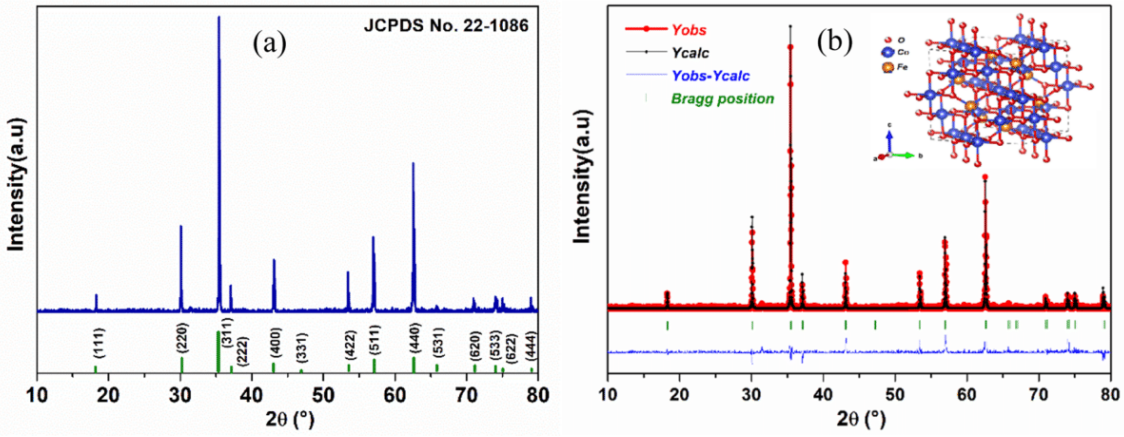

Fig. 3. **a** X-ray diffraction patterns of CFO powder; **b** Rietveld fitted X-ray diffraction patterns of CFO nanoparticles.

conspicuous (3 1 1) reflection and found to be 57.6 nm and the grain size of 160 nm determined using ImageJ® software. Table 1 lists the refined structural parameters of CFO powder.

Raman spectra were collected in the temperature range of 303–823 K to study the temperature effect on the spinel structure of the CFO, as shown in Fig. 4. The group theory analysis predicts the following ten optical phonons for the spinel structure: $5T_{1u} + A_{1g} + E_g + 3T_{2g}$. The five T_{1u}modesare IR active, while the other modes ($A_{1g} + E_g + 3T_{2g}$) are Raman active assigned to the motion of oxygen ions, A-site and B-site in the spinel structure [37]. Moreover, the A_{1g} mode is assigned to symmetric stretching of the oxygen anions along the Fe-O (Co-O) in the tetrahedral sub-lattice. E_g and first $T_{2g}(1)$ modes belong to the symmetric and asymmetric bending of the oxygen anions. The second $T_{2g}(2)$ mode arises due to asymmetric stretching of the Fe-O (Co-O) bonds, and the third $T_{2g}(3)$ corresponds to the translational shift of the entire FeO_4 tetrahedron.

At room temperature, A_{1g} (1) and A_{1g} (2) modes located at frequencies 616 and 693 cm^{-1} are assigned to the stretching vibrations of the Fe–O and Co–O bonds in tetrahedral sites, respectively. At the frequencies below 600 cm^{-1}, the Raman modes (~208, ~303, ~468, and ~ 568 cm^{-1}) correspond to E_g and T_{2g} revealing the vibration of the spinel structure [38].

By heating, the A_{1g} (1) and A_{1g} (2) become softened and broad, resulting in the thermal effect on cation distribution in ferrite systems. In addition, the $A_{1g}(1)$ mode shifts to lower frequencies due to the migration of cations in a tetrahedral structure. At the same time, E_g and T_{2g} (3) phonon modes show the blue-shifting tendency associated with the cation migration in octahedral sites. In reality, the Fe^{3+} cations move from O-site to T-site, while the Co^{2+} cations move in the opposite direction from T-site to O-site. This dislocation of cations causes a disorder

Table 1
Refined structural parameters for $CoFe_2O_{4-\delta}$ nanoparticles at room temperature.

Structure Spinel	Unit cell parameters			Atom fraction			Molecular formula F	Average crystallite size(nm) By XRD	Average grain size(nm) by SEM
	a(Å)	Angle (°)	V(Å^3)	Co	Fe	O			
$Fd\,\bar{3}\,m$	8.4013	$\alpha = \beta = \gamma = 90$	592.9792	0.1446	0.2892	0.5661	$CoFe_2O_{3.9627}$	57.6	160

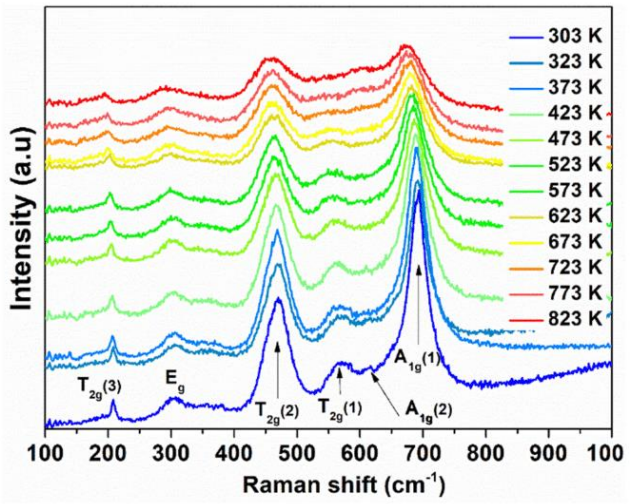

Fig. 4. Raman spectra of the CFO nanoparticles for several selected temperatures ranging from 303 K to 823 K.

in the CFO structure that makes an inequality between these two valances.

This phenomenon increases with the increase of the temperature leading to disruption of the order of the cations. Thus, the magnetic properties of the CFO might be destroyed, giving rise to the paramagnetic phase at high temperatures [39,40].

5. Magnetic properties

5.1. Temperature dependence of magnetic properties

Fig. 5 (a) plots the temperature dependences of ZFC (blue curve) and FC (red curve) magnetization curves obtained in CFO powder under a magnetic field of 0.4 Oe. At 300 K, the magnetization was 8.16 emu g^{-1}, decreasing with increasing temperature. At around 800 K, the magnetization drops sharply to zero, which corresponds to the phase transition from ordered (FM) to disordered (PM) state, as reported by Franco and Silva [33]. This discontinuous magnetization jump reveals that our CFO powder exhibits a first-order FM-PM phase transition at Curie temperature T_C. The Tc was determined from the derivative dM/dT(brown curve) and found to be 785 K Fig. 5 (a).

The Tc value is confirmed using the Curie law (equation (1)) by fitting the thermal variation of the inverse of the magnetic susceptibility ($\chi^{-1} = \frac{H}{M}$) plotted at 400 Oe:

$$\chi = \frac{C}{T - \theta_p} \tag{1}$$

C denotes the Curie constant, while θ_p represents the Weiss temperature [41].

From the slope of the linear fit plot of $\chi(T)$ in the paramagnetic phase, the C is estimated at 0.30 K emu g^{-1}. The corresponding θ_p of 789.95 K is closer to the Tc (785 K), as shown in Fig. 5 (b).

Fig. 6 displays the CFO nanoparticles' hysteresis loops (M−H), measured under an applied magnetic field of 25 kOe and recorded at different temperatures (300 K − 900 K). It should be noted that the magnetic measurements were corrected to account for the demagnetization field, and the internal field is calculated using the following expression [42]:

$$H = H_{app} - N.M,$$

where H_{app} denotes the external magnetic field, M denotes magnetization, and N is the demagnetization tensor that depends on particles' geometry.

In our case, a powder of randomly packed spherical particles could be a good approximation, and the demagnetization factor may be expressed as [43]:

$$N = \frac{1}{3} + f\left(D_z - \frac{1}{3}\right),$$

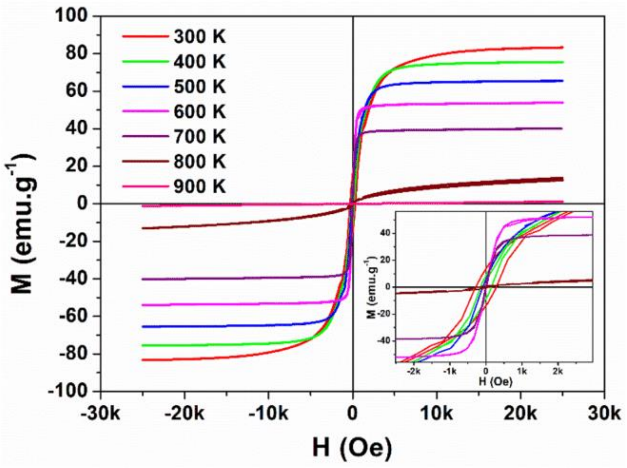

Fig. 6. Isothermal magnetization curves of CFO at different temperatures under an applied magnetic field of 25 kOe.

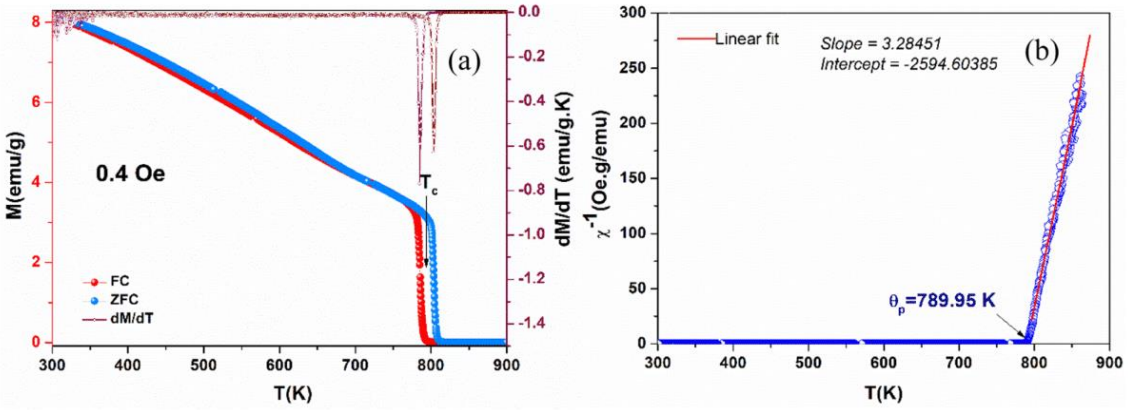

Fig. 5. The FC-ZFC curves (a) and reciprocal magnetic susceptibility χ^{-1} (T) (b), for the CFO sample measured at an applied magnetic field of 0.4 Oe.

where D_z denotes the demagnetization factor of the powder sample's geometrical shape, and f denotes the relative density. For spherical shape, the demagnetization factor is equal to 1/3 [43]. The corrections have been made to the M versus H measurements for each temperature, and it appears that there is only a 0.0002 Oe difference between the internal H and external H_{app} magnetic applied field.

For T < Tc zone, a saturated hysteresis loop is observed, which describes CFO's ferro/ferrimagnetic character. The saturation of magnetization is attained even at 20 kOe. At room temperature (300 K), the CFO sample exhibits a saturated magnetization M_s of 83 emu/g. Magnetization decreases as the temperature increases and disappears completely when T > Tc, indicating the appearance of paramagnetic character [7,41]. This decrease is accompanied by a decrease in M_s, remnant magnetization (M_r) and coercive field (H_c), being equal to zero at close to T_c. Nevertheless, this is not a hint of superparamagnetism because the blocking temperature T_b for CFO particles of 160 nm is much higher than T_c ($T_b = KV/25k_B$, where K, V, and k_B are anisotropy constants, particle volume, and Boltzmann constants, respectively) [33]. The details of the hysteresis curve for various temperatures are shown in the inset. The high M_s (83 emu g^{-1}) observed at low H_c (284 Oe) reveals the soft magnetic nature of CFO. This could be useful for designing multifunctional devices to change the magnetization with a small external magnetic field [38]. The high obtained M_s is due to the large particle sizes (160 nm) compared with CFO nanoparticles (35 nm) elaborated by hydrothermal that shows a M_s of 68.5 emu g^{-1} [11]. Indeed, the larger grains tend to consist of more magnetic domains. However, domain wall movement magnetization requires less energy than domain rotation magnetization. Therefore, the magnetization or demagnetization of the material is easy by the domain wall movement with large grain size. As a result, a large grain sample is predicted to have low H_c and high M_s, as reported by [25]. Subsequently, our sample shows improved results than those reported by other works using different synthesis methods of CFO, as summarized in Table 2. Specifically, CFO elaborated by sol–gel auto combustion shows a M_s of 69.59 emu g^{-1} under a magnetic field of 10 kOe with a high H_c of 647 Oe [44]. On the other hand, using the solid-state method, Rajath Varma obtained a M_s value of 82 emu g^{-1} under a high applied field of 60 kOe [45]. As a result, the different values of M_s and H_c of all reported materials (Table 2) demonstrate the synthesis method's effect or the microstructure of CFO on their magnetic properties.

Table 2
Comparison of magnetic properties Ms and Hc at 300 K of $CoFe_2O_4$ particles obtained by various synthesis processes.

Synthesis method	Particle size (nm)	Magnetic field (kOe)	M_s (emu g^{-1})	H_c (Oe)	References
Sol-gel auto combustion	160	25	83	284	This work
sol–gel auto combustion	25	10	69.59	647	[44]
Wet chemical route	21	15	68	1250	[28]
Co-precipitation	34–40	15	74	650	[11]
Hydrothermal	Rods (length: 139.63 / width: 35.23)	15	68.5	1250	[11]
Solid state	290	60	82	304	[45]
Sol–gel	36.5	30	66.7	1163.9	[14]
Polymer complex	32	60	67	1625	[45]

6. Magnetocaloric properties

In order to investigate the magnetocaloric effect of our material, the indirect method based on M(H) measurement was performed. The magnetic entropy changes ΔS and the adiabatic temperature changes ΔT versus the magnetic field (H) are given by the Maxwell Eqs. (2) and (3). Using the upper branches of all the recorded M(H) curves at each measurement temperature, the polynomial fits allow us to determine the variation of magnetization as a function of temperature ($\frac{\partial M}{\partial T}$) under various applied magnetic fields between 5 and 24 kOe. The resulting curves of ΔS and ΔT are plotted in Fig. 7 (a) and (b), respectively.

$$\Delta S(T,H) = \int_0^H \left(\frac{\partial M}{\partial T}\right)_H dH \tag{2}$$

$$\Delta T(T,H) = \int_{H1}^{H2} \frac{T}{C_P}\left(\frac{\partial M}{\partial T}\right)_H dH \tag{3}$$

Both curves reveal two magnetic anomalies. The anomaly that occurred at 700 K corresponds to the FM-PM phase transition. However, the first anomaly observed at 600 K on the ΔT curves and at 450 K on the ΔS curves can be attributed to lattice distortion and domain wall dynamics or pinning of domains. This process is activated by temperature, leading to the maximal reorientation at Curie temperature. Moreover, we can also observe on the M(H) measurement (Fig. 5) the vertical jump straight up of the magnetization M as shown on the ΔT reordered curve at 600 K. Maximal entropy of 6.2 $J.kg^{-1}K^{-1}$ is observed at the FM-PM phase transition temperature that corresponds to an adiabatic electrocaloric temperature change of 11.2 K. The high magnetocaloric value can be attributed to the first-order phase transition of our CFO. The latent heat released/absorbed during first-order conversion mainly improves magnetocaloric response [5,6]. From another viewpoint, the improved value of ΔT can be related to the grain size, as reported by [24,25]. In another way, smaller particle sizes have more negligible magnetic hysteresis, resulting in less energy lost in the thermal process, and thus the electrocaloric effect is more significant.

For industrial refrigeration applications, the performance of MCE of the CFO sample is evaluated using the Relative Cooling Power (RCP) defined by Eq. (4):

$$RCP = -\Delta S_M^{\max} \times \delta_{FWHM} \tag{4}$$

Here ΔS_M^{max} refers to the maximum value of the magnetic entropy, and $\delta_{FWHM} = (T_{hot} - T_{cold})$ is the full width at half maximum of the curve ΔS_M^{max}.

The RCP value increases proportionally with the applied magnetic field (Fig. 8). Therefore, the excellent RCP value of 687.56 J Kg^{-1} obtained under a low applied magnetic field (24 kOe) leads to a state that such a sample could be considered a potential candidate for magnetic refrigeration application in the 600 K − 800 K temperature range.

To investigate the magnetic refrigeration efficiency, the ΔS, ΔT and RCP alone are insufficient to identify the potential of the refrigerant material for applications in solid-state refrigeration technologies. In this respect, the temperature-averaged entropy change (TEC) was calculated using the following expression as reported by [46]:

$$TEC(\Delta T_{H-C}) = \frac{1}{\Delta T_{H-C}} \max\left\{ \int_{T_{mid}+\Delta T_{H-C}}^{T_{mid}-\Delta T_{H-C}} |\Delta S_M(T)| dT \right\}$$

Herein $\Delta T_{H\text{-}C}$ denotes the temperature difference between the device's cold and hot heat exchangers. T_{mid} is the temperature at which the TEC($\Delta T_{H\text{-}C}$) is maximized for a given $\Delta T_{H\text{-}C}$.

It should be mentioned that the obtained values of ΔS, ΔT, RCP and TEC are much higher than those reported in the literature in the ferromagnetic oxide systems (Table 3). Moreover, even with a high applied magnetic field, cobalt ferrites doped with copper show a moderate ΔS value of 0.6 J Kg^{-1} $K^{-1}$with an RCP of 62.55 J Kg^{-1} [41]. For $Mg_{0.6}Cu_{0.4}Fe_2O_4$ nanoparticles elaborated by the sol–gel technique, the

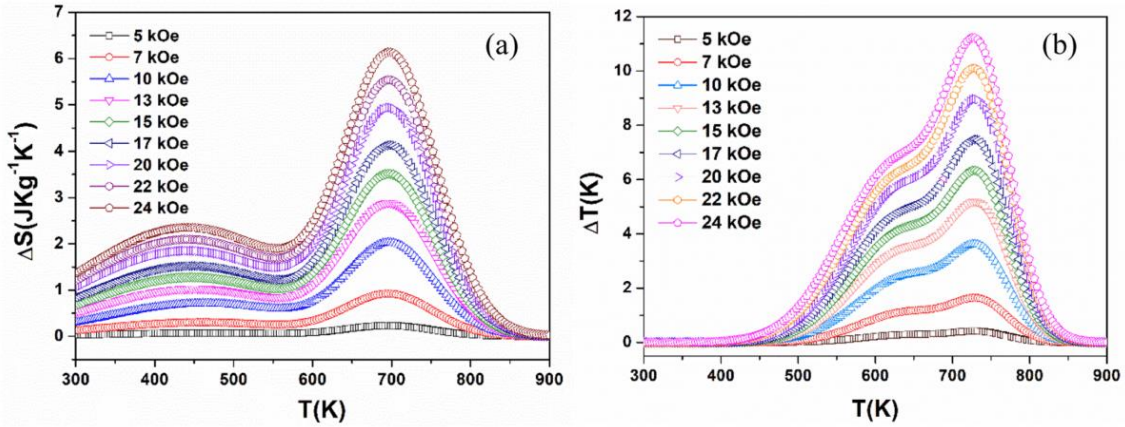

Fig. 7. Magnetic entropies change ΔS, and the adiabatic temperature changes ΔT as a function of temperature under various magnetic fields for $CoFe_2O_4$ powder.

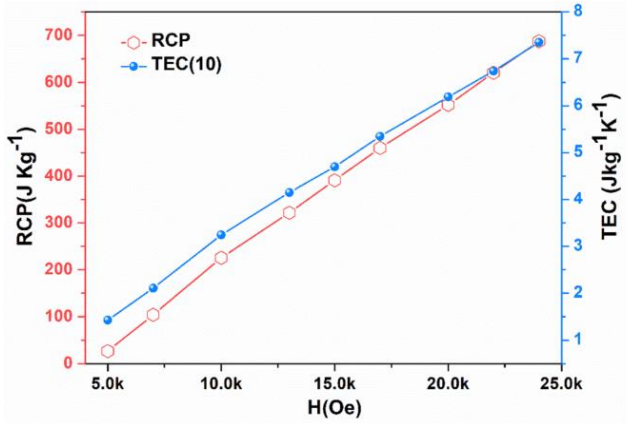

Fig. 8. Magnetic field dependence of the RCP and TEC.

maximum MCE value reported was 1.09 J kg^{-1} K^{-1} under an applied field of 50 kOe. In our previous work [7], a high RCP of 79.19 J Kg^{-1} with a ΔT of 5.6 K under 60 kOe was achieved in perovskite manganite $La_{0.5}Ca_{0.5-x}\square_xMnO_3$. In addition, our CFO shows an important value of TEC of 7.34 J $Kg^{-1}K^{-1}$ compared with other magnetic materials such as $La_{0.8}Ca_{0.2}MnO_3$ ceramic (TEC = 4.5 J $Kg^{-1}K^{-1}$) under 20 kOe, and in $La_{1.2}Pr_{0.2}Ca_{1.6}Mn_2O_7$ ceramic upon 25 kOe (TEC = 6.98 J $Kg^{-1}K^{-1}$) [47]. This comparison makes our CFO nanopowder a good candidate for magnetic heating and cooling applications.

7. Conclusion

In conclusion, we investigated the structural, magnetic, and magnetocaloric properties of $CoFe_2O_4$ ferrite (CFO) nanoparticles elaborated by sol–gel auto combustion. According to X-ray diffraction analysis and Raman spectra, the CFO crystallizes in a cubic spinel structure with a space group of $Fd\ \bar{3}\ m$. Magnetic measurements reveal that our CFO exhibits the first-order PM - FM phase transition with a Curie temperature of 785 K. The maximal magnetic entropy change and relative cooling power are both enhanced, making our CFO a suitable candidate for both environmentally friendly magnetic refrigeration and medical applications that need temperatures above 300 K.

CRediT authorship contribution statement

Youness Hadouch: Investigation, Methodology, Data curation, Writing – original draft, Validation. **Daoud Mezzane:** Visualization, Methodology, Writing – review & editing, Validation, Supervision. **M'barek Amjoud:** Visualization, Writing – review & editing, Validation, Supervision. **Lahoucine Hajji:** Investigation, Methodology, Validation. **Yaovi Gagou:** Formal analysis, Validation, Supervision. **Zdravko Kutnjak:** Writing – review & editing, Visualization, Validation. **Valentin Laguta:** Writing – review & editing, Visualization, Validation. **Yakov Kopelevich:** Visualization, Validation. **Mimoun El Marssi:** Visualization, Validation, Writing – review & editing, Supervision.

Table 3
Magnetocaloric properties of ferromagnetic oxides.

Material	T_C(K)	Magnetic field (kOe)	ΔS (J Kg^{-1} K^{-1})	ΔT (K)	TEC (J $Kg^{-1}K^{-1}$)	RCP (J Kg^{-1})	References
$CoFe_2O_4$	785	24	6.15	11.24	7.34	687.56	This work
$CoFeCuO_4$	688	50	0.6	–	–	62.55	[41]
$Zn_{0.2}Ni_{0.4}Cu_{0.4}Fe_2O_4$	705	50	1.61	–	–	233	[8]
$NiFe_2O_4$	845	25	0.75	–	–	60	[9]
$Ni_{0.5}Zn_{0.5}Fe_2O_4$	481	25	1.15	–	–	161	[9]
$Mg_{0.6}Cu_{0.4}Fe_2O_4$	630	50	1.09	–	–	136	[48]
$La_{0.8}Ca_{0.2}MnO_3$	105	20	0.732		4.5	99.05	[49]
$La_{0.813}K_{0.16}Mn_{0.987}O_3$	338	15	2.11	–	1.47	77.62	[50]
$La_{1.2}Pr_{0.2}Ca_{1.6}Mn_2O_7$	274	25	4.25	–	6.98	110	[47]
$La_{0.7}Sr_{0.3}MnO_3$	364	1	1.6	–	–	0.4	[51]
$La_{0.5}Ca_{0.5-x}\square_xMnO_3$	254	60	2.70	5.6	–	79.19	[7]
$Ho_{60}Co_{20}Ni_{20}$	20.4	50	18.4	–	18.3	668.2	[52]
$Er_{60}Co_{20}Ni_{20}$	11.5	50	15.5	–	15.4		[52]
$EuTi_{0.9}Cr_{0.1}O_3$	–	20	30	4.2	–	125	[53]
$EuDy_2O_4$	−17.4	80	25	16	–	415	[54]

Declaration of Competing Interest

The authors declare that they have no known competing financial interests or personal relationships that could have appeared to influence the work reported in this paper.

Data availability

No data was used for the research described in the article.

Acknowledgements

The authors gratefully acknowledge the generous financial support of CNRST Priority Program PPR 15/2015, the European Union's Horizon 2020 research and FAPESP and CNPq, Brazilian agencies.

Formatting of funding sources

CNRST Priority Program PPR 15/2015.

The European Union's Horizon 2020 research.

References

[1] A. Smith, Who discovered the magnetocaloric effect?: Warburg, Weiss, and the connection between magnetism and heat, Eur. Phys. J. H 38 (4) (Sep. 2013) 507–517, https://doi.org/10.1140/epjh/e2013-40001-9.

[2] V.K. Pecharsky, K.A. Gschneidner, Tunable magnetic regenerator alloys with a giant magnetocaloric effect for magnetic refrigeration from ~20 to ~290 K, Appl. Phys. Lett. 70 (24) (Jun. 1997) 3299–3301, https://doi.org/10.1063/1.119206.

[3] V.K. Pecharsky, K.A.G. Jr, Magnetocaloric e!ect and magnetic refrigeration, J. Magn. Magn. Mater. (1999) 13.

[4] E.V. Gopalan, I.A. Al-Omari, D.S. Kumar, Y. Yoshida, P.A. Joy, M. R. Anantharaman, Inverse magnetocaloric effect in sol–gel derived nanosized cobalt ferrite, Appl. Phys. A 99 (2) (May 2010) 497–503, https://doi.org/10.1007/s00339-010-5573-8.

[5] J.Y. Law, V. Franco, L.M. Moreno-Ramírez, A. Conde, D.Y. Karpenkov, I. Radulov, K.P. Skokov, O. Gutfleisch, A quantitative criterion for determining the order of magnetic phase transitions using the magnetocaloric effect, Nat. Commun. 9 (1) (2018), https://doi.org/10.1038/s41467-018-05111-w.

[6] N.T. Trung, V. Biharie, L. Zhang, L. Caron, K.H.J. Buschow, E. Brück, From single- to double-first-order magnetic phase transition in magnetocaloric Mn1−xCrxCoGe compounds, Appl. Phys. Lett. 96 (16) (2010) 162507, https://doi.org/10.1063/1.3399774.

[7] S. Ben Moumen, Y. Gagou, M. Chettab, D. Mezzane, M. Amjoud, S. Fourcade, L. Hajji, Z. Kutnjak, M. El Marssi, Y. El Amraoui, Y. Kopelevich, I.A. Luk'yanchuk, Synthesis of La0.5Ca0.5−x□xMnO3 nanocrystalline manganites by sucrose assisted auto combustion route and study of their structural, magnetic and magnetocaloric properties, J. Mater. Sci.: Mater. Electron. 30 (23) (2019) 20459–20470.

[8] E. Oumezzine, S. Hcini, M. Baazaoui, E.K. Hlil, M. Oumezzine, Structural, magnetic and magnetocaloric properties of Zn0.6−xNixCu0.4Fe2O4 ferrite nanoparticles prepared by Pechini sol-gel method, Powder Technol. 278 (Jul. 2015) 189–195, https://doi.org/10.1016/j.powtec.2015.03.022.

[9] M.S. Anwar, F. Ahmed, B.H. Koo, Enhanced relative cooling power of Ni1−Zn Fe2O4 (0.0 ⩽x⩽ 0.7) ferrites, Acta Mater. 71 (Jun. 2014) 100–107, https://doi.org/10.1016/j.actamat.2014.03.002.

[10] S. Amiri, H. Shokrollahi, The role of cobalt ferrite magnetic nanoparticles in medical science, Mater. Sci. Eng. C 33 (1) (Jan. 2013) 1–8, https://doi.org/10.1016/j.msec.2012.09.003.

[11] R. Safi, A. Ghasemi, R. Shoja-Razavi, E. Ghasemi, T. Sodaee, Rietveld structure refinement, cations distribution and magnetic features of CoFe2O4 nanoparticles synthesized by co-precipitation, hydrothermal, and combustion methods, Ceram. Int. 42 (5) (Apr. 2016) 6375–6382, https://doi.org/10.1016/j.ceramint.2016.01.032.

[12] Q. Lin, J. Lin, Y. He, R. Wang, J. Dong, The Structural and Magnetic Properties of Gadolinium Doped CoFe $_{2\ O}$ 4 Nanoferrites, J. Nanomater. 2015 (2015) 1–6, https://doi.org/10.1155/2015/294239.

[13] M. Eshraghi, P. Kameli, Magnetic properties of CoFe2O4 nanoparticles prepared by thermal treatment of ball-milled precursors, Curr. Appl. Phys. 11 (3) (May 2011) 476–481, https://doi.org/10.1016/j.cap.2010.08.032.

[14] R.E. Lu, K.G. Chang, B. Fu, Y.J. Shen, M.W. Xu, S. Yang, X.P. Song, M. Liu, Y. D. Yang, Magnetic properties of different CoFe $_{2\ O}$ 4 nanostructures: nanofibers versus nanoparticles, J. Mater. Chem. C 2 (40) (2014) 8578–8584, https://doi.org/10.1039/C4TC01415D.

[15] F. Sharifianjazi, M. Moradi, N. Parvin, A. Nemati, A. Jafari Rad, N. Sheysi, A. Abouchenari, A. Mohammadi, S. Karbasi, Z. Ahmadi, A. Esmaeilkhanian, M. Irani, A. Pakseresht, S. Sahmani, M. Shahedi Asl, Magnetic CoFe2O4 nanoparticles doped with metal ions: A review, Ceram. Int. 46 (11) (2020) 18391–18412, https://doi.org/10.1016/j.ceramint.2020.04.202.

[16] P. Poddar, J. Gass, D.J. Rebar, S. Srinath, H. Srikanth, S.A. Morrison, E. E. Carpenter, Magnetocaloric effect in ferrite nanoparticles, J. Magn. Magn. Mater. 307 (2) (2006) 227–231, https://doi.org/10.1016/j.jmmm.2006.04.007.

[17] V. Franco, J.S. Blázquez, J.J. Ipus, J.Y. Law, L.M. Moreno-Ramírez, A. Conde, Magnetocaloric effect: From materials research to refrigeration devices, Prog. Mater. Sci. 93 (Apr. 2018) 112–232, https://doi.org/10.1016/j.pmatsci.2017.10.005.

[18] M.A. Benedict, S.A. Sherif, M. Schroeder, D.G. Beers, The impact of magnetocaloric properties on refrigeration performance and machine design, Int. J. Refrig. 74 (Feb. 2017) 576–583, https://doi.org/10.1016/j.ijrefrig.2016.12.004.

[19] D.-H. Kim, D.E. Nikles, D.T. Johnson, C.S. Brazel, Heat generation of aqueously dispersed CoFe2O4 nanoparticles as heating agents for magnetically activated drug delivery and hyperthermia, J. Magn. Magn. Mater. 320 (19) (Oct. 2008) 2390–2396, https://doi.org/10.1016/j.jmmm.2008.05.023.

[20] S.Y. Srinivasan, K.M. Paknikar, D. Bodas, V. Gajbhiye, Applications of cobalt ferrite nanoparticles in biomedical nanotechnology, Nanomed. 13 (10) (May 2018) 1221–1238, https://doi.org/10.2217/nnm-2017-0379.

[21] R.S. Melo, P. Banerjee, A. Franco, Hydrothermal synthesis of nickel doped cobalt ferrite nanoparticles: optical and magnetic properties, J. Mater. Sci. Mater. Electron. 29 (17) (2018) 14657–14667, https://doi.org/10.1007/s10854-018-9602-2.

[22] S. Agrawal, A. Parveen, A. Azam, Structural, electrical, and optomagnetic tweaking of Zn doped CoFe2−Zn O4− nanoparticles, J. Magn. Magn. Mater. 414 (Sep. 2016) 144–152, https://doi.org/10.1016/j.jmmm.2016.04.059.

[23] K.E. Sickafus, J.M. Wills, N.W. Grimes, Structure of Spinel, J. Am. Ceram. Soc. 82 (12) (Dec. 2004) 3279–3292, https://doi.org/10.1111/j.1151-2916.1999.tb02241.x.

[24] A. Verma, T.C. Goel, R.G. Mendiratta, M.I. Alam, Dielectric properties of NiZn ferrites prepared by the citrate precursor method, Mater. Sci. Eng. B 60 (2) (Jun. 1999) 156–162, https://doi.org/10.1016/S0921-5107(99)00019-7.

[25] L.i. Lv, J.-P. Zhou, Q. Liu, G. Zhu, X.-Z. Chen, X.-B. Bian, P. Liu, Grain size effect on the dielectric and magnetic properties of NiFe2O4 ceramics, Phys. E Low-Dimens. Syst. Nanostructures 43 (10) (2011) 1798–1803, https://doi.org/10.1016/j.physe.2011.06.014.

[26] S. Xi, W. Lu, Y. Sun, 'Magnetic properties and magnetocaloric effect of La $_{0.8}$ Ca $_{0.2}$ MnO $_3$ nanoparticles tuned by particle size', J. Appl. Phys., 111(6) Mar. (2012), 063922. doi: 10.1063/1.3699037.

[27] W. Tang, W. Lu, X. Luo, B. Wang, X. Zhu, W. Song, Z. Yang, Y. Sun, Particle size effects on La0.7Ca0.3MnO3: size-induced changes of magnetic phase transition order and magnetocaloric study, J. Magn. Magn. Mater. 322 (16) (2010) 2360–2368, https://doi.org/10.1016/j.jmmm.2010.02.038.

[28] K. Maaz, A. Mumtaz, S.K. Hasanain, A. Ceylan, Synthesis and magnetic properties of cobalt ferrite (CoFe2O4) nanoparticles prepared by wet chemical route, J. Magn. Magn. Mater. 308 (2) (Jan. 2007) 289–295, https://doi.org/10.1016/j.jmmm.2006.06.003.

[29] M. Cernea, P. Galizia, I. Ciuchi, G. Aldica, V. Mihalache, L. Diamandescu, C. Galassi, CoFe 2 O 4 magnetic ceramic derived from gel and densified by spark plasma sintering, J. Alloys Compd. 656 (2016) 854–862, https://doi.org/10.1016/j.jallcom.2015.09.271.

[30] I. Zalite, G. Heidemane, J. Grabis, M. Maiorov, in: Powder Technology, InTech, 2018, https://doi.org/10.5772/intechopen.76809.

[31] A. Sutka, G. Mezinskis, Sol-gel auto-combustion synthesis of spinel-type ferrite nanomaterials, Front. Mater. Sci. 6 (2) (Jun. 2012) 128–141, https://doi.org/10.1007/s11706-012-0167-3.

[32] B.G. Toksha, S.E. Shirsath, S.M. Patange, K.M. Jadhav, Structural investigations and magnetic properties of cobalt ferrite nanoparticles prepared by sol–gel auto combustion method, Solid State Commun. 147 (11–12) (Sep. 2008) 479–483, https://doi.org/10.1016/j.ssc.2008.06.040.

[33] A. Franco, F.C. e Silva, High temperature magnetic properties of cobalt ferrite nanoparticles, Appl. Phys. Lett. 96 (17) (2010) 172505, https://doi.org/10.1063/1.3422478.

[34] C. Vázquez-Vázquez, M. Lovelle, C. Mateo, M.A. López-Quintela, M.C. Buján-Núñez, D. Serantes, D. Baldomir, J. Rivas, Magnetocaloric effect and size-dependent study of the magnetic properties of cobalt ferrite nanoparticles prepared by solvothermal synthesis, Phys. Status Solidi A 205 (6) (2008) 1358–1362.

[35] G. Kumar, R.K. Kotnala, J. Shah, V. Kumar, A. Kumar, P. Dhiman, M. Singh, Cation distribution: a key to ascertain the magnetic interactions in a cobalt substituted Mg–Mn nanoferrite matrix, Phys. Chem. Chem. Phys. 19 (25) (2017) 16669–16680, https://doi.org/10.1039/C7CP01993A.

[36] Y. Hadouch, S. Ben Moumen, H. Mezzourh, D. Mezzane, M. Amjoud, B. Asbani, A. G. Razumnaya, Y. Gagou, B. Rožič, Z. Kutnjak, M. El Marssi, Electrocaloric effect and high energy storage efficiency in lead-free Ba0.95Ca0.05Ti0.89Sn0.11O3 ceramic elaborated by sol–gel method, J. Mater. Sci. Mater. Electron. 33 (4) (Jan 2022) 2067–2079, https://doi.org/10.1007/s10854-021-07411-2.

[37] P. Chandramohan, M.P. Srinivasan, S. Velmurugan, S.V. Narasimhan, Cation distribution and particle size effect on Raman spectrum of CoFe2O4, J. Solid State Chem. 184 (1) (Jan. 2011) 89–96, https://doi.org/10.1016/j.jssc.2010.10.019.

[38] D.K. Pradhan, S. Kumari, V.S. Puli, P.T. Das, D.K. Pradhan, A. Kumar, J.F. Scott, R. S. Katiyar, Correlation of dielectric, electrical and magnetic properties near the magnetic phase transition temperature of cobalt zinc ferrite, Phys. Chem. Chem. Phys. 19 (1) (2017) 210–218, https://doi.org/10.1039/C6CP06133H.

[39] P.N. Anantharamaiah, P.A. Joy, Enhancing the strain sensitivity of CoFe $_{2\ O}$ 4 at low magnetic fields without affecting the magnetostriction coefficient by substitution of small amounts of Mg for Fe, Phys. Chem. Chem. Phys. 18 (15) (2016) 10516–10527, https://doi.org/10.1039/C6CP00369A.

[40] 'Temperature dependent phonon Raman scattering of highly *a* -axis oriented CoFe $_2$ O $_4$ inverse spinel ferromagnetic films grown by pulsed laser deposition', Appl. Phys. Lett., vol. 100, no. 7, p. 071905, Feb. 2012, doi: 10.1063/1.3683520.

[41] M. Nasri, C. Henchiri, R. Dhahri, J. Khelifi, E. Dhahri, J.F.M.L. Mariano, Study of structural, magnetic, magnetocaloric properties and critical behavior of CoFeCuO4 spinel ferrite, Inorg. Chem. Commun. 133 (2021) 108933, https://doi.org/10.1016/j.inoche.2021.108933.
[42] R. Bjørk, Z. Zhou, The demagnetization factor for randomly packed spheroidal particles, J. Magn. Magn. Mater. 476 (Apr. 2019) 417–422, https://doi.org/10.1016/j.jmmm.2019.01.005.
[43] R. Bjørk, C.R.H. Bahl, Demagnetization factor for a powder of randomly packed spherical particles, Appl. Phys. Lett. 103 (10) (2013) 102403, https://doi.org/10.1063/1.4820141.
[44] R.H. Kadam, S.T. Alone, M.L. Mane, A.R. Biradar, S.E. Shirsath, Phase evaluation of Li+ substituted CoFe2O4 nanoparticles, their characterizations and magnetic properties, J. Magn. Magn. Mater. 355 (Apr. 2014) 70–75, https://doi.org/10.1016/j.jmmm.2013.11.054.
[45] P.C.R. Varma, R.S. Manna, D. Banerjee, M.R. Varma, K.G. Suresh, A.K. Nigam, Magnetic properties of CoFe2O4 synthesized by solid state, citrate precursor and polymerized complex methods: A comparative study, J. Alloys Compd. 453 (1–2) (Apr. 2008) 298–303, https://doi.org/10.1016/j.jallcom.2006.11.058.
[46] L.D. Griffith, Y. Mudryk, J. Slaughter, V.K. Pecharsky, Material-based figure of merit for caloric materials, J. Appl. Phys. 123 (3) (2018) 034902, https://doi.org/10.1063/1.5004173.
[47] A. Kumar, I. Hussain, S.N. Khan, B.H. Koo, Large magnetocaloric effects in Pr-doped La1.4-xPrxCa1.6Mn2O7 bilayer manganites, J. Alloys Compd. 845 (2020) 156218, https://doi.org/10.1016/j.jallcom.2020.156218.
[48] S. Hcini, N. Kouki, A. Omri, A. Dhahri, M.L. Bouazizi, Effect of sintering temperature on structural, magnetic, magnetocaloric and critical behaviors of Ni-Cd-Zn ferrites prepared using sol-gel method, J. Magn. Magn. Mater. 464 (Oct. 2018) 91–102, https://doi.org/10.1016/j.jmmm.2018.05.045.
[49] S. Choura-Maatar, M.M. Nofal, R. M'nassri, W. Cheikhrouhou-Koubaa, N. Chniba-Boudjada, A. Cheikhrouhou, Enhancement of the magnetic and magnetocaloric properties by Na substitution for Ca of La0.8Ca0.2MnO3 manganite prepared via the Pechini-type sol–gel process, J Mater Sci: Mater Electron 31 (2) (2020) 1634–1645.
[50] W. Zhong, et al., Synthesis, structure and magnetic entropy change of polycrystalline La_VKVMnO_>B, J. Magn. Magn. Mater. (1999) 7.
[51] P.T. Phong, L.V. Bau, L.C. Hoan, D.H. Manh, N.X. Phuc, I.-J. Lee, Effect of B-site Ti doping on the magnetic, low–field magnetocaloric and electrical transport properties of La 0.7 Sr 0.3 Mn 1–x Ti x O 3 perovskites, J. Alloys Compd. 656 (Jan. 2016) 920–928, https://doi.org/10.1016/j.jallcom.2015.10.038.
[52] Y. Wang, D. Guo, B. Wu, S. Geng, Y. Zhang, Magnetocaloric effect and refrigeration performance in RE60Co20Ni20 (RE = Ho and Er) amorphous ribbons, J. Magn. Magn. Mater. 498 (Mar. 2020), 166179, https://doi.org/10.1016/j.jmmm.2019.166179.
[53] Z.-J. Mo, Z.-H. Hao, J. Shen, L. Li, J.-F. Wu, F.-X. Hu, J.-R. Sun, B.-G. Shen, Observation of giant magnetocaloric effect in EuTi 1–x Cr x O 3, J. Alloys Compd. 649 (2015) 674–678, https://doi.org/10.1016/j.jallcom.2015.07.176.
[54] A. Midya, N. Khan, D. Bhoi, P. Mandal, Giant magnetocaloric effect in magnetically frustrated EuHo2O4 and EuDy2O4 compounds, Appl. Phys. Lett. 101 (13) (2012) 132415, https://doi.org/10.1063/1.4754849.

Chapter 4

ELABORATION AND CHARACTERIZATION OF CFO-BCTSn COMPOSITES

I. Introduction

In this chapter, the strain-mediated magnetoelectric (ME) coupling between BCTSn piezoelectric and CFO magnetostrictive components are established in two types of connectivity's:

- (1-x) $Ba_{0.95}Ca_{0.05}Ti_{0.89}Sn_{0.11}O_3$-(x) $CoFe_2O_4$ particulate composites with x=0.0; 0.1; 0.2; 0.3; 0.4 and 0.5;
- CFO/BCTSn core-shell nanofibers;

The structural, morphological, ferroelectric/piezoelectric, magnetic, and magnetoelectric properties are thoroughly investigated. The experimentally-determined magnetoelectric coupling coefficient was very important in core-shell nanofibers connectivity, attributed to the nanofibers' large interfacial areas and excellent interconnectivity between the two ferroic phases.

The first work in this chapter was published in "Journal of Materials Science: Materials in Electronics" on February 20, 2023. The manuscript is titled:

Piezoelectric, magnetic and magnetoelectric properties of a new lead-free multiferroic (1-x) $Ba_{0.95}Ca_{0.05}Ti_{0.89}Sn_{0.11}O_3$-(x) $CoFe_2O_4$ particulate composites.

https://doi.org/10.1007/s10854-023-10145-y

The second work in this chapter was published in "ACS Applied Nano Materials" on June 07, 2023. The manuscript is titled:

Multiferroic $CoFe_2O_4$-$Ba_{0.95}Ca_{0.05}Ti_{0.89}Sn_{0.11}O_3$ Core-Shell Nanofibers for Magnetic Field Sensor Applications.

https://doi.org/10.1021/acsanm.3c01101

J Mater Sci: Mater Electron (2023) 34:725

Piezoelectric, magnetic and magnetoelectric properties of a new lead-free multiferroic (1-x) $Ba_{0.95}Ca_{0.05}Ti_{0.89}Sn_{0.11}O_3$—(x) $CoFe_2O_4$ particulate composites

Youness Hadouch[1,2,*], Daoud Mezzane[1,2], M.'barek Amjoud[1], Nouredine Oueldna[3], Yaovi Gagou[2], Zdravko Kutnjak[4], Valentin Laguta[5,6], Yakov Kopelevich[7], Khalid Hoummada[3], and Mimoun El Marssi[2]

[1] Laboratory of Innovative Materials, Energy and Sustainable Development (IMED), Faculty of Sciences and Technology, Cadi-Ayyad University, BP 549, Marrakech, Morocco
[2] Laboratory of Physics of Condensed Matter (LPMC), Scientific Pole, University of Picardie Jules Verne, 33 Rue Saint-Leu, 80039 Amiens, France
[3] Aix-Marseille University - CNRS, IM2NP Faculté Des Sciences de Saint-Jérôme Case 142, 13397 Marseille, France
[4] Jozef Stefan Institute, Jamova Cesta 39, 1000 Ljubljana, Slovenia
[5] Institute of Physics AS CR, Cukrovarnicka 10, 162 53 Prague, Czech Republic
[6] Institute for Problems of Materials Science, National Ac. of Science, Krjijanovskogo 3, Kyiv 03142, Ukraine
[7] Universidade Estadual de Campinas-UNICAMP, Instituto de Física 'GlebWataghin', R. Sergio Buarque de Holanda 777, Campinas 13083-859, Brazil

Received: 21 December 2022
Accepted: 20 February 2023

ABSTRACT

New multiferroic particulate composites (1-x) $Ba_{0.95}Ca_{0.05}Ti_{0.89}Sn_{0.11}O_3$–(x) $CoFe_2O_4$ with ($x = 0.1$, 0.2, 0.3, 0.4 and 0.5) have been prepared by mechanical mixing of the calcined and milled individual ferroic phases. X-ray diffraction and Raman spectroscopy analysis confirmed the formation of both perovskite $Ba_{0.95}Ca_{0.05}Ti_{0.89}Sn_{0.11}O_3$ (BCTSn) and spinel $CoFe_2O_4$ (CFO) phases without the presence of additional phases. The morphological properties of the composites were provided by using field emission scanning electron microscopy. The BCTSn-CFO composites exhibit multiferroic behavior at room temperature, as evidenced by ferroelectric and ferromagnetic hysteresis loops. For all composites, the converse piezoelectric coefficient was calculated and found to decrease from 203 pm.V^{-1} to 27 pm.V^{-1} in pure BCTSn. when the CFO content increases. The magnetoelectric (ME) coupling was measured under a magnetic field up to 10 kOe and the maximum ME response found to be 0.1 mV.cm^{-1}.Oe^{-1} for the composition 0.7 BCTSn-0.3 CFO exhibiting a high degree of pseudo-cubicity and large density.

Address correspondence to E-mail: hadouch.younes@gmail.com; youness.hadouch@etud.u-picardie.fr

https://doi.org/10.1007/s10854-023-10145-y
Published online: 10 March 2023

1 Introduction

The microelectronics industry has developed progressively compact integrated circuits with even more sophisticated functionalities in response to the rising demand for electronic devices, whether portable or inserted into other systems. This complexity encourages the development of multifunctional materials, which combine well-known features into a single component [1–3].

Researchers have become interested in multiferroic materials exhibiting simultaneous ferroelectric and ferromagnetic orderings because of their attractive physical characteristics and potential uses in spintronics, data storage, and sensors. All of these applications are based on the magnetoelectric effect (ME), which refers to the coupling of a material's electric and magnetic properties [4–6]. A gendered magnetic field results from an applied electric field that distorts the ferroelectric/piezoelectric phase, which in turn distorts the magnetostrictive/magnetic phase. However, this coupling phenomenon can be reversed [7, 8], and the ME effect for composites may be stated as follows [9]:

$$ME_{effect} = \frac{\text{magnetic}}{\text{mechanical}} \times \frac{\text{mechanical}}{\text{electrical}} or \frac{\text{electrical}}{\text{mechanical}} \times \frac{\text{mechanical}}{\text{magnetic}} \quad (1)$$

The multiferroic materials are often classified into single phase [10, 11] and composites [5]. Single-phase materials with intrinsic ME coupling are understudied because of their weak ME effect at or near room temperature, which restricts the applications [12]. Indeed, the ferroelectric mechanism requires formally empty d orbitals, in contrast to the ferromagnetic mechanism, which requires partially filled d orbitals [12, 13]. Additionally, the realization of prospective applications is more difficult for single-phase materials since their transition temperatures are often much lower than room temperature [14]. For instance, $BiFeO_3$ (BFO) exhibits a high ferroelectric-paraelectric transition temperature of approximately 1103 K and a high antiferromagnetic to paramagnetic phase at a Néel temperature of 643 K. However, because of structural problems, it has large leakage currents [14]. On the other hand, synthetic multiferroic composites with various forms of connectivity, such as particulate ceramic (0–3) [14], laminates/films (2–2) [16, 17], and rod/fibers core–shell (1–3) [18], exhibit an excellent extrinsic ME coupling created by an elastic ferroelectric-ferromagnetic interfacial interaction combining high magnetostriction and a large piezoelectric response. On the other hand, particulate-type composites are simple to make and have a uniform ME effect in all directions [19].

Lead (Pb)-based materials are the most often employed ferroelectric phase in multiferroic composites because of their excellent polarization and piezoelectric properties [20]. However, lead-based materials have negative impact on the environment. Therefore, it is necessary to develop new environmentally friendly materials. Barium titanate (BT) is a typical alternative system that has the potential to be an important candidate for piezoelectric applications [21, 22]. Nonetheless, it has a low dielectric constant, a high Curie temperature (Tc = 120 °C), and moderate piezoelectric coefficient d_{33} [23], which necessitates strategies to improve these properties [24]. Site engineering as a solution involves replacing A-sites (Ba^{2+}) with Ca^{2+}, Sr^{2+}, La^{3+}… and/or B-sites (Ti^{4+}) with Zr^{4+}, Sn^{4+}, Hf^{4+}[18]. This results in structural distortions that change the dielectric and ferroelectric characteristics from pure to relaxor [25]. It is been a while the effect of substituting Ba^{2+} with Ca^{2+} in $Ba_{1-x}Ca_xTiO_3$ was investigated by Desheng Fu et al. [26] and reported that d_{33} enhances from 180 up to 310 $pC.N^{-1}$ with $0.02 < x < 0.34$. Numerous studies in this perspective have emphasized the partial substitution of Sn^{4+}, for Ti in $BaTiO_3$, as well as its effect on phase transition dielectric behavior, energy storage, and electrocaloric properties [25, 27, 28]. As a result, co-doping at both sites can result in the formation of the morphotropic phase boundary (MPB) at room temperature, resulting in improved dielectric, piezoelectric, and electrocaloric properties [29, 30]. $Ba(Ti_{0.8}Zr_{0.2})O_3$–$(Ba_{0.7}Ca_{0.3})TiO_3$ (BCZT) is the most studied piezoelectric material with a values of piezoelectric coefficient d_{33} in the range of 500–600 $pC.N^{-1}$ [29, 31]. Due to its high piezoelectric coefficient of d_{33} = 670 $pC.N^{-1}$ and the (MPB) in $(Ba_{0.95}Ca_{0.05})(Ti_{0.89}Sn_{0.11})O_3$ (BCTSn), Zhu et al. demonstrated that this material might be used as an alternative for BCZT in piezoelectric applications [32]. Moreover, we previously reported that $Ba_{0.95}Ca_{0.05}Ti_{0.89}Sn_{0.11}O_3$ exhibited a significant electrocaloric response of ΔT = 0.807 K [33]. Besides that, spinel ferrite CoFe2O4 (CFO) is the most widely used

magnetostrictive phase in magnetic materials which has a strong chemical stability, a high magnetostriction coefficient (λ -110 × 10^{-6}), and a moderate saturation magnetization [34]. This opens the door to a wide range of advanced technological applications, particularly in data storage and biomedical field [35]. Moreover, it should be noted that grain size, microstructure, and composition, which can be monitored during the synthesis process, have a significant impact on ferrite properties [35].

The most studied type (0–3) multiferroic composites in the literature are based on combining of the piezoelectric phase BCZT and the magnetostrictive phase CFO. For example, Praveen et al. studied multiferroic and magnetoelectric properties of [(1-x)($Ba_{0.85}Ca_{0.15}$)($Zr_{0.1}Ti_{0.9}$)O_3-(x) $CoFe_2O_4$] (weight fraction; x = 0, 0.1, 0.2, 0.3, 0.4, 0.5 and 1) ceramic particulate composites [36] and Rani et al. reported the magnetic and magnetocapacitance properties of (x) $CoFe_2O_4$ -(1-x)(0.5Ba($Zr_{0.2}Ti_{0.8}$)O_3-0.5($Ba_{0.7}Ca_{0.3}$)TiO_3)[37].

In this paper, we have prepared a newly developed (0–3) magnetoelectric composites by combining the $Ba_{0.95}Ca_{0.05}Ti_{0.89}Sn_{0.11}O_3$ (BCTSn) and $CoFe_2O_4$ (CFO). The structural, morphological and multiferroic properties of the (1-x) $Ba_{0.95}Ca_{0.05}Ti_{0.89}Sn_{0.11}O_3$–(x)$CoFe_2O_4$ with (x = 0.1, 0.2, 0.3, 0.4 and 0.5) composites have been systematically investigated as a function of weight fraction (x).

2 Material and methods

2.1 Chemical synthesis

Ferroelectric ($Ba_{0.95}Ca_{0.05}$)($Ti_{0.89}Sn_{0.11}$)O_3 (BCTSn) and ferromagnetic $CoFe_2O_4$ (CFO) were synthesized using solgel and solgel self-combustion methods, respectively. The preparation of both pristine BCTSn and CFO has been thoroughly described in our previous work [33, 34]. Polycrystalline (1-x) BCTSn – (x) CFO particulate composites with different weight fractions x (x = 0.1, 0.2, 0.3, 0.4 and 0.5) were fabricated by mechanical mixing of the calcined and milled individual ferroic phases of BCTSn and CFO and then pressed into cylindrical pellets under 50 bars using the uniaxial hydraulic press and sintered at 1300 °C for 4 h (Fig. 1). Finally, the pellets were coated with silver paste on both surfaces for electrical and magnetoelectrical measurements.

2.2 Characterization

The XRD patterns of (1-x) BCTSn—(x) CFO ceramic composites were obtained by X-ray diffraction using the Panalytical X-Pert Pro with Cu-Kα radiation (λ = 1.54059 Å) at room temperature. The grain morphology of ceramics was analyzed using the scanning electron microscopy (SEM) in a HELIOUS 600 nanolab setup from FEI. The Raman spectra were recorded using a micro-Raman Renishaw spectrometer equipped with a CCD detector. Magnetic properties were measured using a physical property measurement system (PPMS-DynaCool) Quantum design apparatus that operated at room temperature under a magnetic field range of 0–2.5 kOe. The polarization–electric field (P–E) hysteresis loops were performed by CPE1701, PloyK, USA, with a high-voltage power supply (Trek 609–6, USA) at room temperature and 20 Hz. The piezoelectric measurements were measured by using an AixACCT 6 TF 2000 Analyzer with a SIOS Meβtechnik GmbH laser interferometer and a TREK model 609E-6 high-voltage amplifier. Magnetoelectric measurements were done using conventional Bruker EPR spectrometer EMX plus operating at 400–600 Hz frequency range at room temperature.

3 Results and discussion:

3.1 Structural and morphological analysis

The collected XRD data of pristine BCTSn, CFO and the composite systems[(1-x) BCTSn-(x) CFO with x = 0.1, 0.2, 0.3, 0.4 and 0.5] sintered at 1300 °C for 4 h are shown in Fig. 2. It is apparent from the XRD patterns that all diffraction peaks of ferroelectric (black line) and ferrite (red line) phases appear in the composite samples without the presence of any impurities, proving that there was no chemical reaction between the ferroelectric and ferrite phases during the sintering process.

Figure 3 shows the structural refinement of the composite systems [(1-x) BCTSn-x CFO with x = 0.1, 0.2, 0.3, 0.4 and 0.5] using the software FULLPROF. The structural refinement of both pristine $Ba_{0.95}Ca_{0.05}Ti_{0.89}Sn_{0.11}O_3$ and $CoFe_2O$ was discussed in our previously reported works [33, 34]. The results revealed the coexistence of two distinct phases: BCTSn (*Amm2 & P4mm*) and CFO (*Fd* $\bar{3}$ *m*), and no

Fig.1 Schematic diagram of the fabrication process of (1-x) BCTSn—(x) CFO sintered ceramics composite

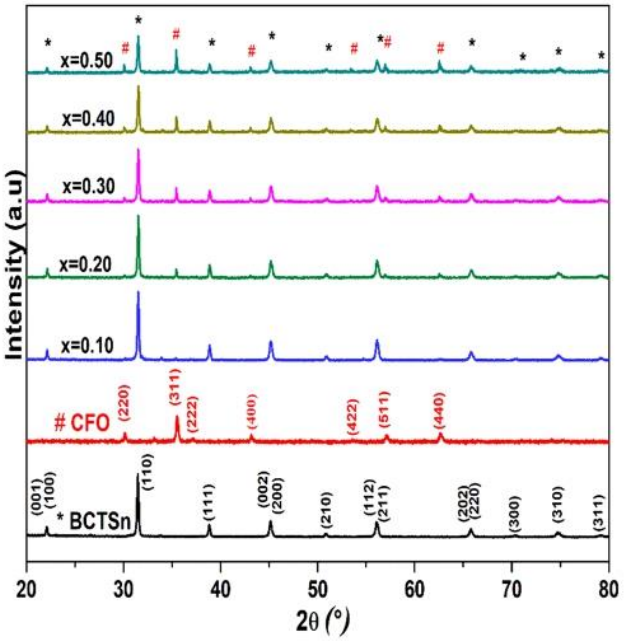

Fig. 2 XRD patterns of the (1-x) BCTSn—(x) CFO composites

peak has been identified for other crystal symmetries. Table 1 lists the corresponding ratios of all the phases, and the results are in good agreement with the weight percentage ratios used in the synthesis of composites. This proves that the di-phase multiferroic composites were successfully synthesized. It should be noted that the lattice constants of the spinel and perovskite phases change from one composition to another. This could be due to strain created at the multiferroic phase boundary caused by the crystal structure mismatch [19]. Figure 3f shows the lattice distortion (c/a) of the orthorhombic and tetragonal phases in BCTSn. In general, the variation of lattice distortion (c/a) in ferroelectric could be correlated with the magnetoelectric coupling of the multiferroic composite [19]. The crystal is relatively close to pseudocubic symmetry if the lattice distortion (c/a) in both ferroelectric phases (orthorhombic and tetragonal) is reduced, which decreases the strain and improves domain switching [19]. In our case, the reduced value of (c/a) in both ferroelectric phases was noticed at $x = 0.3$. Accordingly, the composite with the composition of 0.7 BCTSn and 0.3 CFO exhibited the highest degree of pseudocubicity.

To further investigate the (1-x) BCTSn-(x) CFO composite structure, Raman spectra were recorded in the frequency range of 100–900 cm^{-1} (Fig. 4). The optical active Raman modes for CFO ($A_{1g} + E_g + 3T_{2g}$) are identified at position peaks ($\sim$ 212, $\sim$ 314, $\sim$ 474, $\sim$ 581, $\sim$ 619 and $\sim$ 696 cm^{-1}), resulting from the motion of oxygen ions and both tetrahedral and octahedral sites ions in CFO spinel structure [38]. The modes at $\sim$ 619 and $\sim$ 696 cm^{-1} correspond to the symmetric stretching vibration of FeO_4 tetrahedral sub lattice, and those at $\sim$ 314 and $\sim$ 581 cm^{-1} depict the symmetric and asymmetric bending of the oxygen anions in the octahedral sublattice respectively. The second $T_{2g}(2)$ mode at $\sim$ 474 cm^{-1} corresponds to asymmetric stretching of the Fe–O (Co–O) bonds, while the $T_{2g}(3)$ at $\sim$ 212 cm^{-1} is ascribed to the translational shift of the whole FeO_4 tetrahedron [34]. For BCTSn phase, 4 A and 2 E modes are observed at 166, 195, 264, 303, 519, 722 cm^{-1} [39]. The peaks on the lower-frequency side (< 300 cm^{-1}) are associated with Ba/Ca-O vibrations, while those on the higher wavenumber side correspond to Ti/Sn–O vibrations [39]. The obtained Raman spectra for all compositions constitute Raman modes of the pure BCTSn and CFO

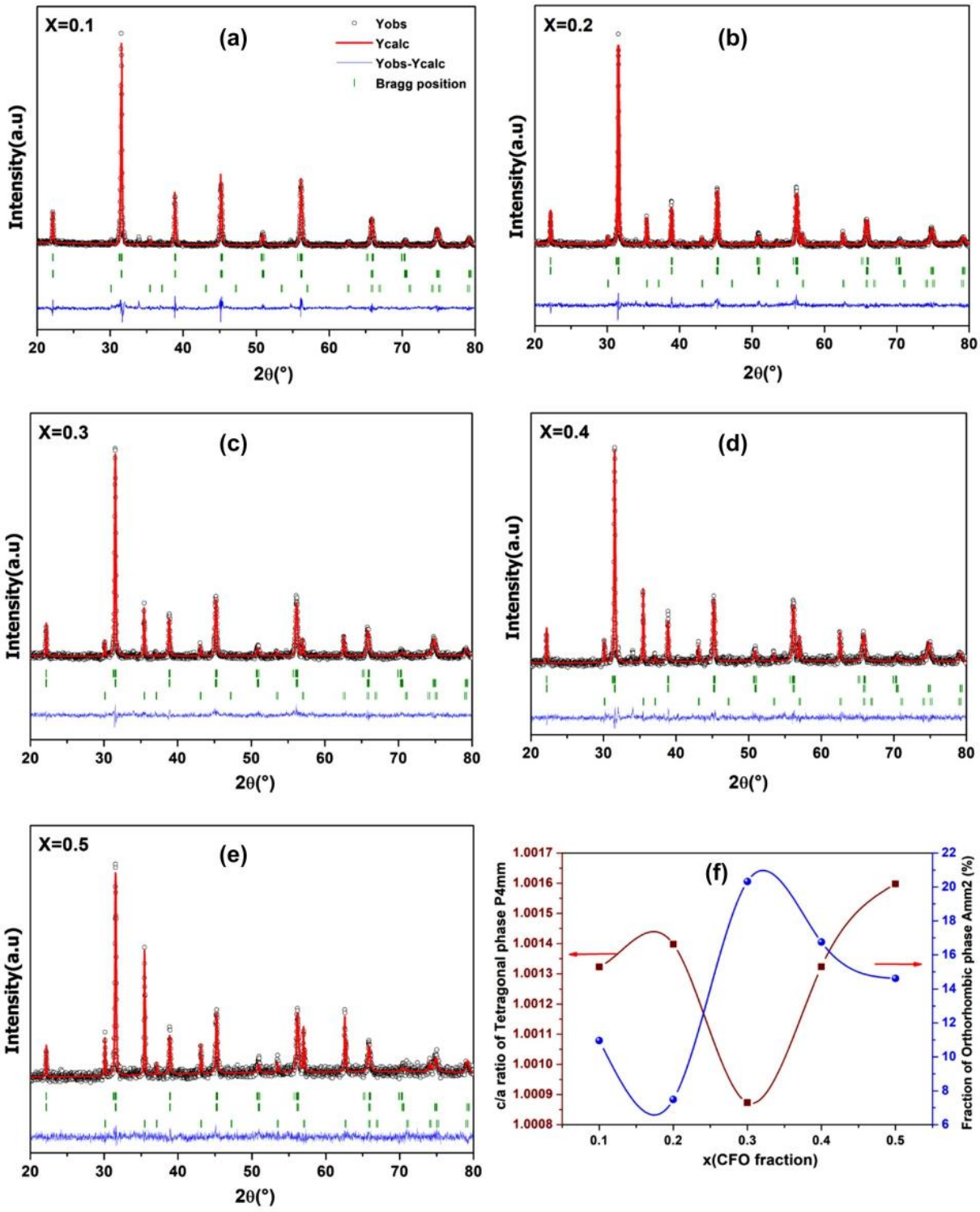

Fig. 3 **a-e** The Rietveld refined XRD patterns for the composites: (1-x) BCTSn-(x) CFO, **f** variation of lattice distortion and % fraction of crystal phase Amm2 with CFO content in (1-x) BCTSn-(x) CFO composites

phases individually without any strange Raman bands[40]. These results support the successful preparation of (0–3)-type connectivity for BCTSn-CFO multiferroic composite materials.

Table 1 Rietveld refined XRD parameters for (1-x) BCTSn—(x) CFO composite samples at room temperature

Composite (1-x) BCTSn—(x) CFO	Phase	Lattice parameters			Volume (Å)^3	Fraction %
		a (Å)	b (Å)	c (Å)		
$x = 0.1$	Fd $\bar{3}$ m	8.3721	-	-	586.81772	8.95
	Amm2	4.0040	5.7261	5.7261	131.28404	10.96
	P4mm	4.0069	4.0069	4.0122	64.41686	80.08
$x = 0.2$	Fd $\bar{3}$ m	8.3792	-	-	588.31195	18.27
	Amm2	4.0069	5.7273	5.7273	131.43419	7.49
	P4mm	4.0057	4.0057	4.0113	64.36385	74.23
$x = 0.3$	Fd $\bar{3}$ m	8.4002	-	-	592.74634	28.89
	Amm2	4.0097	5.7273	5.7273	131.52276	20.32
	P4mm	4.0089	4.0089	4.0124	64.4844	50.79
$x = 0.4$	Fd $\bar{3}$ m	8.3854	-	-	589.61884	41.35
	Amm2	4.0102	5.7278	5.7278	131.56541	16.75
	P4mm	4.0064	4.0064	4.0117	64.39276	41.90
$x = 0.5$	Fd $\bar{3}$ m	8.3949	-	-	591.62509	48.86
	Amm2	4.0108	5.7276	5.7281	131.59231	14.61
	P4mm	4.0053	4.0053	4.0117	64.35741	36.53

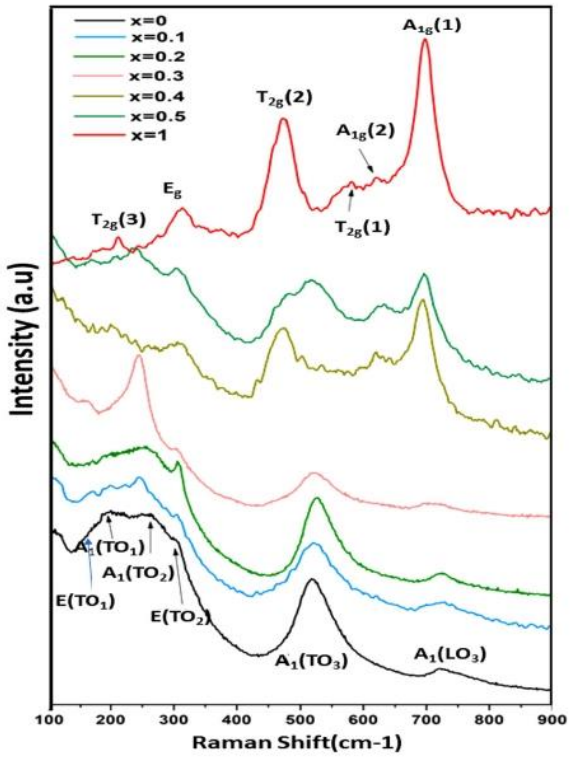

Fig. 4 Raman spectra of CFO, BCTSn and (1-x) BCTSn—(x) CFO composites

Figure 5a–e shows the SEM micrograph of sintered pellets of 0.7 BCTSn—0.3 CFO multiferroic composites. Due to the difference in molecular weights, BCTSn grains seem brighter while CFO grains appear darker gray. Figure 5g and h shows the EDX analysis of two different regions of the 0.7 BCTSn—0.3 CFO composite. The smaller bright gains show strong Ba, Ca, Ti and Sn peaks with the appearance of weak Co and Fe peaks. This implies that the smaller grains correspond to the BCTSn phase. The EDX spectrum of the larger dark grains, on the other hand, shows strong Co and Fe peaks and weak Ba, Ca, Ti and Sn peaks. As a result, the larger grains correspond to the CFO phase. Morphologically, the CFO grains are well faceted, as opposed to the BCTSn grains, which are shaped like a sphere.

The density of the sintered composites increases with increasing CFO fraction reaching a maximum of 5.5 at $x = 0.3$ and then remains constant (Fig. 5f). This variation is due to the high densification of CFO at the 1300 °C sintering temperature, whereas BCTSn exhibits very poor densification at this temperature, resulting in a porous microstructure, and may still be in the early stages of sintering because the presence of a ferrite phase with high porosity and conductivity correct poling was not achieved, resulting in a breakdown of the ferroelectric, piezoelectric, and magnetoelectric properties of the composites. Furthermore, the CFO grains are randomly dispersed in the BCTSn matrix which affects the density of

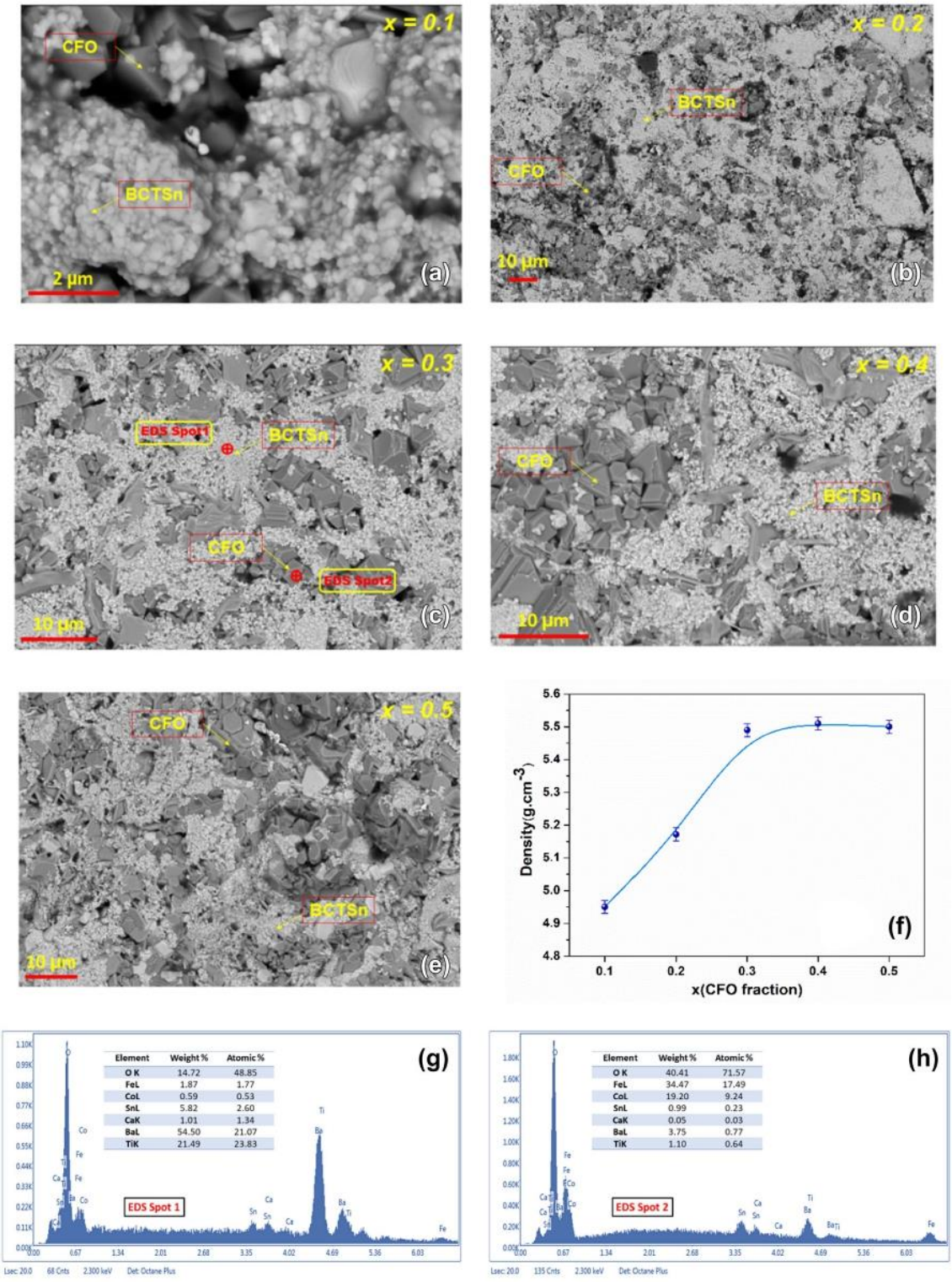

Fig. 5 **a–e** SEM micrographs, **f** bulk density as a function of ferrite content of various (1-x) BCTSn—(x) CFO composites and **g** and **h** EDS spectrum for composite with $x = 0.3$

ceramics and, as a result, the multiferroic properties of composites.

3.2 Magnetic properties of magnetoelectric composites

Figure 6 shows the room-temperature magnetization vs magnetic field (M-H) hysteresis loops of the particulate composites (1-x) BCTSn—(x) CFO and that of pure CFO in the inset. All the composites' obtained hysteresis loops showed identical behavior to pristine CFO, confirming the materials' ferromagnetic composition. Different magnetic parameters, including magnetic coercive field (H_c), saturation magnetization (M_s) and remanent magnetization (M_r), are obtained and listed in Table 2. Because of the decrease in the magnetic moment per unit volume caused by the presence of the non-magnetic BCTSn phase, M_s and M_r value both reduce systemically as the BCTSn content rises. $CoFe_2O_4$ coercivity is influenced by the form and structure of the grains, as was described in our earlier work [34]. Therefore, as CFO content rises, the increase in coercivity is most likely caused by the formation of $CoFe_2O_4$ clusters and interconnected structures. To compare the magnetic properties of the composites to the original magnetic phase of CFO, the reduced magnetization (M_r/M_s) of the individual composite was calculated (Table 2). It has been noticed that the values of reduced magnetization vary around one percent (1%), suggesting that there is no significant chemical diffusion or interaction between BCTSn and CFO phases since the chemical reactions can modify the original magnetic behavior of CFO [19].

3.3 Ferroelectric properties of magnetoelectric composites

The polarization (P)-electric field (E) hysteresis loops of all BCTSn-CFO composites including, that of pure BCTSn under a maximum applied electric field of 20 $kV.cm^{-1}$ are shown in Fig. 7. The ferroelectric hysteresis loops were measured at a frequency of 10 Hz. The obtained hysteresis loops confirm the ferroelectric nature of all composites. In addition, electrcic coercive field (E_c), maximal polarization (P_{max}) and remanent polarization (P_r) were extracted from Fig. 7 and are listed in Table 3. It should be noted that compared to BCTSn, all composites exhibit lower Pr and higher Ec. This can be explained by the lossy nature of the composites, which increases when conductive ferrite particles are added. It is also worth noting that the values of P_{max} decrease as CFO content in composites increases. In reality, the electric dipoles in ferroelectric systems are arranged in a specific order. However, due to the presence of ferrites, the long-range ordering of these electric dipoles is disrupted, thus reducing the electric polarization. Furthermore, the increased CFO concentration around BCTSn particles in the composite inhibits the movement of domain walls within BCTSn grains. As a result, when a strong electric field is applied, the

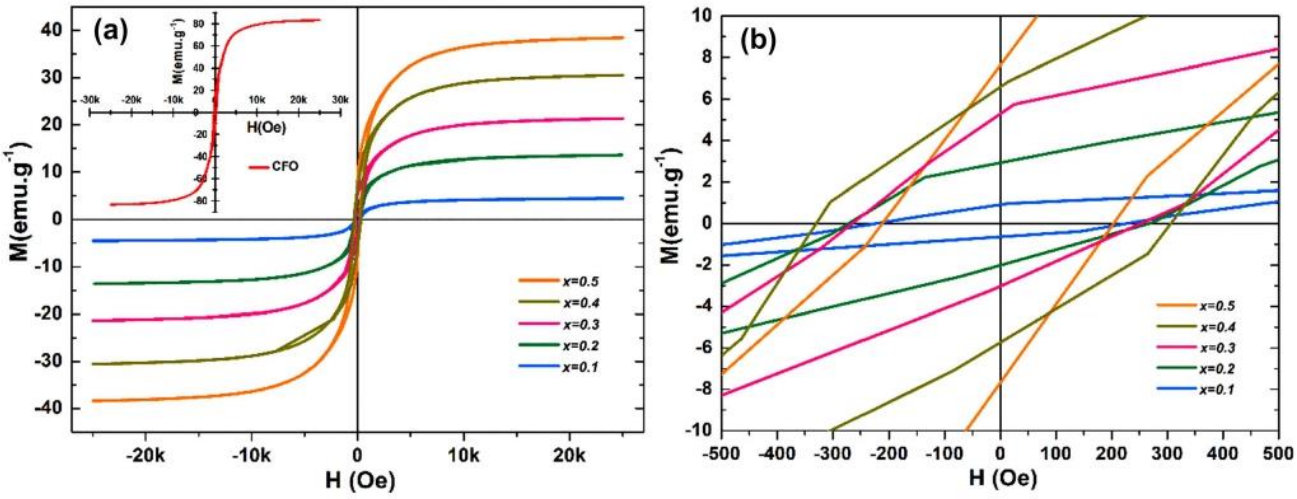

Fig. 6 **a** Magnetic hysteresis loops of the particulate composites (1-x) BCTSn—(x) CFO with $x = 0.10$, 0.20, 0.30, 0.40, and 1.0 measured at room temperature (Inset shows M–H curve of pure CFO). **b** Enlarged view of room-temperature M–H curve of all compositions

Table 2 Different magnetic parameters are determined using the hysteresis loop H_c,M_r, M_s, and $M_r/M_s$for different compositions

Composite (1-x) BCTSn—(x) CFO	H_c: magnetic coercive field (Oe)	M_r: remanent magnetization (emu g^{-1})	M_s: saturation magnetization (emu g^{-1})	M_r/M_s reduced magnetization
Pure CFO [34]	284	14.96	83.00	0.1802
$x = 0.5$	203.81	7.38	38.41	0.1921
$x = 0.4$	305.66	6.18	30.61	0.2018
$x = 0.3$	253.35	4.23	21.38	0.1978
$x = 0.2$	268.58	2.72	13.66	0.1991
$x = 0.1$	228.94	0.88	4.53	0.1942

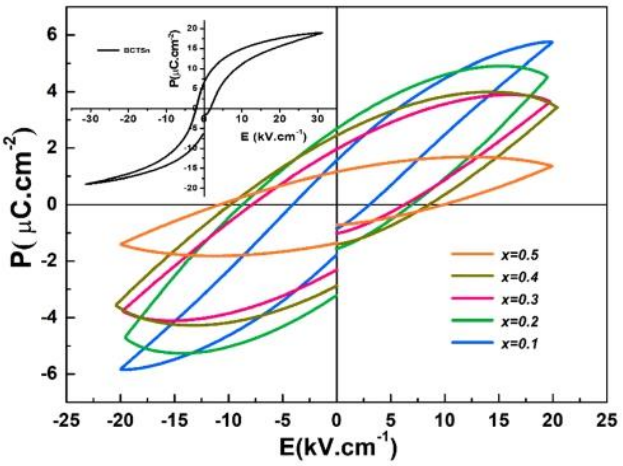

Fig. 7 Ferroelectric hysteresis loops of the particulate composites (1-x) BCTSn—(x) CFO with $x = 0.10, 0.20, 0.30, 0.40$, and 0.0 at room temperature (inset shows P–E curve of pure BCTSn)

BCTSn matrix cannot generate dipoles, reducing of ferroelectric polarization [19, 41]. It should be pointed out that the applied electric field of pristine BCTSn reaches 30 $kV.cm^{-1}$, compare to 20 $kV.cm^{-1}$ of multiferroic composite, explained by the conductivity of the CFO ferromagnetic phase. This can minimize the composite's piezoelectric properties and thus its magnetoelectric properties.

3.4 Piezoelectric properties

Figure 8 shows the variation of large-signal piezoelectric coefficient (also known as converse piezoelectric coefficient) as a function of CFO content. Electrical poling is required to investigate the piezoelectric properties of composites due to the random orientation of domains in the as-prepared material. Indeed, the ferroelectric domains become aligned with the applied electric field used in poling process, accumulating positive and negative electric charge at the grains' sides, resulting in an internal electric field that can improve the piezoelectric properties. For this, all pellet samples were polarized under an electric field of 20 $kV.cm^{-1}$ at room temperature. The values of converse piezoelectric coefficient (d^*_{33}) of the (1-x) BCTSn—(x) CFO composites decrease from 203 $pm.V^{-1}$ in pure BCTSn to 27 $pm.V^{-1}$ when the content of CFO increases from x = 0 to x = 0.5. When compared to the d^*_{33} reported by Zhu et al., the maximum d^*_{33} of 203 $pm.V^{-1}$ obtained for pure BCTSn is not strictly the saturated piezoelectric value[42]. This could be due to our ceramic's low density as a result of its low sintering temperature of 1300 °C for 4 h, as well as the low electrical field used for poling the samples. Furthermore, due to the

Table 3 Different magnetic parameters determined using the hysteresis loops. E_c, P_r, and P_{max} for different compositions

Composite (1-x) BCTSn—(x) CFO	E_c: coercive field ($kV.cm^{-1}$)	P_r: remanent polarization ($\mu C.cm^{-2}$)	P_{max}:maximal polarization ($\mu C.cm^{-2}$)
$x = 0$ [33]	1.68	6.77	18.93
$x = 0.1$	3.03	1.55	5.74
$x = 0.2$	6.95	2.67	4.91
$x = 0.3$	6.26	1.95	4.01
$x = 0.4$	8.53	2.44	3.97
$x = 0.5$	9.84	1.16	1.69

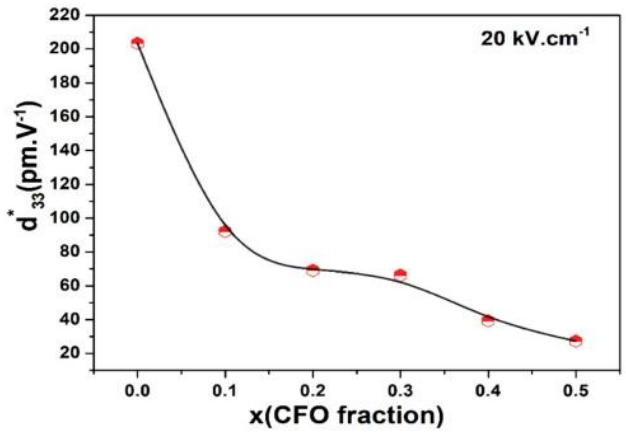

Fig. 8 Variation of the large-signal piezoelectric coefficient d^*_{33} of the composites (1-x) BCTSn—(x) CFO with $x = 0.10$, 0.20, 0.30, 0.40, and 0.50 at 10 Hz frequency at the room temperature

conducting nature of ferrite, ceramic polarization will be extremely difficult. As a result, with the addition of the CFO, the piezoelectricity decreases. In short, the piezoelectric properties are generally influenced by density, grain size, sintering temperature, *and poling conditions*.

3.5 Magnetoelectric properties

The ME effect can be described by the ME voltage coefficient(α_{ME}), which can be calculated by the following relation [43]:

$$\alpha_{ME} = \left(\frac{\partial E}{\partial H}\right) = \frac{V}{d \times H} \quad (2)$$

where V is the induced ME voltage across the sample, d represents the thickness of the sample and H is the applied magnetic field.

Magnetoelectric coupling was studied for the (1-x) BCTSn- (x) CFO samples at room temperature using a dynamical method [44]. The sample was firstly poled at 295 K in the field of 20–25 kV.cm^{-1}. Then the magnetoelectric current or voltage induced by a weak *ac* magnetic field of $H_{ac} = 1.8$ Oe at frequency 400–600 Hz was measured at room temperature as a function of the *dc* bias field utilizing a high-sensitive lock-in-amplifier [44, 45]. Both magnetic fields were applied normal to the surface of the sample. In every experiment, more than two runs were repeated with a reversed direction of *dc* magnetic field, resulting in a change of signal sign. In this way, a possible spurious electromagnetic induction signal was distinguished from a true ME whose sign depends on the polarization × magnetic field product [6]. The measured data for four samples ($x = 0.1$, 0.2, 0.3, and 0.4) are shown in Fig. 9. The ME response increases with the increase in the CFO magnetic content up to $x = 0.3$, and then it sharply decreases at further the growth of the CFO phase (inset Fig. 9). This is related to the fact that at $x > 0.4$, the sample cannot be well poled and there excises some optimal ratio between ferroelectric and magnetic components [5]. Indeed, increasing the CFO content (above 30%) reduces the composite's overall resistivity and charge leakage due to an increase in migratory electrons along the interface between the two phases. Consequently, electric poling becomes more difficult to create dipole by applying a magnetic field, resulting in a reduction in ME coupling in composites [19]. The ME coefficient has a maximum at the field of about 2.5 kOe related to the maximal values of the derivative of the strain on H value and approximately coincides with the maximum of the dM/dH (i.e., magnetic susceptibility) value. There is also a weak hysteresis in the ME response attributed to hysteresis in the M-H loops.

This ME coupling is explained by the fact that the magnetic field creates a strain in the ferrite phase, and the strain causes stress in the ferroelectric phase due to the mechanical interactions of the ferrite and perovskite phases. Because stress promotes polarization, a voltage is produced in the grains [46]. As a result, the area of the interface between ferroelectric and ferromagnetic grains is critical in this type of strain-mediated ME coupling [47].

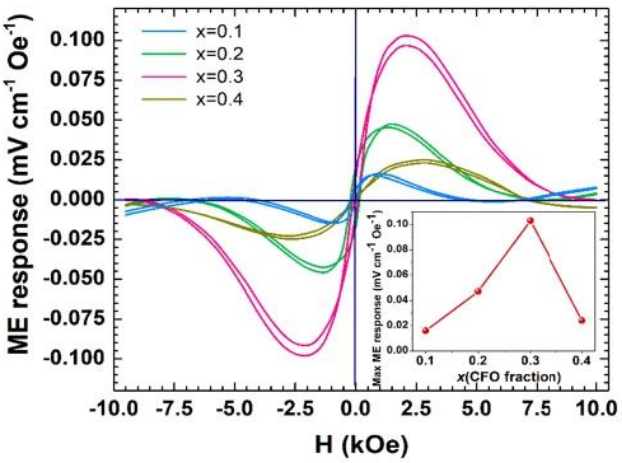

Fig. 9 Amplitude of the ME coupling coefficient for the samples with $x = 0.1$, 0.2, 0.3, and 0.4 as a function of the *dc* magnetic field

If we compare our data with similar data published for $BaTiO_3$ – $CoFe_2O_4$ ceramic composites, one can notice that the ME voltage coefficient in the studied by us BCTSn – CFO composites is weaker than that in the $BaTiO_3$—$CoFe_2O_4$ system where it is mainly in the range 0.14—0.2 $mV.cm^{-1}$ Oe^{-1} but strongly depends on method the of preparation [47]. Other comparable results on multiferroic composites have been published by various research groups [48–52]. It is expected that the efficiency of ME coupling in BCTSn – CFO ceramic composites can be substantially enhanced through variation of the sizes and shapes of the grains of FE and FM phases as well as the synthesis of core–shell nanostructures.

4 Conclusion

To conclude, a new magnetoelectric (1–x) BCTSn—(x) CFO lead-free (0–3) particulate composites have been successfully synthesized by mechanical mixing of the individual ferroic phases. The composites' structure, ferroelectric, magnetic, and magnetoelectric properties were studied. XRD, Raman and SEM analysis confirm the coexistence of perovskite BCTSn and spinel CFO phases and phase purity. Ferroelectric and magnetic hysteresis loop measurements demonstrated that the BCTSn-CFO lead-free composites have multiferroic characteristics at room temperature. Converse piezoelectric coefficient (d^*_{33}) was measured and reported here for the all composites. The largest ME coefficient is 0.1 mv cm^{-1} Oe^{-1} measured in 0.7BCTSn-0.3CFO composition, which is close to pseudocubic symmetry and relatively dense, reducing lattice strain and hence promoting domain switching. The obtained magnetoelectric results of the BCTSn-CFO composites might be improved by varying the sizes and grain morphology in the FE and FM phases, as well as the design of other nanostructured couplings between the magnetic and ferroelectric components.

Acknowledgements

This research is financially supported by the European Union Horizon 2020 Research and Innovation actions MSCA-RISE-ENGIMA (No. 778072), MSCA-RISE-MELON (No. 872631), FAPESP and CNPq, Brazilian agencies.

Author contributions

All authors certify that they have participated sufficiently in the work to take public responsibility for the content. Furthermore, each author certifies that this work will not be submitted to other journal or published in any other publication before. YH: contributed to investigation, methodology, data curation, writing original draft, and validation. DM: contributed to visualization, methodology, writing—review and editing, validation, and supervision. MA: contributed to visualization, writing—review and editing, validation, and supervision. NO: contributed to formal analysis, writing—review and editing, and validation. YG: contributed to formal analysis, writing, validation, and supervision. ZK: contributed to writing—review and editing, visualization, and validation. VL: contributed to writing—review and editing, visualization, and validation. YK: contributed to review and editing, visualization, and validation. KH: contributed to review and editing, visualization, and validation. MEM: contributed to visualization, validation, writing—review and editing, and supervision.

Funding

The European Union's Horizon 2020 research; MSCA-RISE-ENGIMA (No. 778072); MSCA-RISE-MELON (No. 872631).

Data availability

Not applicable.

Code availability

Not applicable.

Declarations

Conflicts of interest Not applicable.

Ethica approval Not applicable.

Consent to participate We confirm that all authors mentioned in the manuscript have participated in, read and approved the manuscript, and have given

their consent for the submission and subsequent publication of the manuscript.

Consent for publication We confirm that all the authors mentioned in the manuscript have agreed to publish this paper.

References

1. J. Ma, J. Hu, Z. Li, C.W. Nan, Recent progress in multiferroic magnetoelectric composites: from bulk to thin films. Adv. Mater. (2011). https://doi.org/10.1002/chin.201118183
2. B. Xiao, W. Zheng, Y. Dong, N. Ma, P. Du, Multiferroic ceramic composite with in situ glassy barrier interface and novel electromagnetic properties. J. Phys. Chem. (2014). https://doi.org/10.1021/jp411167g
3. Y. Zhu, J. Shen, K. Zhou, C. Chen, X. Yang, C. Li, Multifunctional magnetic composite microspheres with in situ growth au nanoparticles: a highly efficient catalyst system. J. Phys. Chem. C **115**(5), 1614–1619 (2011). https://doi.org/10.1021/jp109276q
4. W. Eerenstein, N.D. Mathur, J.F. Scott, Multiferroic and magnetoelectric materials. Nature **442**(7104), 759–765 (2006). https://doi.org/10.1038/nature05023
5. C.W. Nan, M.I. Bichurin, S. Dong, D. Viehland, G. Srinivasan, Multiferroic magnetoelectric composites: historical perspective, status, and future directions. J. Appl. Phys. **103**(3), 031101 (2008). https://doi.org/10.1063/1.2836410
6. M. Fiebig, Revival of the magnetoelectric effect. J. Phys. D: Appl. Phys. **38**(8), R123–R152 (2005). https://doi.org/10.1088/0022-3727/38/8/R01
7. M. Etier, V.V. Shvartsman, S. Salamon, Y. Gao, H. Wende, D.C. Lupascu, The direct and the converse magnetoelectric effect in multiferroic cobalt ferrite-barium titanate ceramic composites. J. Am. Ceram. Soc. **99**(11), 3623–3631 (2016). https://doi.org/10.1111/jace.14362
8. V.V. Shvartsman, F. Alawneh, P. Borisov, D. Kozodaev, D.C. Lupascu, Converse magnetoelectric effect in $CoFe_2O_4$–$BaTiO_3$ composites with a core–shell structure. Smart Mater. Struct. **20**(7), 075006 (2011). https://doi.org/10.1088/0964-1726/20/7/075006
9. S. Ben Moumen et al., Structural, dielectric and magnetic studies of (0–3) type multiferroic (1–x) BaTi0.8Sn0.2O3–(x) La0.5Ca0.5MnO3 ($0 \leq x \leq 1$) composite ceramics. J. Mater. Sci.: Mater. Electron. **31**(21), 19343–19354 (2020). https://doi.org/10.1007/s10854-020-04468-3
10. H.J. Xiang, S.H. Wei, M.H. Whangbo, J.L.F. Da Silva, Spin-orbit coupling and ion displacements in multiferroic TbMnO3. Phys. Rev. Lett. **101**(3), 037209 (2008). https://doi.org/10.1103/PhysRevLett.101.037209
11. C.-Y. Kuo et al., Single-domain multiferroic BiFeO3 films. Nat. Commun. **7**(1), 12712 (2016). https://doi.org/10.1038/ncomms12712
12. P.R. Mickel, H. Jeen, P. Kumar, A. Biswas, A.F. Hebard, Proximate transition temperatures amplify linear magnetoelectric coupling in strain-disordered multiferroic BiMnO 3. Phys. Rev. B. **93**(13), 134205 (2016). https://doi.org/10.1103/PhysRevB.93.134205
13. A. Jain, Y.G. Wang, N. Wang, Y. Li, F.L. Wang, Tuning the dielectric, ferroelectric and electromechanical properties of Ba0.83Ca0.10Sr0.07TiO3–MnFe2O4 multiferroic composites. Ceram. Int. **46**(6), 7576–7585 (2020). https://doi.org/10.1016/j.ceramint.2019.11.257
14. M. Hadouchi, F.L. Marrec, Z. Mahhouti, J. Belhadi, M.E. Marssi, A. Lahmar, Enhanced magnetization in multiferroic nanocomposite Bi0.9Gd0.1Fe0.9Mn0.05X0.05O3 (X= Cr, Co) thin films. Thin Solid Films. **709**, 138025 (2020). https://doi.org/10.1016/j.tsf.2020.138025
15. P.J. Praveen, V.R. Monaji, S.D. Kumar, V. Subramanian, D. Das, Enhanced magnetoelectric response from lead-free (Ba0.85Ca0.15)(Zr0.1Ti0.9)O3 – CoFe2O4 laminate and particulate composites. Ceram. Int. **44**(4), 4298–4306 (2018). https://doi.org/10.1016/j.ceramint.2017.12.018
16. H. Yang, J. Zhang, Y. Lin, T. Wang, High Curie temperature and enhanced magnetoelectric properties of the laminated Li0.058(Na0.535K0.48)0.942NbO3/Co0.6 Zn0.4Fe1.7Mn0.3O4 composites. Sci. Rep. **7**(1), 44855 (2017). https://doi.org/10.1038/srep44855
17. M. Lorenz et al., Epitaxial coherence at interfaces as origin of high magnetoelectric coupling in multiferroic $BaTiO_3$–$BiFeO_3$ superlattices. Adv. Mater. Interf. **3**(11), 1500822 (2016). https://doi.org/10.1002/admi.201500822
18. M. Rafique, A. Herklotz, K. Dörr, S. Manzoor, Giant room temperature magnetoelectric response in strain controlled nanocomposites. Appl. Phys. Lett. **110**(20), 202902 (2017). https://doi.org/10.1063/1.4983357
19. L.K. Pradhan, R. Pandey, R. Kumar, M. Kar, Lattice strain induced multiferroicity in PZT-CFO particulate composite. J. Appl. Phys. **123**(7), 074101 (2018). https://doi.org/10.1063/1.5008607
20. M. Naveed-Ul-Haq et al., Strong converse magnetoelectric effect in (Ba, Ca)(Zr, Ti)O3–NiFe2O4 multiferroics: a relationship between phase-connectivity and interface coupling. Acta Materialia **144**, 305–313 (2018). https://doi.org/10.1016/j.actamat.2017.10.048
21. R.A. Bucur, I. Badea, A.I. Bucur, S. Novaconi, Dielectric, ferroelectric and piezoelectric proprieties of GdCoO3 doped

(K0.5Na0.5)NbO3. J. Alloy. Comp. **630**, 43–47 (2015). https://doi.org/10.1016/j.jallcom.2015.01.030
22. L.Q. Cheng, J.F. Li, A review on one dimensional perovskite nanocrystals for piezoelectric applications. J. Mater. **2**(1), 25–36 (2016). https://doi.org/10.1016/j.jmat.2016.02.003
23. Q. Lou et al., Ferroelectric properties of Li-doped $BaTiO_3$ ceramics. J. Am. Ceram. Soc. **101**(8), 3597–3604 (2018). https://doi.org/10.1111/jace.15480
24. M. Acosta et al., $BaTiO_3$ -based piezoelectrics: fundamentals, current status, and perspectives. Appl. Phys. Rev. **4**(4), 041305 (2017). https://doi.org/10.1063/1.4990046
25. B. Asbani et al., Dielectric permittivity enhancement and large electrocaloric effect in the lead free (Ba0.8Ca0.2)1-xLa2x/3TiO3 ferroelectric ceramics. J. Alloy. Comp. **730**, 501–508 (2018). https://doi.org/10.1016/j.jallcom.2017.09.301
26. D. Fu, M. Itoh, S. Koshihara, T. Kosugi, S. Tsuneyuki, Anomalous phase diagram of ferroelectric (Ba, Ca) TiO 3 single crystals with giant electromechanical response. Phys. Rev. Lett. **100**(22), 227601 (2008). https://doi.org/10.1103/PhysRevLett.100.227601
27. Y. Yao et al., Large piezoelectricity and dielectric permittivity in $BaTiO_3$ –$xBaSnO_3$ system: the role of phase coexisting. EPL **98**(2), 27008 (2012). https://doi.org/10.1209/0295-5075/98/27008
28. N. Horchidan et al., Multiscale study of ferroelectric–relaxor crossover in BaSnxTi1−xO3 ceramics. J. European Ceram. Soc. **34**(15), 3661–3674 (2014). https://doi.org/10.1016/j.jeurceramsoc.2014.06.005
29. W. Liu, X. Ren, Large piezoelectric effect in Pb-free ceramics. Phys. Rev. Lett. **103**(25), 257602 (2009). https://doi.org/10.1103/PhysRevLett.103.257602
30. W. Liu, L. Cheng, S. Li, Prospective of (BaCa)(ZrTi)O3 lead-free piezoelectric ceramics. Crystals **9**(3), 179 (2019). https://doi.org/10.3390/cryst9030179
31. V. Madhu Babu, J. Paul Praveen, D. Das, Synthesis and aging behaviour study of lead-free piezoelectric BCZT ceramics. Chem. Phys. Lett. **772**, 138560 (2021). https://doi.org/10.1016/j.cplett.2021.138560
32. L.F. Zhu, B.P. Zhang, L. Zhao, J.-F. Li, High piezoelectricity of $BaTiO_3$ –$CaTiO_3$ –$BaSnO_3$ lead-free ceramics. J. Mater. Chem. C **2**(24), 4764–4771 (2014). https://doi.org/10.1039/C4TC00155A
33. Y. Hadouch et al., Electrocaloric effect and high energy storage efficiency in lead-free Ba0.95Ca0.05Ti0.89Sn0.11O3 ceramic elaborated by sol–gel method. J. Mater. Sci. (2022). https://doi.org/10.1007/s10854-021-07411-2
34. Y. Hadouch, Enhanced relative cooling power and large inverse magnetocaloric effect of cobalt ferrite nanoparticles synthesized by auto-combustion method. J. Magnetism Magnetic Mater. (2022). https://doi.org/10.1016/j.jmmm.2022.169925
35. Z. Mahhouti et al., Chemical synthesis and magnetic properties of monodisperse cobalt ferrite nanoparticles. J. Mater. Sci.: Mater. Electron. **30**(16), 14913–14922 (2019). https://doi.org/10.1007/s10854-019-01863-3
36. J. Paul Praveen, M.V. Reddy, J. Kolte, S. Dinesh Kumar, V. Subramanian, D. Das, Synthesis, characterization, and magneto-electric properties of (1–x)BCZT- x CFO ceramic particulate composites. Int. J. Appl. Ceram. Technol. **14**(2), 200–210 (2017). https://doi.org/10.1111/ijac.12640
37. J. Rani, K.L. Yadav, S. Prakash, Dielectric and magnetic properties of x CoFe 2 O 4 –(1–x)[0.5Ba(Zr 0.2 Ti 0.8)O 3–0.5(Ba 0.7 Ca 0.3)TiO 3] composites. Mater. Res. Bulletin **60**, 367–375 (2014). https://doi.org/10.1016/j.materresbull.2014.09.013
38. M.G. Majumdar, Analysis of stress-coupled magneto-electric effect in BaTiO3–CoFe2O4 composites using raman spectroscopy. Int. J. Sci. Eng. Res. **3**(11), 8 (2012)
39. M. Zahid et al., Enhanced near-ambient temperature energy storage and electrocaloric effect in the lead-free BaTi0.89Sn0.11O3 ceramic synthesized by sol–gel method. J. Mater. Sci.: Mater. Electron. **33**(16), 12900–12911 (2022). https://doi.org/10.1007/s10854-022-08233-6
40. S. Dabas, P. Chaudhary, M. Kumar, S. Shankar, O.P. Thakur, Structural, microstructural and multiferroic properties of BiFeO3–CoFe2O4 composites. J. Mater. Sci.: Mater. Electron. **30**(3), 2837–2846 (2019). https://doi.org/10.1007/s10854-018-0560-5
41. A.S. Kumar, C.S.C. Lekha, S. Vivek, K. Nandakumar, M.R. Anantharaman, S.S. Nair, Effect of CoFe2O4 weight fraction on multiferroic and magnetoelectric properties of (1–x)Ba0.85Ca0.15Zr0.1Ti0.9O3−xCoFe2O4 particulate composites. J Mater. Sci.: Mater. Electron. **30**(9), 8239–8248 (2019). https://doi.org/10.1007/s10854-019-01140-3
42. L.-F. Zhu et al., Phase transition and high piezoelectricity in (Ba, Ca)(Ti 1–x Sn x)O 3 lead-free ceramics. Appl. Phys. Lett. **103**(7), 072905 (2013). https://doi.org/10.1063/1.4818732
43. M. Breitenbach, H. Deniz, S.G. Ebbinghaus, Magnetoelectric and HR-STEM investigations on eutectic CoFe2O4–Ba1–xSrxTiO3 composites. J. Phys. Chem. Solids **135**, 109076 (2019). https://doi.org/10.1016/j.jpcs.2019.109076
44. M.M. Vopson, Y.K. Fetisov, G. Caruntu, G. Srinivasan, Measurement techniques of the magneto-electric coupling in multiferroics. Materials **10**(8), 963 (2017). https://doi.org/10.3390/ma10080963
45. V.V. Laguta et al., Room-temperature paramagnetoelectric effect in magnetoelectric multiferroics Pb(Fe1/2Nb1/2)O3 and its solid solution with PbTiO3. J. Mater. Sci. **51**(11),

5330–5342 (2016). https://doi.org/10.1007/s10853-016-9836-4

46. A.A. Momin, M.A. Zubair, Md.F. Islam, A.K.M.A. Hossain, Enhance magnetoelectric coupling in xLi0.1-Ni0.2Mn0.6Fe2.1O4–(1–x)BiFeO3 multiferroic composites. J. Mater. Sci: Mater. Electron. **30**(14), 13033–13046 (2019). https://doi.org/10.1007/s10854-019-01665-7
47. A. Plyushch et al., Magnetoelectric coupling in nonsintered bulk BaTiO3–xCoFe2O4 multiferroic composites. J. Alloy. Comp. **917**, 165519 (2022). https://doi.org/10.1016/j.jallcom.2022.165519
48. D.S.F. Viana et al., Synthesis and multiferroic properties of particulate composites resulting from combined size effects of the magnetic and ferroelectric phases. Ceram. Int. **48**(1), 931–940 (2022). https://doi.org/10.1016/j.ceramint.2021.09.177
49. R.-F. Zhang, C.-Y. Deng, L. Ren, Z. Li, J.-P. Zhou, Dielectric, ferromagnetic and maganetoelectric properties of BaTiO3–Ni0.7Zn0.3Fe2O4 composite ceramics. Mater. Res. Bulletin **48**(10), 4100–4104 (2013). https://doi.org/10.1016/j.materresbull.2013.06.026
50. R. Köferstein, F. Oehler, S.G. Ebbinghaus, Fine-grained magnetoelectric Sr0.5Ba0.5Nb2O6–CoFe2O4 composites synthesized by a straightforward one-pot method. Mater. Chem. Phys. **278**, 125616 (2022). https://doi.org/10.1016/j.matchemphys.2021.125616
51. C.M. Kanamadi et al., Dielectric and magnetic properties of (x)CoFe2O4+(1–x)Ba0.8Sr0.2TiO3 magnetoelectric composites. Mater. Chem. Phys. **116**(1), 6–10 (2009). https://doi.org/10.1016/j.matchemphys.2009.03.003
52. S.S. Chougule, D.R. Patil, B.K. Chougule, Electrical conduction and magnetoelectric effect in ferroelectric rich (x)Ni0.9Zn0.1Fe2O4+(1–x)PZT ME composites. J. Alloy. Comp. **452**(2), 205–209 (2008). https://doi.org/10.1016/j.jallcom.2006.11.020

ACS APPLIED NANO MATERIALS

www.acsanm.org Article

Multiferroic $CoFe_2O_4$–$Ba_{0.95}Ca_{0.05}Ti_{0.89}Sn_{0.11}O_3$ Core–Shell Nanofibers for Magnetic Field Sensor Applications

Youness Hadouch,* Daoud Mezzane, M'barek Amjoud, Valentyn Laguta, Khalid Hoummada, Voicu Octavian Dolocan, Mustapha Jouiad, Mohammed Lahcini, Hana Uršič, Val Fišinger, Nikola Novak, Zdravko Kutnjak, Yaovi Gagou, Igor Lukyanchuk, and Mimoun El Marssi

Cite This: https://doi.org/10.1021/acsanm.3c01101 Read Online

ACCESS | Metrics & More | Article Recommendations

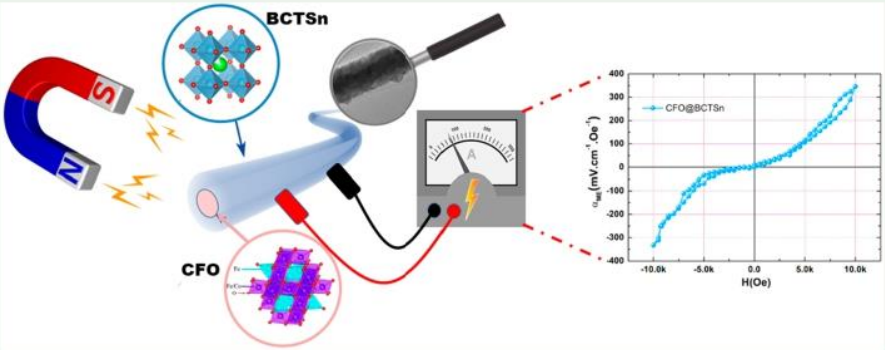

ABSTRACT: Multiferroic materials with coexisting of at least two ferroic orders (ferromagnetic, ferroelectric, or ferroelastic) have recently attracted the interest of researchers due to their potential applications as multifunctional devices. Herein, we report the synthesis and detailed characterization of the multiferroic $CoFe_2O_4$–$Ba_{0.95}Ca_{0.05}Ti_{0.89}Sn_{0.11}O_3$ core–shell nanofibers (CFO@BCTSn NFs) prepared by a sol–gel coaxial electrospinning technique. The scanning and transmission electron microscopes were used to check nanofibers' core–shell structure/configuration, with fiber diameters ranging from 150 to 250 nm. The X-ray diffraction analysis confirms the presence of both the spinel structure of the CFO and the perovskite structure of the BCTSn. Piezoresponse force microscopy and magnetic hysteresis were used to confirm the multiferroicity of CFO@BCTSn NFs. Notably, the maximum magnetization and remanent magnetization of NFs are found to be 11.63 emu g^{-1} and 1.43 emu g^{-1}, respectively. Meanwhile, the maximum piezoelectric response d_{33}^{eff} is around 6 pm V^{-1}. The magnetoelectric (ME) coefficient obtained for the CFO@BCTSn NFs is 346 mV cm^{-1} Oe^{-1} at the field of 10 kG. These findings may lead to development of nanoscale Pb-free magnetic field sensors and magnetoelectric device applications.

KEYWORDS: *core–shell, nanofiber, electrospinning, piezoelectric, multiferroic, magnetoelectric*

1. INTRODUCTION

Magnetoelectric materials have attracted much attention in recent years.[1,2] The coupling between the electric and the magnetic ordering, can convert an electric field into a magnetic field and vice versa via the mechanical interactions between the ferroelectric and ferromagnetic phases.[3] This provides access to several technology applications, such as multiple-state memory devices that can be written electrically and read magnetically, electrically controlled microwave phase shifter or voltage-controlled ferromagnetic resonance, magnetically controlled electro-optic or piezoelectric devices, magnetoelectric memory cells, and ultrasensitive magnetic sensors, which have received a lot of attention in recent years.[4−10]

Two types of magnetoelectric materials exist: (i) Single-phase multiferroic materials have electric and magnetic fields intrinsically coupled.[11,12] However, magnetoelectric couplings in these types of materials are typically very weak.[13] (ii) Multiphase composites consist of distinct piezoelectric and magnetostrictive phases that are spatially segregated and interconnected through an interface. The magnetoelectric coupling is induced indirectly via a strain interaction between piezoelectric and magnetostrictive effects.[14−25] In addition to conventional solid-state multiferroic materials, multiferroic

Received: March 14, 2023
Accepted: May 22, 2023

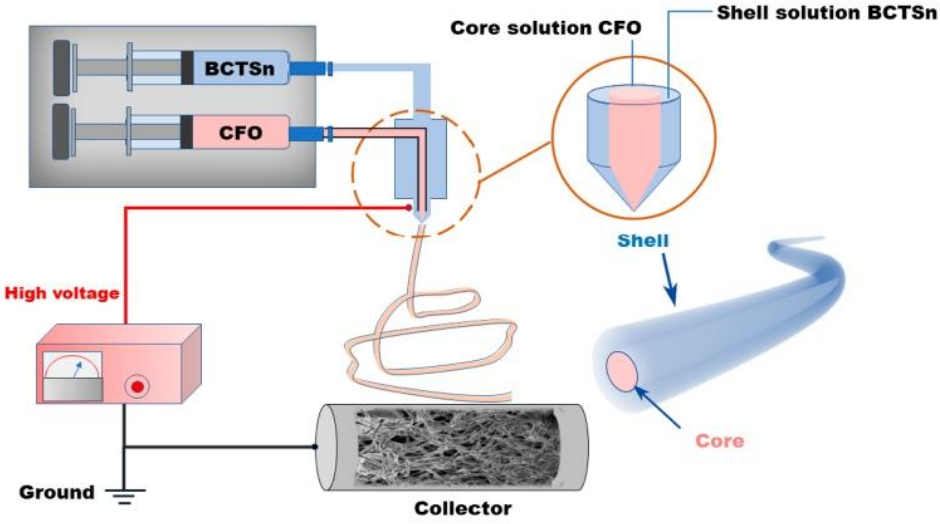

Figure 1. Coaxial electrospinning of core−shell nanofibers: setup schematics.

fluids have been proposed and can exhibit a substantial magnetoelectric effect. They are elaborated by dispersing ferromagnetic and ferroelectric particles in an insulating base fluid to create a multiferroic fluid.[26−29]

The significant factor in achieving strong ME effects in these composites is to transfer as much strain as possible from one phase of the composite to another.[2,30] Consequently, the interface area between ferromagnetic and ferroelectric grains plays a crucial role in the strain-mediated ME coupling in this type of composites.[24,31−34]

Many approaches and designs have been investigated to create hybrid multiferroic composites, called connectives, including 0−3, 2−2, and 1−3 type connectivity.[25,35] The most studied type of connectivity is 0−3, also known as particulate composites.[14,16−18,22,36−43] In this type, the magnetic particles are enclosed by the piezoelectric phase. Specifically, these composites are made by combining the piezoelectric and magnetostrictive phases, resulting in inhomogeneous dispersion of the magnetic phase and agglomeration of these particles due to their attractive nature and surface energy. Agglomeration reduces the interface surface between the two ferroic phases, lowering the ME effect.[25] In addition to conventional solid-state multiferroic materials, multiferroic fluids have also been proposed, and they can show a very strong magnetoelectric effect.

Based on this, the best way to intimate the contact between the two phases in ceramic multiferroic materials is to create one-dimensional (1D) interfaces at the nanoscale.[44,45] The coaxial core−shell nanofibers, with a large interfacial surface and high surface-to-volume ratio, are the most commonly recommended for meeting these requirements.[23,31−33,46] Several techniques, such as template-assistant approaches, hydrothermal methods, and electrospinning techniques, have been used to create 1D multiferroic nanocomposites.[47,48] In particular, electrospinning is a feasible and adaptable method for creating multiferroic composite NFs with ultralong and continuous structures. It offers a number of benefits in practice, including the ability to regulate the nanostructures' size, the high aspect ratio, and the low cost efficiency. Additionally, it is possible to easily control the properties of nanofibers using electrospinning parameters like the electric field, solution viscosity, humidity, and annealing temperature.[49,50] On a fundamental level, the study of multiferroic nanofibers presents a particular interest. Exotic polar topological states, like vortex and helix polarization tubes, were predicted but not yet confirmed experimentally.[51−55] However, understanding of the coupling of such topological formations with magnetism is on track. In a theoretical study published 13 years ago, Zhang et al. showed that nanofiber composites have orders of magnitude stronger magnetoelectric responses than multiferroic composite thin films of similar compositions.[1] Despite all of these benefits, very few studies have reported the synthesis of nanostructured composite fibers using a sol−gel-assisted electrospinning technique. Furthermore, a small portion of these studies has focused on the magnetoelectric coupling of electrospun fibers.[23,33,56,57] These examples used cobalt ferrite $CoFe_2O_4$ (CFO) as a magnetostrictive phase with a large magnetoelastic coefficient (greater than 200 ppm).[58−61] Due to its significant piezoelectric properties, $PbZr_{0.52}Ti_{0.48}O_3$ (PZT) is the ferroelectric material most frequently used in these composites.[23,24,33,62] Unfortunately, Pb-based material is restricted globally because of its negative environmental impact. Therefore, barium titanate $BaTiO_3$ (BT) and its derivatives are the main alternatives for a Pb-free multiferroic composite.

We have recently reported results obtained on $(1 - x)Ba_{0.95}Ca_{0.05}Ti_{0.89}Sn_{0.11}O_3-xCoFe_2O_4$ particulate composites, and the maximum ME coefficient has been found around 0.1 mV cm^{-1} Oe^{-1} at 2.1 kOe for x = 0.3.[63] This value, while comparable to similar systems, remains low for such a multiferroic application. This study suggests that the efficiency of ME coupling in BCTSn−CFO sintered pellets can be significantly improved by varying the shapes and sizes of the piezoelectric and magnetostrictive phase grains, as well as through the synthesis of core−shell nanostructures.

This work has a dual-fold major goal. First, it aims to elaborate composite core−shell nanofibers with a $CoFe_2O_4$ core and a $Ba_{0.95}Ca_{0.05}Ti_{0.89}Sn_{0.11}O_3$ shell using the electrospinning method. Second, it intends to investigate the structural, morphological, ferroelectric, piezoelectric, magnetic, and magnetoelectric properties of the elaborated CFO@BCTSn NFs.

https://doi.org/10.1021/acsanm.3c01101
ACS Appl. Nano Mater. XXXX, XXX, XXX−XXX

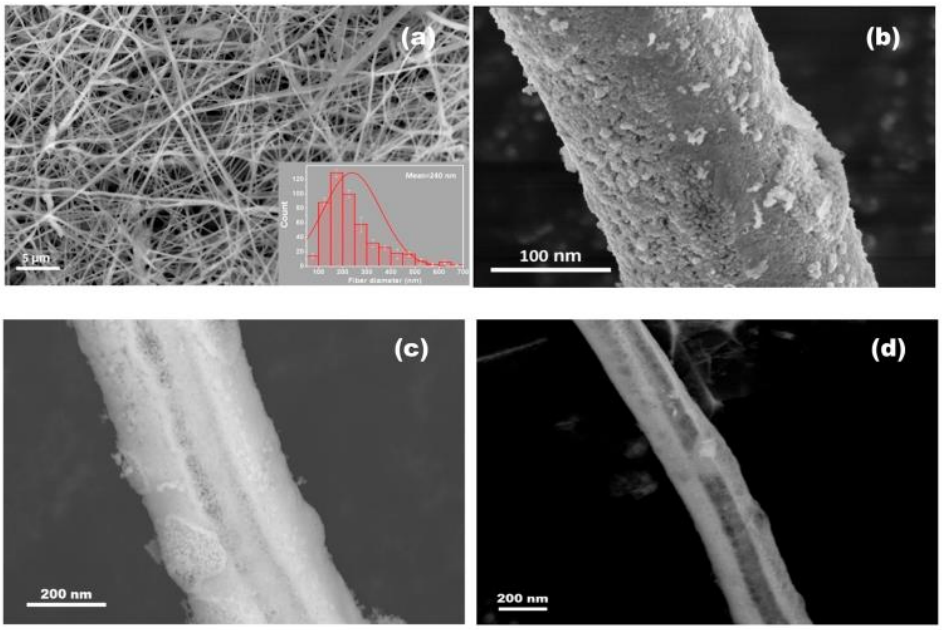

Figure 2. SEM images: (a) annealed CFO@BCTSn NFs. (inset, fiber diameter distribution) and (b–d) annealed single CFO@BCTSn NF.

2. EXPERIMENTAL SECTION

2.1. Material Synthesis. Poly(vinylpyrrolidone) (Alfa Aesar, MW 1300000), barium acetate [$Ba(CH_3COO)_2$, Merck, ≥99.0%], calcium acetate [$Ca(CH_3COO)_2$, Loba Chemie, ≥97.0%], tin chloride dihydrate [$SnCl_2{\cdot}2H_2O)_4$, Fluka, ≥96.0%], titanium(IV) isopropoxide [$C_{12}H_{28}O_4Ti$, Sigma-Aldrich, ≥97.0%], iron nitrate nonahydrate [$Fe(NO_3)_3{\cdot}9H_2O$, Oxford, ≥99.0%], cobalt nitrate hexahydrate [$Co(NO_3)_2{\cdot}6H_2O$, Alfa Aesar, ≥98.0%], ethanol absolute [CH_3CH_2OH, Biosmart, ≥99.9%], acetic acid [$C_2H_4O_2$, VWR Chemicals], 100.0%], 2-methoxyethanol [$C_3H_8O_2$, Oxford, ≥99.0%], and dimethylformamide [C_3H_7NO, Sigma-Aldrich, ≥99.8%] were used to prepare $Ba_{0.95}Ca_{0.05}Ti_{0.89}Sn_{0.11}O_3$ (BCTSn) and $CoFe_2O_4$ (CFO) electrospinning solutions.

CFO@BCTSn nanofibers were prepared by sol–gel process based electrospinning method as follows. For CFO solution, 1 mmol of $(Co(NO_3)_2{\cdot}6H_2O)$ and 2 mmol of $(Fe(NO_3)_3{\cdot}9H_2O)$ were dissolved into a mixed solution of 2 mL of ethanol and 2 mL of DMF and stirred continuously for 3 h. BCTSn precursor solution was synthesized by dissolving a stoichiometric portion of $Ba(CH_3COO)_2$ and $Ca(CH_3COO)_2$ in acetic acid and of $(SnCl_2{\cdot}2H_2O)$ and $(C_{12}H_{28}O_4Ti)$ in 2-methoxyethanol separately. The polymer solution was prepared by dissolving PVP in ethanol under vigorous stirring for 4 h. The CFO and BCTSn solutions were added to the PVP solution and stirred continuously to form homogeneous CFO and BCTSn polymer solutions, with the concentrations of PVP controlled around 0.045 and 0.030 g mL^{-1}, respectively. Individual polymer solutions were transferred into glass syringes for electrospinning. The coaxial spinneret and electrospinning setup are depicted in Figure 1. The spinning process was carried out at dc voltage with a distance of 12 cm between the needle tip and the collector. The BCTSn and CFO polymer solutions were pumped at a rate of 0.5 and 0.3 mL h^{-1}, respectively. The as-spun NFs were dried at 80 °C under vacuum for 12 h before being annealed at 700 °C for 4 h in an air atmosphere.

2.2. Characterizations. The core–shell nanofibers microstructure was analyzed using scanning electron microscopy (SEM) in a HELIOS 600 nanolab from Thermofisher and a (JEOL–ARM200F Cold FEG) high-resolution analytical transmission electron microscope (TEM) operating at 200 kV. The fiber diameter distribution was estimated by ImageJ software based on more than 500 fibers, and the Gaussian function was used to fit the distribution. The apparent density was measured with a pycnometer. The XRD patterns of CFO@BCTSn NFs were performed at room temperature on a Rigaku (SmartLab SE) with Cu Kα radiation ($\lambda_{K\alpha}$ = 1.54056 Å) at a scan rate of 2 deg min^{-1} and an angular scan range (2θ) between 20 and 80°. The local piezoelectric imaging of CFO@BCTSn NFs was performed by an atomic force microscope (AFM, Jupiter XR Asylum Research, Oxford Instruments, CA, USA) equipped with a piezoresponse force module (PFM). Pt-coated silicon tips with a radius of curvature ~ 10 nm (OMCL-AC240TM-R3, Olympus, Japan) were used for the PFM analysis. To prevent the CFO@BCTSn NFs from sticking to the PFM tip, the fibers were fixed to the Si substrate by heating at 600 °C for 30 min. We chose the semiconductive Si substrate to avoid electrical breakdown through the air and short-circuiting between the tip and the conductive substrate when scanning over the fiber edge and touching the substrate with the PFM tip. PFM scanning was performed in virtual ground mode as described in our previous work.[64,65] The images were scanned in dual AC resonance-tracking (DART) mode and in DART lateral mode. An electrical voltage of 4 V and a frequency of ~250 kHz for vertical and ~690 kHz for lateral modes were applied. In the vertical direction, the local PFM amplitude and phase hysteresis loops were measured in DART switching spectroscopy mode (DART-SS). The measurements were performed in off-electric-field mode with the pulsed dc step signal and the superimposed ac drive signal, as described in ref 66. The sequence of rising steps of the dc electric field was driven at 20 Hz and a maximum amplitude of 15 V; the frequency of the triangular envelope was 0.2 Hz; a superimposed sinusoidal ac signal with an amplitude of 4 V and a frequency of ~250 kHz was used. Three cycles were measured. Local piezoelectric values were determined in an off-resonance measurement in PFM single-frequency mode by applying AC voltage with the amplitude 7 V and frequency 240 kHz, which is ~40 kHz below the contact resonance frequency (at 280 kHz). Magnetic properties were measured by demonstrating a magnetic hysteresis (M-H) loop at room temperature using a SQUID magnetometer Quantum Design MPMSXL under a magnetic field range of 0–50 kOe. For magnetoelectric measurements, a conventional Bruker EPR spectrometer EMX plus was used. For this measurement, a rectangular sample with dimensions of 3 × 5 × 0.3 mm^3 was prepared by bonding the nanofibers with epoxy resin. Before the measurement, the sample was coated with silver electrodes and poled at room temperature by applying a dc electric field of 10 kV/cm for 10 min (more details are described in ref 67).

https://doi.org/10.1021/acsanm.3c01101
ACS Appl. Nano Mater. XXXX, XXX, XXX–XXX

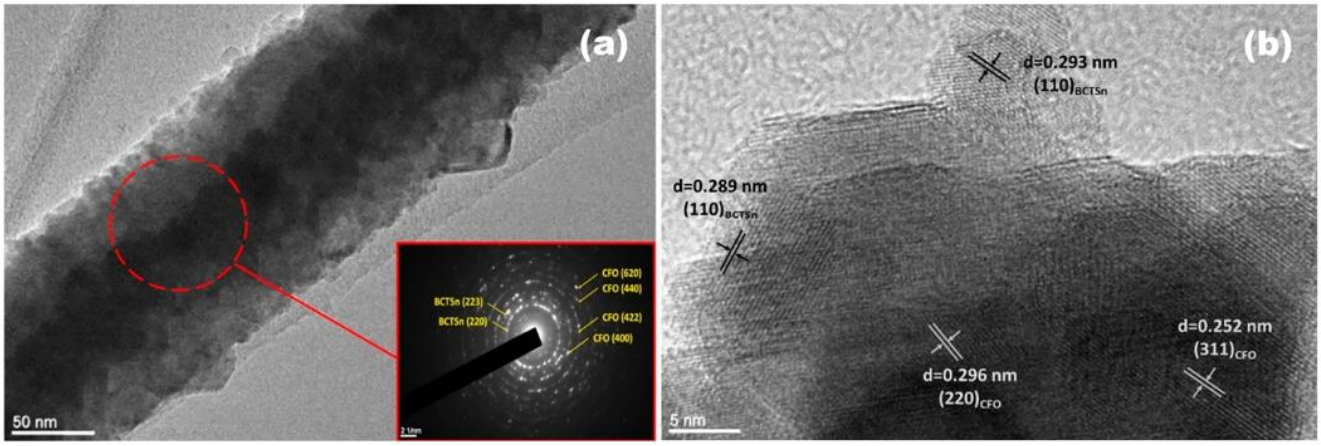

Figure 3. (a) TEM image of CFO@BCTSn NF (inset, diffraction pattern acquired from the red-colored circle) and (b) HRTEM image of CFO@BCTSn NF.

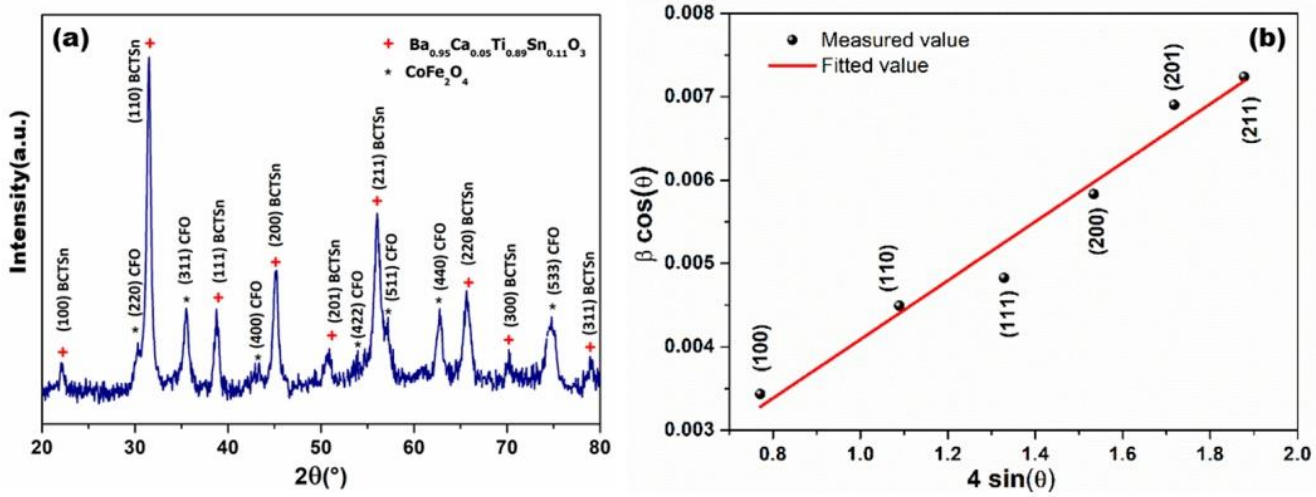

Figure 4. (a) Room-temperature XRD pattern and (b) Williamson–Hall (W–H) plot of CFO@BCTSn NFs.

3. RESULTS AND DISCUSSION

3.1. CFO@BCTSn NFs: Morphology and Structure. The morphologies of the annealed CFO@BCTSn NFs were observed by SEM and TEM. Figure 2a depicts an SEM image of the CFO@BCTSn NFs, demonstrating that individual NFs have a continuous structure with a low relative density of 71% and diameters ranging from 150 to 250 nm. The surface of a single CFO@BCTSn NF is shown in Figure 2b, indicating that the fiber is composed of small grains in the range of tens of nanometers that may be of the BCTSn phase because they form the fiber's shell. Detailed observations of an individual fiber are depicted in Figure 2c,d. The core and shell are well-identified, with a 110 nm diameter CFO core and a 370 nm thick BCTSn shell.

The CFO@BCTSn NFs microstructures were further visualized by TEM. Figure 3a depicts a TEM image of an individual nanofiber made up of nanocrystallites of CFO and BCTSn that are connected individually. Figure 3b illustrates the interference of two crystallographic orientations originating from BCTSn and CFO crystals. The SAED pattern in the inset of Figure 3a obtained from the red-colored-circle zone shows multiple diffraction rings, suggesting a polycrystalline structure of CFO@BCTSn NFs. The crystallographic planes (400), (440), (422), and (620) are assigned to CFO,[68] while the planes (220) and (223) are assigned to BCTSn,[69] confirming the coexistence of both magnetic and ferroelectric phases.

The XRD data of CFO@BCTSn NFs are shown in Figure 4a, where two types of diffraction peaks are seen that agree with the standards for the Spinel structure (JCPDS No. 01-1121) and the perovskite structure (JCPDS No. 31-0174). In addition, the average crystallite size of CFO is approximately 4.4 nm, while that of BCTSn is approximately 5.1 nm, based on a detailed investigation of the peaks broadening of (311) and (100) reflections using the Debye–Scherrer formula.[69]

The lattice strain in the CFO@BCTSn NFs is calculated using the Williamson–Hall (W–H) method.[23] The lattice strain of the composite is estimated by using the peaks in the XRD patterns that correspond to BCTSn, as shown in Figure 4a.

$$\beta \cos\theta = 4\varepsilon \sin\theta + \frac{k\lambda}{D} \quad (1)$$

where k (=0.9) is the shape factor, λ is the wavelength of the X-ray, θ is the peak position in degrees, D is the average crystallite size, ε is the lattice strain, and β is the full width at half-maxima (fwhm). According to eq 1, the plot of $\beta \cos\theta$ vs

https://doi.org/10.1021/acsanm.3c01101
ACS Appl. Nano Mater. XXXX, XXX, XXX–XXX

4 sin θ should be a linear function, with the slope indicating the strain in the sample. In CFO@BCTSn NFs, the lattice strain is 3.64×10^{-3}. This positive value indicates that the strain in the CFO@BCTSn NFs is tensile.[23] It is well-known that lattice strain improves polarization stability and piezoelectric properties in the ferroelectric phase of ME composites.[70,71]

These obtained results confirm the successful preparation of the 1D CFO@BCTSn NFs multiferroic composite material. The multiferroic properties of the CFO@BCTSn NFs are then investigated by measuring their ferromagnetic, ferroelectric, and ME coupling.

3.2. CFO@BCTSn NFs Magnetic Properties. The magnetization vs magnetic field for CFO@BCTSn NFs at 300 K is shown in Figure 5. The M-H loop shows a classical

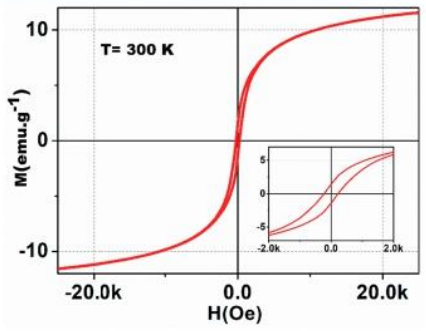

Figure 5. Magnetic hysteresis loops for the CFO@BCTSn NFs at room temperature.

ferromagnetic behavior with a very small paramagnetic component due to the possible interdiffusion of a small number of magnetic atoms in the shell. The inset displays a zoom of the area depicted by the rectangle. We determine a coercive field of 221 Oe, a remanent magnetization M_r of 1.43 emu g^{-1} (only 12% of the maximum value), and a maximum magnetization M_s of 11.63 emu g^{-1} at room temperature. It should be stressed that the magnetization is not completely saturated under 25 kOe. The magnetization was determined using the total mass of the core−shell fibers, and therefore, this value should be taken as a minimum value as the presence of the nonmagnetic BCTSn phase contributed to the total weight of the sample. Its actual value can be several times larger. The M_s of bulk CFO has a value between 80 and 94 emu/g (for an ideal inverse spinel CFO M_s is 71.4 emu g^{-1}).[61,72,73] In 50 BCTSn−50 CFO sintered pellets,[63] a M_s of 38.4 emu g^{-1} was measured, while in pure CFO nanoparticles,[61] the measured M_s was close to the bulk value. In pure CFO fibers elaborated by electrospinning method (image not shown), we find a magnetization of 78.75 emu g^{-1} at room temperature, close to the bulk value. Note that CFO@BCTSn NFs have a smaller squareness ratio (M_r/M_s) than pure CFO bulk, which was determined to be 0.83 when magnetized along the easy axis or 0.46 for the non-oriented material.[74] A low M_r value was also observed in very thin films[75] and in nanoparticles.[76] A higher squareness ratio of 0.19 was measured in CFO@BCTSn pellets.[63] The magnetic properties of materials are significantly influenced by the crystallite size and the method of preparation. For example, Lu et al. presented a comparative investigation on the magnetic properties of nanofibers and nanoparticles and found that the M_s, M_r, and H_c of CFO nanofibers are different than those of nanoparticles.[77] The low squareness ratio at room temperature (which increases to 0.63 at low temperature) could suggest a blocking temperature around or below room temperature, which will be studied in future experiments.

3.3. Ferroelectric Properties of CFO@BCTSn NFs. The vertical and lateral PFM images of the nanofibers on the Si substrate are shown in Figure 6. Comparing the topography panels a and b with the PFM panels c−f, it is clear where the nanofibers are positioned on the Si substrate. The nanofibers

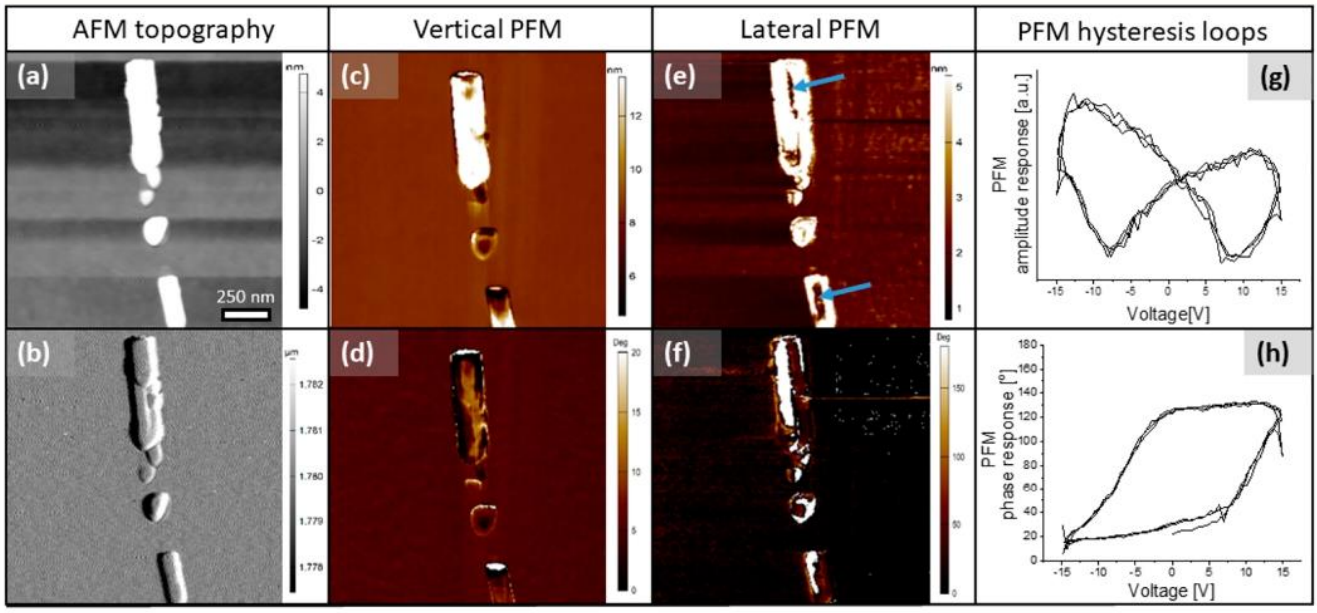

Figure 6. AFM/PFM images of CFO@BCTSn NFs: AFM topography of (a) height and (b) deflection; vertical PFM of (c) amplitude and (d) phase; lateral PFM of (e) amplitude and (f) phase. PFM local hysteresis loops obtained by switching spectroscopy mode: (g) amplitude and (h) phase loops (three cycles).

https://doi.org/10.1021/acsanm.3c01101
ACS Appl. Nano Mater. XXXX, XXX, XXX−XXX

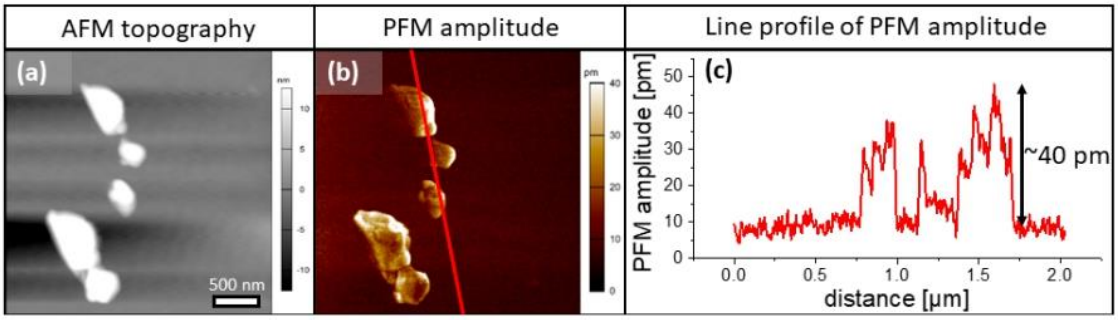

Figure 7. (a) AFM topography: height image. (b) Vertical PFM amplitude image measured in off-resonance PFN single-frequency mode. (c) PFM amplitude: line profile (see red line in panel b) of CFO@BCTSn NFs on Si substrate.

show enhanced piezoelectric response, which can be seen as bright areas in panels c and e, except in the center of the nanofibers visible in the lateral PFM amplitude image, where there is no piezoelectric signal (the dark spots marked with blue arrows). These areas could possibly correspond to the magnetic phase inside the nanofibers. Furthermore, local PFM loops measured in switching spectroscopy mode indicate the switching behavior of ferroelectric domains inside the nanofibers (Figure 6g,h).

To determine the local piezoelectric coefficient d_{33}^{eff} of the prepared nanofibers, the PFM analysis was performed in PFN single-frequency mode (Figure 7) at a frequency of 240 kHz, which is 40 kHz away from the resonant frequency of the tip–sample system (at 280 kHz). More than 10 line profile analyses were extracted; an example is shown in Figure 7c. The maximum piezoelectric response d_{33}^{eff} was 40 pm/7 V ~ 6 pm/V. We are aware that this is only an approximate value for d_{33}^{eff} since the substrate Si is semiconducting. However, we tried to fix the nanofibers also on Pt-coated substrates, but in this case, the plates did not adhere completely to the substrate. Hence, the nanofibers moved during the PFM scan and the analysis was not possible.

3.4. Magnetoelectric Properties of CFO@BCTSn NFs.

The ME coupling coefficient between the BCTSn and CFO phases was calculated using a commonly used formula, as described in our previous study.[63]

$$\alpha_{\text{ME}} = \left(\frac{\partial E}{\partial H}\right) = \frac{V}{dH_{\text{ac}}} \tag{2}$$

d refers for the sample's thickness, V is the induced ME voltage across the sample, and H_{ac} is the applied AC magnetic field.

The room-temperature magnetoelectric coefficient (α_{ME}) of the CFO@BCTSn NFs has been measured by applying an AC magnetic field of 1.78 Oe at a frequency of 564 Hz. When the DC magnetic field is increased, the ME coefficient shows a nonlinear increase, reaching a value of 346 mV cm^{-1} Oe^{-1} at 10 kOe of the DC magnetic field, which is the maximum field allowed by our setup. But it tends to increase further at higher magnetic fields, as shown in Figure 8.

Because of the mechanical interactions between the ferrite and ferroelectric/piezoelectric perovskite phases throughout the fiber, the magnetic field induces strain in the ferrite phase, which results in stress in the ferroelectric phase. This stress produces a voltage in the shell via the piezoelectric effect.[39]

As discussed in our previous work,[63] the interface area between ferroelectric and ferromagnetic phases and phase connectivity is crucial in the strain-mediated ME composites.

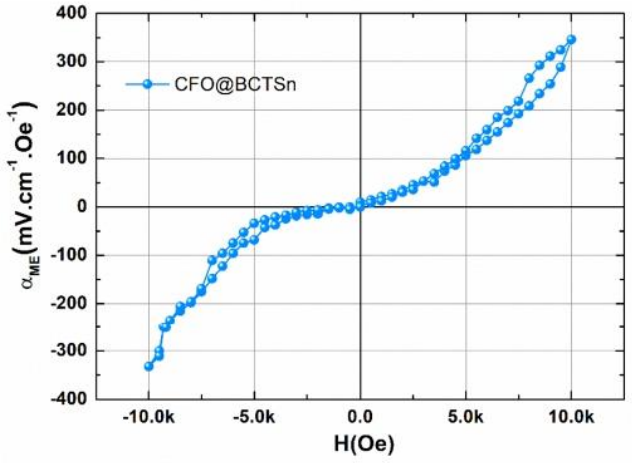

Figure 8. Dependence of the magnetoelectric coefficient of CFO@BCTSn NFs on the DC magnetic field at room temperature.

The improved magnetoelectric coefficient obtained in the CFO@BCTSn NFs directly relates to the electrospinning process. Indeed, the CFO@BCTSn NFs produced by electrospinning comprise nanoscale BCTSn and CFO grains as shown in SEM images (Figure 2). Such nanoscale grains can make a large interfacial area, favoring mechanical interactions between the piezoelectric and magnetostrictive phases. In addition, our composite fibers also have good phase connectivity, as observed in the TEM images (Figure 3). This can ensure complete strain transfer between the CFO and BCTSn phases, enhancing the magnetoelectric properties of these composites. As a result, the observed α_{ME} is higher than the α_{ME} = 13.3 mV cm^{-1} Oe^{-1} reported for $BaTiO_3/CoFe_2O_4$ composite fibers,[78] α_{ME} = 150.58 mV cm^{-1} Oe^{-1} reported for CFO@BT@PDA/(P(VDF-TrFE), and α_{ME} = 51 mV cm^{-1} Oe^{-1} reported for $CoFe_2O_4$ nanorods embedded in a $BaTiO_3$ matrix.[56] However, the obtained α_{ME} value in the CFO@BCTSn NFs is lower than 2.95 × 10^4 mV cm^{-1} Oe^{-1} reported for core–shell nanofibers made of $CoFe_2O_4$–$Pb(Zr_{0.52}Ti_{0.48})O_3$,[33] which may be attributed to the d_{33} piezoelectric coefficient of $Pb(Zr_{0.52}Ti_{0.48})O_3$ that is three or four times higher than that of the co-doped $BaTiO_3$.[57] According to this comparison, CFO@BCTSn NFs have the potential to be used as room-temperature magnetic field sensors.

4. CONCLUSION

In summary, CFO@BCTSn NFs have been successfully elaborated by the coaxial electrospinning method. The

https://doi.org/10.1021/acsanm.3c01101
ACS Appl. Nano Mater. XXXX, XXX, XXX–XXX

structural, morphological, and multiferroic properties of these nanofibers have been investigated. XRD and SAED analyses have confirmed the presence of perovskite and spinel structures in the CFO@BCTSn NFs. The morphology of the core−shell nanofibers has been observed by SEM and TEM images that endorse the core−shell connectivity. PFM mappings and M-H hysteresis loops were used to prove that the synthesized fibers exhibit both ferroelectric and ferromagnetic properties. The M_s and M_r values under a magnetic field of 25 kOe were 11.63 emu g^{-1} and 1.43 emu g^{-1}, respectively, while the piezoelectric response d_{33}^{eff} was approximately 6 pm V^{-1}. The ME coefficient obtained for the CFO@BCTSn NFs is 346 mV cm^{-1} Oe^{-1}, making them a promising candidate for nanoscale room-temperature ultrasensitive magnetic sensor applications.

AUTHOR INFORMATION

Corresponding Author

Youness Hadouch − *Laboratory of Innovative Materials, Energy and Sustainable Development (IMED), Faculty of Sciences and Technology, Cadi-Ayyad University, BP 549 Marrakech, Morocco; Laboratory of Physics of Condensed Matter (LPMC), University of Picardie Jules Verne, Scientific Pole, 80039 Cedex 1 Amiens, France;* orcid.org/0000-0002-8087-9494; Email: youness.hadouch@etud.u-picardie.fr, hadouch.younes@gmail.com

Authors

Daoud Mezzane − *Laboratory of Innovative Materials, Energy and Sustainable Development (IMED), Faculty of Sciences and Technology, Cadi-Ayyad University, BP 549 Marrakech, Morocco; Laboratory of Physics of Condensed Matter (LPMC), University of Picardie Jules Verne, Scientific Pole, 80039 Cedex 1 Amiens, France*

M'barek Amjoud − *Laboratory of Innovative Materials, Energy and Sustainable Development (IMED), Faculty of Sciences and Technology, Cadi-Ayyad University, BP 549 Marrakech, Morocco*

Valentyn Laguta − *Institute of Physics AS CR, 162 53 Prague, Czech Republic; Institute for Problems of Materials Science, National Academy of Science, Kyiv 03142, Ukraine*

Khalid Hoummada − *IM2NP Faculté des Sciences de Saint-Jérôme Case 142, Aix-Marseille University—CNRS, 13397 Marseille, France*

Voicu Octavian Dolocan − *IM2NP Faculté des Sciences de Saint-Jérôme Case 142, Aix-Marseille University—CNRS, 13397 Marseille, France;* orcid.org/0000-0001-8991-261X

Mustapha Jouiad − *Laboratory of Physics of Condensed Matter (LPMC), University of Picardie Jules Verne, Scientific Pole, 80039 Cedex 1 Amiens, France;* orcid.org/0000-0002-7587-1500

Mohammed Lahcini − *Laboratory of Innovative Materials, Energy and Sustainable Development (IMED), Faculty of Sciences and Technology, Cadi-Ayyad University, BP 549 Marrakech, Morocco; Mohamed VI Polytechnic University, 43150 Ben Guerir, Morocco;* orcid.org/0000-0003-1049-7906

Hana Uršič − *Jozef Stefan Institute, 1000 Ljubljana, Slovenia;* orcid.org/0000-0003-4525-404X

Val Fišinger − *Jozef Stefan Institute, 1000 Ljubljana, Slovenia*

Nikola Novak − *Jozef Stefan Institute, 1000 Ljubljana, Slovenia*

Zdravko Kutnjak − *Jozef Stefan Institute, 1000 Ljubljana, Slovenia*

Yaovi Gagou − *Laboratory of Physics of Condensed Matter (LPMC), University of Picardie Jules Verne, Scientific Pole, 80039 Cedex 1 Amiens, France*

Igor Lukyanchuk − *Laboratory of Physics of Condensed Matter (LPMC), University of Picardie Jules Verne, Scientific Pole, 80039 Cedex 1 Amiens, France*

Mimoun El Marssi − *Laboratory of Physics of Condensed Matter (LPMC), University of Picardie Jules Verne, Scientific Pole, 80039 Cedex 1 Amiens, France*

Complete contact information is available at: https://pubs.acs.org/10.1021/acsanm.3c01101

Author Contributions

We confirm that all authors mentioned in the manuscript have actively participated in, reviewed, and approved the content of the manuscript. Furthermore, they have provided their consent for the submission and subsequent publication of the manuscript. We confirm our active involvement in the work and assume public responsibility for its content. Additionally, each author declares that the work will not be submitted to any other journal or published elsewhere prior to this submission. Y.H.: Investigation, methodology, data curation, writing original draft, and validation. D.M.: Visualization, methodology, writing—review and editing, validation, and supervision. M.A.: Visualization, writing—review and editing, validation, and supervision. V.L.: Writing—review and editing, visualization, and validation. K.H.: review and editing, visualization, and validation. V.O.D.: Writing—review and editing, visualization, and validation. M.J.: Review and editing, visualization, and validation. M.L.: Review and editing, visualization, and validation. H.U.: Writing—Review and editing, visualization, and validation. V.F.: Formal analysis, writing, and validation. N.N.: Review and editing, visualization, and validation. Z.K.: Writing—Review and editing, visualization, and validation. Y.G.: Formal analysis, writing, validation, and supervision. I.L.: Review and editing, visualization, and validation. M.E.M.: Visualization, validation, writing—review and editing, and supervision.

Notes

The authors declare no competing financial interest.

ACKNOWLEDGMENTS

The European Union Horizon 2020 Research and Innovation actions MSCA-RISE-ENGIMA (No. 778072) and MSCA-RISE-MELON (No. 872631) have provided financial support for this study. H.U. acknowledges the Slovenian Research Agency (N2-0212, P2-0105) and thanks J. Cilenšek and V. Fišinger for help in the laboratory. Z.K. acknowledges the Slovenian Research Agency support (P1-0125).

REFERENCES

(1) Zhang, C. L.; Chen, W. Q.; Xie, S. H.; Yang, J. S.; Li, J. Y. The Magnetoelectric Effects in Multiferroic Composite Nanofibers. *Appl. Phys. Lett.* **2009**, *94* (10), 102907.

(2) Baji, A.; Mai, Y.-W.; Yimnirun, R.; Unruan, S. Electrospun Barium Titanate/Cobalt Ferrite Composite Fibers with Improved Magnetoelectric Performance. *RSC Adv.* **2014**, *4* (98), 55217−55223.

(3) Sreenivasulu, G.; Zhang, J.; Zhang, R.; Popov, M.; Petrov, V.; Srinivasan, G. Multiferroic Core-Shell Nanofibers, Assembly in a Magnetic Field, and Studies on Magneto-Electric Interactions. *Materials* **2018**, *11* (1), 18.

(4) Ortega, N.; Kumar, A.; Scott, J. F.; Katiyar, R. S. Multifunctional Magnetoelectric Materials for Device Applications. *J. Phys.: Condens. Matter* **2015**, *27* (50), 504002.
(5) Fetisov, Y. K.; Srinivasan, G. Electric Field Tuning Characteristics of a Ferrite-Piezoelectric Microwave Resonator. *Appl. Phys. Lett.* **2006**, *88* (14), 143503.
(6) Eerenstein, W.; Mathur, N. D.; Scott, J. F. Multiferroic and Magnetoelectric Materials. *Nature* **2006**, *442* (7104), 759−765.
(7) Nan, C.-W.; Bichurin, M. I.; Dong, S.; Viehland, D.; Srinivasan, G. Multiferroic Magnetoelectric Composites: Historical Perspective, Status, and Future Directions. *J. Appl. Phys.* **2008**, *103* (3), 031101.
(8) Fiebig, M. Revival of the Magnetoelectric Effect. *J. Phys. D: Appl. Phys.* **2005**, *38* (8), R123−R152.
(9) Bichurin, M.; Petrov, R.; Sokolov, O.; Leontiev, V.; Kuts, V.; Kiselev, D.; Wang, Y. Magnetoelectric Magnetic Field Sensors: A Review. *Sensors* **2021**, *21* (18), 6232.
(10) Sharma, I.; Renu; Pananjay Tiwari, A. Review on Multiferroic in Magnetic Field Sensor Applications. *Int. J. Basic Appl. Sci.* **2022**, *11*, 37−48.
(11) Xiang, H. J.; Wei, S.-H.; Whangbo, M.-H.; Da Silva, J. L. F. Spin-Orbit Coupling and Ion Displacements in Multiferroic TbMnO 3. *Phys. Rev. Lett.* **2008**, *101* (3), 037209.
(12) Kuo, C.-Y.; Hu, Z.; Yang, J. C.; Liao, S.-C.; Huang, Y. L.; Vasudevan, R. K.; Okatan, M. B.; Jesse, S.; Kalinin, S. V.; Li, L.; Liu, H. J.; Lai, C.-H.; Pi, T. W.; Agrestini, S.; Chen, K.; Ohresser, P.; Tanaka, A.; Tjeng, L. H.; Chu, Y. H. Single-Domain Multiferroic BiFeO3 Films. *Nat. Commun.* **2016**, *7* (1), 12712.
(13) Mickel, P. R.; Jeen, H.; Kumar, P.; Biswas, A.; Hebard, A. F. Proximate Transition Temperatures Amplify Linear Magnetoelectric Coupling in Strain-Disordered Multiferroic BiMnO 3. *Phys. Rev. B* **2016**, *93* (13), 134205.
(14) Kanamadi, C. M.; Das, B. K.; Kim, C. W.; Kang, D. I.; Cha, H. G.; Ji, E. S.; Jadhav, A. P.; Jun, B. − E.; Jeong, J. H.; Choi, B. C.; Chougule, B. K.; Kang, Y. S. Dielectric and Magnetic Properties of (x)CoFe2O4+(1−x)Ba0.8Sr0.2TiO3Magnetoelectric Composites. *Mater. Chem. Phys.* **2009**, *116* (1), 6−10.
(15) Shvartsman, V. V.; Alawneh, F.; Borisov, P.; Kozodaev, D.; Lupascu, D. C. Converse Magnetoelectric Effect in CoFe $_2$ O $_4$ − BaTiO $_3$ Composites with a Core−Shell Structure. *Smart Mater. Struct.* **2011**, *20* (7), 075006.
(16) Majumdar, M. G. Analysis of Stress-Coupled Magneto-Electric Effect in BaTiO3-CoFe2O4 Composites Using Raman Spectroscopy. *IJSER J.* **2012**, *3* (11), 8.
(17) Zhang, R.-F.; Deng, C.-Y.; Ren, L.; Li, Z.; Zhou, J.-P. Dielectric, Ferromagnetic and Maganetoelectric Properties of BaTiO3−Ni0.7Zn0.3Fe2O4 Composite Ceramics. *Mater. Res. Bull.* **2013**, *48* (10), 4100−4104.
(18) Kumar, A. S.; Lekha, C. S. C.; Vivek, S.; Nandakumar, K.; Anantharaman, M. R.; Nair, S. S. Effect of CoFe2O4 Weight Fraction on Multiferroic and Magnetoelectric Properties of (1 − x)-Ba0.85Ca0.15Zr0.1Ti0.9O3 − XCoFe2O4 Particulate Composites. *J. Mater. Sci: Mater. Electron* **2019**, *30* (9), 8239−8248.
(19) Wang, Y.; Pu, Y.; Shi, Y.; Cui, Y. Ferroelectric, Magnetic, Magnetoelectric Properties of the Ba0.9Ca0.1Ti0.9Zr0.1O3/CoFe2O4 Laminated Composites. *J. Mater. Sci: Mater. Electron* **2017**, *28* (15), 11125−11131.
(20) Patil, D.; Kim, J.-H.; Chai, Y. S.; Nam, J.-H.; Cho, J.-H.; Kim, B.-I.; Kim, K. H. Large Longitudinal Magnetoelectric Coupling in NiFe $_2$ O $_4$ − BaTiO $_3$ Laminates. *Appl. Phys. Express* **2011**, *4* (7), 073001.
(21) Kola, L.; Swain, A. B.; Subramanian, V.; Murugavel, P. Large Magnetoelectric Response in Lead Free BaTi1−xSnxO3/NiFe2O4 Bilayer Laminated Composites. *J. Mater. Sci: Mater. Electron* **2019**, *30* (7), 6725−6733.
(22) Pradhan, L. K.; Pandey, R.; Kumar, R.; Kar, M. Lattice Strain Induced Multiferroicity in PZT-CFO Particulate Composite. *J. Appl. Phys.* **2018**, *123* (7), 074101.
(23) Yadav, S. K.; Hemalatha, J. Electrospinning and Characterization of Magnetoelectric NdFeO3−PbZr0.52Ti0.48O3 Core−Shell Nanofibers. *Ceram. Int.* **2022**, *48* (13), 18415−18424.
(24) Xie, S. H.; Li, J. Y.; Liu, Y. Y.; Lan, L. N.; Jin, G.; Zhou, Y. C. Electrospinning and Multiferroic Properties of NiFe2O4−Pb(Zr0.52Ti0.48)O3 Composite Nanofibers. *J. Appl. Phys.* **2008**, *104*, 024115.
(25) Kaviraj, P.; Pramanik, R.; Arockiarajan, A. Influence of Individual Phases and Temperature on Properties of C o F e 2 O 4 - B a T i O 3 Magnetoelectric Core-Shell Nanocomposites. *Ceram. Int.* **2019**, *45* (9), 12344−12352.
(26) Wu, H.; Ao, H.; Li, W.; Zeng, Z.; Gao, R.; Fu, C.; Chen, G.; Deng, X.; Wang, Z.; Lei, X.; Cai, W. Improvement of Magnetoelectric Coupling Effect in Ba0.8Sr0.2TiO3-Co0.5Cu0.5Fe2O4Multiferroic Fluids by Tuning the Composition. *Materials Today Chemistry* **2021**, *21*, 100511.
(27) Gao, R.; Xu, Z.; Bai, L.; Zhang, Q.; Wang, Z.; Cai, W.; Chen, G.; Deng, X.; Cao, X.; Luo, X.; Fu, C. Electric Field-Induced Magnetization Rotation in Magnetoelectric Multiferroic Fluids. *Adv. Electron. Mater.* **2018**, *4* (6), 1800030.
(28) Gao, R.; Zhang, Q.; Xu, Z.; Wang, Z.; Chen, G.; Fu, C.; Deng, X.; Cai, W. Anomalous Magnetoelectric Coupling Effect of CoFe $_2$ O $_4$ − BaTiO $_3$ Binary Mixed Fluids. *ACS Appl. Electron. Mater.* **2019**, *1* (7), 1120−1132.
(29) Gao, R.; Zhang, Q.; Xu, Z.; Wang, Z.; Cai, W.; Chen, G.; Deng, X.; Cao, X.; Luo, X.; Fu, C. Strong Magnetoelectric Coupling Effect in BaTiO $_3$ @CoFe $_2$ O $_4$ Magnetoelectric Multiferroic Fluids. *Nanoscale* **2018**, *10* (25), 11750−11759.
(30) Huang, W.; Yang, S.; Li, X. Multiferroic Heterostructures and Tunneling Junctions. *Journal of Materiomics* **2015**, *1* (4), 263−284.
(31) Liu, Y.; Sreenivasulu, G.; Zhou, P.; Fu, J.; Filippov, D.; Zhang, W.; Zhou, T.; Zhang, T.; Shah, P.; Page, M. R.; Srinivasan, G.; Berweger, S.; Wallis, T. M.; Kabos, P. Converse Magneto-Electric Effects in a Core−Shell Multiferroic Nanofiber by Electric Field Tuning of Ferromagnetic Resonance. *Sci. Rep* **2020**, *10* (1), 20170.
(32) Molavi, A. M.; Alizadeh, P. Electrospinning of Multiferroic CoFe2O4@ Ba(Zr0.2Ti0.8)O3−0.5(Ba0.7Ca0.3)TiO3 Nano-Structured Fibers via Two Different Routes. *Mater. Charact.* **2021**, *172*, 110880.
(33) Xie, S.; Ma, F.; Liu, Y.; Li, J. Multiferroic CoFe2O4−Pb(Zr0.52Ti0.48)O3 Core-Shell Nanofibers and Their Magnetoelectric Coupling. *Nanoscale* **2011**, *3* (8), 3152.
(34) Nan, C.-W.; Bichurin, M. I.; Dong, S.; Viehland, D.; Srinivasan, G. Multiferroic Magnetoelectric Composites: Historical Perspective, Status, and Future Directions. *J. Appl. Phys.* **2008**, *103* (3), 031101.
(35) Lyubchyk, A.; Filonovich, S. A.; Mateus, T.; Mendes, M. J.; Vicente, A.; Leitão, J. P.; Falcão, B. P.; Fortunato, E.; Águas, H.; Martins, R. Nanocrystalline Thin Film Silicon Solar Cells: A Deeper Look into p/i Interface Formation. *Thin Solid Films* **2015**, *591*, 25−31.
(36) Padmapriya, D.; Dhayanithi, D.; Rashid, A.; Rahul, M. T.; Kalarikkal, N.; Muneeswaran, M.; Giridharan, N. V. Composition-Dependent Structural, Electrical, Magnetic and Magnetoelectric Properties of (1 − x)BaTiO3−xCoFe2O4 Particulate Composites. *Bull. Mater. Sci.* **2020**, *43* (1), 276.
(37) Rani, J.; Yadav, K. L.; Prakash, S. Dielectric and Magnetic Properties of x CoFe 2 O 4 − (1 − x)[0.5Ba(Zr 0.2 Ti 0.8)O 3 − 0.5(Ba 0.7 Ca 0.3)TiO 3] Composites. *Mater. Res. Bull.* **2014**, *60*, 367−375.
(38) Praveen J, P.; Monaji, V. R.; Kumar, S. D.; Subramanian, V.; Das, D. Enhanced Magnetoelectric Response from Lead-Free (Ba0.85Ca0.15)(Zr0.1Ti0.9)O3 − CoFe2O4 Laminate and Particulate Composites. *Ceram. Int.* **2018**, *44* (4), 4298−4306.
(39) Momin, A. A.; Zubair, M. A.; Islam, Md. F.; Hossain, A. K. M. A. Enhance Magnetoelectric Coupling in XLi0.1Ni0.2Mn0.6-Fe2.1O4−(1 − x)BiFeO3Multiferroic Composites. *J. Mater. Sci: Mater. Electron* **2019**, *30* (14), 13033−13046.
(40) Walther, T.; Straube, U.; Köferstein, R.; Ebbinghaus, S. G. Hysteretic Magnetoelectric Behavior of CoFe $_2$ O $_4$ − BaTiO $_3$

https://doi.org/10.1021/acsanm.3c01101
ACS Appl. Nano Mater. XXXX, XXX, XXX−XXX

Composites Prepared by Reductive Sintering and Reoxidation. *J. Mater. Chem. C* **2016**, *4* (21), 4792−4799.
(41) Breitenbach, M.; Deniz, H.; Ebbinghaus, S. G. Magnetoelectric and HR-STEM Investigations on Eutectic CoFe2O4−Ba1−XSrxTiO3 Composites. *J. Phys. Chem. Solids* **2019**, *135*, 109076.
(42) Pan, P.; Tao, J.; Ma, F.; Zhang, N. Magnetodielectric Effect in (1 − x)(Ba0.88Ca0.12)(Ti0.88Zr0.12)O3 − XCoFe2O4. *J. Magn. Magn. Mater.* **2018**, *453*, 91−95.
(43) Agarwal, S.; Caltun, O. F.; Sreenivas, K. Magneto Electric Effects in BaTiO3−CoFe2O4 Bulk Composites. *Solid State Commun.* **2012**, *152* (21), 1951−1955.
(44) Zhang, Z.; Wang, L.; Wang, J.; Jiang, X.; Li, X.; Hu, Z.; Ji, Y.; Wu, X.; Chen, C. Mesoporous Silica-Coated Gold Nanorods as a Light-Mediated Multifunctional Theranostic Platform for Cancer Treatment. *Adv. Mater.* **2012**, *24* (11), 1418−1423.
(45) Scott, J. F. Applications of Magnetoelectrics. *J. Mater. Chem.* **2012**, *22* (11), 4567.
(46) Cernea, M.; Vasile, B. S.; Surdu, V. A.; Trusca, R.; Sima, M.; Craciun, F.; Galassi, C. Piezoelectric/Ferromagnetic BNT-BT0.08/CoFe2O4 Coaxial Core−Shell Composite Nanotubes for Nanoelectronic Devices. *J. Alloys Compd.* **2018**, *752*, 381−388.
(47) Fu, B.; Lu, R.; Gao, K.; Yang, Y.; Wang, Y. Substrate Clamping Effect onto Magnetoelectric Coupling in Multiferroic $BaTiO_3$-$CoFe_2O_4$ Core-Shell Nanofibers via Coaxial Electrospinning. *EPL* **2015**, *112* (2), 27002.
(48) Makarova, T. L.; Zakharchuk, I.; Geydt, P.; Lahderanta, E.; Komlev, A. A.; Zyrianova, A. A.; Lyubchyk, A.; Kanygin, M. A.; Sedelnikova, O. V.; Kurenya, A. G.; Bulusheva, L. G.; Okotrub, A. V. Assessing Carbon Nanotube Arrangement in Polystyrene Matrix by Magnetic Susceptibility Measurements. *Carbon* **2016**, *96*, 1077−1083.
(49) Wang, Z.; Liu, X.; Lv, M.; Chai, P.; Liu, Y.; Zhou, X.; Meng, J. Preparation of One-Dimensional $CoFe_2O_4$ Nanostructures and Their Magnetic Properties. *J. Phys. Chem. C* **2008**, *112* (39), 15171−15175.
(50) Fu, J.; Zhang, J.; Peng, Y.; Zhao, J.; Tan, G.; Mellors, N. J.; Xie, E.; Han, W. Unique Magnetic Properties and Magnetization Reversal Process of CoFe2O4 Nanotubes Fabricated by Electrospinning. *Nanoscale* **2012**, *4* (13), 3932.
(51) Naumov, I. I.; Bellaiche, L.; Fu, H. Unusual Phase Transitions in Ferroelectric Nanodisks and Nanorods. 2004, *432*.
(52) Lahoche, L.; Luk'Yanchuk, I.; Pascoli, G. Stability of Vortex Phases in Ferroelectric Easy-Plane Nano-cylinders. *Integr. Ferroelectr.* **2008**, *99* (1), 60−66.
(53) Prosandeev, S.; Malashevich, A.; Gui, Z.; Louis, L.; Walter, R.; Souza, I.; Bellaiche, L. Natural Optical Activity and Its Control by Electric Field in Electrotoroidic Systems. *Phys. Rev. B* **2013**, *87* (19), 195111.
(54) Pavlenko, M. A.; Di Rino, F.; Boron, L.; Kondovych, S.; Sené, A.; Tikhonov, Y. A.; Razumnaya, A. G.; Vinokur, V. M.; Sepliarsky, M.; Lukyanchuk, I. A. Phase Diagram of a Strained Ferroelectric Nanowire. *Crystals* **2022**, *12* (4), 453.
(55) Kondovych, S.; Pavlenko, M.; Tikhonov, Y.; Razumnaya, A.; Lukyanchuk, I. Vortex States in a $PbTiO_3$ Ferroelectric Cylinder. *arXiv Preprint (Mesoscale and Nanoscale Physics)*, October 29, 2022. arXiv:2112.10129. http://arxiv.org/abs/2112.10129 (accessed 2023-02-23).
(56) Deng, Y.; Zhou, J.; Wu, D.; Du, Y.; Zhang, M.; Wang, D.; Yu, H.; Tang, S.; Du, Y. Three-Dimensional Phases-Connectivity and Strong Magnetoelectric Response of Self-Assembled Feather-like CoFe2O4−BaTiO3 Nanostructures. *Chem. Phys. Lett.* **2010**, *496* (4−6), 301−305.
(57) Hao, J.; Li, W.; Zhai, J.; Chen, H. Progress in High-Strain Perovskite Piezoelectric Ceramics. *Materials Science and Engineering: R: Reports* **2019**, *135*, 1−57.
(58) Amiri, S.; Shokrollahi, H. The Role of Cobalt Ferrite Magnetic Nanoparticles in Medical Science. *Materials Science and Engineering: C* **2013**, *33* (1), 1−8.
(59) Safi, R.; Ghasemi, A.; Shoja-Razavi, R.; Ghasemi, E.; Sodaee, T. Rietveld Structure Refinement, Cations Distribution and Magnetic Features of CoFe2O4 Nanoparticles Synthesized by Co-Precipitation, Hydrothermal, and Combustion Methods. *Ceram. Int.* **2016**, *42* (5), 6375−6382.
(60) Lin, Q.; Lin, J.; He, Y.; Wang, R.; Dong, J. The Structural and Magnetic Properties of Gadolinium Doped $CoFe_2O_4$ Nanoferrites. *J. Nanomater.* **2015**, *2015*, 1−6.
(61) Hadouch, Y.; Mezzane, D.; Amjoud, M.; Hajji, L.; Gagou, Y.; Kutnjak, Z.; Laguta, V.; Kopelevich, Y.; El Marssi, M. Enhanced Relative Cooling Power and Large Inverse Magnetocaloric Effect of Cobalt Ferrite Nanoparticles Synthesized by Auto-Combustion Method. *J. Magn. Magn. Mater.* **2022**, *563*, 169925.
(62) Xie, S. H.; Li, J. Y.; Qiao, Y.; Liu, Y. Y.; Lan, L. N.; Zhou, Y. C.; Tan, S. T. Multiferroic CoFe2O4−Pb(Zr0.52Ti0.48)O3 Nanofibers by Electrospinning. *Appl. Phys. Lett.* **2008**, *92* (6), 062901.
(63) Hadouch, Y.; Mezzane, D.; Amjoud, M.; Oueldna, N.; Gagou, Y.; Kutnjak, Z.; Laguta, V.; Kopelevich, Y.; Hoummada, K.; Marssi, M. E. Piezoelectric, Magnetic and Magnetoelectric Properties of a New Lead-Free Multiferroic (1-x) Ba0.95Ca0.05Ti0.89Sn0.11O3—(x) CoFe2O4 Particulate Composites. *J. Mater. Sci.: Mater. Electron.* **2023**, *34* (8), 725.
(64) Hanani, Z.; Izanzar, I.; Merselmiz, S.; El Assimi, T.; Mezzane, D.; Amjoud, M.; Uršič, H.; Prah, U.; Ghanbaja, J.; Saadoune, I.; Lahcini, M.; Spreitzer, M.; Vengust, D.; El Marssi, M.; Kutnjak, Z.; Luk'yanchuk, I. A.; Gouné, M. A Flexible Self-Poled Piezocomposite Nanogenerator Based on $H_2(Zr_{0.1}Ti_{0.9})_3O_7$ Nanowires and Polylactic Acid Biopolymer. *Sustainable Energy Fuels* **2022**, *6* (8), 1983−1991.
(65) Makovec, D.; Križaj, N.; Meden, A.; Dražić, G.; Uršič, H.; Kostanjšek, R.; Šala, M.; Gyergyek, S. Ferroelectric Bismuth-Titanate Nanoplatelets and Nanowires with a New Crystal Structure. *Nanoscale* **2022**, *14* (9), 3537−3544.
(66) Uršič, H.; Prah, U. Investigations of Ferroelectric Polycrystalline Bulks and Thick Films Using Piezoresponse Force Microscopy. *Proc. R. Soc. A* **2019**, *475* (2223), 20180782.
(67) Laguta, V. V.; Morozovska, A. N.; Eliseev, E. A.; Raevski, I. P.; Raevskaya, S. I.; Sitalo, E. I.; Prosandeev, S. A.; Bellaiche, L. Room-Temperature Paramagnetoelectric Effect in Magnetoelectric Multiferroics Pb(Fe1/2Nb1/2)O3 and Its Solid Solution with PbTiO3. *J. Mater. Sci.* **2016**, *51* (11), 5330−5342.
(68) Zi, Z.; Sun, Y.; Zhu, X.; Yang, Z.; Dai, J.; Song, W. Synthesis and Magnetic Properties of CoFe2O4 Ferrite Nanoparticles. *J. Magn. Magn. Mater.* **2009**, *321* (9), 1251−1255.
(69) Hadouch, Y.; Ben Moumen, S.; Mezzourh, H.; Mezzane, D.; Amjoud, M.; Asbani, B.; Razumnaya, A. G.; Gagou, Y.; Rožič, B.; Kutnjak, Z.; El Marssi, M. Electrocaloric Effect and High Energy Storage Efficiency in Lead-Free Ba0.95Ca0.05Ti0.89Sn0.11O3 Ceramic Elaborated by Sol−Gel Method. *J. Mater. Sci: Mater. Electron* **2022**, *33* (4), 2067−2079.
(70) Verma, K. C.; Singh, M.; Kotnala, R. K.; Goyal, N. Magnetic Field Control of Polarization/Capacitance/Voltage/Resistance through Lattice Strain in BaTiO3-CoFe2O4Multiferroic Nanocomposite. *J. Magn. Magn. Mater.* **2019**, *469*, 483−493.
(71) Lyu, J.; Fina, I.; Solanas, R.; Fontcuberta, J.; Sánchez, F. Tailoring Lattice Strain and Ferroelectric Polarization of Epitaxial BaTiO3 Thin Films on Si(001). *Sci. Rep* **2018**, *8* (1), 495.
(72) Liu, W.; Chan, Y.; Cai, J.; Leung, C.; Mak, C.; Wong, K.; Zhang, F.; Wu, X.; Qi, X. D. Understanding the Formation of Ultrafine Spinel CoFe2O4 Nanoplatelets and Their Magnetic Properties. *J. Appl. Phys.* **2012**, *112* (10), 104306.
(73) Ponce, A. S.; Chagas, E. F.; Prado, R. J.; Fernandes, C. H. M.; Terezo, A. J.; Baggio-Saitovitch, E. High Coercivity Induced by Mechanical Milling in Cobalt Ferrite Powders. *J. Magn. Magn. Mater.* **2013**, *344*, 182−187.
(74) Guillaud, C. Elementary Mechanisms of Magnetization in Mixed Oxides of Iron and Cobalt. *Rev. Mod. Phys.* **1953**, *25* (1), 64−73.
(75) Sangeneni, N.; Taddei, K.; Bhat, N.; Shivashankar, S. Magnetic Properties of Superparamagnetic, Nanocrystalline Cobalt Ferrite Thin

https://doi.org/10.1021/acsanm.3c01101
ACS Appl. Nano Mater. XXXX, XXX, XXX−XXX

Films Deposited at Low Temperature. *J. Magn. Magn. Mater.* **2018**, *465*, 590−597.
(76) Xu, S.; Ma, Y.; Geng, B.; Sun, X.; Wang, M. The Remanence Ratio in CoFe2O4 Nanoparticles with Approximate Single-Domain Sizes. *Nanoscale Res. Lett.* **2016**, *11* (1), 471.
(77) Lu, R. E.; Chang, K. G.; Fu, B.; Shen, Y. J.; Xu, M. W.; Yang, S.; Song, X. P.; Liu, M.; Yang, Y. D. Magnetic Properties of Different $CoFe_2O_4$ Nanostructures: Nanofibers versus Nanoparticles. *J. Mater. Chem. C* **2014**, *2* (40), 8578−8584.
(78) Baji, A.; Mai, Y.-W.; Yimnirun, R.; Unruan, S. Electrospun Barium Titanate/Cobalt Ferrite Composite Fibers with Improved Magnetoelectric Performance. *RSC Adv.* **2014**, *4* (98), 55217−55223.

https://doi.org/10.1021/acsanm.3c01101
ACS Appl. Nano Mater. XXXX, XXX, XXX−XXX

General conclusion and future perspectives

This manuscript describes an investigation into novel nanoscale magnetoelectric composite materials, with the goal of enhancing the magnetoelectric effect in multiferroic composites. Specifically, lead-free magnetoelectric composites consisting of (1–x) $Ba_{0.95}Ca_{0.05}Ti_{0.89}Sn_{0.11}O_3$ - (x) $CoFe_2O_4$ ($0 \leq x \leq 0.5$) with (0–3) and Core-shell nanofibers (1-3) connectivities have been successfully synthesized using mechanical mixing of elaborated powders and electrospinning methods. The individual phases, ferroelectric BCTSn and ferromagnetic CFO, and their composites were studied and characterized using XRD, Raman, and EDX analysis, confirming the coexistence of their pure phases. The ferroelectric study of BCTSn revealed improved energy storage performance, while magnetic measurements showed a first-order PM-FM phase transition in CFO with an enhanced RCP of 687.56 J Kg^{-1} and a large value of magnetocaloric temperature change of $\Delta T = 11.2$ K. Ferroelectric and magnetic hysteresis loop measurements were used to confirm the composites' room temperature multiferroic characteristics. For all composites, the converse piezoelectric coefficient (d^*_{33}) was measured and reported. PFM mappings were used to confirm the ferroelectric and piezoelectric properties of CFO@BCTSn NFs, and M-H hysteresis loops were employed to prove their ferromagnetic properties. The largest ME coefficient (0.1 $mVcm^{-1}Oe^{-}1$) for the CFO-BCTSn particulate composite (0-3) was reported in the composition of 0.7BCTSn-0.3CFO, which is close to pseudocubic symmetry and relatively dense, reducing lattice strain and hence promoting domain switching. Interestingly, a significant ME coefficient of 346 mV cm-1 Oe-1 is observed in CFO@BCTSn NFs. These finding demonstrate that designing nanostructured couplings, the interfacial area can be increased, favoring mechanical interactions between the piezoelectric and magnetostrictive phases and improving the magnetoelectric effect. The existence of high ME coefficients in nanostructured composites reveals that the magnetoelectric effect may be further enhanced by the design of nanostructured couplings. Overall, the present study provides a strong starting point for the further development of magnetoelectric composite materials with enhanced capabilities for a wide variety of applications including energy harvesting, sensing, and information storage.

The performance of the developed composites would be improved on several of future research topics. The following research may focus on the points listed below:

- Investigate how the magnetoelectric properties could be affected by the thickness of shell/core;
- Examine how the elaborate composites' magnetoelectric effect would be impacted by temperature;
- Analyze how different interfaces between the piezoelectric and magnetostrictive phases would impact the magnetoelectric effect;
- Design of other magnetoelectric composites by varying the piezoelectric phases;
- Elaborate composites for multiferroic energy harvesting devices made of BCTSn-CFO and polymer;
- Develop theoretical models to understand the underlying mechanisms behind the observed properties of the composite;
- • Explore the possibility of incorporating the composite into already-available technology, including MEMS devices or magnetic sensors.

DESIGN AND CHARACTERIZATION OF MULTIFERROIC COMPOSITES SPINEL/PEROVSKITE WITH (0-3) AND CORE SHELL NANOFIBER CONNECTIVITIES

Abstract

Multiferroic magnetoelectric materials, which show both ferroelectricity and ferromagnetism, have recently sparked a surge in scientific curiosity and amazing technological promise in novel multifunctional devices. This thesis focuses on the development of new magnetoelectric composites with (0-3) and core-shell nanofiber connectivities. First, the properties of the pristine phases, ferroelectric ($Ba_{0.95}Ca_{0.05}Ti_{0.89}Sn_{0.11}O_3$) BCTSn and ferromagnetic ($CoFe_2O_4$) CFO, were studied separately. The investigations include a detailed examination of their structural and morphological properties, as well as an examination of electrocaloric (of BCTSn) and magnetocaloric (of CFO) effects. The energy storage properties of the BCTSn phase were also investigated. Second, the room temperature multiferroic properties of (0-3) composites were confirmed using ferroelectric and magnetic hysteresis loop measurements. For CFO@BCTSn NFs, the ferroelectric and piezoelectric properties were confirmed by PFM mappings and the M-H hysteresis loops were used to prove the ferromagnetic properties. For CFO-BCTSn particulate composite, the largest ME coefficient is 0.1 mV cm^{-1} Oe^{-1} observed in 0.7BCTSn-0.3CFO composition. However, CFO@BCTSn NFs show a high ME coefficient of 346 mV cm^{-1} Oe^{-1}. These findings suggest that designing nanostructured couplings can enhance the interfacial area, promoting mechanical interactions between the piezoelectric and magnetostrictive phases, thus improving the magnetoelectric effect.

Résumé

Les matériaux magnétoélectriques multiferroïques, qui présentent à la fois de la ferroélectricité et du ferromagnétisme, ont récemment suscité un regain de curiosité scientifique et une promesse technologique étonnante dans de nouveaux dispositifs multifonctionnels. Cette thèse porte sur le développement de nouveaux composites magnétoélectriques avec des connectivités de nanofibres (0-3) et cœur-coquille. Premièrement, les propriétés des phases primitives, ferroélectrique ($Ba_{0.95}Ca_{0.05}Ti_{0.89}Sn_{0.11}O_3$) BCTSn et ferromagnétique ($CoFe_2O_4$) CFO, ont été étudiées séparément. Les investigations comprennent un examen détaillé de leurs propriétés structurales et morphologiques, ainsi qu'un examen des effets électrocaloriques (de BCTSn) et magnétocaloriques (de CFO). Les propriétés de stockage d'énergie de la phase BCTSn ont également été étudiées. Deuxièmement, les propriétés multiferroïques à température ambiante des composites (0-3) ont été confirmés à l'aide de mesures de boucles d'hystérésis ferroélectriques et magnétiques. Pour les nanofibres de CFO@BCTSn, les propriétés ferroélectriques et piézoélectriques ont été confirmées par des cartographies PFM et les boucles d'hystérésis M-H ont été utilisées pour prouver les propriétés ferromagnétiques. Pour le composite particulaire CFO-BCTSn, le plus grand coefficient ME est de 0,1 mV cm^{-1} Oe^{-1} observé dans la composition 0,7 BCTSn-0,3 CFO. Cependant, les nanofibres de CFO@BCTSn montrent un coefficient ME élevé de 346 mV cm^{-1} Oe^{-1}. Ces résultats suggèrent que la conception de couplages nanostructurés peut améliorer la zone interfaciale, favorisant les interactions mécaniques entre les phases piézoélectrique et magnétostrictive, améliorant ainsi l'effet magnétoélectrique.